

AWARD NUMBER: W81XWH-18-1-0413

TITLE: TBI-Related Risk Factors for Alzheimer's Disease: Early Detection and Prognosis via Multimodal Brain Imaging and Connectomics

PRINCIPAL INVESTIGATOR: Andrei Irimia, PhD

CONTRACTING ORGANIZATION: University of Southern California

REPORT DATE: JANUARY 2022

TYPE OF REPORT: Final

PREPARED FOR: U.S. Army Medical Research and Development
Command Fort Detrick, Maryland 21702-5012

DISTRIBUTION STATEMENT: Approved for public release; distribution is unlimited

The views, opinions and/or findings contained in this report are those of the author(s) and should not be construed as an official Department of the Army position, policy or decision unless so designated by other documentation.

REPORT DOCUMENTATION PAGE

Form Approved
OMB No. 0704-0188

Public reporting burden for this collection of information is estimated to average 1 hour per response, including the time for reviewing instructions, searching existing data sources, gathering and maintaining the data needed, and completing and reviewing this collection of information. Send comments regarding this burden estimate or any other aspect of this collection of information, including suggestions for reducing this burden to Department of Defense, Washington Headquarters Services, Directorate for Information Operations and Reports (0704-0188), 1215 Jefferson Davis Highway, Suite 1204, Arlington, VA 22202-4302. Respondents should be aware that notwithstanding any other provision of law, no person shall be subject to any penalty for failing to comply with a collection of information if it does not display a currently valid OMB control number. **PLEASE DO NOT RETURN YOUR FORM TO THE ABOVE ADDRESS.**

1. REPORT DATE JANUARY 2022			2. REPORT TYPE FINAL		3. DATES COVERED 09/15/2018 - 09/14/2021	
4. TITLE AND SUBTITLE TBI-Related Risk Factors for Alzheimer's Disease: Early Detection and Prognosis via Multimodal Brain Imaging and Connectomics					5a. CONTRACT NUMBER W81XWH-18-1-0413	
					5b. GRANT NUMBER	
					5c. PROGRAM ELEMENT NUMBER	
6. AUTHOR(S) ANDREI IRIMIA, PHD E-Mail: IRIMIA@USC.EDU					5d. PROJECT NUMBER	
					5e. TASK NUMBER	
					5f. WORK UNIT NUMBER	
7. PERFORMING ORGANIZATION NAME(S) AND ADDRESS(ES) UNIVERSITY OF SOUTHERN CALIFORNIA 3720 S FLOWER ST FL 3 LOS ANGELES CA 90007-4318					8. PERFORMING ORGANIZATION REPORT NUMBER	
9. SPONSORING / MONITORING AGENCY NAME(S) AND ADDRESS(ES) U.S. Army Medical Research and Development Command Fort Detrick, Maryland 21702-5012					10. SPONSOR/MONITOR'S ACRONYM(S)	
					11. SPONSOR/MONITOR'S REPORT NUMBER(S)	
12. DISTRIBUTION / AVAILABILITY STATEMENT Approved for Public Release; Distribution Unlimited						
13. SUPPLEMENTARY NOTES						
14. ABSTRACT The purpose of this study is to utilize multimodal imaging to identify AD risk factors specific to the TBI population. The study scope involves (1) finding TBI-affected structural/connectomic features which are significantly associated with AD risk; and (2) imaging biomarkers which are statistically independent from other well-documented AD risk factors and which can assist with early identifying TBI survivors at risk for AD. In this reporting period, we performed automatic identification of AD/TBI pathology, calculated volumetrics, implemented connectomic/topological analyses, found TBI/AD-related connectome differences, published our results and disseminated them. Results indicate that the TBI-affected brains of older adults experience neurodegeneration on a scale which rivals that of age- and sex-matched AD patients. We also found properties of the TBI-affected brain whose characteristics are commensurate with the likelihood of TBI survivors to exhibit accelerated neurodegeneration, which may lead to the identification of early biomarkers of high AD risk.						
15. SUBJECT TERMS traumatic brain injury, Alzheimer's disease, risk biomarkers, magnetic resonance imaging, connectomics, network theory						
16. SECURITY CLASSIFICATION OF:			17. LIMITATION OF ABSTRACT Unclassified	18. NUMBER OF PAGES 94	19a. NAME OF RESPONSIBLE PERSON USAMRDC	
a. REPORT Unclassified	b. ABSTRACT Unclassified	c. THIS PAGE Unclassified			19b. TELEPHONE NUMBER (include area code)	

TABLE OF CONTENTS

	<u>Page</u>
1. Introduction	4
2. Keywords	4
3. Accomplishments	4
4. Impact	15
5. Changes/Problems	16
6. Products	17
7. Participants and Other Collaborating Organizations	21
8. Special Reporting Requirements	22
9. Appendices	22

1. INTRODUCTION:

Although traumatic brain injury (TBI) victims are more likely to develop Alzheimer’s disease (AD), it is difficult to estimate AD risk in TBI patients. For this reason, it would be extremely useful to understand how TBI may lead to AD, and to identify new ways to predict how likely it is for a TBI victim to develop AD. The purpose of this scientific study is to utilize sophisticated imaging and connectomic methods to study the brains of older adults who are either healthy, TBI survivors, AD patients, or both. The main hypothesis of the study is that the TBI-affected brain has certain anatomic properties which, if known, could help scientists to predict the likelihood of AD after TBI with high accuracy. The secondary hypothesis of the study is that at least some of these properties are different from those which are already known to be risk factors for AD (e.g. obesity, smoking, a history of high blood pressure, or certain inherited traits). This project thus aims to identify novel AD risk factors specific to the TBI population. The ability to accurately identify TBI victims at high risk for AD could have substantial consequences for the healthcare of such individuals; understanding the relationship between TBI and AD could advance our scientific and clinical knowledge regarding these two conditions.

2. KEYWORDS:

traumatic brain injury, Alzheimer’s disease, risk biomarkers, magnetic resonance imaging, connectomics, network theory.

3. ACCOMPLISHMENTS:

What were the major goals of the project?

The primary aim of this study is to test the hypothesis that the TBI-affected brain has structural and/or connectomic features which are significantly associated, in a statistical sense, with AD risk and which can allow TBI survivors to be stratified based on such risk. Our secondary hypothesis is that some of these biomarker-like features are specific to the TBI-affected brain, i.e. that they are statistically independent from other known and well-documented AD risk factors. The study aims to use multimodal neuroimaging—including magnetic resonance imaging (MRI) and diffusion tensor imaging (DTI)—to understand the differences between four populations: (1) the healthy aging brain, (2) the TBI-affected brain, (3) the AD-affected brain, and (4) the brain affected by both TBI and AD. We aim to use advanced computational neuroanatomy, neural network analysis and connectomics to identify statistically significant differences between these four groups, with the goal of identifying new biomarkers which can be used to reliably estimate AD risk in TBI survivors. We use a 2×2 factorial experimental design (factors: single mild TBI, AD) to identify and quantify the neuroanatomic and connectomic features of older adults (aged 65+) whose existence is modulated by TBI/AD interactions. Expert-validated, TBI/AD-tailored computational analyses of high-quality, multimodal MRI and DTI volumes acquired at high resolution from an adequately powered volunteer sample have allowed us to quantify brain volumetrics and morphometrics in the presence of TBI/AD-related (non-)hemorrhagic lesions. In each volunteer, MRI/DTI volume information is then used to map the macroscale connectome, its topology and to infer its network-theoretic properties, which are subsequently compared across groups.

Milestone	Timeline	Status
Project Run-in		
	Months	
Local IRB Approval	1	Granted
HRPO Approval	1-2	Granted
Maintain all IRB approvals	1-3	Approved
Train research staff in all research protocols	1-2	Completed
Create, revise, distribute research protocol manual	1-2	Completed
Identification of AD risk factors in TBI survivors		
	Months	
Perform automatic identification of AD/TBI pathology	1-6	Completed
Calculate volumetrics and morphometrics	1-6	Completed
Implement connectomic and topological analyses	1-6	Completed
Find TBI/AD-related connectome differences	7-16	Completed
Internal validation of volumetrics/morphometrics	7-10	Completed
Confirmation by TBI/AD clinicians	11-14, 26-28	Completed
Internal validation of connectomic/topological analysis	13-18	Completed
Implement statistical analysis of results	19-24	Completed
Reliability testing	23-26	Completed
Alternative hypotheses testing as needed	25-32	Completed
Revisions to methods as needed	22-34	Completed
Open software release via NITRC	32-36	Completed
Product: methodological manuscripts on analysis	6-18	Completed
Product: software for TBI/AD connectome analysis	12	Completed
Product: manuscripts on TBI/AD connectome analysis	18-24	Completed
Product: manuscripts on statistical analysis	24-36	Completed
Product: presentations at national meetings	9, 21, 35	Completed

What was accomplished under these goals?

(1) Major activities

Throughout this annual reporting period, the following major activities were either completed or are ongoing:

- (A) reliability testing
- (B) confirmation by TBI/AD clinicians
- (C) alternative hypothesis testing as needed
- (D) revisions to methods as needed

(2) Specific objectives

The specific objective of this scientific study is to identify novel AD risk factors specific to the TBI population by applying sophisticated imaging and connectomic methods to the MRI/CT brain scans

of older adults who are either healthy, TBI survivors, AD patients, or both. By the end of Y3 of this project, the activities needed to meet the objectives of the study were completed.

(3) *Significant results*

Activity (A). We leveraged functional magnetic resonance imaging (fMRI), network theory, and machine learning (ML) to study the extent to which geriatric mild TBI (mTBI) can lead to AD-like alteration of resting-state activity in the default mode network (DMN). This network was found to contain modules whose extent of AD-like, post-traumatic degradation can be accurately prognosticated based on the acute cognitive deficits of geriatric mTBI patients with cerebral microbleeds.

Activity (B). For the purposes of our study on the effect of cognitive impairment after TBI on AD risk, cerebral microbleeds (CMBs) were identified in each subject using an automatic algorithm for CMB segmentation and the validity of the findings were confirmed by two human experts with training in CMB identification from SWI, who had been blinded to automatic segmentation results. A third human expert then resolved disputes between the first two experts.

Activity (C). We used GLM design matrices containing network-theoretic measures computed for the connectome of each subject. These measures include topological genus, assortativity, global clustering coefficient, modularity, mean rich club coefficient, characteristic path length, the small world coefficient, efficiency, mean betweenness centrality, the participation coefficient and the diversity coefficient. All proposed global measures of connectivity were examined, and differences in measures of connectivity were only tested for all WM streamlines against their counterparts in healthy controls (HCs). We investigated which connectomic variables are significantly different between groups. This GLM allows us to determine (A) the effect which distance from a bleed has upon local measures of connectomic organization, and (B) which connectomic variables best discriminate between groups (using LDA).

Following our meta-analysis of brain volumetrics, we performed a large-scale regression using cortical volumetrics from a cohort of 3321 HCs to map age and sex effects on gray matter atrophy. By taking the ratio (males' divided by females') of regression-fitted slopes of the linear model for each cortical region, we identified regions with outsize sexual dimorphism in terms of annual rate of percent decrease in GM volume, as depicted in **Fig 1**.

With our investigation of changes in functional connectivity (FC) after TBI in the primary resting-state networks (RSNs) of the brain we aimed to establish the relationship between age at injury/sex and changes in FC within the 7 canonical RSNs. We quantified changes in rs-FC using GLMs and statistical detection of cortical surface clusters where rs-FC changes were driven by age (younger vs. older than 40) and sex. Our fMRI seed correlation analysis examined all major RSNs in the brain as identified by Yeo et al. from a large dataset of rs-fMRI data. These RSNs were the visual (V), somatomotor (SM), dorsal (DA) and ventral attention (VA), limbic (L), frontoparietal (FP), and default mode (DM) networks. A color-coded overlay of the seven networks is shown in **Fig 2**. Changes in FC after injury $\Delta\rho$ were

defined as the difference between the acute and chronic partial correlation coefficients, i.e., as $\Delta\rho = \rho_c - \rho_a$. Then, each of the seven RSNs were treated as a seed region to find clusters of significant differences in $\Delta\rho$ across groups (age or sex). Across age, this calculation yielded clusters of significant differences when treating SM, VA, and DMN as seed regions. These clusters are visualized in **Fig 3.**, and the differences in effect size between age groups are shown in **Fig 4.** Across sex, significant differences in FC changes were observed in all seven scenarios. The clusters of significant differences are visualized in **Fig 5** and **Fig 6.**, while the differences in effect size between sexes are shown in **Fig 7.**

Our investigation of demyelination in mTBI revealed distinct spatiotemporal patterns. At the acute timepoint, TBI participants exhibit significantly less myelin content across 34% of the cortex than HCs, shown in **Fig 8.** These differences are greatest at occipital regions and the paracentral lobules and sulci. At the chronic timepoint, TBI participants experience significant demyelination relative to the acute timepoint, with the most severe losses at the temporal, cingulate, and insular regions and the least severe losses at the occipital regions, shown in **Fig 9B.** Therefore, occipital regions are both vulnerable to acute TBI-related demyelination and resistant to chronic TBI-related demyelination. This indicates that the mechanisms underlying acute versus chronic TBI-related demyelination differ and have distinct spatiotemporal patterns across the cortex. One plausible explanation is that physical injury has a greater contribution to acute than chronic demyelination. A previous study mapping *R* in victims of *repeat* TBI found that lateral occipital areas were especially vulnerable to greater numbers of head injuries, matching our findings in acute TBI. Greater numbers of head injuries would indicate an increase in primary (physical) demyelination, but not necessarily in secondary (biochemical) demyelination. One important difference in pattern between typical aging and chronic TBI is observed at the sensorimotor cortex. This region is relatively vulnerable to typical age-related demyelination, but relatively resistant to chronic TBI-related demyelination. The sensorimotor cortex is known to be similarly resistant to white matter demyelination and cortical thinning in Alzheimer's disease.

Activity (D). The regression model used to partial out confounding effects in the investigation on demyelination after mTBI went through several revisions. Ultimately a linear mixed effects model was implemented to compare cortical myelin content across groups (mTBI participants vs HCs). Sex was included as a fixed effect, while age at injury was included as a between-subject covariate. Effects of variation in the length of time between scans (interscan interval, ISI) were confounding, but including raw ISI values in the model would have removed the random effect of time, a measure of interest. Initially the issue was circumvented by annualizing demyelination values. This had the drawback of assuming constant demyelination over time. A more sophisticated method without this drawback was implemented. We calculated, for each subject, the deviation of their ISI from the grand mean of ISI values across groups. This deviation was included in the statistical model as a random effect, partialing out the confound of variation in ISI between groups while preserving the random effect of time.

Initially, our analysis of changes in FC after TBI across groups used a single seed region, which was the DMN as defined by the 17-network Yeo parcellation. Due in part to significantly optimizing our implementation of FS-FAST by parallelizing across the subjects and timepoints (acute and chronic) the calculation of the nuisance regressors (WM, ventricles,

and CSF timeseries) and the timeseries for the seed regions represented by the modules (networks of the Yeo 2011 parcellation), we were able to expand this analysis. We revised our methods to use every network of the 7-network Yeo parcellation as a seed.

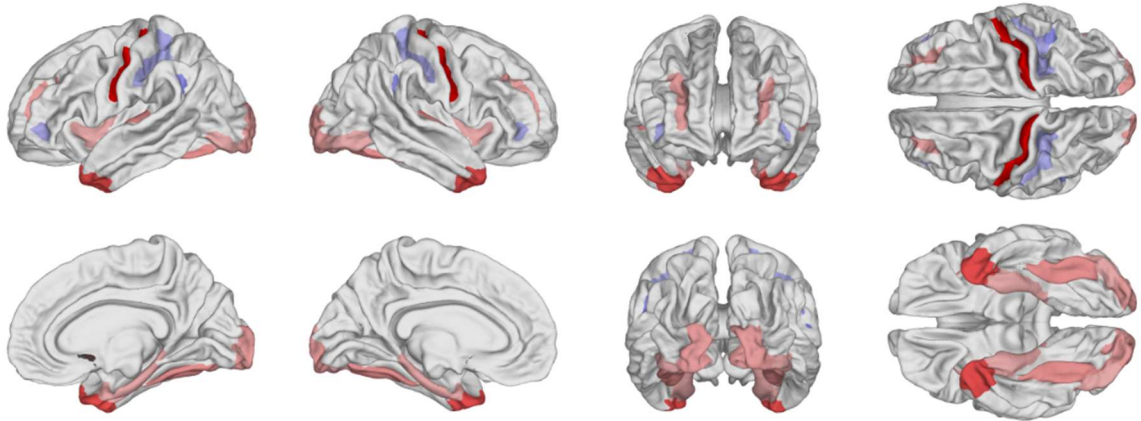


Figure 1. Cortical overlay of the areas with M/F slope ratio outside the range of [0.5, 1.5]. Red indicates higher M/F ratio or faster volume decrease in males, while blue indicates faster volume decrease in females.

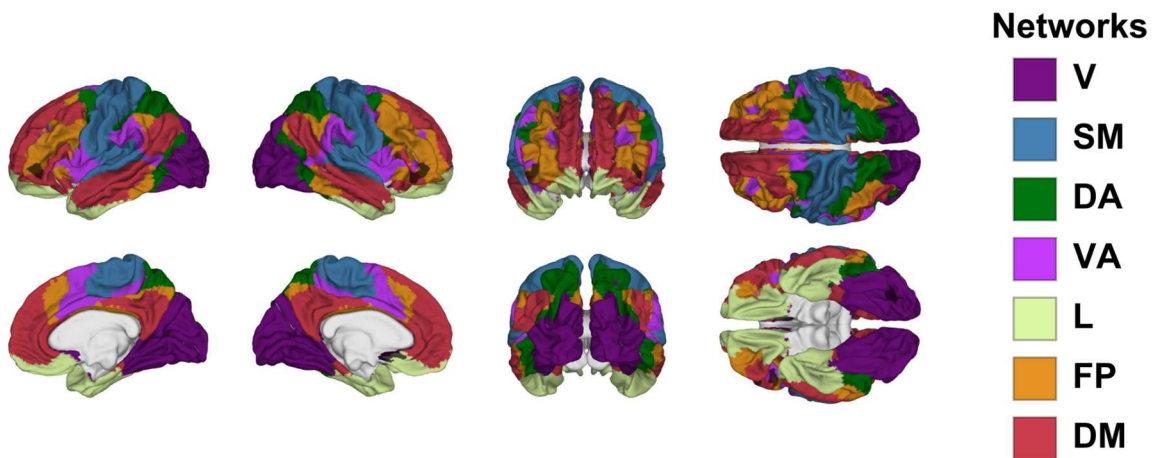


Figure 2. The seven large-scale RSNs of the brain as defined by the Yeo parcellation. The seven networks cover the entire cortical surface.

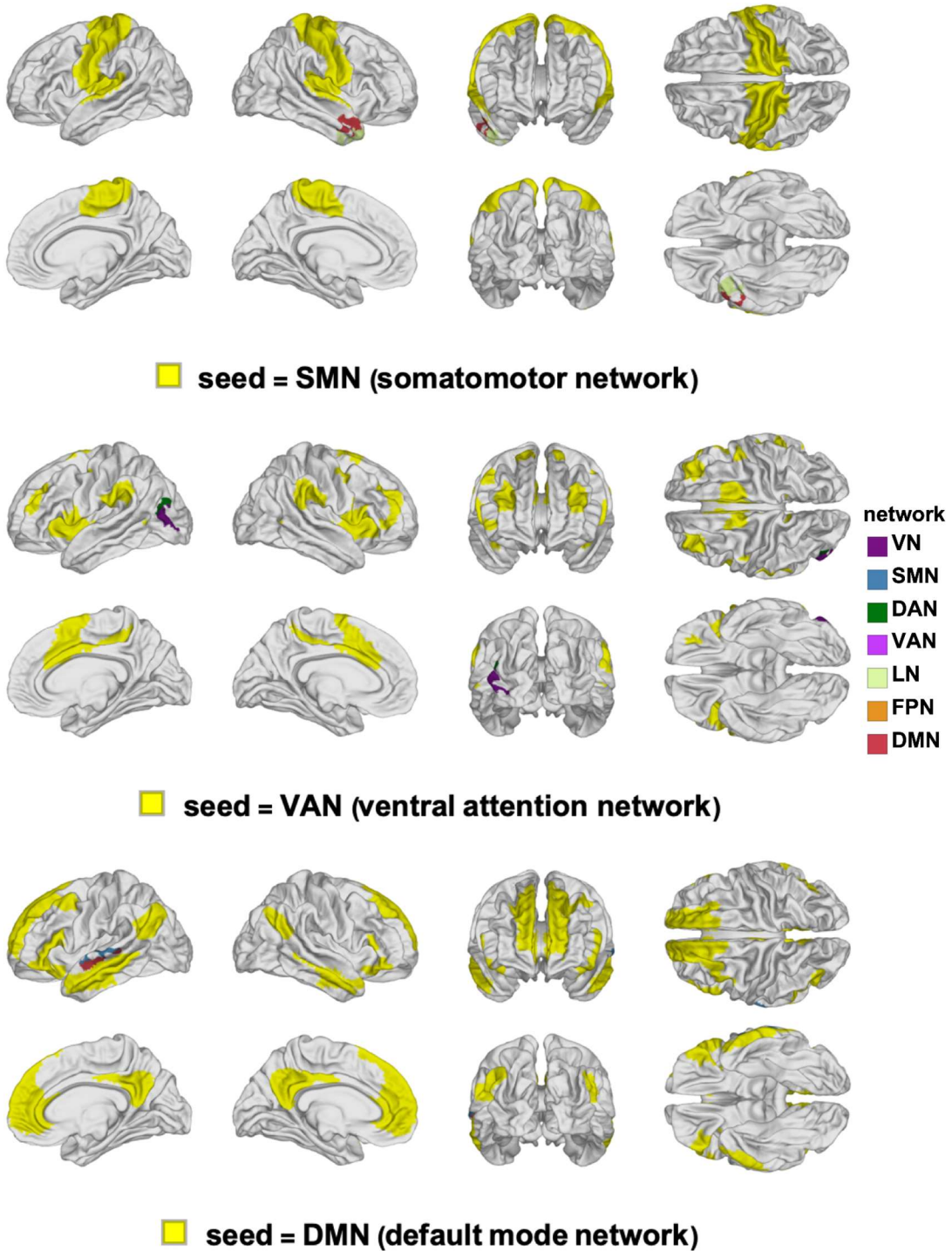


Figure 3. Clusters of FC changes that differ significantly between young adults (YAs) and old adults (OAs). In each panel, the seed RSN is shown in yellow and the significant clusters are indicated using the color(s) of the RSN(s) with which they overlap. We follow the color scheme of Yeo *et al.* (color scheme displayed in **Fig. 2**). The seed networks are the SMN (A), VAN (B), and DMN (C). No significant clusters were found for the rest of RSNs.

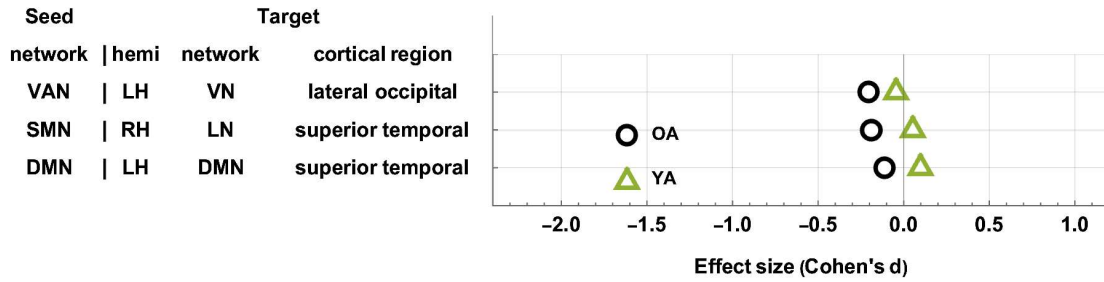


Figure 4. Age-related differences in FC change after TBI. Older adults (OAs) exhibit FC decreases across all statistically significant target clusters, whereas younger adults (YAs) exhibit relatively few changes across the ~6-month follow-up period. The horizontal axis encodes the observed change in the mean value of ρ associated with the seed network timeseries. All 3 statistically significant clusters identified are listed. In each row, we list the fMRI seed RSN, target hemisphere, target RSN, cortical region the cluster is located in, and the effect sizes (Cohen's d) for the OA and YA.

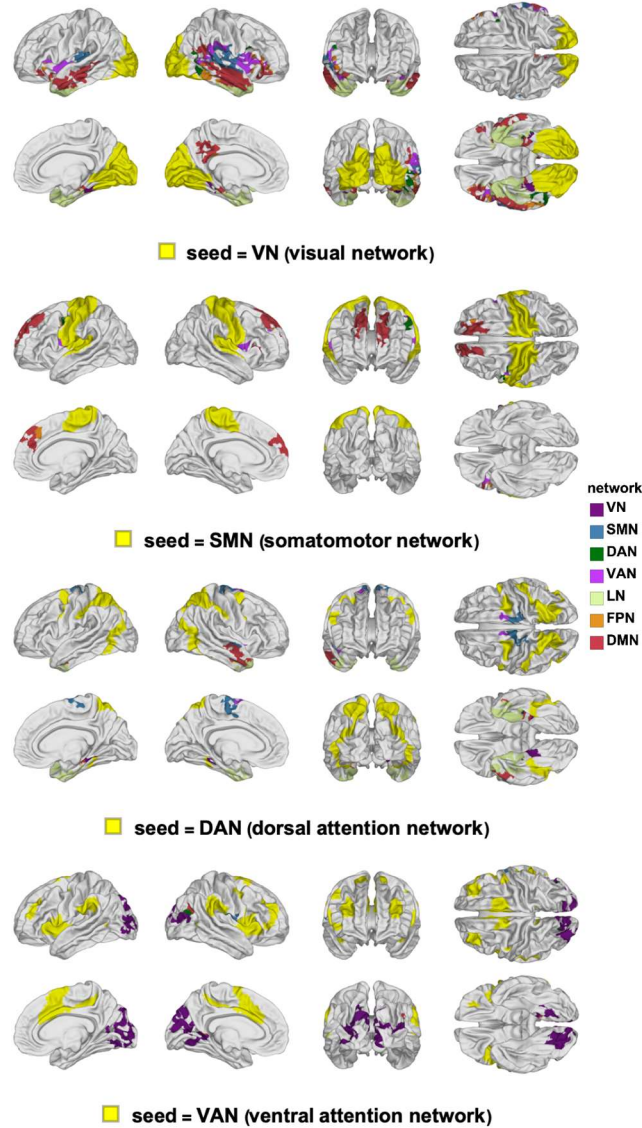


Figure 5. Cortical clusters of statistically significant FC changes that differ significantly by sex. In each panel, the seed RSN is shown in yellow and the significant clusters are indicated using the color(s) of the RSN(s) with which they overlap. We follow the color scheme of Yeo *et al.* (color scheme displayed in Fig. 2). Seed regions depicted correspond to the VN (A), SMN (B), DAN (C), and VAN (D).

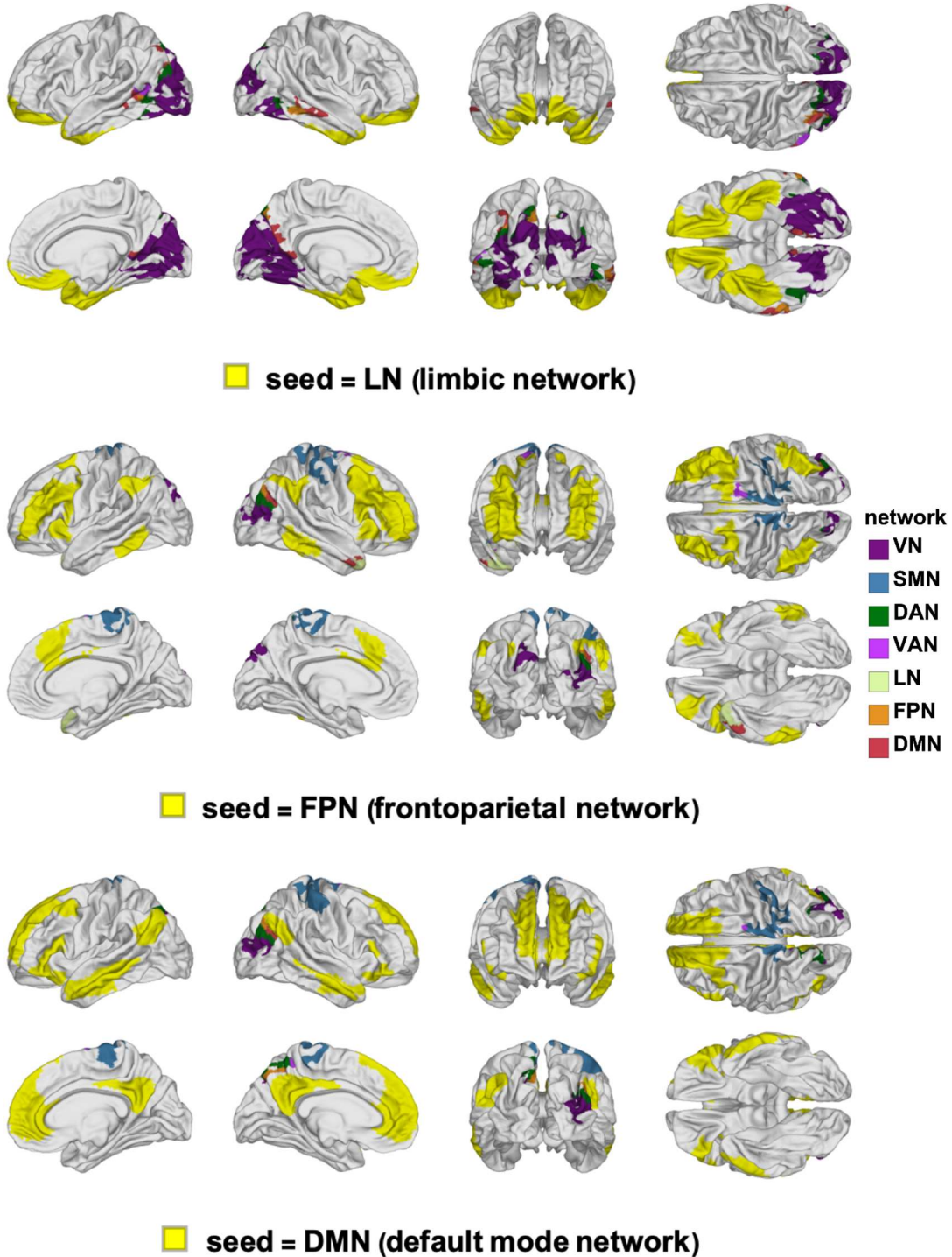


Figure 6. Cortical clusters of statistically significant FC changes that differ significantly by sex. In each panel, the seed RSN is shown in yellow and the significant clusters are indicated using the color(s) of the RSN(s) with which they overlap. We follow the color scheme of Yeo *et al.* (color scheme displayed in Fig. 2). Seed regions depicted correspond to the LN (A), FPN (B), and DMN (C).



Figure 7. Sex-related differences in FC change after TBI. Males typically show much larger differences in FC than females, with some exceptions. The horizontal axis encodes the observed change in the mean value of ρ associated with the seed network timeseries. In each row, we list the fMRI seed RSN, target hemisphere, target RSN, cortical region the cluster is located in, and the effect sizes (Cohen's d).

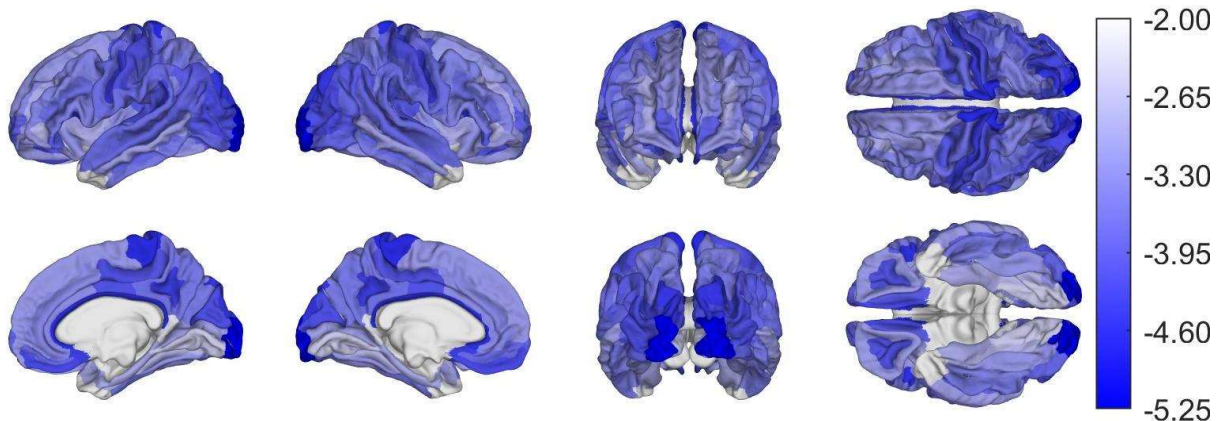


Figure 8. Cortical plot demonstrating average percent differences in myelin content between healthy controls and TBI subjects ~7 days after injury. Darker blue indicates that TBI participants have less myelin than healthy controls.

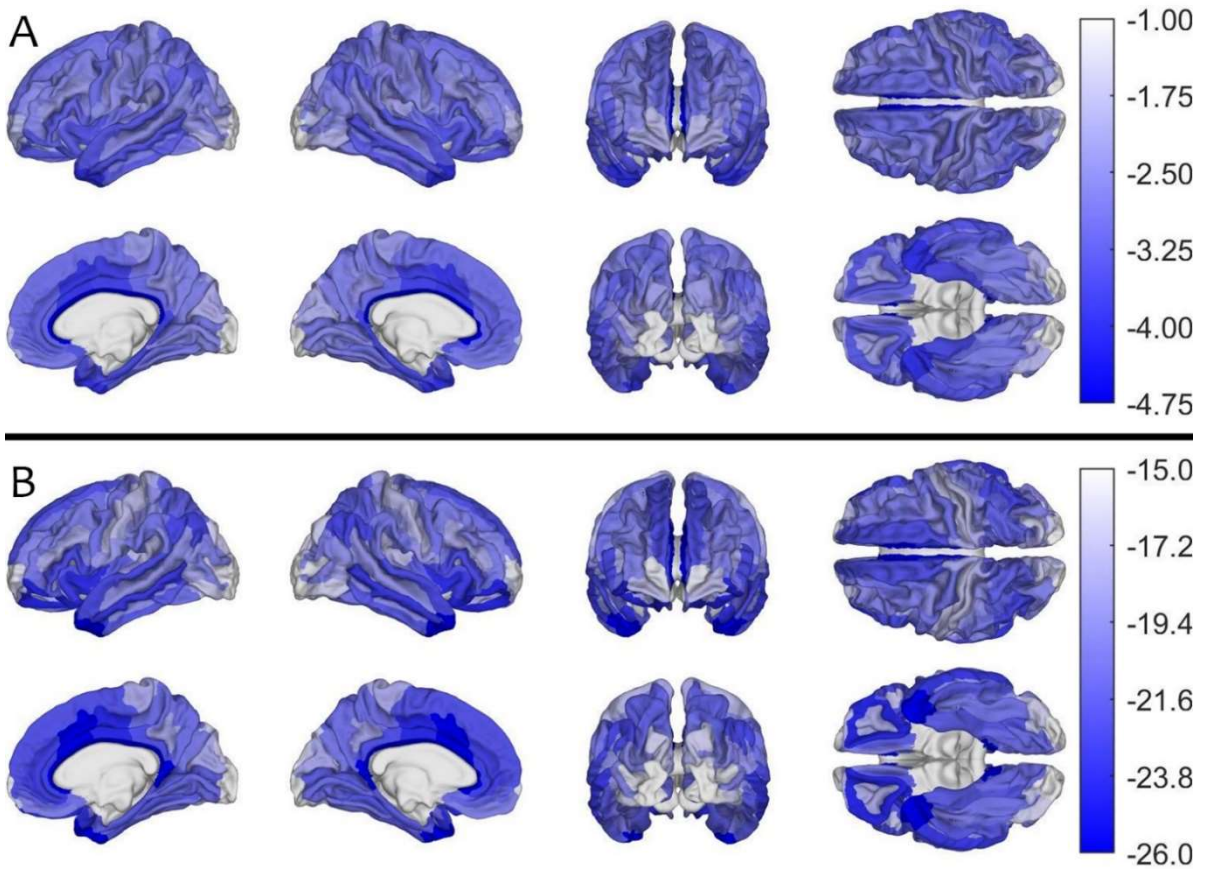


Figure 9. Cortical maps of percentage change in myelin ΔR across timepoints for (A) HCs and (B) TBI participants. ΔR values were averaged over subjects and then within each region. Note that different color axes are used for each group to emphasize between-group differences across the cortex. Darker blue indicates more demyelination.

What opportunities for training and professional development has the project provided?

Although the project was not specifically intended to provide training and professional development, the PI has been able to provide one-on-one mentorship thanks to this award. Specifically, one postdoctoral researcher (Anar Amgalan), two junior scientists (Kenneth Rostowsky, Alex Maher), and one graduate student (Nahian Chowdhury) benefitted from the learning opportunities provided by this project.

How were the results disseminated to communities of interest?

The PI was invited to speak at both domestic and international conferences. He presented the results of the study and participated as a member of a live panel at the Fourteenth Symposium of the International Neurotrauma Society in Melbourne, Australia. He similarly presented the results of the study and participated in a live panel at the Traumatic Brain Injury Symposium held by the University of California, Los Angeles. He was also invited to speak at the annual conference of the Gerontological Society of America in Phoenix, Arizona. Furthermore, the PI has been invited to present the results of the study at numerous internal events and conferences, such as the USC Alzheimer's Disease Research Center's conference.

The PI regularly educates students on the results of the study, via seminars and regular courses. He was also invited to lecture in graduate-level biomedical engineering and advanced neuroscience courses, in which he included results of the study.

Following the release of the manuscript *Acute cognitive impairment after traumatic brain injury predicts the occurrence of brain atrophy patterns similar to those observed in Alzheimer's disease*, USC published a press release on the manuscript, which was featured by *US News and World Report* and by *The Atlanta Journal-Constitution*, two major US news venues.

4. IMPACT:

What was the impact on the development of the principal discipline(s) of the project?

While it has already been argued extensively within the TBI and AD research communities that moderate-to-severe TBI predisposes its victims to AD significantly, the extent to which this is the case for mTBI victims is far less clear. Our findings on the association of geriatric mTBI with AD-like changes in functional brain connectivity as early as ~6 months post-injury advanced the goal of acutely forecasting mTBI patients' chronic deviations from normality along AD-like functional trajectories. This has led to better understanding of the increase in AD risk due to mTBI.

In a book chapter now in production by Elsevier, we explained how CMBs are among the smallest lesions of the cerebrum which can be visualized using MRI to indicate blood-brain barrier (BBB) impairment; as such, this class of hemorrhages are important for the evaluation and macroscale detection of geriatric patients' microscale pathologies associated with neurovascular disease and/or neurodegeneration. We detailed a streamlined protocol for MRI/CT multimodal imaging data acquisition, archiving and digital processing, including methods tailored for the analysis of susceptibility-weighted imaging (SWI) and diffusion-weighted imaging (DWI) scans to reveal CMB-

related alterations of the human connectome. Our provision of an efficient and effective MRI/CT method tailored for CMB and connectome analysis will bolster future progress in this important field of scientific inquiry.

Our investigation of FC changes after TBI injury in the RSNs of the human brain is, to our knowledge, the first systematic study of a comparable sample size that investigates post-TBI longitudinal changes in FC focusing on the large-scale RSNs. Our quantification of differences in FC changes after TBI across sex and age will inform future fMRI studies, allowing for more nuanced cohort selection and analysis of results.

The spatiotemporal patterns of demyelination observed will influence subsequent research on cortical demyelination in TBI. The indication of differential cortical vulnerability to physical versus biochemical demyelination will be further explored in future studies. Our findings also demonstrate the dynamic effect of time since injury on demyelination, proving the need to control for this factor to ensure precise and accurate findings. Our observations of shared patterns in TBI-related cortical demyelination and AD-related cortical thinning and white matter demyelination will inform future exploration of the biological mechanism by which TBI heightens risk for AD.

What was the impact on other disciplines?

Our scoping meta-analysis aggregated normative reference values for brain volume (BV) and three related volumetrics—gray matter volume (GMV), white matter volume (WMV) and cerebrospinal fluid volume (CSFV)—from typically-aging adults studied cross-sectionally using magnetic resonance imaging (MRI). Drawing from an aggregate sample of 9,473 adults, this study provides (A) regression coefficients β describing the age-dependent trajectories of volumetric measures by sex within the range from 20 to 70 years based on both linear and quadratic models, and (B) average values for BV, GMV, WMV and CSFV at the representative ages of 20 (young age), 45 (middle age) and 70 (old age). The results provided synthesizes ~20 years of brain volumetrics research and allow one to estimate BV at any age between 20 and 70. This is likely to be widely applicable in fields such as image processing and in determining deviations from normality in a wide range of pathology. Our further investigation into sex effects on cortical volumetrics revealed notable sexual dimorphism in spatial patterns of gray matter atrophy. These distinctive spatial patterns must be taken into account by any study involving cortical volume, encompassing a wide variety of disciplines.

The biological mechanisms underlying TBI-related demyelination are a topic of ongoing research. A variety of potential mechanisms have been outlined, but the interplay between them remains unclear. Our findings indicate both spatial and temporal differences in demyelination mechanism, which is likely to guide future research in molecular biology to clarify the relationship between demyelinating processes after TBI.

What was the impact on technology transfer?

Nothing to report.

What was the impact on society beyond science and technology?

TBI treatment can be challenging partly due to the difficulties of assessing and treating its neurocognitive and affective sequelae. The effects of a single TBI may persist for years and can limit patients' activities due to somatic complaints (headaches, vertigo, sleep disturbances, nausea, light or sound sensitivity), affective sequelae (post-traumatic depressive symptoms, anxiety, irritability, emotional instability) and mild cognitive impairment (MCI, including social cognition disturbances, attention deficits, information processing speed decreases, memory degradation and executive dysfunction). Despite a growing amount of research, study comparison and knowledge synthesis in this field are problematic due to TBI heterogeneity and factors like injury mechanism, age at or time since injury. The relative lack of standardization in neuropsychological assessment strategies for quantifying sequelae adds to these challenges. Our review of cognitive and affective consequences of TBI in relation to neuropsychological testing strategies, to neurobiological and neuroimaging correlates, and to patient age at and assessment time after injury highlights non-negligible cognitive and affective impairments following TBI. We highlight the need for well-standardized batteries for cognitive subdomains—rather than only domains—with high ecological validity. These findings will improve public knowledge of the cognitive impacts of TBI. Moreover, development of the tests we suggest will improve clinical outcomes for victims of TBI.

5. CHANGES/PROBLEMS:

Nothing to report.

Changes in approach and reasons for change

Nothing to report.

Actual or anticipated problems or delays and actions or plans to resolve them

Nothing to report.

Changes that had a significant impact on expenditures

Nothing to report.

Significant changes in use or care of human subjects, vertebrate animals, biohazards, and/or select agents

Significant changes in use or care of human subjects

Nothing to report.

Significant changes in use or care of vertebrate animals

Not applicable (no use or care of vertebrate animals).

Significant changes in use of biohazards and/or select agents

Not applicable (no biohazards and/or select agents).

6. PRODUCTS:

- **Publications, conference papers, and presentations**

Journal publications.

Fang-Cheng Yeh, **Andrei Irimia**, Dhiego Chaves de Almeida Bastos and Alexandra J Golby (2021) Tractography methods and findings in brain tumors and traumatic brain injury *NeuroImage* volume 245, article no. 118651 (21 pages). (*acknowledgement of federal support: yes*)

Kenneth A. Rostowsky and **Andrei Irimia** for the Alzheimer's Disease Neuroimaging Initiative (2021) Acute cognitive impairment after traumatic brain injury predicts the occurrence of brain atrophy patterns similar to those observed in Alzheimer's disease *GeroScience* volume 43, pages 2015–2039. (*acknowledgement of federal support: yes*)

Emily L. Dennis, Karen Caeyenberghs, Kristen R. Hoskinson, Tricia L. Merkley, Stacy J. Suskauer, Robert F. Asarnow, Talin Babikian, Brenda Bartnik-Olson, Kevin Bickart, Erin D. Bigler, Linda Ewing-Cobbs, Anthony Figaji, Christopher C. Giza, Naomi J. Goodrich-Hunsaker, Cooper B. Hodges, Elizabeth S. Hovenden, **Andrei Irimia**, Marsh Königs, Harvey S. Levin, Hannah M. Lindsey, Jeffrey E. Max, Mary R. Newsome, Alexander Olsen, Nicholas P. Ryan, Adam T. Schmidt, Matthew S. Spruiell, Benjamin S. Wade, Ashley L. Ware, Christopher G. Watson, Anne L. Wheeler, Keith O. Yeates, Brandon A. Zielinski, Peter Kochunov, Neda Jahanshad, Paul M. Thompson, David F. Tate and Elisabeth A. Wilde for the ENIGMA-TBI Consortium (2021) White matter disruption in pediatric traumatic brain injury: results from ENIGMA pediatric moderate to severe traumatic brain injury *Neurology* volume 97, pages E299-E309. (*acknowledgement of federal support: yes*)

David F. Tate, Emily L. Dennis, John T. Adams, Maheen M. Adamson, Heather G. Belanger, Erin D. Bigler, Heather C. Bouchard, Alexandra L. Clark, Lisa M. Delano-Wood, Seth G. Disner, Blessen C. Eapen, Carol E. Franz, Elbert Geuze, Naomi J. Goodrich-Hunsaker, Kihwan Han, Jasmeet P. Hayes, Sidney R. Hinds II, Cooper B. Hodges, Elizabeth S. Hovenden, **Andrei Irimia**, Kimbra Kenney, Inga K. Koerte, William S. Kremen, Harvey S. Levin, Hannah M. Lindsey, Rajendra A. Morey, Mary R. Newsome, John Ollinger, Mary J. Pugh, Randall S. Scheibel, Martha E. Shenton, Danielle R. Sullivan, Brian A. Taylor, Maya Troyanskaya, Carmen Velez, Benjamin S. Wade, Xin Wang, Ashley L. Ware, Ross D. Zafonte, Paul M. Thompson and Elisabeth A. Wilde for the ENIGMA-TBI Consortium (2021) Coordinating global multi-site studies of military-relevant traumatic brain injury: opportunities, challenges and harmonization guidelines *Brain Imaging and Behavior* volume 15, pages 585–613. (*acknowledgement of federal support: yes*)

Books or other non-periodical, one-time publications.

Andrei Irimia, Kenneth A. Rostowsky, E. Meng Law and Helena Chang Chui (2022) Cerebral hemorrhages in traumatic brain injury (*book chapter; acknowledgement of federal support: yes*)

F Sibia, RM Custer, **Andrei Irimia**, F Sepehrband, AW Toga and RP Cabeen (2021) Relationship between structural magnetic resonance imaging and the development of psychological distress in mild traumatic brain injury patients *Fiftieth Annual Meeting of the Society for Neuroscience* (SfN '21), November 13-16, 2021, Chicago, IL

Nahian F. Chowdhury, Sean O. Mahoney, Shania H. Wang and **Andrei Irimia** (2021) Significant association of mild traumatic brain injury with both acute and chronic demyelination of the cerebral cortex *Thirty-Ninth Annual Symposium of the National Neurotrauma Society* (NNS '21), July 11-14, 2021, held virtually. Published in *Journal of Neurotrauma*, volume 38, page A105.

David J. Robles, Ammar Dharani, Kenneth A. Rostowsky, Nikhil N. Chaudhari, Van Ngo, Frank Zhang, Lauren J. O'Donnell and **Andrei Irimia** (2021) Chronic white matter degradation after mild traumatic brain injury as a function of age, sex and cerebral microbleed count *Thirty-Ninth Annual Symposium of the National Neurotrauma Society* (NNS '21), July 11-14, 2021, held virtually. Published in *Journal of Neurotrauma*, volume 38, page A21.

Anar Amgalan, Alexander S. Maher, Michelle Y. Ha and **Andrei Irimia** (2021) Age and sex dependence of changes in resting-state functional correlation networks after traumatic brain injury *Thirty-Ninth Annual Symposium of the National Neurotrauma Society* (NNS '21), July 11-14, 2021, held virtually. Published in *Journal of Neurotrauma*, volume 38, page A18

Kenneth A. Rostowsky and **Andrei Irimia** for the Alzheimer's Disease Neuroimaging Initiative (2021) Comparison of cerebral atrophy patterns across Alzheimer's disease and geriatric cases of mild traumatic brain injury *Thirty-Ninth Annual Symposium of the National Neurotrauma Society* (NNS '21), July 11-14, 2021, held virtually. Published in *Journal of Neurotrauma*, volume 38, page A67

Andrei Irimia, Alexander S. Maher, Kenneth A. Rostowsky, Nikhil N. Chaudhari, Nahian F. Chowdhury and Elliot B. Jacobs for the Alzheimer's Disease Neuroimaging Initiative (2021) Alzheimer's dementia-like patterns of cortical thinning and functional connectivity degradation after mild traumatic brain injury *Military Health System Research Symposium of the Military Health System* (MHSRS '21), August 23-26, 2021, US Army Medical Research and Development Command, Kissimmee, FL.

Rachel Lin, Nikhil N. Chaudhari, Nahian F. Chowdhury, Kenneth A. Rostowsky and **Andrei Irimia** (2021) Statistical analysis of cerebral microbleed distances to cortical regions *Annual Symposium of the Center for Undergraduate Research in Viterbi Engineering*, May 18, 2021, Los Angeles, CA.

Layal Wehbe, David J. Robles, Ammar Dharani and **Andrei Irimia** (2021) How male sex predicts white matter degeneration after mild traumatic brain injury *Annual Symposium of the Center for Undergraduate Research in Viterbi Engineering*, May 18, 2021, Los Angeles, CA.

Benjamin J. Hacker, Jessica Zhu, Nahian F. Chowdhury, David J. Robles, Kenneth A. Rostowsky and **Andrei Irimia** (2021) The fractional anisotropy of white matter connectivity

in typical aging vs. mild traumatic brain injury *Annual Symposium of the Center for Undergraduate Research in Viterbi Engineering*, May 18, 2021, Los Angeles, CA.

Jessica Zhu, Benjamin J. Hacker, Nahian F. Chowdhury, David J. Robles, Kenneth A. Rostowsky and **Andrei Irimia** (2021) Differences in white matter fractional anisotropy between health and mild traumatic brain injury *Annual Symposium of the Center for Undergraduate Research in Viterbi Engineering*, May 18, 2021, Los Angeles, CA.

Benjamin J. Hacker, Jessica Zhu, Nahian F. Chowdhury, David J. Robles, Kenneth A. Rostowsky and **Andrei Irimia** (2021) The fractional anisotropy of white matter connectivity in typical aging vs. mild traumatic brain injury *Annual Symposium of the Center for Undergraduate Research in Viterbi Engineering*, May 18, 2021, Los Angeles, CA.

Benjamin J. Hacker, Jessica Zhu, Nahian F. Chowdhury, David J. Robles, Kenneth A. Rostowsky and **Andrei Irimia** (2021) Comparison of fractional anisotropy along white matter connections in health vs. mild traumatic brain injury *Twenty-Third Annual USC Undergraduate Symposium for Scholarly and Creative Work*, April 10, 2021, Los Angeles, CA.

Jun H. Kim, HJ Lee, Shania H. Wang, Van Ngo, Sean O. Mahoney, David J. Robles and **Andrei Irimia** (2021) Estimation of accelerated brain aging following mild traumatic brain injury using multivariate statistical analysis *Twenty-Third Annual USC Undergraduate Symposium for Scholarly and Creative Work*, April 10, 2021, Los Angeles, CA.

Anar Amgalan, Alexander S. Maher, Michelle Y. Ha, and **Andrei Irimia** (2021) Sex and age differences in functional correlation of the default mode and frontoparietal networks after traumatic brain injury *Twenty-Third Annual USC Undergraduate Symposium for Scholarly and Creative Work*, April 10, 2021, Los Angeles, CA.

Nahian F. Chowdhury, Sean O. Mahoney, Van Ngo, Shania H. Wang, Kenneth A. Rostowsky, Nikhil N. Chaudhari, Benjamin J. Hacker and **Andrei Irimia** (2021) Widespread cortical demyelination in geriatric cases of mild traumatic brain injury and in Alzheimer's disease *Seventy-Sixth Annual Scientific Meeting of the Gerontological Society of America* (GSA '21), November 10-14, 2021, Phoenix, AZ, USA. Published in *Innovation in Aging*, volume 5, suppl. 1, page 677.

Shania H. Wang, Nahian F. Chowdhury, Sean O. Mahoney and **Andrei Irimia** (2021) Comparing cortical demyelination in geriatric mild traumatic brain injury and Alzheimer's disease *Seventy-Sixth Annual Scientific Meeting of the Gerontological Society of America* (GSA '21), November 10-14, 2021, Phoenix, AZ, USA. Published in *Innovation in Aging*, volume 5, suppl. 1, page 637.

David J. Robles, Ammar Dharani, Nikhil N. Chaudhari, Kenneth A. Rostowsky, Michelle Y. Ha, Layal Wehbe, Van Ngo, Frank Zhang, Lauren J. O'Donnell and **Andrei Irimia** (2021) Age, sex and cerebral microhemorrhages affect white matter integrity across adulthood after mild traumatic brain injury *Seventy-Sixth Annual Scientific Meeting of the Gerontological*

Society of America (GSA '21), November 10-14, 2021, Phoenix, AZ, USA. Published in *Innovation in Aging*, volume 5, suppl. 1, page 829.

Andrei Irimia, Alexander S. Maher, Kenneth A. Rostowsky, Nikhil N. Chaudhari, Nahian F. Chowdhury, Elliot B. Jacobs, David J. Robles and Ammar Dharani (2021) Early prediction of cognitive deficits after traumatic brain injury based on Alzheimer's disease-like patterns of neurodegeneration *Multiscale brain aging in the context of neurodegeneration and Alzheimer's disease. Symposium at the Seventy-Sixth Annual Scientific Meeting of the Gerontological Society of America* (GSA '21), November 10-14, 2021, Phoenix, AZ, USA. Published in *Innovation in Aging*, volume 5, suppl. 1., pages 372-373.

Anar Amgalan, Alexander S. Maher, Michelle Y. Ha and **Andrei Irimia** (2021) Sex and age differences in the functional correlation of the default mode network after traumatic brain injury *Seventy-Sixth Annual Scientific Meeting of the Gerontological Society of America* (GSA '21), November 10-14, 2021, Phoenix, AZ, USA. Published in *Innovation in Aging*, volume 5, suppl. 1, pages 830-831.

Kenneth A. Rostowsky and **Andrei Irimia** for the Alzheimer's Disease Neuroimaging Initiative (2021) Quantification of similar neurodegeneration patterns across geriatric concussions and Alzheimer's disease *Seventy-Sixth Annual Scientific Meeting of the Gerontological Society of America* (GSA '21), November 10-14, 2021, Phoenix, AZ, USA. Published in *Innovation in Aging*, volume 5, suppl. 1., page 639.

Shania H. Wang, Nahian F. Chowdhury, Sean O. Mahoney and **Andrei Irimia** for the Alzheimer's Disease Neuroimaging Initiative (2021) Comparing cortical demyelination in geriatric traumatic brain injury and Alzheimer's disease *Twenty-Seventh Annual Meeting of the Organization on Human Brain Mapping* (OHBM '21), June 21-25, 2021, Seoul, South Korea (held virtually).

Hyung J. Lee, Nahian F. Chowdhury, Kenneth A. Rostowsky, Nikhil N. Chaudhari, David J. Robles and **Andrei Irimia** for the Alzheimer's Disease Neuroimaging Initiative (2021) Differences in brain connectivity trends across Alzheimer's disease and mild traumatic brain injury *Twenty-Seventh Annual Meeting of the Organization on Human Brain Mapping* (OHBM '21), June 21-25, 2021, Seoul, South Korea (held virtually).

David J. Robles, Ammar Dharani, Kenneth A. Rostowsky, Van Ngo, Frank Zhang, Lauren J. O'Donnell and **Andrei Irimia** (2021) White matter integrity change across six months after mild traumatic brain injury *Twenty-Seventh Annual Meeting of the Organization on Human Brain Mapping* (OHBM '21), June 21-25, 2021, Seoul, South Korea (held virtually).

Anar Amgalan, Alexander S. Maher, Michelle Y. Ha and **Andrei Irimia** (2021) Sex differences of functional correlation in the default mode network after traumatic brain injury *Twenty-Seventh Annual Meeting of the Organization on Human Brain Mapping* (OHBM '21), June 21-25, 2021, Seoul, South Korea (held virtually).

Kenneth A. Rostowsky and **Andrei Irimia** for the Alzheimer's Disease Neuroimaging Initiative (2021) Traumatic brain injury and Alzheimer's disease share patterns of connectomic degradation and cortical thinning *Twenty-Seventh Annual Meeting of the Organization on Human Brain Mapping (OHBM '21)*, June 21-25, 2021, Seoul, South Korea (held virtually).

David J. Robles, Nikhil N. Chaudhari, Kenneth A. Rostowsky and **Andrei Irimia** for the Alzheimer's Disease Neuroimaging Initiative (2021) Statistical association of regional cortical thickness with cerebral microbleed load and blood-brain barrier disruption in mild traumatic brain injury and Alzheimer's disease *Crossroads of Biology Conference on Brain Barriers (BB '21)* (D Agalliu, M Lehtinen and B van Hollebeke, eds.), April 7-9, 2021, Cold Spring Harbor, NY (held virtually).

Andrei Irimia, Nikhil N. Chaudhari, Ammar Dharani, Kenneth A. Rostowsky, David J. Robles, Frank Zhang and Lauren J. O'Donnell (2021) Blood-brain barrier breakdown, white matter degradation and cognitive impairment after traumatic brain injury revealed by susceptibility weighted imaging *Crossroads of Biology Conference on Brain Barriers (BB '21)*, April 7-9, 2021, Cold Spring Harbor, NY (held virtually).

Nahian F. Chowdhury, Kenneth A. Rostowsky, Nikhil N. Chaudhari, Hyung J. Lee, David J. Robles and **Andrei Irimia** for the Alzheimer's Disease Neuroimaging Initiative (2021) Comparing the impacts of Alzheimer's disease and geriatric traumatic brain injury on cortical networks *Forty-First Alzheimer's Association International Conference (AAIC '21)*, July 25-30, 2021, Denver, CO. (*To be published in Alzheimer's and Dementia*)

Nahian F. Chowdhury, Sean O. Mahoney and **Andrei Irimia** for the Alzheimer's Disease Neuroimaging Initiative (2021) Quantifying the longitudinal effects of Alzheimer's disease upon myelin content in gray matter *Forty-First Alzheimer's Association International Conference (AAIC '21)*, July 25-30, 2021, Denver, CO. (*To be published in Alzheimer's and Dementia*)

Kenneth A. Rostowsky, Anar Amgalan and **Andrei Irimia** for the Alzheimer's Disease Neuroimaging Initiative (2021) Alzheimer's disease-like brain atrophy patterns after mild traumatic brain injury can be predicted based on acute cognitive deficits *Forty-First Alzheimer's Association International Conference (AAIC '21)*, July 25-30, 2021, Denver, CO. Published in *Alzheimer's and Dementia*, volume 17, page E054779. 34 of 74

Shania H. Wang, Nahian F. Chowdhury, Sean O. Mahoney and **Andrei Irimia** for the Alzheimer's Disease Neuroimaging Initiative (2021) Spatial patterns of cortical demyelination in geriatric cases of traumatic brain injury and in Alzheimer's disease *Forty-First Alzheimer's Association International Conference (AAIC '21)*, July 25-30, 2021, Denver, CO. (*To be published in Alzheimer's and Dementia*)

Alexander S. Maher, Nikhil N. Chaudhari, Elliot B. Jacobs, Sean O. Mahoney, Van Ngo and **Andrei Irimia** for the Alzheimer's Disease Neuroimaging Initiative (2021) Statistical equivalence of resting state functional correlation patterns in the default mode networks of

patients with Alzheimer's disease vs. geriatric victims of mild traumatic brain injury *Fourteenth Symposium of the International Neurotrauma Society* (INTS '21), February 7-11, 2021, Melbourne, Australia (held virtually).

Kenneth A. Rostowsky, Nikhil N. Chaudhari and **Andrei Irimia** for the Alzheimer's Disease Neuroimaging Initiative (2021) Statistically equivalent distribution of cortical thinning and white matter degradation in geriatric patients with mild traumatic brain injury relative to Alzheimer's disease *Fourteenth Symposium of the International Neurotrauma Society* (INTS '21), February 7-11, 2021, Melbourne, Australia (held virtually).

Other publications, conference papers and presentations.

Andrei Irimia (2021) Resting state connectivity in the default mode network is affected similarly in Alzheimer's disease and traumatic brain injury. *Exploring the nexus between TBI and dementia* (live panel), *Fourteenth Symposium of the International Neurotrauma Society* (INTS '21), February 9, 2021, Melbourne, Australia (held virtually).

Andrei Irimia (2021) Early prediction of cognitive deficits after traumatic brain injury based on Alzheimer's disease-like patterns of neurodegeneration. *Multiscale brain aging in the context of neurodegeneration and Alzheimer's disease* (research symposium), *presentation at the Seventy-Sixth Annual Scientific Meeting of the Gerontological Society of America* (GSA '21), November 10-14, 2021, Phoenix, AZ, USA (held virtually). Published in *Innovations in Aging*, volume 5, pages 372-373.

Andrei Irimia (2021) Alzheimer's disease-like trajectories of brain structure and function after geriatric cases of mild traumatic brain injury. *Traumatic Brain Injury Symposium* (live panel), Lundquist Institute, April 23, 2021, University of California, Los Angeles, CA (held virtually).

- **Website(s) or other Internet site(s)**

Journal papers, conference publications and main results are disseminated online via the PI's official webpage on the website of the USC Leonard Davis School of Gerontology (www.gero.usc.edu) as well as through the PI's personal website (www.andrei-irimia.com), which is a mirror site of the official university webpage.

- **Technologies or techniques**

We detailed a streamlined protocol for MRI/CT multimodal imaging data acquisition, archiving and digital processing, including methods tailored for the analysis of susceptibility-weighted imaging (SWI) and diffusion-weighted imaging (DWI) scans to reveal CMB-related alterations of the human connectome.

- **Inventions, patent applications, and/or licenses**

Nothing to report.

- **Other Products**

The research activities resulted in the development of Matlab and Python programming code and software for the analysis of imaging data. This material is available from the PI upon request and will be made available to the public on GitHub or in a similar venue when the software product is mature.

7. PARTICIPANTS and OTHER COLLABORATING ORGANIZATIONS

What individuals have worked on the project?

Name: Andrei Irimia, PhD
Project Role: Principal Investigator
Researcher Identifier: 0000-0002-9254-9388
Nearest person month worked: 1
Contribution to Project: Dr. Irimia oversees all aspects of the project and ensures regulatory compliance. He carries out and/or supervises all data analyses, publication efforts and dissemination activities.

Name: Kenneth A. Rostowsky
Project Role: junior scientist
Researcher Identifier: Not available
Nearest person month worked: 1
Contribution to Project: Mr. Rostowsky assisted with data curation, with the execution of computer programs and with the interpretation of the results.

Name: Anar Amgalan
Project Role: postdoctoral researcher
Researcher Identifier: Not available
Nearest person month worked: 2
Contribution to Project: Dr. Amgalan assisted with data curation, with execution of fMRI seed-based analysis and with the interpretation of the results.

Name: Alexander S. Maher
Project Role: junior scientist
Researcher Identifier: Not available
Nearest person month worked: 2
Contribution to Project: Mr. Maher assisted with data curation, with the execution of fMRI seed-based analysis and with the interpretation of the results.

Name: Nahian F. Chowdhury
Project Role: graduate student
Researcher Identifier: Not available
Nearest person month worked: 2
Contribution to Project: Mr. Chowdhury assisted with data curation, with the execution of cortical myelin mapping and with the interpretation of the results.

Has there been a change in the active other support of the PD/PI(s) or senior/key personnel since the last reporting period?

Nothing to report.

What other organizations were involved as partners?

Organization Name: Harvard Medical School
Location of organization: Cambridge, MA
Partner's contribution to the project: Our collaborators at Harvard Medical School provided expertise and advice with our use of their freely available software for image analysis. This expertise was provided at no cost to our team. The Harvard team also contributed to the interpretation of our results and to our publication efforts.

Organization Name: University of California
Location of organization: Los Angeles, CA
Partner's contribution to the project: Our collaborators at UCLA provided expertise and advice with our use of their freely available software for Riemannian curve matching. This expertise was provided at no cost to our team. The UCLA team also contributed to the interpretation of our results and to our publication efforts.

8. SPECIAL REPORTING REQUIREMENTS

COLLABORATIVE AWARDS: Not applicable (this is not a collaborative award).

QUAD CHARTS: The updated quad chard is attached to this progress report.

9. APPENDICES:

A selection of publications resulting from the work done in Y3 of this award are included as appendices.

TBI-related risk factors for Alzheimer's disease

AZ170072

W81XWH-18-1-0413



PI: Andrei Irimia, PhD

Org: University of Southern California

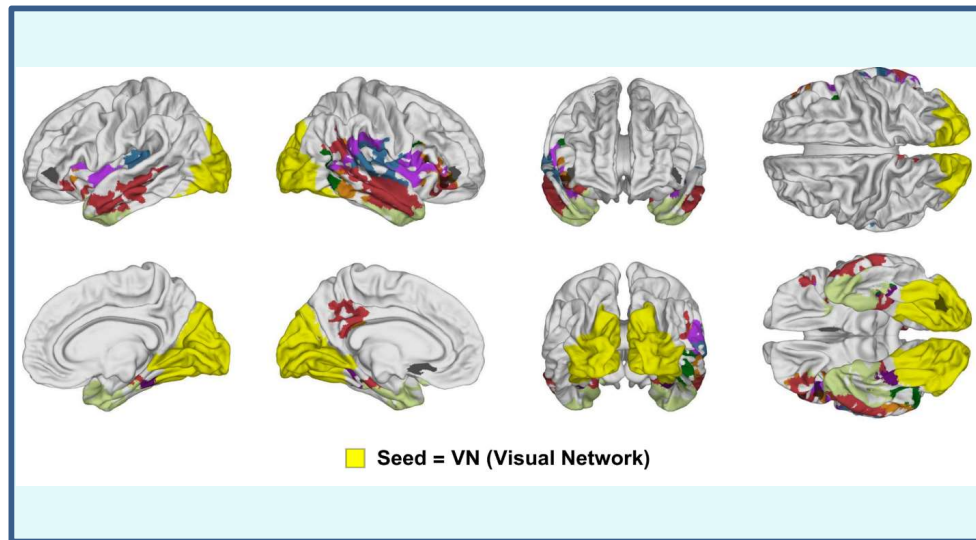
Award Amount: \$371,250.00

Study/Product Aim(s)

Aim: to understand the differences between (1) the healthy aging brain, (2) the TBI-affected brain, (3) the AD- affected brain, and (4) the brain affected by both TBI and AD.

Approach

TBI/AD-tailored computational analyses of magnetic resonance imaging (MRI) and diffusion tensor imaging (DTI) volumes will provide volumetrics, morphometrics, connectomics, network topology and network-theoretic properties. Longitudinal differences in the trajectories of brain structure and connectomics in TBI-/AD- (i.e. healthy control), TBI+/AD-, TBI-/AD+ and TBI+/AD+ volunteers. A general linear model (GLMs) will be implemented to identify volumetric, morphometric and connectomic signatures present only in the brains of TBI survivors and whose properties are significantly correlated with the severity of their AD-like cognitive impairment and, potentially, with the likelihood of TBI survivors to develop this condition.



Changes in the coupling of the visual network during fMRI resting state activity. Shown in yellow is the visual network. Shown in other colors are significant clusters whose coupling to the visual network decreases significantly after TBI as a function of sex.

Timeline and Cost

Activities	CY	18	19	20	21
Segmentation & connectomics		█			
Topological analysis & validation			█		
Statistical & reliability analysis				█	
Identification of AD biomarkers					█
Estimated Budget (\$K)		\$21.9	\$75.0	\$75.0	\$78.1

Goals/Milestones

CY18 Goal – Segmentation & connectomics

Pathology identification Volumetrics & morphometrics

CY19 Goals – Topological analysis & validation

Connectomics & topology analysis Connectomic differences between groups Validation Confirmation by clinicians

CY20 Goal – Statistical & reliability analysis

Statistical analysis Reliability testing Revisions to methods
 Biomarker identification Internal validation of biomarker analysis

CY21 Goal – Identification of AD biomarkers

Testing alternative hypotheses Manuscript redaction & publication

Budget Expenditure to Date

Projected Expenditure: \$371,250.00

Actual Expenditure: \$371,250.00

Updated: 10/15/21



Acute cognitive deficits after traumatic brain injury predict Alzheimer’s disease-like degradation of the human default mode network

Andrei Irimia  · Alexander S. Maher ·
Nikhil N. Chaudhari · Nahian F. Chowdhury ·
Elliot B. Jacobs ·
the Alzheimer’s Disease Neuroimaging Initiative

Received: 9 June 2020 / Accepted: 29 July 2020 / Published online: 2 August 2020
© American Aging Association 2020

Abstract Traumatic brain injury (TBI) and Alzheimer’s disease (AD) are prominent neurological conditions whose neural and cognitive commonalities are poorly understood. The extent of TBI-related neurophysiological abnormalities has been hypothesized to reflect AD-like neurodegeneration because TBI can increase vulnerability to AD. However, it remains challenging to prognosticate AD risk partly because the functional relationship between acute posttraumatic sequelae and chronic AD-like degradation remains elusive. Here, functional magnetic resonance imaging (fMRI), network theory, and machine learning (ML)

are leveraged to study the extent to which geriatric mild TBI (mTBI) can lead to AD-like alteration of resting-state activity in the default mode network (DMN). This network is found to contain modules whose extent of AD-like, posttraumatic degradation can be accurately prognosticated based on the acute cognitive deficits of geriatric mTBI patients with cerebral microbleeds. Aside from establishing a predictive physiological association between geriatric mTBI, cognitive impairment, and AD-like functional degradation, these findings advance the goal of acutely forecasting mTBI patients’ chronic deviations from normality along AD-like functional trajectories. The association of geriatric mTBI with AD-like changes in functional brain connectivity as early as ~6 months post-injury carries substantial implications for public health because TBI has relatively high prevalence in the elderly.

Andrei Irimia and Alexander S. Maher contributed equally to this work.

Data used in preparation of this article were obtained from the Alzheimer’s Disease Neuroimaging Initiative (ADNI) database (adni.loni.usc.edu). As such, the investigators within the ADNI contributed to the design and implementation of ADNI and/or provided data but did not participate in the analysis or writing of this report. A complete listing of ADNI investigators can be found at: http://adni.loni.usc.edu/wp-content/uploads/how_to_apply/ADNI_Acknowledgement_List.pdf

Keywords Alzheimer’s disease · Traumatic brain injury · Default mode network · Resting state · Geriatrics · Functional connectome

A. Irimia · A. S. Maher · N. N. Chaudhari ·
N. F. Chowdhury · E. B. Jacobs
Ethel Percy Andrus Gerontology Center, Leonard Davis School of Gerontology, University of Southern California, Los Angeles, CA, USA

A. Irimia (✉)
Denney Research Center, Department of Biomedical Engineering,
Viterbi School of Engineering, University of Southern California,
Los Angeles, CA, USA
e-mail: irimia@usc.edu

Introduction

Traumatic brain injury (TBI) can result in functional brain alterations causing neural and cognitive deficits [1, 2]. Even after mild TBI (mTBI), any cognitive domain can be affected by such deficits [3], whose manifestation may accelerate the onset of mild cognitive impairment (MCI) [4, 5], particularly in geriatric patients [6]. Although neurotrauma increases the risk for

Alzheimer's disease (AD) [7], there is little knowledge on how TBI affects functional trajectories and gives rise to neuropathophysiology. Furthermore, the relationship between TBI severity and AD-like brain dysfunction is poorly understood, and the mechanisms whereby TBI can elicit functional abnormalities which increase AD risk remains unclear. One hypothesis is that posttraumatic functional changes exhibit patterns which progressively resemble those of AD [5, 8, 9]; if this is the case, characterizing AD-like brain alterations after TBI could assist in improving AD risk assessment and the early identification of TBI patients at higher risk for this disease.

The default mode network (DMN) is a large-scale brain network which is most commonly active when a person is at wakeful rest [10]. In this resting state (RS), individuals lie quietly awake without performing tasks or being exposed to stimuli, and their DMN activity can be recorded using techniques like functional magnetic resonance imaging (fMRI). RS fMRI recordings only require passive participation from study participants, such that the prospect of isolating AD prognosticators from such data is logistically and clinically appealing. Although DMN alterations have been quantified in both AD and TBI [11–13], whether and how posttraumatic DMN abnormalities reflect AD-like functional degradation remains unknown. Because the DMN includes some of the longest white matter tracts in the brain (including tracts which integrate brain activity across the corpus callosum) [14], this network is particularly vulnerable to diffuse axonal injury after trauma [15]. Thus, studying TBI-related alterations in the DMN of subjects with cerebral microbleeds (CMBs, which are biomarkers of non-focal axonal injury [16])—as opposed to changes in other, less broadly distributed networks—is attractive. To identify posttraumatic biomarkers of AD risk, focusing on mTBI is appealing because the mTBI population is considerably larger, more homogeneous, and logistically easier to study than that of patients with moderate-to-severe TBI. Additionally, geriatric TBI is a promising setting for studying how this condition can lead to AD-like neural degradation because the comparison of AD patients to young or middle-aged TBI patients is confounded by aging effects.

This study leverages fMRI recordings acquired from healthy controls (HCs), geriatric mTBI participants with CMBs, and AD patients to provide evidence that, within ~ 6 months post-mTBI, functional connectivity (FC) within the DMN exhibits deviations from normality

whose spatiotemporal properties are statistically indistinguishable from those of similar deviations observed in AD. A linear combination of *acute* posttraumatic cognitive scores is found to be significantly and sensitively associated with *chronic* AD-like RS DMN alterations. Additionally, a supervised machine learning (ML) classifier is found to accurately identify mTBI patients with relatively broad *chronic* abnormalities in the DMN based on *acute* cognitive performance. These findings establish a detailed functional and connectomic relationship between mTBI-related acute cognition and AD-like DMN features, whose further characterization may facilitate the early identification of geriatric mTBI patients with CMBs at relatively high risk for AD.

Methods

Participants

This study was conducted with the Institutional Review Board approval. Included were one HC group ($N_1 = 48$, 22 females; age: $\mu = 69$ y, $\sigma = 5$ y, range: 58–79 y) and two study groups: geriatric mTBI ($N_2 = 29$, 13 females; age: $\mu = 68$ y, $\sigma = 6$ y; range: 57–79 y) and AD ($N_3 = 37$, 19 females; age: $\mu = 70$ y, $\sigma = 8$ y; range: 55–84 y). HC and AD subjects were selected from the AD Neuroimaging Initiative (ADNI) cohort, whose eligibility criteria are described elsewhere [17]. A total of 15 HC volunteers (31%), 9 TBI participants (38%), and 17 AD patients (46%) were hypertensive. Some ADNI participants were receiving hormonal treatment (HC: $N = 14$ or 29%; AD: $N = 9$ or 24%); some were taking medications for neurological and/or psychiatric disease (HC: $N = 20$ or 42%; TBI: $N = 18$ or 62%; AD: $N = 36$ or 97%), vascular disease (HC: $N = 29$ or 60%; TBI: $N = 19$ or 65%; AD: $N = 22$ or 59%), or metabolic disease (HC: $N = 6$ or 13%; TBI: $N = 3$ or 10%; AD: $N = 5$ or 14%). To be included, all participants had to have Montreal Cognitive Assessment (MoCA) scores and a complete session of RS fMRI data. HC participants had been clinically evaluated as having normal cognition; their MoCA scores ranged from 22 to 29 ($\mu = 26$, $\sigma = 2$). AD patients' scores ranged from 6 to 25 ($\mu = 17$, $\sigma = 5$), and all had a clinical AD diagnosis; TBI participants' scores were acquired within 48 h post-injury and were between 20 and 29 ($\mu = 23$, $\sigma = 2$). The Mini-Mental State Examination (MMSE) scores were available for both HC ($\mu = 29$, $\sigma = 1$; range: 26 to 30), TBI volunteers ($\mu = 22$,

$\sigma = 7$; range: 13 to 29), and AD participants ($\mu = 20$, $\sigma = 5$; range: 9 to 28). AD patients had Clinical Dementia Rating (CDR) sub-scores between 2 and 17 ($\mu = 6$, $\sigma = 4$), while HCs had CDR sub-scores between 0 and 2 ($\mu = 1$, $\sigma = 0.7$); CDR scores were not available for TBI participants. For HCs, the number of apolipoprotein E (ApoE) $\epsilon 4$ alleles was zero for 54% of the sample, one for 31%, and two for 15%. For AD patients, 24% had no $\epsilon 4$ alleles, 46% had one, and 30% had two. No ApoE allele information was available for TBI participants. TBI volunteers had fMRI recordings acquired ~6 months post-injury ($\mu = 5.6$ months, $\sigma = 0.5$ months) at 3 T, i.e., the same scanner field strength as the HC and AD participants. They had to have (a) a TBI due to a fall, (b) no clinical findings on acute T_1/T_2 -weighted MRI, (c) no clinical findings other than CMBs on susceptibility-weighted imaging (SWI), (d) an acute Glasgow Coma Scale score greater than 12 ($\mu = 13.7$, $\sigma = 0.5$) upon initial medical examination, (e) loss of consciousness of fewer than 30 min ($\mu \approx 4$ min, $\sigma \approx 8$ min), (f) posttraumatic amnesia of fewer than 24 h ($\mu \approx 3.5$ h, $\sigma \approx 3.2$ h), and (g) a lack of clinical history involving pre-traumatic neurological disease, psychiatric disorder, or drug/alcohol abuse. CMBs were identified in each subject using an automatic algorithm for CMB segmentation [18] and the validity of the findings were confirmed by two human experts with training in CMB identification from SWI, who had been blinded to automatic segmentation results. Disagreements between these experts were resolved by a third one (AI). Null hypotheses of group differences in age and cognition were tested using Welch's two-tailed t test for samples with unequal variances. The null hypothesis of independence between sex and group membership was tested using Pearson's χ^2 test. Effect sizes were quantified using Cohen's d for Welch's t test and the ϕ coefficient for Pearson's χ^2 test.

Neuroimaging

HC and AD participant data used in the preparation of this article were obtained from the Alzheimer's Disease Neuroimaging Initiative (ADNI) database (<http://adni.loni.usc.edu>). ADNI was launched in 2003 as a public-private partnership, led by Principal Investigator Michael W. Weiner, MD. The primary goal of ADNI has been to test whether serial MRI, positron emission tomography (PET), other biological markers, and clinical and neuropsychological assessment can be combined to

measure the progression of MCI and early AD. For up-to-date information, see www.adni-info.org. fMRI volumes were acquired at 3 T using the ADNI acquisition protocol [19]. An average of 140 fMRI volumes was obtained using the following parameters: $T_R = 3$ s; $T_E = 30$ ms; flip angle = 80° ; slice thickness ≈ 3.3 mm; 48 slices). TBI subjects' fMRI data were acquired in a Siemens Trio TIM 3 T scanner using an acquisition protocol very similar to the ADNI protocol.

Preprocessing

fMRI analysis was implemented using the FreeSurfer (FS) Functional Analysis Stream (FS-FAST, <https://surfer.nmr.mgh.harvard.edu/fswiki/FsFast>) with default parameters for (a) motion correction, (b) frame censoring, (c) frequency filtering, (d) brain masking, (e) intensity normalization, (f) co-registration of fMRI volumes to T_1 -weighted volumes, (g) surface sampling to the FS atlas, (h) smoothing (kernel with full width of 5 mm at half maximum), (i) surface and volume sampling to the Montreal Neurological Institute (MNI) atlas containing 305 subjects, and (j) smoothing for subcortical structure analysis. The first four volumes in each fMRI time series were discarded to preserve signal equilibrium and to account for each participant's adaptation to the sequence; the rest were used for analysis [20]. Nuisance variables (cerebrospinal fluid, white matter, and motion correction parameters) were accounted for using FS-FAST.

fMRI seeds

Seeds were derived in a two-step process. In the first step, the cortical delineation of the DMN defined by Yeo et al. [14] was used to parcel the cortex. This delineation includes the following cortical regions: (a) *frontal* (prefrontal cortex, precentral ventral cortex, anterior cingulate cortex, etc.), (b) *medial temporal/retrosplenial* (the parahippocampal complex), (c) *lateral temporal* (the inferior temporal gyrus and superior temporal sulcus), (d) *lateral parietal* (inferior parietal, intraparietal regions, etc.), and (e) *medial parietal/posterior cingulate* (posterior cingulate cortex and part of the precuneus). In the second step, Yeo regions were divided into gyral/sulcal parcels based on the intersection of the Yeo regions with the cortical parcellation scheme of Destrieux et al. [21]. In other words, the final

set of fMRI seeds consisted of all the regions which resulted from the intersection of the Yeo and Destrieux schemes. This was deemed to provide greater spatial detail to the analysis, particularly for DMN regions with substantial cortical coverage (e.g., the frontal DMN, which includes a large contiguous portion of cerebral cortex). The intersection of the Destrieux and Yeo schemes led to the delineation of 46 DMN regions (22 cortical regions and the hippocampus for each hemisphere; see caption to Fig. 1).

FC analysis

Both within each subject's space and within MNI space, individual fMRI time series s were consolidated using `isxconcat-sess`. A weighted least-squares (WLS) general linear model (GLM) was implemented using `mri_glmfit` to identify pairs of anatomic regions (i, j) whose fMRI signals s_i and s_j had a statistically significant partial correlation ρ_{ij} . For each DMN seed parcel i , a subject-level, voxel-wise analysis was implemented to identify spatially contiguous clusters in target region j ($i \neq j$) within which ρ_{ij} is significant. How ρ_{ij} differed in each study group (TBI or AD) relative to HC was investigated using the same GLM. Effect sizes were quantified using Cohen's f^2 .

Equivalence testing

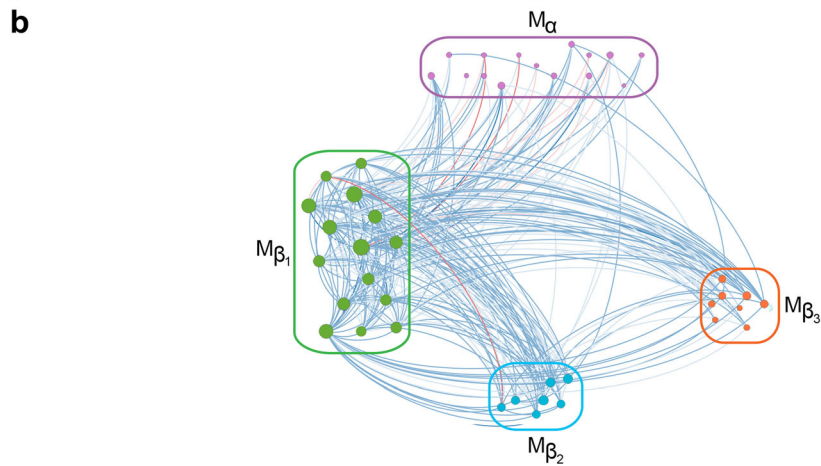
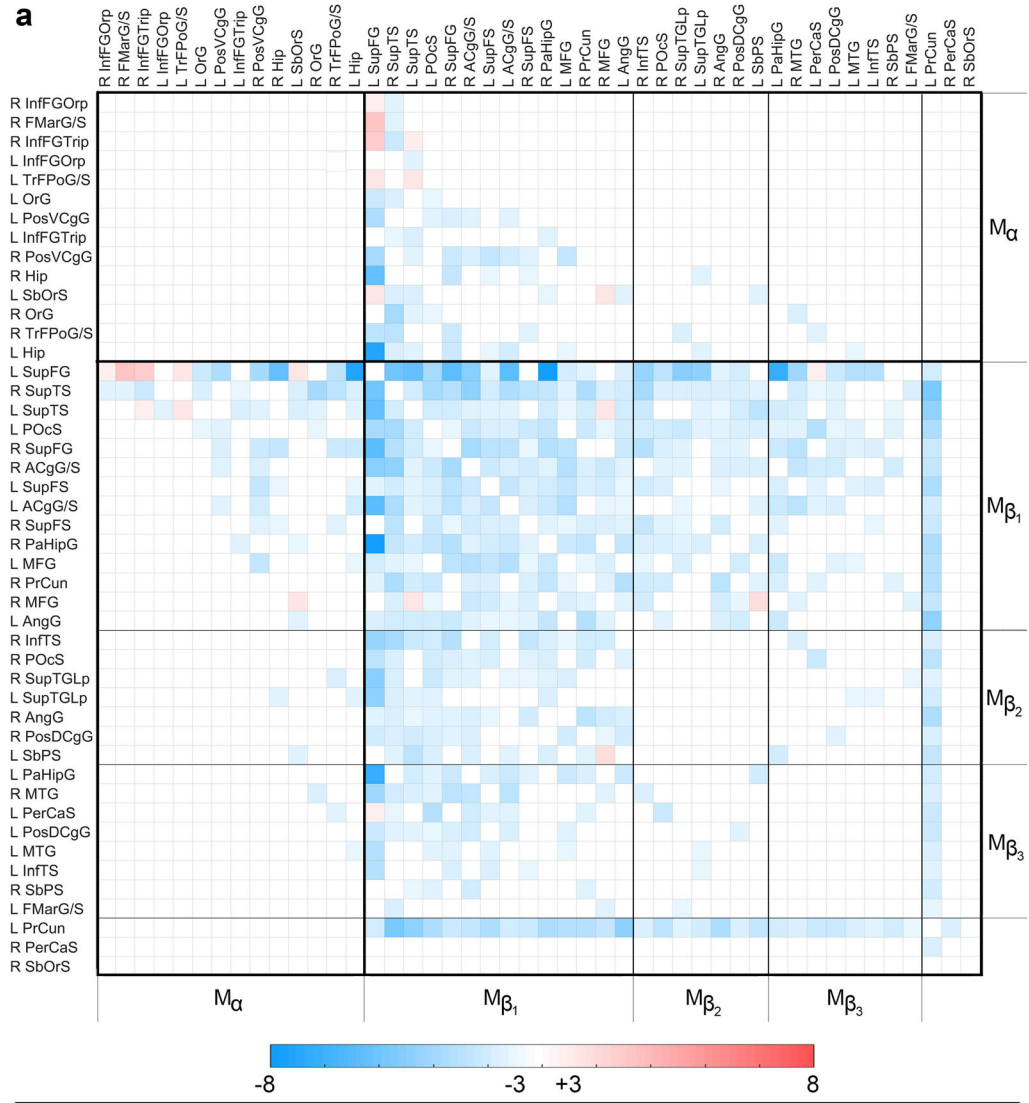
One key premise of this study is that brain features which are both (a) significantly different from HCs in both TBI and AD and (b) significantly similar across TBI and AD can be said to be *AD-like*. Thus, a brain feature observed in TBI patients can be said to be AD-like if the feature in question differs from HCs in both TBI and AD and is also significantly similar across both TBI and AD. If ρ_{ij} differs significantly from HCs in both TBI and AD, a null hypothesis of *statistical equivalence* can be tested to determine whether ρ_{ij} is AD-like. Formally, for two samples A and B , a null hypothesis of equivalence can be stated as $\mu_A(\rho_{ij}) \neq \mu_B(\rho_{ij})$ rather than as the conventional null hypothesis $\mu_A(\rho_{ij}) = \mu_B(\rho_{ij})$. The null hypothesis of equivalence fails to be accepted if the two means fall within the interval $(-\delta, \delta)$, where δ is the equivalence margin of the test [22]. In statistical parlance, equivalence implies that the correlations $\rho_{ij}(A)$ and $\rho_{ij}(B)$ are sufficiently close that neither can be considered greater or smaller than the other [23]. Equivalence hypotheses can be tested using the two one-sided t tests (TOSTs) [24]; in this study, δ is assigned a

conservative value equal to 0.2 times the width of the 95% confidence interval for the difference $\mu_A(\rho_{ij}) - \mu_B(\rho_{ij})$. To identify TBI and AD participants' correlations which deviate appreciably from normality (i.e., from the HC group) in both former groups, the null hypothesis of equivalence is only tested if both $\mu_{TBI}(\rho_{ij})$ and $\mu_{AD}(\rho_{ij})$ differ significantly from $\mu_{HC}(\rho_{ij})$. Effect sizes were quantified using Cohen's f^2 . Multiple comparison corrections using 300 permutations and a cluster-wise p -value threshold of 0.05 were implemented for all statistical tests. Equivalence testing was implemented using the freely available MATLAB software (<https://www.mathworks.com/matlabcentral/fileexchange/63204>).

(Dis)similarity matrices

Two *dissimilarity matrices* $D(TBI, HC)$ and $D(AD, HC)$ were assembled to describe mean differences in ρ_{ij} between HCs and each of the study groups (TBI and AD), respectively. Each matrix element $D_{ij}(TBI, HC)$ is set to the value of the t statistic for the test of the null

Fig. 1 (A) The dissimilarity matrix $D(HC, TBI)$ displays significant differences in the FC ρ between the HC and mTBI groups. Each cell $D_{ij}(HC, TBI)$ encodes the result of testing the null hypothesis of no mean difference in ρ_{ij} between groups. Cells corresponding to region pairs for which the null hypothesis fails to be rejected are drawn in white. Elsewhere, the color-coded quantity is a t statistic with 75 *df*. If $\rho_{ij}(TBI) > \rho_{ij}(HC)$, t is positive and D_{ij} is drawn in red; otherwise, t is negative and D_{ij} is drawn in blue. Boundaries between M_α and M_β are delineated by thick black lines; boundaries between the submodules of M_β are delineated by thinner lines. Regions are labeled using the connectogram abbreviations of Irimia et al. [64]. Frontal regions are the FMarG/S, InfFGOrp, InfFGTrip, MFG, OrG, SbOrS, SupFG, SupFS, and TrFPoG/S; limbic regions are the ACgG/S, PerCaS, PosDCgG, and PosVCgG; temporal regions are the InfTS, PaHipG, SupTGLp, and SupTS; parietal regions are the AngG, POcS, PrCun, and SbPS. (B) Graph representation of $D(HC, TBI)$. Nodes are color-coded and grouped by module. Edge colors encode t score values, according to the color bar in (A). Abbreviations: R, right; L, left; Hip, hippocampus. Cortical region abbreviations: ACgG/S, anterior cingulate gyrus and sulcus; AngG, angular gyrus; FMarG/S, frontomarginal gyrus and sulcus; InfFGOrp, inferior frontal gyrus, orbital part; InfFGTrip, inferior frontal gyrus, triangular part; InfTS, inferior temporal sulcus; MFG, middle frontal gyrus; OrG, orbital gyrus; PaHipG, parahippocampal gyrus; PerCaS, pericallosal sulcus; POcS, parieto-occipital sulcus; PosDCgG, posterior dorsal cingulate gyrus; PosVCgG, posterior ventral cingulate gyrus; PrCun, precuneus; SbOrS, suborbital sulcus; SbPS, subparietal sulcus; SupFG, superior frontal gyrus; SupFS, superior frontal sulcus; SupTGLp, superior temporal gyrus, lateral part; SupTS, superior temporal sulcus; TrFPoG/S, transverse frontopolar gyrus and sulcus



hypothesis $\rho_{ij}(TBI) - \rho_{ij}(HC) = 0$, and a similar procedure is used for $D_{ij}(AD, HC)$. A similarity matrix $S(TBI, AD)$ was also calculated to describe significant statistical equivalences of ρ_{ij} across study groups. Each matrix element S_{ij} is set to the TOST t statistic which had the smallest magnitude.

Network analysis

To investigate DMN-related commonalities and differences between TBI and AD, three analyses were carried out. The first two involved studying $D(HC, TBI)$ and $D(HC, AD)$ to group DMN nodes based on how TBI modulated their correlation differences relative to HCs and ADs, respectively. The third one examined $S(TBI, AD)$ to identify DMN nodes affected equivalently in both TBI and AD. To identify network modules, the Louvain algorithm for community detection [25] was applied 100 times for each matrix to identify module partitions. The symmetric reverse Cuthill-McKee (RCM) ordering [26] of each module was then calculated to rearrange nodes within each module. This method permutes the rows and columns of a symmetric sparse matrix to form a band matrix with minimal bandwidth, i.e., whose nonzero elements are optimally close to the diagonal. The algorithm identifies a pseudo-peripheral vertex of the network, and then utilizes a breadth-first search to order vertices by decreasing distance from the pseudo-peripheral vertex. When applied to each module of S , such blocks are arranged along the main diagonal and produce a visual representation which facilitates module inspection and analysis. Network analysis was implemented using the freely available Brain Connectivity Toolbox (sites.google.com/site/bctnet).

Network randomization

To determine whether modules' node memberships were dependent upon the DMN parcellation scheme used in the study, the DMN was repartitioned randomly 100 times to generate alternative parcellations which had the same number of nodes as the original DMN but different cortical patches corresponding to each node. An approach similar to those of Gordon et al. [27] and Irimia and Van Horn [28] was used to obtain randomized parcellations of the DMN. Briefly, random points within the cortical coverage of the DMN were selected. From these seeds, parcels were simultaneously expanded outward on the cortical mesh until they met

either other parcels or the boundary of the DMN. The procedure for identifying network modules was implemented for each randomized parcellation, and the modularity structure of the network was found each time by applying the Louvain algorithm 100 times to each matrix. The spatial overlap between each original module and the randomized modules was quantified using the Sorensen-Dice coefficient [29].

Acute cognitive impairment vs. chronic brain function

A multivariate regression analysis was implemented to study the relationship between TBI patients' *acute* MoCA scores and the number of their *chronic* FCs which were statistically equivalent to those of AD patients. The latter involved region pairs with the largest absolute values of S_{ij} (highest similarity across TBI and AD): (a) the right superior temporal sulcus and the right anterior cingulate gyrus/sulcus, (b) the left and right superior frontal gyri, (c) the left hippocampus and superior temporal sulcus, and (d) the left middle frontal gyrus and the ventral part of the posterior cingulate gyrus. The predictor variables were the entries in S associated with these region pairs, and the response variable was the MoCA score. Sex, age at MRI acquisition, and educational attainment were included as covariates. Cohen's f^2 was used as a measure of effect size and the null hypothesis of overall regression was tested using Fisher's F test [30]. To confirm and to broaden regression findings, a support vector machine (SVM) was implemented in MATLAB (<http://mathworks.com>) with default parameters and using the iterative single data algorithm (ISDA), a linear kernel function, and a heuristically assigned kernel scale parameter. The SVM was trained and cross-validated tenfold to distinguish (a) TBIs with relatively *moderate* AD-like DMN deviations from normality (i.e., with 7 or fewer statistical equivalences across TBI and AD) from other TBIs and also (b) TBIs with relatively *extensive* abnormalities (i.e., with at least 15 equivalences) from other TBIs. Let N_E be the number of significant equivalences identified ($N_E = 22$ here, see Fig. 3). Then the threshold values of 7 and 15 correspond to $\lfloor N_E/3 \rfloor$ and $\lceil 2N_E/3 \rceil$, respectively (Fig. 3). For the SVM, the number of true negatives (TNs), true positives (TPs), false negatives (FNs), and false positives (FPs) was computed, as were the true positive rate (TPR, or sensitivity), true negative rate (TNR, or specificity), positive prediction value (PPV, or precision) and Matthews' correlation coefficient

(MCC) [31]. Regression and SVM analyses were implemented in MATLAB using the `glmfit`, `fitcsvm`, and `predict` functions.

Visualization

Matrices were visualized to identify and examine DMN modules (Fig. 1, Fig. 2, and Fig. 3). Matrix entries were thresholded by statistical significance; for example, if ρ_{ij} does not differ significantly between the groups compared, the cell for D_{ij} is drawn in white. Similarly, if ρ_{ij} does not differ significantly between TBI and AD, and the cell for S_{ij} is also drawn in white. For statistically significant results, dissimilarity matrix cells are drawn in either red or blue, depending on their sign (see the caption to Fig. 3). To facilitate inspection, the cortical regions within each module were drawn on an average atlas representation of the brain. Graph representations of each functional correlation matrix were also generated using Gephi software (<http://gephi.org>). In these, each region's node was depicted as a circle whose diameter was proportional to the number of cortical regions to which the region represented by the node was functionally connected. Similarly, edges were colored using shades of blue or red to reflect the t score of lowest magnitude associated with the TOSTs for statistical equivalence testing.

Results

Demographics

Three cohorts were studied: HC participants (48 subjects, 22 females; age $\mu \pm \sigma = 69 \pm 5$ years (y)), geriatric mTBI subjects with CMBs (29 subjects, 13 females; 68 ± 6 y), and AD patients (37 subjects, 18 females; 74 ± 8 y). Further demographic descriptors are provided in the “Methods” section. CMB counts were found to range from 0 to 43 ($\mu \pm \sigma = 13 \pm 9$) in HCs, from 0 to 89 ($\mu \pm \sigma = 17 \pm 14$) in mTBI volunteers, and from 0 to 6 ($\mu \pm \sigma = 1.0 \pm 1.7$) in AD patients. No significant differences in mean age were found between HC and TBI participants ($t = 0.52$, $df = 47$, $p = 0.60$, Cohen's $d = 0.36$), between HC and AD volunteers ($t = -0.95$, $df = 55$, $p = 0.17$, Cohen's $d = 0.16$), or between TBI and AD patients ($t = -1.24$, $df = 64$, $p = 0.11$, Cohen's $d = 0.46$). No significant differences in sex ratios were found

across groups ($\chi^2 = 0.22$, $df = 1$, $p = 0.90$, $\phi = 0.09$). Significant differences in MoCA scores were found between HC and acute TBI participants ($t = 5.7$, $df = 50$, $p < 0.001$, Cohen's $d = 1.50$), between HC and AD participants ($t = 9.0$, $df = 44$, $p < 0.001$, Cohen's $d = 2.36$), but not between acute TBI participants and AD patients ($t = 0.4$, $df = 61$, $p = 0.65$, Cohen's $d = 1.58$). Similarly, significant differences in MMSE scores were found between HC and acute TBI participants (Welch's $t = 5.4$, $df \approx 28.7$, $p < 0.001$, Cohen's $d = 1.2$), between HC and AD participants (Welch's $t = 10.8$, $df \approx 37.2$, $p < 0.001$, Cohen's $d = 2.7$), but not between acute TBI participants and AD patients (Welch's $t = 1.3$, $df \approx 48.7$, $p = 0.1$, Cohen's $d = 0.3$).

(Dis)similarity matrices and modularity

Participants' DMNs were delineated and then parcelled into gyri and sulci based on the morphometric boundaries between cortical structures, as previously described. For each pair of regions i and j , clusters of significant functional correlations ρ_{ij} were then identified. Two *dissimilarity matrices* $D(TBI, HC)$ and $D(AD, HC)$ were computed to quantify significant mean differences in ρ_{ij} between HC and each of the study groups (TBI and AD, respectively). A *similarity matrix* $S(TBI, AD)$ was also calculated to describe significant statistical equivalences of ρ_{ij} across TBI and AD. Both similarity and dissimilarity were quantified using Student's t scores (see Methods).

To determine which brain regions are similarly vulnerable to TBI- and to AD-related deviations from normality (i.e., from HCs), network modules were identified within each (dis)similarity matrix. For reproducibility, the dependence of module composition upon the anatomy-based parcellation scheme was also explored. This was done by repartitioning the DMN randomly and repeatedly to create alternative parcellations which had the same number of nodes—but different spatial configurations—as the original, anatomy-based parcellation. The process of identifying network modules was then repeated for each of these randomized parcellations. At every iteration, DMN modules were identified in each dissimilarity matrix; the number N_R of randomized modules ($\mu \pm \sigma = 2.01 \pm 0.3$) was not found to differ significantly from the number of modules N_A obtained using the anatomic parcellation ($N_A = 2$; Student's $t > 0.37$, $df = 99$, Cohen's $d = 0.03$). Furthermore, the original and randomized modules overlapped spatially with high consistency across the 100

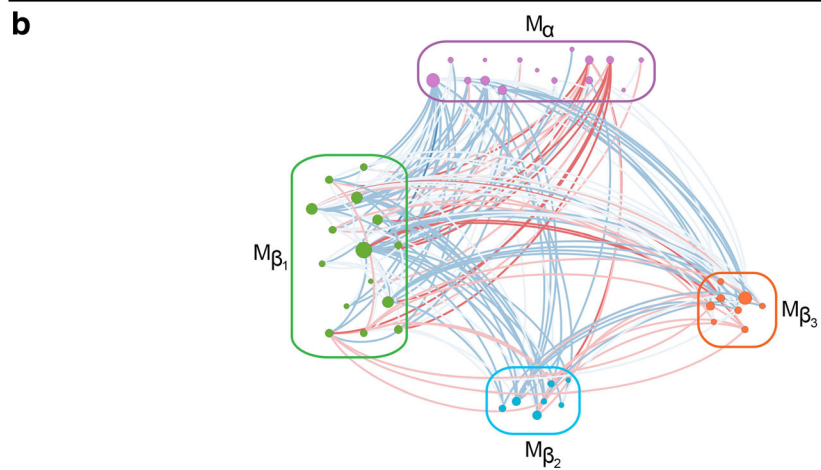
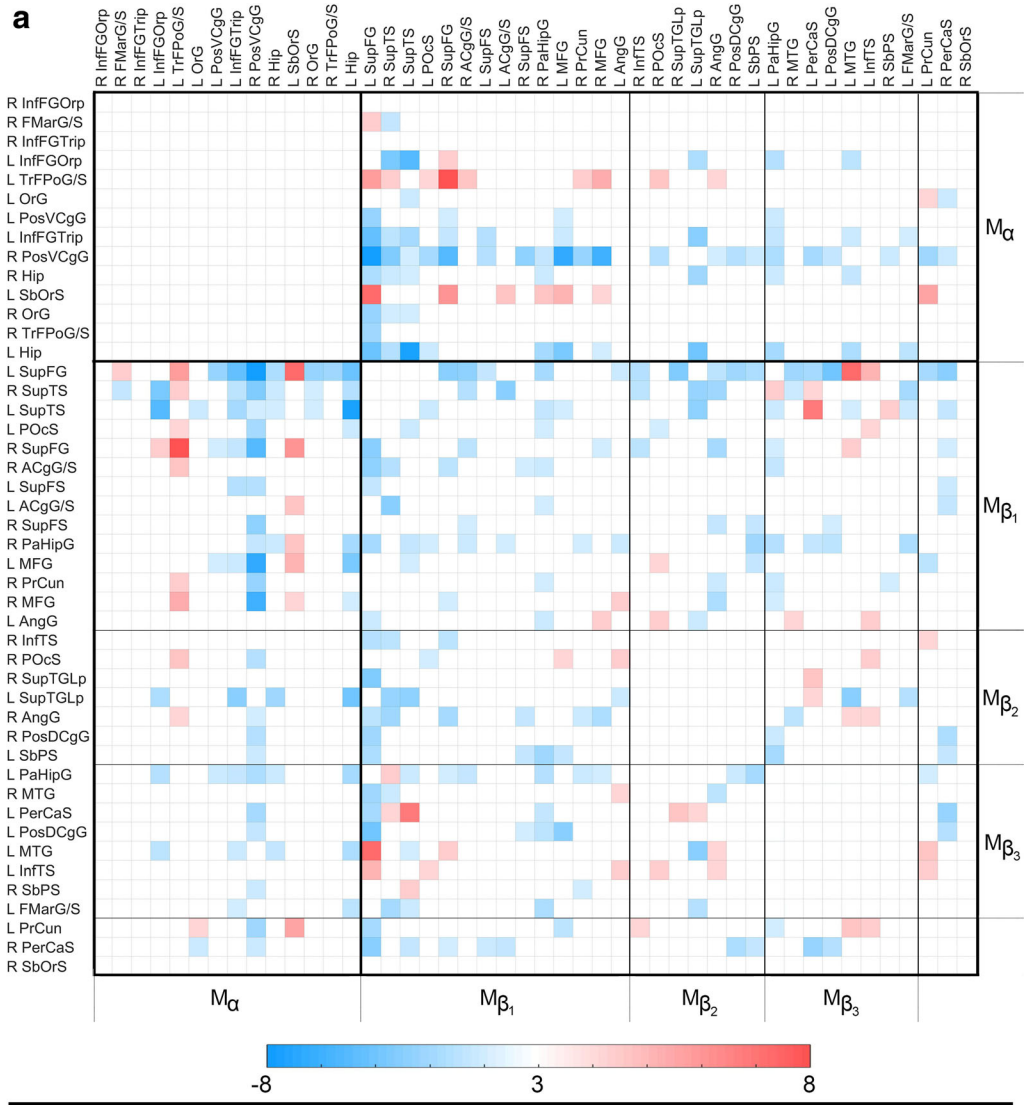


Fig. 2 Like Fig. 1, for $D(HC, AD)$. The color-coded quantity is a t statistic with 82 df . See the caption of Fig. 1 for abbreviations

randomizations (Sørensen-Dice coefficient $\mu \pm \sigma = 0.94 \pm 0.06$; 95% CI = [92.89, 95.10]). Thus, the randomized modules' nodal memberships and spatial coverages agreed with those of the original modules.

DMN modules in mTBI versus HC

RCM orderings [26] were used to display modules along the main diagonal of each (dis)similarity matrix. The RCM-ordered modules of $D(HC, TBI)$ and $D(HC, AD)$ are displayed in Fig. 1 and Fig. 2, respectively, as are the graph representations of the corresponding dissimilarity matrices. M_α , the first module common to both $D(HC, TBI)$ and $D(HC, AD)$, includes (a) the hippocampus, (b) ventral and dorsal prefrontal cortex, and (c) the ventral aspect of the posterior cingulate gyrus. Significant functional correlations between nodes within M_α do not differ significantly across TBI and HC (Fig. 1); this may indicate that, on average, the geriatric mTBI patients did not experience substantial FC alterations within brain areas covered by M_α within the first ~ 6 months post-injury. M_β , the second module along the diagonal of $D(HC, TBI)$, contains all the DMN regions outside M_α . Within M_β , correlations are consistently weaker in mTBI participants relative to HCs. Furthermore, the superior frontal gyrus and precuneus are found to be the two structures whose TBI-related FC deviations from normality are the broadest across the DMN. FC differences between TBI and HC involve relatively few pathways connecting M_α and M_β . Thus, although M_α connections are considerably less affected by TBI compared with M_β , some pathways between these modules are not.

DMN modules in AD versus HC

Whereas FC is typically weaker in TBI than in HC (Fig. 1), AD patients' FC deviations from normality vary considerably (Fig. 2). These deviations can be grouped into five modules which occur bilaterally; the first is identical to M_α and the rest are subdivisions of M_β (M_{β_1} through M_{β_4}). Across AD and TBI, M_α , M_{β_3} , and M_{β_4} are similar in that their intramodular FCs do not differ significantly from those of HC participants. M_{β_1} is a frontotemporal module with relatively few intramodular FC differences between AD and HC but with considerably more differences of this kind involving intermodular connections. M_{β_2} contains broadly distributed frontal, limbic, and parietal regions; comparing the HC and AD groups from the standpoint

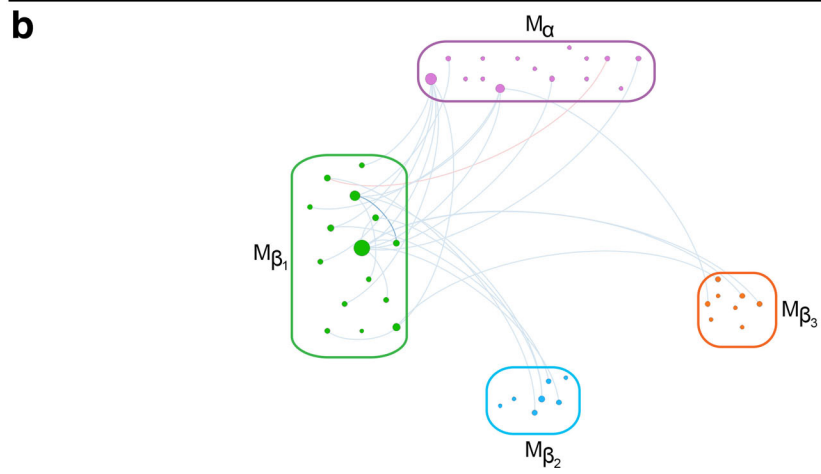
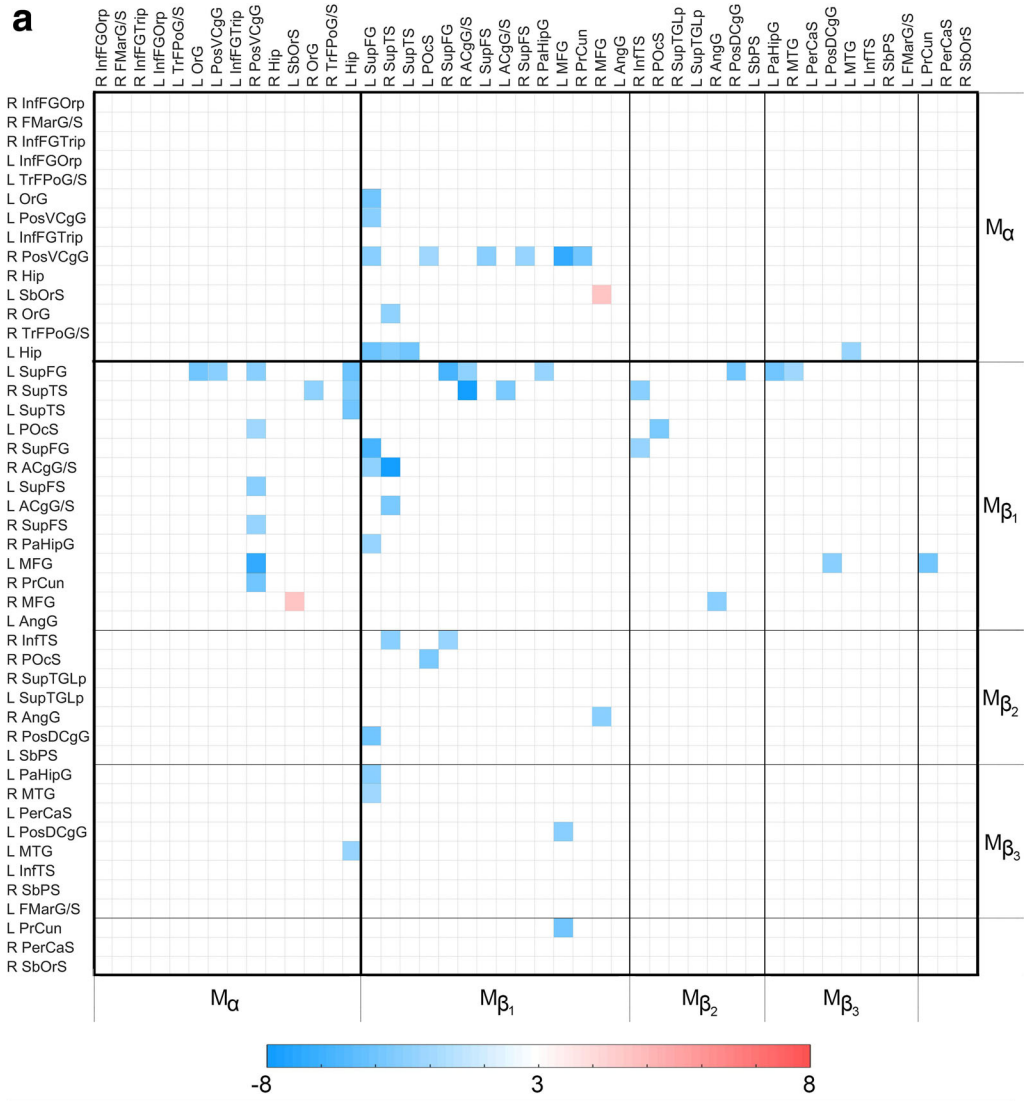
of correlations within M_{β_2} reveals sparse group differences involving both intra- and intermodular connections. Like in the case of M_α , AD patients' M_{β_3} and M_{β_4} modules do not have intramodular correlations which differ significantly from HC, although both subunits exhibit numerous such differences involving intermodular connections.

DMN modules in TBI versus AD

Figure 3 displays the similarity matrix $S(TBI, AD)$ and its graph representation to identify regions with statistical equivalences across study groups. Regions exhibiting such similarities involve the dorsolateral prefrontal cortex, the lateral temporal lobe, and the ventral aspect of the posterior cingulate gyrus. The hippocampus is topologically proximal to the latter two areas; furthermore, hippocampo-cortical correlations are substantially affected in both TBI and AD. Nevertheless, only few hippocampo-cortical correlations are statistically equivalent across these conditions. The strongest similarities between TBI and AD involve connectivity between the lateral temporal lobe and anterior cingulate cortex, as well as between dorsolateral prefrontal cortex and each of the following three structures: the hippocampus, the lateral temporal lobe, and the posterior cingulate cortex.

Acute cognition versus chronic DMN in TBI

Upon testing the association between MoCA scores and the number of FC similarities (i.e., pairwise statistical equivalences) between TBI and AD, the null hypothesis of the test for overall multivariate regression was rejected ($F = 1.6$, $df_1 = 5$, $df_2 = 111$, $p < 0.0034$, Cohen's $f^2 = 0.39$). In other words, this test rejected the null hypothesis according to which there was no multivariate correlation between (a) MoCA scores and (b) the number of FC similarities involving TBI and AD. To study further the relationship between acute cognition and chronic DMN dysfunction, two support vector machines (SVM) were used. The first one was trained on 50% of each cohort to distinguish TBI participants with relatively moderate AD-like DMN deviations from normality (i.e., with 7 or fewer statistical equivalences across TBI and AD) from other TBI participants. Another SVM was trained on 50% of each sample to distinguish TBI participants with relatively extensive abnormalities (i.e., with 15 or more equivalences) from the rest of the TBI participants. The means and standard deviations for the number of TNs, TPs, FNs,



◀ **Fig. 3** The similarity matrix $S(TBI, AD)$ displays statistically significant equivalences of functional correlation ρ between the TBI and AD groups. Each cell S_{ij} encodes the result of testing the null hypothesis of equivalence in ρ_{ij} across these two groups. This null hypothesis is only tested if both TBI and AD differ significantly from HC. In other words, if there is no significant mean difference in ρ between/either (a) HC and TBI and/or (b) HC and AD, S_{ij} is drawn in white. If both study groups differ from the HC group but no significant statistical equivalence is found across TBI and AD, S_{ij} is also drawn in white. Elsewhere, the color-coded quantity is the value of the TOST procedure's t statistic with the smallest magnitude. The color-coded quantity is a t statistic with 63 df . If a statistical equivalence is associated with a relatively stronger correlation in both TBI and AD relative to HC, t is positive and S_{ij} is drawn in red; if the correlation is weaker relative to HC, t is negative and S_{ij} is drawn in blue. Boundaries between M_α and M_β are delineated by thick black lines; boundaries between the submodules of M_β are delineated by thinner lines. See the caption of Fig. 1 for abbreviations. (B) Graph representation of $S(TBI, AD)$. Nodes are color-coded and grouped by module. Edge colors encode t score values, according to the color bar in (A)

and FPs were computed, as were their TPRs (i.e., sensitivities), TNRs (i.e., specificities), PPVs (i.e., precisions), and MCCs. Across 100 scenarios, the SVM trained to identify TBI patients whose similarities to AD were relatively modest (7 or fewer equivalences) achieved the following means and standard deviations: TN = 18.0 ± 0.8 ; TP = 9.0 ± 0.6 ; FN = 1.0 ± 0.6 ; FP = 1.0 ± 1.0 ; TPR = 0.90 ± 0.06 ; TNR = 0.95 ± 0.06 ; PPV = 0.91 ± 0.1 ; and MCC = 0.85 ± 0.1 . The SVM trained to predict which TBI patients' similarities to AD were relatively broad (15 or more equivalences) yielded the following results: TN = 17.1 ± 0.7 ; TP = 10.0 ± 0.7 ; FN = 0.9 ± 0.7 ; FP = 1.1 ± 1.0 ; TPR = 0.9 ± 0.1 ; TNR = 0.95 ± 0.1 ; PPV = 0.9 ± 0.1 ; and MCC = 0.86 ± 0.1 . Figure 4A displays cortical maps of M_α and M_β on the surface of an average brain atlas, contrasting the fact that M_α includes primarily frontal regions whereas M_β includes the rest of the DMN. Figure 4B displays DMN parcels whose *chronic* DMN similarities across TBI and AD were accurately predicted from *acute* MoCA scores using the two SVMs. These regions include areas of the dorsolateral prefrontal, lateral temporal, posterior cingulate, and parahippocampal cortices.

Discussion

Significance

mTBI patients with relatively high rates of neural degradation may be at commensurately high risk for AD,

and the estimation of such risk can be assisted by knowledge of how TBI modifies brain function along AD-like trajectories. Thus, an important indication of this study is that the DMNs of geriatric mTBI patients can exhibit distinct patterns of AD-like RS FC as early as ~ 6 months post-injury. If this is the case, our finding highlights older adults' substantial vulnerability to TBI [32] and may be unsurprising given that the highest incidence of TBI is in older adults [5], where even injuries of mild severity can increase AD risk [8]. An alternative, more general interpretation is that geriatric mTBI patients exhibit RS FC patterns which may occur in several neurodegenerative diseases among which AD can be counted.

The outcome of the test of overall regression indicates a significant, inverse association between TBI patients' *acute* MoCA scores and the extent of their *chronic* DMN similarities to AD. This outcome is confirmed by the SVM classifications, which achieved sensitivities and specificities which compare favorably with those for blood and imaging biomarkers of AD [33]. Our results may be useful for predicting the risk of AD-like functional degradation after TBI because mTBI patients' acute cognitive scores are predictive of their AD-like DMN features. Thus, our study is significant in three distinct ways. Firstly, it identifies a set of functional DMN features which are common to both geriatric mTBI and AD. Secondly, it demonstrates that the analysis of RS FC in the DMN using the present approach can reveal the extent to which mTBI-affected function may transition onto AD-like trajectories. Thirdly, it suggests that, if AD-like abnormalities are indeed commensurate to mTBI patients' AD risk, the DMN features described here can be used to improve AD risk estimation. An alternative and potentially broader implication is that our results can be used to improve risk estimation not only in AD but also in other neurodegenerative conditions whose brain degradation patterns resemble those of AD in their early stages.

Connectomic pathophysiology

Although DMN subdivisions have been mapped with high stability across health and disease [14], such subunits' relative vulnerability to TBI is not well understood. An intriguing finding of this study is that the node memberships of M_α , M_{β_2} , and M_{β_4} are consistently similar across the TBI and AD groups (Fig. 1 and

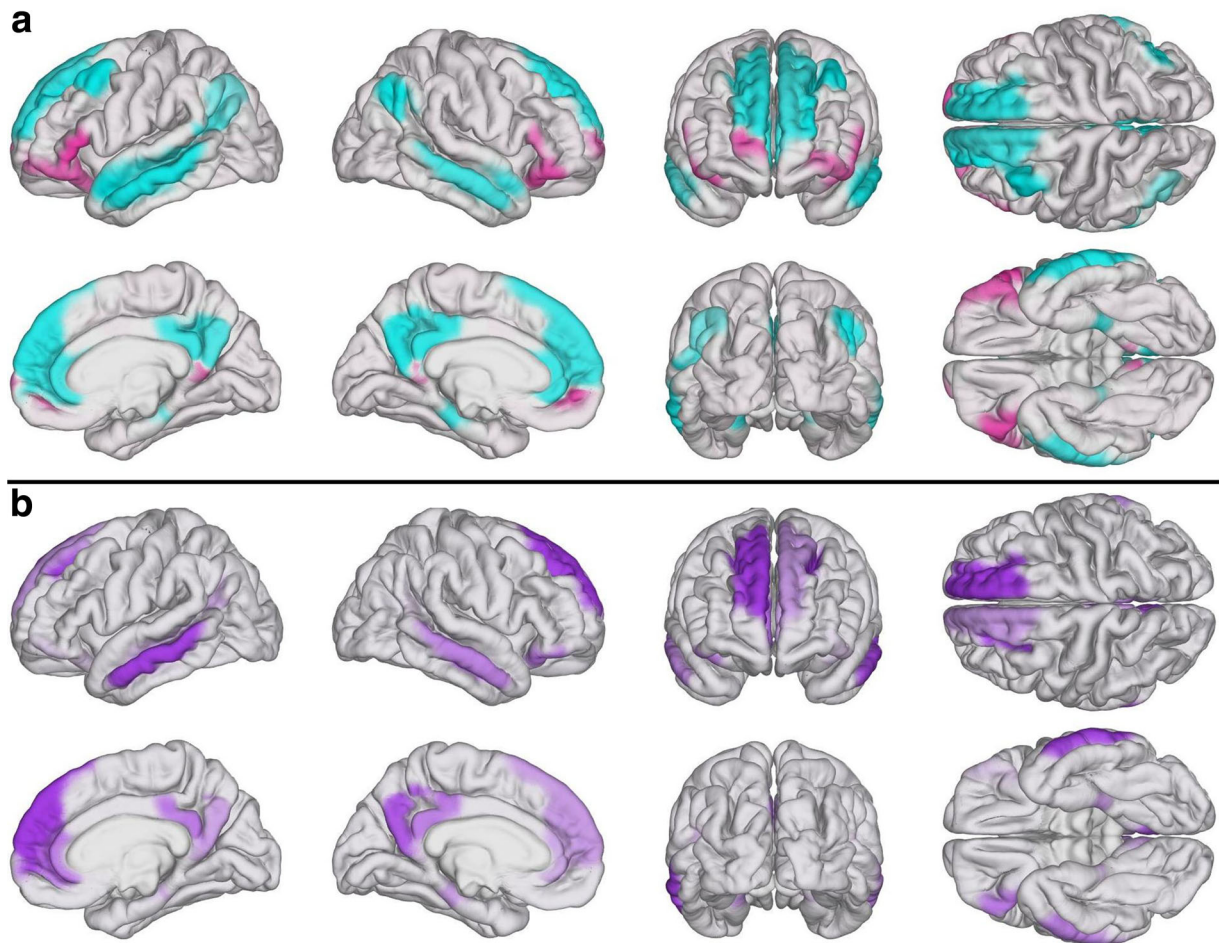


Fig. 4 Cortical maps of DMN modules. (A) M_α (magenta) and M_β (cyan) mapped on the surface of an average brain atlas. (B) TBI-affected brain regions in $S(TBI, AD)$ (see Fig. 3) whose *chronic* similarity to AD was predicted based on *acute* cognitive scores using SVMs

Fig. 2). The probability of such an occurrence being due to chance is low given the results of our randomization analysis and the fact that the modules of each dissimilarity matrix were identified independently of one another. Instead, it is more likely that this likeness of modularity could be due to intrinsic properties of the DMN which modulate their susceptibility to TBI and AD, and perhaps even to neurodegenerative processes in general.

M_α contains primarily fronto-hippocampo-limbic connections. For this reason, the existence of modular structure resemblances between TBI and AD may imply that both conditions impact intermodular connections within M_α , M_{β_2} , and M_{β_4} in ways which are substantially different from how they affect the rest of the DMN. Since the three modules are distinct, however,

their existence may also indicate that, although FC within DMN subunits can be robust to geriatric mTBI, such robustness can manifest itself in distinct ways via mechanisms which are yet to be determined. Although appealing, the task of exploring such network-theoretic differences between DMN subunits could not be undertaken adequately here due to the small effect sizes implied by such differences. More specifically, such minute effect sizes require commensurately large samples to avoid high probabilities for errors of type I and/or II when contrasting module properties across groups. Thus, future research should aim further to study DMN similarities between TBI and AD.

The properties of the M_α module summarized in Fig. 1 and Fig. 2 suggest that geriatric mTBI affects certain FCs between frontal, limbic, and

hippocampal areas in ways which differ from those pertaining to other DMN regions. This is perhaps unsurprising given that many frontal areas experience atrophy as early as middle age [34] and that the frontal lobe appears to exhibit distinct trajectories in TBI compared with AD [35–37]. On the other hand, although FC involving the hippocampus and cingulate areas is sensitive to both TBI and AD from the early stages of both conditions [38–40], their interactions within the RS DMN remain poorly understood and require further research. Interestingly, only very few hippocampocortical connectivity alterations were found to be statistically similar across AD and mTBI (Fig. 3), despite such connections being significantly affected by both conditions. This may suggest that geriatric mTBI and AD affect this connectivity ensemble in different ways and that the functional abnormalities observed in this study might be associated with dissimilar functional trajectories within DMN modules during posttraumatic neurodegeneration. Here it is important to remind the reader of the aphorism according to which “absence of evidence is not evidence of absence.” In our context, this means that the absence of a statistical similarity finding between TBI and AD—as represented by blank connectivity matrix cells in Fig. 3—does not imply evidence for the absence of such similarities. Instead, there are at least two possible scenarios. The first of these involves the situation where a similarity exists but its effect size is not large enough for its adequately powered detection to be possible in this sample. In the second scenario, although the FCs of both TBI participants and AD patients differ significantly from the FCs of HCs, the former two are not significantly equivalent. To provide an example of this, consider the scenario where the mean FC between two regions is 0 in HC, 0.8 in TBI, and -0.8 in AD, and the standard deviation of each measure is 0.01. Clearly, the FCs of the TBI group (0.8) and that of the AD group (-0.8) are both significantly different from that of HCs (0); nevertheless, the FCs of the TBI and AD groups differ substantially from each other (0.8 vs. -0.8), such that these FCs are not statistically equivalent. This simple example highlights the need to interpret statistical equivalent findings carefully.

In this study, the most prominent common feature of M_{α} , M_{β_3} , and M_{β_4} is the extent to which the intermodular connections of these three modules deviate from normality in both mTBI and AD. Furthermore, none of these modules exhibits intramodular connectivity which differs significantly from HCs in either clinical condition. These findings suggest, at the very least, that posttraumatic functional connections can be grouped according to their relative vulnerability to injury-related neurodegeneration. This is analogous to the similar task of grouping structural connections based on their vulnerability to injury, which entails mapping the structural scaffold of the human connectome [41]. Nevertheless, findings like ours may be difficult to interpret further in the absence of connectome-wide characterizations of connectivity between the DMN and the rest of the brain. Thus, future studies should aim to clarify how DMN subdivisions differ from the standpoint of their response to TBI or AD.

There are relatively few statistical similarities between TBI and AD (Fig. 3), despite the much greater number of significant differences between HC and TBI, as well as between HC and AD (Fig. 1 and Fig. 2). To contextualize this, it is important to note that the statistical similarities observed in this study between TBI and AD were detected only ~ 6 months after geriatric TBI of mild severity. Presumably, injuries of greater severity can be associated with additional significant similarities, and future research should test this hypothesis. For example, the severity of TBI- and AD-related digestive disturbances may be associated with connectomic disruptions which affect similar cortical areas and which may be associated with injury/disease severity [42–45].

It is not unlikely that the pathophysiological processes giving rise to the relatively few observed similarities between TBI and AD continue to affect the aging brain long after injury. Thus, the number of DMN-related similarities between TBI and AD may be proportional to how late after injury such similarities are measured and quantified. Specifically, if the neuropathological processes initiated by TBI continue to affect the DMN long after injury, it is possible that TBI and AD patients' DMNs start to resemble each other more and more as the time since injury increases. If this is the case, the number of statistical similarities observed here may provide a lower bound on the number of similarities between geriatric mTBI and AD. In such a scenario, the later fMRI recordings are acquired post-injury, the

greater DMN degradation there should be along AD trajectories. Whether this conjecture is valid should be investigated by future studies.

Neurovascular pathophysiology

The occurrence of CMBs in geriatric mTBI patients is relevant to the spatial profile and severity of posttraumatic WM alterations [16, 32, 46]. Previously, we showed that the trajectories and integrities of WM fasciculi passing through the vicinity (penumbrae) of posttraumatic CMBs can be altered in ways which persist for at least 6 months post-injury [47, 48]. Furthermore, other studies have found that CMB count is associated with network alterations in patients with early AD as well [49]. Since CMBs are associated with structural connectivity changes in both TBI and AD, these manifestations of blood-brain barrier breakdown may also modulate functional connectivity patterns shared by TBI and AD. In the present study, however, AD patients' CMB counts were quite low, which suggests that CMB-related network changes previously observed in AD are relatively unlikely to drive the RS FC similarities between mTBI participants and AD patients described here. One could argue that, in ideal circumstances, (dis)similarities between HCs, mTBI patients, and AD participants should be studied in the absence of CMBs; this, however, is particularly challenging in older adults. For example, in geriatric TBI patients, posttraumatic CMBs are frequently co-morbid with CMBs of hypertensive etiology, as well as with CMBs due to cerebral amyloid angiopathy (CAA), which is also a risk factor for AD. Because of the relatively high combined prevalence of neurovascular disease, CAA, and hypertension in older adults [46], studying TBI-related brain network alterations in the absence of CMBs may be either logistically impractical or of limited relevance to the pathophysiological processes of the average person's aging brain. In other words, studying functional network alterations in CMB-free older individuals may limit the utility of the insights gained from such studies to a relatively minor subset of the aging adult population. Although elucidating how CMBs modulate the extent of AD-like FC patterns in the mTBI-affected brain is beyond our scope, this study's inclusion of individuals with a wide range of CMB counts assists in resolving AD-like FC trajectories in a sample whose neurovascular profile reflects, at least to some extent, the radiological findings of aging adults with TBI and/or

AD. Future research should aim to clarify the extent to which CMBs modulate the extent and severity of AD-like FC deviations from normality in geriatric mTBI patients.

Comparison to prior studies

Arguably, the statistical similarities between study groups (TBI and AD) are of greatest interest in this study. Nevertheless, differences between HC and TBI and between HC and AD are also relevant because they underlie key comparisons between TBI and AD [50]. Fortunately, the comparison of our results to those of previous studies strengthen the case for our own analysis and broadens the scientific consensus on DMN differences between (a) HC vs. TBI and (B) HC vs. AD.

Our findings are in broad agreement with those of important previous studies on DMN abnormalities after TBI. For instance, Mayer et al. [13] reported that, compared with mTBI, HC subjects have stronger FC between the (a) anterior and posterior cingulate cortices, (b) anterior cingulate cortex and the superior frontal gyrus, (c) anterior cingulate cortex and the supramarginal gyrus, (d) the inferior parietal lobule and posterior parietal cortex, (e) the inferior parietal lobule and the middle frontal gyrus, (f) prefrontal cortex and the superior parietal lobule, and between (g) prefrontal cortex and the superior frontal gyrus. Our findings are in remarkable agreement with those of Mayer et al. (Figure 1). Furthermore, like in the present study, Johnson et al. [11] identified stronger FC in HC participants compared with TBI volunteers between posterior cingulate cortex and the hippocampal formation. These authors also found that (a) the lateral parietal lobes have significantly more bilateral RS FCs to the dorsolateral prefrontal cortex in HCs, that (b) mTBIs show only ipsilateral connections between these regions, and that (c) RS FCs between medial prefrontal and lateral parietal cortices are primarily observed in mTBI. These three sets of findings are replicated by our own study (Figure 1).

Influential prior results on DMN differences between HC and AD are confirmed by ours. For example, as we did, Greicius et al. [51] found that AD patients exhibit deficient activity involving the hippocampus and posterior cingulate cortex. In AD patients, Damoiseaux et al. found stronger FCs between (a) the frontal poles and other anterior frontal regions, (b) the left superior frontal gyrus and other frontal regions, and between (c) the

precuneus and the frontal poles, but weaker FCs involving regions like the superior and middle frontal gyri. Our results confirm the findings of Greicius et al. (Fig. 2) as well as those of Zhang et al. [52], who found reduced RS FCs between (a) posterior cingulate cortex and the hippocampus, (b) posterior cingulate cortex and the precuneus, and between (c) dorsolateral prefrontal cortex and middle temporal areas. Additionally, as we did, Zhang et al. found stronger RS FCs between the precuneus and many dorsolateral prefrontal regions.

Equivalence testing

This study uses equivalence testing, which originates in pharmacokinetics [53]. There, marketing new drugs requires testing whether their effectiveness is undistinguishable from that of older and more expensive competitors. Here, testing whether TBI-related DMN alterations are equivalent to AD-related alterations assists in illustrating how TBI and AD can result in statistically indistinguishable patterns of DMN deviations from normality (i.e., from HCs). Using equivalence testing in studies like ours is key because attempting to establish equivalence using statistical tests of conventional null hypotheses (e.g., $\mu_1 = \mu_2$) frequently leads to incorrect conclusions. Specifically, a significant result after such a test establishes a difference, whereas a non-significant one simply implies that equivalence cannot be ruled out. Thus, the risk of wrongly inferring equivalence can be very high, such that proper equivalence testing is needed instead [23]. In the current context, it is important to emphasize that equivalence testing was implemented here only for pairs of regions whose partial correlations ρ_{ij} differed significantly from HCs in *both* AD and mTBI. If this constraint had not been imposed, distinguishing normal from abnormal statistical equivalence patterns would not have been possible within this statistical inference framework.

Modularity structure

Here, DMN modules were identified from dissimilarity matrices rather than from FC matrices, as typical of functional connectomics studies [54]. Thus, the modules found in this study should be interpreted as groups of nodes whose FCs deviate from normality in similar ways, rather than as sets of nodes which are similarly connected to one another. The concept of deriving modularity properties from dissimilarity matrices is not new

and is, in fact, the basis of multidimensional scaling (MDS)—an ordination technique for information visualization and dimensionality reduction which has been used widely for decades [55]. In MDS, like here, dissimilarity matrices can be conceptualized as distance matrices whose entries are calculated using a distance function whose definition can be conveniently assigned depending on the nature of the data. In this study, the distance in question is a t score, which is a proper statistical metric defined as the standardized difference between two group means. This framework is univariate and therefore accommodates only one measure at a time, i.e., functional correlation in our case. However, should additional connectivity measures (e.g., Granger causality, phase locking value) or functional modalities (e.g., electro- or magnetoencephalography) be available [56–58], this formalism could be extended to an arbitrary number of dimensions using the (multivariate) Mahalanobis distance and/or non-Euclidian metrics, like in generalized MDS [59].

Replicability

Our findings should be replicated in larger cohorts for confirmation and improvement of statistical estimates. Although the samples used in this study were of moderate size, the effects reported here reflect relatively large mean differences between cohorts. This is perhaps unsurprising because, across a variety of studies and methodologies, even TBI of *mild* severity has been associated consistently with large statistical effects related to anatomical and physiological measures [60]. Furthermore, the mTBI participants studied here did not have clinical findings on MRI except for sporadic, SWI-detectable CMBs; this is rare in TBI studies. Thus, the present study facilitates the comparison of TBI to AD partly due to the uniquely suitable profile of the geriatric TBI sample involved, whose MRI profile is relatively rare; this lends strength and uniqueness to the present study. Specifically, the effect sizes characterized here are more likely to be due to functional—rather than to structural—pathology because the structural MRI findings of these geriatric mTBI patients are minimal. For this reason, the large statistical effects of TBI upon the DMN are quite likely responsible for the large effect sizes reported. This contrasts with many other neurological conditions, where FC metrics often exhibit relatively smaller effect sizes, such that considerably larger samples are often required to detect effects of interest

with adequate statistical power. It also contrasts with most other TBI studies, where gross TBI pathology on MRI findings is the norm. Nevertheless, despite the unique characteristics of our sample, further research in a larger cohort remains necessary for replication. This observation also pertains to our SVM findings, which may not be applicable to TBI cohorts of greater severity, even if only due to the greater heterogeneity of moderate-to-severe TBI relative to mTBI. Thus, our findings should not be interpreted as being broadly applicable to TBIs of any severity. Furthermore, the predictive value of our SVM relies heavily on acute MoCAs, whose values do not convey well the rich subtleties of posttraumatic cognitive impairment [61]. Thus, future studies should aim to utilize more detailed descriptors, preferably across all cognitive domains [62], to take better advantage of SVMs' potential for functional outcome prediction. Finally, it should be mentioned that replication of our findings using electrophysiological techniques like electro- and magnetoencephalography (EEG and MEG, respectively) [56, 63] would be very helpful in establishing the spatiotemporal parameters of the (dis)similarities observed here.

Limitations

It is important to acknowledge the possibility that the similarities between mTBI and AD described here may also be shared by mTBI with other neurodegenerative conditions. Although exploring whether this is the case is outside the scope of this study, future research should attempt to clarify whether the similarity patterns identified are representative not only of mTBI similarities to AD but also of the relationship between mTBI and other neurodegenerative conditions like Parkinson's disease, for which TBI is also a risk factor. Furthermore, because many participants were on medications for neurological, psychiatric, vascular, and/or metabolic disease when scans were acquired, the extent to which comorbidities affect the results of this study is unclear. Fortunately, the proportion of volunteers on medications for vascular and metabolic disease was approximately equal for the mTBI and AD groups, such that confounds due to these treatments are likely to be less severe than in the scenario where large discrepancies between groups existed. By contrast, the proportion of subjects undergoing treatment involving medications for neurological/psychiatric disease was much higher for the AD group (97%) than in the mTBI group (62%), mostly because almost all AD

patients were taking cognition-enhancing medications. The effects of comorbidities upon AD-like FC trajectories in mTBI patients are worthy of further study.

One potential limitation of FC studies like ours is that results can be affected by how the DMN is defined and by the cortical parcellation used for fMRI seed analysis. Here, the DMN was defined based on the Yeo delineation and parcelled based on the intersection of this delineation with the Destrieux parcellation scheme. Nevertheless, the use of other parcellation schemes of similar spatial resolution may not alter conclusions substantially because the randomization analysis undertaken yielded network modules whose anatomic coverage was consistent. Last but not least, the equivalence margin used in this study was 0.2, which is considered to be relatively conservative [23]; as the margin becomes narrower and narrower, however, more and more hypotheses of equivalence are rejected. Unfortunately, there is currently no consensus-based standard for the "ideal" equivalence margin which life scientists should utilize.

Conclusion

This study provides evidence that geriatric mTBI is associated with DMN deviations from normality which are statistically indistinguishable from those observed in AD. The DMN regions affected can be grouped into modules based on their vulnerability, with striking similarities in the composition and properties of these modules across the two neurological conditions. Multivariate regression analysis identified a clear relationship between acute cognitive deficits and chronic DMN alterations. Furthermore, SVM classifications suggested that DMN features may be useful for early prognostication of the extent and severity associated with posttraumatic neuropathophysiology. Nevertheless, the neurodegenerative processes of TBI and AD differ substantially despite their potential commonalities. Thus, the similarities in DMN alteration trajectories shared by these conditions and reported here may not be driven by similar trends toward functional reorganization. Because the methodological limitations of functional neuroimaging prevent us from a mechanistic exploration of this hypothesis, future research should study the pathophysiological mechanisms shared by TBI and AD in further detail.

Acknowledgments The authors thank Maria Calvillo, Lei Cao, Yu Hu, Jun H. Kim, Sean O. Mahoney, Van Ngo, Kenneth A. Rostowsky, and Shania Wang for their assistance.

Computer code availability The computer code used in this study is freely available. FreeSurfer and FS-FAST are freely available (<https://surfer.nmr.mgh.harvard.edu>). Equivalence testing was implemented using freely available MATLAB software (<https://www.mathworks.com/matlabcentral/fileexchange/63204>). Network analysis was implemented using the freely available Brain Connectivity Toolbox (<https://sites.google.com/site/bctnet/>). Network visualizations were generated using Gephi (<http://gephi.org>). Regression and SVM analyses were implemented in MATLAB (<http://mathworks.com>) using the `glmfit`, `fitcsvm`, and `predict` functions.

Authors' contributions A.I. contributed to the study design, data analysis, and result interpretation and wrote the manuscript. A.S.M., N.N.C., N.F.C., and E.B.J. contributed to the study design, data analysis, and result interpretation.

Funding information This work was supported by NIH grant R01 NS 100973 to A.I., by DoD award W81-XWH-1810413 to A.I., by a Hanson-Thorell Research Scholarship to A.I., and by the Undergraduate Research Associate Program (URAP) at the University of Southern California. Data collection and sharing for this project was funded by the Alzheimer's Disease Neuroimaging Initiative (ADNI, NIH Grant U01 AG024904) and DoD ADNI (DoD award number W81XWH-12-2-0012). ADNI is funded by the National Institute on Aging, the National Institute of Biomedical Imaging and Bioengineering, and through generous contributions from the following: AbbVie, Alzheimer's Association; Alzheimer's Drug Discovery Foundation; Araclon Biotech; BioClinica, Inc.; Biogen; Bristol-Myers Squibb Company; CereSpir, Inc.; Cogstate; Eisai Inc.; Elan Pharmaceuticals, Inc.; Eli Lilly and Company; EuroImmun; F. Hoffmann-La Roche Ltd. and its affiliated company Genentech, Inc.; Fujirebio; GE Healthcare; IXICO Ltd.; Janssen Alzheimer Immunotherapy Research & Development, LLC.; Johnson & Johnson Pharmaceutical Research & Development LLC.; Lumosity; Lundbeck; Merck & Co., Inc.; Meso Scale Diagnostics, LLC.; NeuroRx Research; Neurotrack Technologies; Novartis Pharmaceuticals Corporation; Pfizer Inc.; Piramal Imaging; Servier; Takeda Pharmaceutical Company; and Transition Therapeutics. The Canadian Institutes of Health Research is providing funds to support ADNI clinical sites in Canada. Private sector contributions are facilitated by the Foundation for the National Institutes of Health (www.fnih.org). The grantee organization is the Northern California Institute for Research and Education, and the study is coordinated by the Alzheimer's Therapeutic Research Institute at the University of Southern California. ADNI data are disseminated by the Laboratory for Neuro Imaging at the University of Southern California. Data availability MRI data acquired from HC and AD participants are publicly available from the ADNI database (<http://adni.loni.usc.edu>). For TBI participants, primary data generated during and/or analyzed during the current study are available subject to a data transfer agreement. At the request of some participants, their written permission is additionally required in a limited number of cases.

Compliance with ethical standards

Conflicts of interest The authors declare no actual or perceived competing interests.

References

- de Freitas Cardoso MG, Faleiro RM, de Paula JJ, Kummer A, Caramelli P, Teixeira AL, et al. Cognitive impairment following acute mild traumatic brain injury. *Front Neurol*. 2019;10:198.
- Irimia A, Goh SY, Torgerson CM, Vespa P, Van Horn JD. Structural and connectomic neuroimaging for the personalized study of longitudinal alterations in cortical shape, thickness and connectivity after traumatic brain injury. *J Neurosurg Sci*. 2014;58(3):129–44.
- Tripodis Y, Alosco ML, Ziropiannis N, Gavett BE, Chaisson C, Martin B, et al. The effect of traumatic brain injury history with loss of consciousness on rate of cognitive decline among older adults with normal cognition and Alzheimer's disease dementia. *J Alzheimers Dis*. 2017;59(1):251–63. <https://doi.org/10.3233/Jad-160585>.
- Griesbach GS, Masel BE, Helvie RE, Ashley MJ. The impact of traumatic brain injury on later life: effects on normal aging and neurodegenerative diseases. *J Neurotrauma*. 2018;35(1):17–24. <https://doi.org/10.1089/neu.2017.5103>.
- Gardner RC, Dams-O'Connor K, Morrissey MR, Manley GT. Geriatric traumatic brain injury: epidemiology, outcomes, knowledge gaps, and future directions. *J Neurotrauma*. 2018;35:889–906. <https://doi.org/10.1089/neu.2017.5371>.
- Van Horn JD, Irimia A, Torgerson CM, Bhattarai A, Jacokes Z, Vespa PM. Mild cognitive impairment and structural brain abnormalities in a sexagenarian with a history of childhood traumatic brain injury. *J Neurosci Res*. 2018;96(4):652–60. <https://doi.org/10.1002/jnr.24084>.
- Faden AI, Loane DJ. Chronic Neurodegeneration after traumatic brain injury: Alzheimer disease, chronic traumatic encephalopathy, or persistent neuroinflammation? *Neurotherapeutics*. 2015;12(1):143–50. <https://doi.org/10.1007/s13311-014-0319-5>.
- Gardner RC, Burke JF, Nettiksimmons J, Kaup A, Barnes DE, Yaffe K. Dementia risk after traumatic brain injury vs nonbrain trauma: the role of age and severity. *JAMA Neurol*. 2014;71(12):1490–7. <https://doi.org/10.1001/jamaneurol.2014.2668>.
- Gardner RC, Yaffe K. Epidemiology of mild traumatic brain injury and neurodegenerative disease. *Mol Cell Neurosci*. 2015;66:75–80. <https://doi.org/10.1016/j.mcn.2015.03.001>.
- Raichle ME. The brain's default mode network. *Annu Rev Neurosci*. 2015;38:433–47. <https://doi.org/10.1146/annurev-neuro-071013-014030>.
- Johnson B, Zhang K, Gay M, Horovitz S, Hallett M, Sebastianelli W, et al. Alteration of brain default network in subacute phase of injury in concussed individuals:

- resting-state fMRI study. *Neuroimage*. 2012;59(1):511–8. <https://doi.org/10.1016/j.neuroimage.2011.07.081>.
12. Lustig C, Snyder AZ, Bhakta M, O'Brien KC, McAvoy M, Raichle ME, et al. Functional deactivations: change with age and dementia of the Alzheimer type. *Proc Natl Acad Sci U S A*. 2003;100(24):14504–9. <https://doi.org/10.1073/pnas.2235925100>.
 13. Mayer AR, Mannell MV, Ling J, Gasparovic C, Yeo RA. Functional connectivity in mild traumatic brain injury. *Hum Brain Mapp*. 2011;32(11):1825–35. <https://doi.org/10.1002/hbm.21151>.
 14. Yeo BT, Krienen FM, Sepulcre J, Sabuncu MR, Lashkari D, Hollinshead M, et al. The organization of the human cerebral cortex estimated by intrinsic functional connectivity. *J Neurophysiol*. 2011;106(3):1125–65. <https://doi.org/10.1152/jn.00338.2011>.
 15. Zhou Y, Milham MP, Lui YW, Miles L, Reaume J, Sodickson DK, et al. Default-mode network disruption in mild traumatic brain injury. *Radiology*. 2012;265(3):882–92. <https://doi.org/10.1148/radiol.12120748>.
 16. Irimia A, Van Horn JD, Vespa PM. Cerebral microhemorrhages due to traumatic brain injury and their effects on the aging human brain. *Neurobiol Aging*. 2018;66:158–64.
 17. Petersen RC, Aisen PS, Beckett LA, Donohue MC, Gamst AC, Harvey DJ, et al. Alzheimer's Disease Neuroimaging Initiative (ADNI): clinical characterization. *Neurology*. 2010;74(3):201–9. <https://doi.org/10.1212/WNL.0b013e3181cb3e25>.
 18. Fan D, Chaudhari NN, Rostovsky KA, Calvillo M, Lee SK, Chowdhury NF, et al. Post-traumatic cerebral microhemorrhages and their effects upon white matter connectivity in the aging human brain. In: *Conference Proceedings of the IEEE Engineering in Medicine and Biology Society*. Venice: IEEE; 2019. p. 198–203.
 19. Jack CR Jr, Bernstein MA, Fox NC, Thompson P, Alexander G, Harvey D, et al. The Alzheimer's Disease Neuroimaging Initiative (ADNI): MRI methods. *J Magn Reson Imaging*. 2008;27(4):685–91. <https://doi.org/10.1002/jmri.21049>.
 20. Khazae A, Ebrahimzadeh A, Babajani-Feremi A. Identifying patients with Alzheimer's disease using resting-state fMRI and graph theory. *Clin Neurophysiol*. 2015;126(11):2132–41. <https://doi.org/10.1016/j.clinph.2015.02.060>.
 21. Destrieux C, Fischl B, Dale A, Hagren E. Automatic parcellation of human cortical gyri and sulci using standard anatomical nomenclature. *Neuroimage*. 2010;53(1):1–15. <https://doi.org/10.1016/j.neuroimage.2010.06.010>.
 22. Wellek S. A new approach to equivalence assessment in standard comparative bioavailability trials by means of the Mann-Whitney statistic. *Biometrical J*. 1996;38(6):695–710. <https://doi.org/10.1002/bimj.4710380608>.
 23. Walker E, Nowacki AS. Understanding equivalence and noninferiority testing. *J Gen Intern Med*. 2011;26(2):192–6. <https://doi.org/10.1007/s11606-010-1513-8>.
 24. Hoffelder T, Gossel R, Wellek S. Multivariate equivalence tests for use in pharmaceutical development. *J Biopharm Stat*. 2015;25(3):417–37. <https://doi.org/10.1080/10543406.2014.920344>.
 25. Blondel VD, Guillaume JL, Lambiotte R, Lefebvre E. Fast unfolding of communities in large networks. *J Stat Mech-Theory E*. 2008;2008. <https://doi.org/10.1088/1742-5468/2008/10/P10008>.
 26. Cuthill E, McKee J. Reducing the bandwidth of sparse symmetric matrices. New York: Twenty-fourth National Conference of the ACM; 1969.
 27. Gordon EM, Laumann TO, Adeyemo B, Huckins JF, Kelley WM, Petersen SE. Generation and evaluation of a cortical area parcellation from resting-state correlations. *Cereb Cortex*. 2016;26(1):288–303. <https://doi.org/10.1093/cercor/bhu239>.
 28. Irimia A, Van Horn JD. Scale-dependent variability and quantitative regimes in graph-theoretic representations of human cortical networks. *Brain Connect*. 2016;6(2):152–63. <https://doi.org/10.1089/brain.2015.0360>.
 29. Dice LR. Measures of the amount of ecologic association between species. *Ecology*. 1945;26(3):297–302. <https://doi.org/10.2307/1932409>.
 30. Rencher AC. *Methods of multivariate analysis*. New York: John Wiley & Sons, Inc.; 2002.
 31. Matthews BW. Comparison of the predicted and observed secondary structure of T4 phage lysozyme. *Biochim Biophys Acta*. 1975;405(2):442–51. [https://doi.org/10.1016/0005-2795\(75\)90109-9](https://doi.org/10.1016/0005-2795(75)90109-9).
 32. Irimia A, Van Horn JD. Functional neuroimaging of traumatic brain injury: advances and clinical utility. *Neuropsychiatr Dis Treat*. 2015;11:2355–65. <https://doi.org/10.2147/NDT.S79174>.
 33. Zverova M. Alzheimer's disease and blood-based biomarkers - potential contexts of use. *Neuropsychiatr Dis Treat*. 2018;14:1877–82. <https://doi.org/10.2147/NDT.S172285>.
 34. Irimia A, Torgerson CM, Goh SY, Van Horn JD. Statistical estimation of physiological brain age as a descriptor of senescence rate during adulthood. *Brain Imaging Behav*. 2015;9(4):678–89. <https://doi.org/10.1007/s11682-014-9321-0>.
 35. Anderson CV, Bigler ED, Blatter DD. Frontal lobe lesions, diffuse damage, and neuropsychological functioning in traumatic brain-injured patients. *J Clin Exp Neuropsychol*. 1995;17(6):900–8. <https://doi.org/10.1080/01688639508402438>.
 36. Harris TC, de Rooij R, Kuhl E. The shrinking brain: cerebral atrophy following traumatic brain injury. *Ann Biomed Eng*. 2019;47(9):1941–59. <https://doi.org/10.1007/s10439-018-02148-2>.
 37. Anderson V, Jacobs R, Anderson PJ. *Executive functions and the frontal lobes: A lifespan perspective*. New York NY and Oxford UK: Taylor and Francis. 2008;XXVII–XXXIII. https://brainmaster.com/software/pubs/books/Executive_Functions_and_the_Frontal_Lobes.pdf
 38. Venkatesan UM, Dennis NA, Hillary FG. Chronology and chronicity of altered resting-state functional connectivity after traumatic brain injury. *J Neurotrauma*. 2015;32(4):252–64. <https://doi.org/10.1089/neu.2013.3318>.
 39. Iraj A, Benson RR, Welch RD, O'Neil BJ, Woodard JL, Ayaz SI, et al. Resting state functional connectivity in mild traumatic brain injury at the acute stage: independent component and seed-based analyses. *J Neurotrauma*.

- 2015;32(14):1031–45. <https://doi.org/10.1089/neu.2014.3610>.
40. Pasquini L, Scherr M, Tahmasian M, Meng C, Myers NE, Ortner M, et al. Link between hippocampus' raised local and eased global intrinsic connectivity in AD. *Alzheimers Dement*. 2015;11(5):475–84. <https://doi.org/10.1016/j.jalz.2014.02.007>.
 41. Irimia A, Van Horn JD. Systematic network lesioning reveals the core white matter scaffold of the human brain. *Front Hum Neurosci*. 2014;8:51. <https://doi.org/10.3389/fnhum.2014.00051>.
 42. Bradshaw LA, Irimia A, Sims JA, Richards WO. Biomagnetic signatures of uncoupled gastric musculature. *Neurogastroenterol Motil*. 2009;21(7):778–e50. <https://doi.org/10.1111/j.1365-2982.2009.01265.x>.
 43. Irimia A, Bradshaw LA. Artifact reduction in magnetogastrography using fast independent component analysis. *Physiol Meas*. 2005;26(6):1059–73. <https://doi.org/10.1088/0967-3334/26/6/015>.
 44. Irimia A, Bradshaw LA. Ellipsoidal electrogastrographic forward modelling. *Phys Med Biol*. 2005;50(18):4429–44. <https://doi.org/10.1088/0031-9155/50/18/012>.
 45. Irimia A, Richards WO, Bradshaw LA. Magnetogastrographic detection of gastric electrical response activity in humans. *Phys Med Biol*. 2006;51(5):1347–60. <https://doi.org/10.1088/0031-9155/51/5/022>.
 46. Goh SYM, Irimia A, Vespa PM, Van Horn JD. Patient-tailored multimodal neuroimaging, visualization and quantification of human intra-cerebral hemorrhage. *Proceedings of the SPIE Conference on Medical Imaging – PACS and Imaging Informatics: Next Generation and Innovations 2016*:9789.
 47. Maher AS, Rostowsky KA, Chowdhury NF, Irimia A. Neuroinformatics and analysis of connectomic alterations due to cerebral microhemorrhages in geriatric mild neurotrauma. *ACM BCB*. 2018;2018:165–71. <https://doi.org/10.1145/3233547.3233598>.
 48. Rostowsky KA, Maher AS, Irimia A. Macroscale white matter alterations due to traumatic cerebral microhemorrhages are revealed by diffusion tensor imaging. *Front Neurol*. 2018;9:948. <https://doi.org/10.3389/fneur.2018.00948>.
 49. Heringa SM, Reijmer YD, Leemans A, Koek HL, Kappelle LJ, Biessels GJ, et al. Multiple microbleeds are related to cerebral network disruptions in patients with early Alzheimer's disease. *J Alzheimers Dis*. 2014;38(1):211–21. <https://doi.org/10.3233/JAD-130542>.
 50. Irimia A, Van Horn JD. The structural, connectomic and network covariance of the human brain. *Neuroimage*. 2013;66:489–99. <https://doi.org/10.1016/j.neuroimage.2012.10.066>.
 51. Greicius MD, Srivastava G, Reiss AL, Menon V. Default-mode network activity distinguishes Alzheimer's disease from healthy aging: evidence from functional MRI. *Proc Natl Acad Sci U S A*. 2004;101(13):4637–42. <https://doi.org/10.1073/pnas.0308627101>.
 52. Zhang HY, Wang SJ, Liu B, Ma ZL, Yang M, Zhang ZJ, et al. Resting brain connectivity: changes during the progress of Alzheimer disease. *Radiology*. 2010;256(2):598–606. <https://doi.org/10.1148/radiol.10091701>.
 53. Hauck WW, Anderson S. A new statistical procedure for testing equivalence in two-group comparative bioavailability trials. *J Pharmacokinet Biopharm*. 1984;12(1):83–91. <https://doi.org/10.1007/bf01063612>.
 54. Hilger K, Fukushima M, Sporns O, Fiebach CJ. Temporal stability of functional brain modules associated with human intelligence. *Hum Brain Mapp*. 2020;41(2):362–72. <https://doi.org/10.1002/hbm.24807>.
 55. Hout MC, Papesh MH, Goldinger SD. Multidimensional scaling. *Wiley Interdiscip Rev Cogn Sci*. 2013;4(1):93–103. <https://doi.org/10.1002/wcs.1203>.
 56. Irimia A, Goh SY, Torgerson CM, Stein NR, Chambers MC, Vespa PM, et al. Electroencephalographic inverse localization of brain activity in acute traumatic brain injury as a guide to surgery, monitoring and treatment. *Clin Neurol Neurosurg*. 2013;115(10):2159–65. <https://doi.org/10.1016/j.clineuro.2013.08.003>.
 57. Irimia A, Goh SY, Torgerson CM, Chambers MC, Kikinis R, Van Horn JD. Forward and inverse electroencephalographic modeling in health and in acute traumatic brain injury. *Clin Neurophysiol*. 2013;124(11):2129–45.
 58. Irimia A, Van Horn JD. Epileptogenic focus localization in treatment-resistant post-traumatic epilepsy. *J Clin Neurosci*. 2015;22(4):627–31.
 59. Bronstein AM, Bronstein MM, Kimmel R. Generalized multidimensional scaling: a framework for isometry-invariant partial surface matching. *Proc Natl Acad Sci U S A*. 2006;103(5):1168–72. <https://doi.org/10.1073/pnas.0508601103>.
 60. Gibson DB. Effect size as the essential statistic in developing methods for mTBI diagnosis. *Front Neurol*. 2015;6. <https://doi.org/10.3389/fneur.2015.00126>.
 61. de Guise E, Alturki AY, LeBlanc J, Champoux MC, Couturier C, Lamoureux J, et al. The Montreal cognitive assessment in persons with traumatic brain injury. *Appl Neuropsychol Adult*. 2014;21(2):128–35. <https://doi.org/10.1080/09084282.2013.778260>.
 62. Calvillo M, Irimia A. Neuroimaging and psychometric assessment of mild cognitive impairment after traumatic brain injury. *Front Psychol*. 2020;11:1423.
 63. Lima EA, Irimia A, Wikswo JP. The magnetic inverse problem. In: Braginski JCA, editor. *The SQUID Handbook: Applications of SQUIDS and SQUID Systems*: Wiley-VCH; 2006.
 64. Lima EA, Irimia A, Wikswo JP. The magnetic inverse problem. 2008. *The SQUID Handbook, vol 2: Applications of SQUIDS and SQUID Systems*. Clarke J., Braginski AI (Eds.). Wiley-VCH, pages 139–267.

Publisher's note Springer Nature remains neutral with regard to jurisdictional claims in published maps and institutional affiliations.



Acute cognitive impairment after traumatic brain injury predicts the occurrence of brain atrophy patterns similar to those observed in Alzheimer's disease

Kenneth A. Rostowsky · Andrei Irimia · for the Alzheimer's Disease Neuroimaging Initiative

Received: 15 October 2020 / Accepted: 10 March 2021 / Published online: 26 April 2021
© American Aging Association 2021

Abstract Traumatic brain injuries (TBIs) are often followed by persistent structural brain alterations and by cognitive sequelae, including memory deficits, reduced neural processing speed, impaired social function, and decision-making difficulties. Although mild TBI (mTBI) is a risk factor for Alzheimer's disease (AD), the extent to which these conditions share patterns of macroscale neurodegeneration has not been quantified. Comparing such patterns can not only reveal how the neurodegenerative trajectories of TBI and AD are similar, but may also identify brain atrophy features which can be leveraged to prognosticate AD risk after TBI. The primary aim of this study is to systematically map how TBI affects white matter (WM) and gray matter (GM) properties in AD-analogous patterns. Our findings identify substantial similarities in the regional macroscale neurodegeneration patterns associated with mTBI and AD. In cerebral GM, such similarities are most extensive in brain areas involved in memory and executive function, such as the temporal poles and orbitofrontal cortices, respectively. Our results indicate that the spatial pattern of cerebral WM degradation

observed in AD is broadly similar to the pattern of diffuse axonal injury observed in TBI, which frequently affects WM structures like the fornix, corpus callosum, and corona radiata. Using machine learning, we find that the severity of AD-like brain changes observed during the chronic stage of mTBI can be accurately prognosticated based on acute assessments of post-traumatic mild cognitive impairment. These findings suggest that acute post-traumatic cognitive impairment predicts the magnitude of AD-like brain atrophy, which is itself associated with AD risk.

Keywords Traumatic brain injury · Alzheimer's disease · Mild cognitive impairment · Neuroimaging

Abbreviations

ACR	Anterior corona radiata
AD	Alzheimer's disease
ADNI	Alzheimer's Disease Neuroimaging Initiative
AIC	Anterior internal capsule
ApoE	Apolipoprotein E
A β	Amyloid beta
BCC	Body of the corpus callosum
BCF	Body and column of the fornix
CAA	Cerebral amyloid angiopathy
CB	Cingulum bundle
CC	Corpus callosum
CDR	Clinical dementia rating
CDR-SB	Clinical dementia rating sum of boxes
CF	Crus of the fornix

K. A. Rostowsky · A. Irimia
Ethel Percy Andrus Gerontology Center, Leonard Davis School of Gerontology, University of Southern California, Los Angeles, CA, USA

A. Irimia (✉)
Corwin D. Denney Research Center, Department of Biomedical Engineering, Viterbi School of Engineering, University of Southern California, Los Angeles, CA, USA
e-mail: irimia@usc.edu

CI	Confidence interval	PIC	Posterior internal capsule
CMB	Cerebral microbleed	PPV	Positive prediction value
CP	Cerebral peduncle	PS	Processing speed
CST	Corticospinal tract	PTR	Posterior thalamic radiation
CT	Computed tomography	RIC	Retrothalamic internal capsule
DAI	Diffuse axonal injury	ROI	Region of interest
DL	Deep learning	SCC	Splenium of the corpus callosum
DMN	Default mode network	SCbP	Superior cerebellar peduncle
dMRI	Diffusion magnetic resonance imaging	SCR	Superior corona radiata
DTI	Diffusion tensor imaging	SFOF	Superior fronto-occipital fasciculus
DWI	Diffusion weighted imaging	SLR	Superior longitudinal fasciculus
EC	External capsule	SS	Sagittal stratum
FA	Fractional anisotropy	STG	Superior temporal gyrus
FLAIR	Fluid-attenuated inversion recovery	SVM	Support vector machine
FN	False negative	SWI	Susceptibility weighted imaging
FP	False positive	TBI	Traumatic brain injury
FSL	FMRIB software library	TBSS	Tract-based spatial statistics
FWER	Family-wise error rate	TCC	Tapetum of the corpus callosum
GCC	Genu of the corpus callosum	TFCE	Threshold-free cluster enhancement
GCS	Glasgow Coma Scale	TN	True negative
GLM	General linear model	TNR	True negative rate
GM	Gray matter	TOST	Two one-sided <i>t</i> test
GRE	Gradient-recalled echo	TP	True positive
HC	Healthy control	TPR	True positive rate
ICbP	Inferior cerebellar peduncle	UF	Uncinate fasciculus
ICBM	International Consortium of Brain Mapping	VBM	Voxel-based morphometry
IFG	Inferior frontal gyrus	vmPFC	Ventromedial prefrontal cortex
IFOF	Inferior fronto-occipital fasciculus	WM	White matter
ISDA	Iterative single data algorithm	3D	Three-dimensional
JHU	Johns Hopkins University		
LOC	Loss of consciousness		
MCC	Matthews' correlation coefficient		
MCI	Mild cognitive impairment		
ML	Medial lemniscus		
MMSE	Mini mental state examination		
MNI	Montreal Neurological Institute		
MoCA	Montreal cognitive assessment		
MP-RAGE	Magnetization-prepared rapid acquisition gradient echo		
MRI	Magnetic resonance imaging		
MRS	Magnetic resonance spectroscopy		
mTBI	Mild traumatic brain injury		
MTG	Medial temporal gyrus		
NFT	Neurofibrillary tangle		
OFC	Orbitofrontal cortex		
PCR	Posterior corona radiata		
PCT	Pontine crossing tract		
PET	Positron emission tomography		
PFC	Prefrontal cortex		

Introduction

In the United States, around 1.7 million individuals incur traumatic brain injuries (TBIs) annually, with an incidence rate of around 500 TBIs per 100,000 people [1]. The Glasgow Coma Scale (GCS) is an assessment tool often used to rate TBI severity using measures of responsiveness like eye-opening and verbal responses [2]. Within the GCS, TBIs can be classified as mild, moderate, or severe based on neurological measures which include loss of consciousness (LOC) duration. In the United States, mild TBI (mTBI) is the most common classification and accounts for ~80% of all TBI cases [1]. Brain morphometry studies of TBI often utilize magnetic resonance imaging (MRI) and computed tomography (CT) [3] to provide noninvasive in vivo mapping, visualization, and quantification of TBI

sequelae. Furthermore, diffusion MRI (dMRI) can be used to quantify the fractional anisotropy (FA) and other properties of water diffusion along white matter (WM) fibers in the TBI-affected brain to identify abnormalities [4].

Chronic TBI effects on cognitive function can share similarities with those of Alzheimer's disease (AD) [5, 6]. Such effects may be particularly severe in older individuals, who are ~3 times more likely to sustain a TBI than those in any other age group [7, 8]. Such greater vulnerability is partly due to a higher risk for physical injuries (like falls) and to a higher likelihood of pre-existing conditions at the time of injury, resulting in poorer clinical outcomes [7]. Repeated mTBIs are particularly associated with AD risk [9–11], and post mortem studies of mTBI effects on brain microstructure have identified both Amyloid β ($A\beta$) plaques and neurofibrillary tangles (NFTs) of τ protein which resemble those observed in AD [10]. At the macroscale, however, few studies have investigated whether TBI-affected brain structure can change along AD-analogous trajectories, particularly at older ages. Furthermore, the potential relationship between TBI and AD remains underexplored despite the epidemiological significance of both conditions. Independent investigations that used dMRI to compare the FAs of healthy controls (HCs) to those of AD patients and acute mTBI victims found significantly lower FA [4, 12], which is indicative of damage, along WM tracts projecting to the hippocampi and to temporal regions in the brains of AD and mTBI patients [13, 14]. Researchers have also utilized cortical thickness as a measure of gray matter (GM) atrophy and have independently observed similar spatial patterns of cortical thinning in AD and mTBI patients compared to HCs [15–17]. Despite such similarities of findings comparing mTBI and AD to HCs, hardly any studies have combined GM and WM measurements in a longitudinal design to examine whether subacute neurodegeneration after mTBI can occur along AD-analogous trajectories.

Previously, our laboratory showed that the acute cognitive deficits of mTBI patients can predict AD-like chronic alterations in brain *function* with high sensitivity and specificity [18]. To complement these previous findings, the present study leverages MRI-based WM analysis and GM morphometry to compare AD and geriatric mTBI from the standpoint of their observed differences in GM and WM *structure*. The hypothesis of the study is that geriatric mTBI patients are significantly more likely than typically aging adults to exhibit AD-

like trajectories of neurodegeneration, even as early as 6 months post injury. This study aims to illustrate our ability to early identify mTBI patients at high risk for AD-analogous neurodegeneration, and to suggest avenues for the early estimation of AD risk after mTBI that may carry substantial potential benefits to medical science.

Methods

This study was conducted with the approval of the Institutional Review Board at the University of Southern California and was carried out in accordance with the Declaration of Helsinki and with the U.S. Code of Federal Regulations (45 C.F.R. 46).

mTBI participants

mTBI participants ($N = 33$; 15 females; age $\mu = 62.7$ years, $\sigma = 10.6$ years, range = 47–83 years) were recruited with the assistance of board-certified clinicians and/or other health professionals who had treated them as outpatients and who had referred them for further neurocognitive assessment, neurological treatment, and/or neuroimaging. The team strove to minimize recruitment bias by inviting all potential participants who satisfied the study's inclusion criteria and who could provide written informed consent. To be included, mTBI volunteers had to have (a) MRI recordings acquired ~6 months post-injury at 3 T, (b) a TBI due to a fall, (c) no clinical findings on acute T_1/T_2 -weighted MRI, (d) no clinical findings other than cerebral microbleeds (CMBs) on susceptibility weighted imaging (SWI, an MRI sequence type yielding images on which hemorrhages and other iron-rich brain deposits are hypointense), (e) an acute GCS score greater than 12 ($\mu = 14.1$, $\sigma = 0.7$) upon initial medical evaluation, (f) LOC of fewer than 30 min ($\mu \approx 14$ min, $\sigma \approx 3$ min), (g) post-traumatic amnesia of fewer than 24 h ($\mu \approx 5.5$ h, $\sigma \approx 3.2$ h), and (h) a lack of clinical history involving pre-traumatic neurological disease or disorders like dementia and mild cognitive impairment (MCI), psychiatric disorder or drug/alcohol abuse. CMBs were identified from SWI, a gradient-echo MRI sequence that is sensitive to the magnetic properties of tissues and fluids such as blood [19]. Specifically, for mTBI subjects, CMBs were first identified manually in each subject by eight human experts with training in neuroimaging and in

CMB identification from SWIs. Consensus meetings to review CMB ratings were then held by a committee including three of the eight experts; each CMB finding was reviewed and discussed thoroughly during these meetings until consensus was reached on the accuracy of each CMB finding. TBI participants' Montréal Cognitive Assessment (MoCA) scores were acquired within 48 h post-injury and ranged between 23 and 30 ($N = 33$, $\mu = 26$, $\sigma = 5$). Mini Mental State Examination (MMSE) scores were also acquired within 48 h post-injury and ranged between 23 and 30 ($N = 33$, $\mu = 25$, $\sigma = 3$). Global Clinical Dementia Rating (CDR) sum of boxes (CDR-SB) scores were not available for TBI participants. No Apolipoprotein E (ApoE) allele information was available for TBI participants.

AD participants

AD patients ($N = 66$; 26 females; age $\mu = 75.6$ y, $\sigma = 8.9$ y, range = 55–92 y) were selected from the AD Neuroimaging Initiative (ADNI) cohort, whose eligibility criteria are described elsewhere [20]. For AD participants, CMBs were identified by a board-certified neurologist. Where available, AD patients' cognitive assessments were made within 0 to 394 days after imaging ($N = 61$, $\mu = 32$ days, $\sigma = 62$ days). AD patients' MoCA scores ranged from 2 to 28 ($N = 61$, $\mu = 15$, $\sigma = 5$), and all had a clinical AD diagnosis. MMSE scores were available for most AD participants ($N = 61$, $\mu = 22$, $\sigma = 3$; range: 11–29). AD patients had global CDR-SB scores between 1 and 14 ($N = 61$, $\mu = 5.35$, $\sigma = 2.34$). For AD patients with ApoE genotyping ($N = 60$), 30% had no $\epsilon 4$ alleles, 50% had one, and 20% had two.

HC participants

HCs ($N = 81$; 59 females; age $\mu = 68.7$, $\sigma = 7.0$ years, range = 55–87 years) were selected from the ADNI cohort, whose eligibility criteria are described elsewhere [20]. For HC participants, CMBs were identified by a board-certified neurologist. Most HC volunteers' cognitive scores were acquired within 0 to 302 days after imaging ($N = 72$, $\mu = 29$ days, $\sigma = 42$ days). HC participants had been clinically evaluated as having normal cognition; their MoCA scores ranged from 20 to 30 ($N = 72$, $\mu = 26$, $\sigma = 3$). MMSE scores were available for HCs and ranged between 22 and 30 ($N = 72$, $\mu = 29$, $\sigma = 1$). HCs had global CDR-SB scores between 0 and 2 ($N = 72$, $\mu = 0.05$, $\sigma = 0.25$). For HCs

whose ApoE genotype had been determined ($N = 68$), the number of ApoE $\epsilon 4$ alleles was zero for 63% of the sample, one for 34%, and two for 3%.

Data acquisition

HC and AD participant data used for the preparation of this article were obtained from the ADNI database (<http://adni.loni.usc.edu>). ADNI was launched in 2003 as a public–private partnership, led by Principal Investigator Michael W. Weiner, MD. The primary goal of ADNI has been to test whether serial MRI, positron emission tomography (PET), other biological markers, and clinical and neuropsychological assessment can be combined to measure the progression of MCI and early AD. For up-to-date information, see www.adni-info.org. TBI imaging data were acquired at 3 T using the Prisma MAGNETOM Trio TIM MRI scanner model (20-channel head coil, Siemens Corporation, Erlangen, Germany). Data included T_1 - and T_2 -weighted, fluid-attenuated inversion recovery (FLAIR), gradient recalled echo (GRE)/SWI, and dMRI volumes. T_1 -weighted images were acquired using a three-dimensional (3D), magnetization-prepared rapid acquisition gradient echo (MP-RAGE) sequence [repetition time (T_R) = 1,950 ms; echo time (T_E) = 2.98 ms; inversion time (T_I) = 900 ms; voxel size = 1.0 mm \times 1.0 mm \times 1.0 mm]. T_2 -weighted images were acquired using a 3D sequence (T_R = 2,500 ms; T_E = 360 ms; voxel size = 1.0 mm \times 1.0 mm \times 1.0 mm) [4]. Flow-compensated GRE/SWI volumes were acquired axially (T_R = 30 ms; T_E = 20 ms; voxel size = 1.33 mm \times 1.33 mm \times 1.6 mm). dMRI volumes were acquired axially in 64 gradient directions (T_R = 8,300 ms; T_E = 72 ms; voxel size = 2.7 mm \times 2.7 mm \times 2 mm). One volume with $b = 0$ s/mm² and another with $b = 1,000$ s/mm² were also acquired, where b is the diffusion-weighting constant of diffusion-weighted imaging (DWI). All acquired data were anonymized and de-linked prior to archiving and analysis.

Preprocessing

DWI volumes were corrected for susceptibility-induced artifacts, subject motion, and eddy currents using software in the FMRIB Software Library (FSL). Based on a pair of images with opposite phase encoding directions, susceptibility-induced artifacts were estimated [21]. Subsequently, a brain mask was created, and

susceptibility corrections were implemented, followed by eddy current and patient motion corrections, resulting in output containing the artifact-corrected, skull-stripped brain volume. Then, the B vectors of each volume were rotated such that any inadequate rotations caused by patient motion were accounted for. DWI volumes were further processed in FSL by fitting tensors to corrected DWI volumes to perform diffusion tensor imaging (DTI). These latter volumes were then used for voxel-wise FA calculation such that FA maps could be generated for each volume. T_1 -weighted volumes underwent intensity normalization, bias field correction, and motion correction as part of the FreeSurfer 6.0 processing workflow (<http://surfer.nmr.mgh.harvard.edu>).

Cortical reconstruction

The segmentation of subcortical structures, cerebral WM, and cortical GM was based on T_1 -weighted volumes and was implemented in FreeSurfer 6.0 with default execution parameters, as described elsewhere [22, 23]. Briefly, this process includes (1) the removal of non-cerebral voxels using a hybrid watershed/surface deformation procedure, (2) an automated transformation to Talairach space, (3) voxel intensity normalization, (4) segmentation of cortical and subcortical GM, (5) tessellation of the GM/WM boundary, and (6) automated surface topology correction. The reader is referred elsewhere [22, 23] for comprehensive details on each of these steps. Each hemisphere was divided into 74 regions by segmenting subcortical structures and by parceling the cortex into gyri and sulci using the Desikan–Killiany atlas nomenclature [24]. For each subject, cortical thickness was estimated at each cortical location and then resampled onto a seventh-order icosahedral mesh for inter-subject comparison.

Regional labeling and atlasing

WM voxels were mapped onto WM structures in Montreal Neurological Institute (MNI) MNI₁₅₂ space using FSL version 6.0.1 and the Johns Hopkins University (JHU) International Consortium of Brain Mapping (ICBM) DTI₈₁ WM labeling scheme. First, the mean FA skeleton mask was co-registered onto the JHU label map, thereby creating a skeletonized version of the latter. Images were then binarized such that voxels corresponding to statistical significance ($p < 0.05$) were

set to 1, whereas remaining voxels were set to 0; these binarized images were then projected onto the skeletonized label map. The total number of significant voxels in the volume associated with each label was divided by the total number of voxels pertaining to that label so as to calculate the percentage volume of voxels associated with statistical significance and located in each structure. Results were represented graphically for visual interpretation. For cortical thickness calculations, after binarizing each subject's cortical surface overlay based on statistical significance (1 = significant; 0 = not significant), the resulting binary map was registered onto the average cortical surface in the Desikan–Killiany atlas. Then, a similar procedure was used to calculate the percentage of cortical surface area within each cortical region which contained vertices associated with statistical significance. Figure 1 illustrates a conceptual representation of this process.

Tract-based spatial statistics (TBSS)

A TBSS approach was used for the voxel-wise statistical analysis of mean WM FA differences between groups. In contrast to algorithms involving regions of interest (ROIs) or voxel-based morphometry (VBM) approaches, TBSS utilizes a nonlinear registration algorithm to co-register FA maps, resulting in alignment errors which are substantially smaller than those produced by traditional linear registration algorithms [25]. Moreover, TBSS facilitates the calculation of brain-wide statistics such that both global and local differences in FA can be quantified. First, FA volumes had their end slices set to zero to remove outliers which may have been introduced by fitting diffusion tensors to DWI volume data. After this step, nonlinear transforms to FMRIB₅₈ FA standard space were calculated and applied. The FMRIB₅₈ FA space was then affinely aligned to the MNI₁₅₂ space and the resulting transform was applied to each subject's FA volume such that all volumes could be aligned to the 1 mm × 1 mm × 1 mm MNI₁₅₂ space. FA maps were then averaged across subjects to generate a mean FA volume which was skeletonized to reveal FA values along the trajectories of major WM structures. The mean FA skeleton was thresholded to remove values below a default threshold of 0.2, below which the low signal-to-noise ratio results in relatively inaccurate FA measurements.

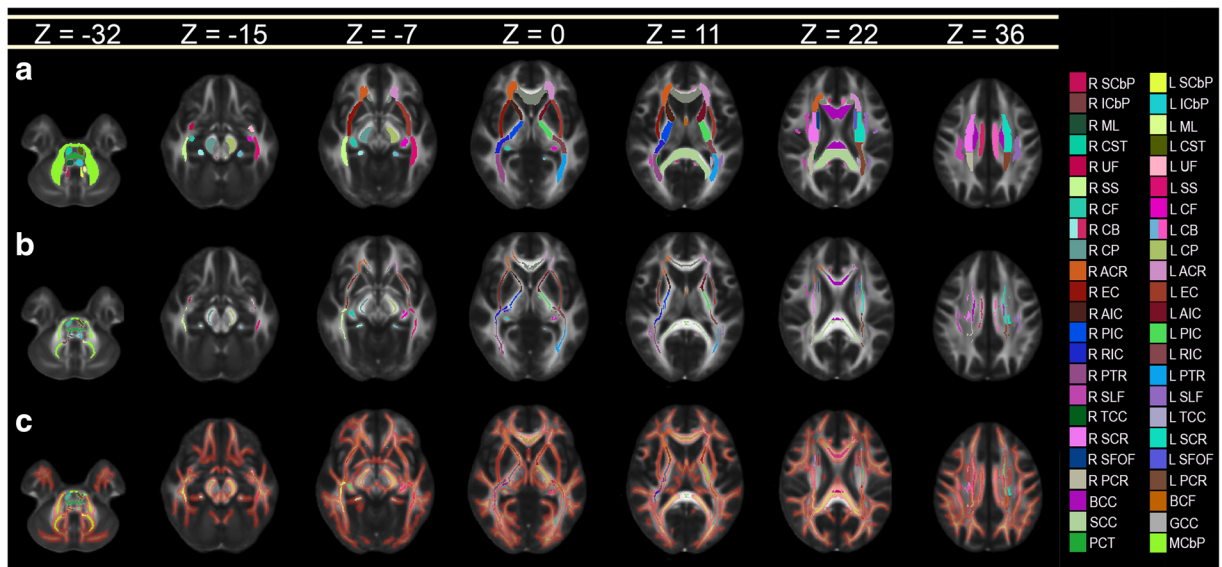


Fig. 1 Conceptual representation of the process for calculating the percentage of voxels associated with statistically significant findings within each neuroanatomic structure. **(a)** WM label map of the JHU atlas. **(b)** Mean WM skeleton mask of all subjects in the study. **(c)** Voxels where mTBI subjects exhibit mean FA values which are significantly lower ($p < 0.05$) than in HCs. The voxel

map is overlaid on the skeletonized label map of the atlas, which is thickened for easier visualization. All images are overlaid on the $1 \text{ mm} \times 1 \text{ mm} \times 1 \text{ mm}$ FMRIB₅₈ FA template, which is an average of FA maps across 58 healthy subjects. Colors encode various WM structures (see Tables 2, 3, and 4 for abbreviations)

Statistical testing of group differences

The statistical significance of differences in age means between the three groups was evaluated using two-tailed Welch's t tests. The significance of group differences in sex composition was tested using a χ^2 test. Group differences in mean FA were calculated between (A) AD and mTBI, (B) AD and HCs, and (C) mTBI and HCs. The null hypothesis H_0 , according to which each pair of groups' mean FA values are equal, was tested using Welch's t test. Using a general linear model (GLM), the confounding effects of sex and age on FA values [26, 27] were regressed out and a nonparametric two-sided t test with 500 permutations and with threshold-based free-cluster enhancement (TFCE) was implemented. This revealed clusters of WM voxels whose mean FA differed significantly between groups. All p values were corrected for multiple comparisons using 500 nonparametric permutations with TFCE, while controlling for the family-wise error rate (FWER) [28, 29].

Statistical testing of group similarities

A premise of this study is that a brain feature f which is both (a) significantly different from HCs in both TBI

and AD, and (b) significantly similar across TBI and AD, can be said to be *AD-analogous*. Thus, a brain feature f observed in TBI patients can be said to be AD-analogous if f differs from HCs in both TBI and AD, and is also significantly similar across both TBI and AD. If f differs significantly from HCs in both TBI and AD, a null hypothesis of *statistical equivalence* can be tested to determine whether f is AD-analogous. Thus, for samples A and B , a null hypothesis of equivalence is stated as $\mu_A(f) \neq \mu_B(f)$, i.e., as the complement of the typical null hypothesis $\mu_A(f) = \mu_B(f)$. A null hypothesis of equivalence fails to be accepted if the two means fall within an interval $(-\delta, +\delta)$, where δ is known as the *equivalence margin* of the test [30]. In a statistical sense, equivalence implies that the values of the empirical estimates of the features $f(A)$ and $f(B)$ are so close that neither estimate can safely be considered to be greater or smaller than the other [31]. In this study, δ is assigned a conservative value equal to 0.2 multiplied by the width of the 95% confidence interval (CI) for the difference $\mu_A(f) - \mu_B(f)$. Equivalence hypotheses were tested using two one-sided t tests (TOSTs) [32]. Specifically, the TOSTs were used to quantify the statistical equivalence of FA means between AD and mTBI cohorts. TOSTs are commonly used to test hypotheses of statistical

equivalence [18], which can be interpreted as a measure of statistical similarity between groups.

To identify WM tracts whose FA means were statistically undistinguishable (i.e., statistically equivalent) across mTBI and AD, the null hypothesis H_0 of equivalence was only tested at locations where the mean FA differed significantly from the mean FA for HCs in both the AD and the TBI groups. This restriction was necessary to ensure that any identified statistical equivalences between AD and TBI were associated with deviations from normality (i.e., from HCs). For GM, like for WM, TOSTs were implemented vertex-wise to determine whether the cortical thickness means of the AD and mTBI groups were statistically similar. As in the case of the WM analysis, testing for the statistical equivalence of mean cortical thickness in the AD and mTBI groups was only implemented at locations where each of these groups had been found to differ significantly from HCs. Cortical maps of statistical equivalence between AD and mTBI were generated for display and smoothed across using five iterations of nearest-neighbor interpolation. Equivalence testing was implemented using freely available MATLAB software (<https://www.mathworks.com/matlabcentral/fileexchange/63204>).

Cognitive impairment vs. brain connectivity alterations

Two support vector machines (SVMs) were designed in MATLAB using the `glmfit`, `fitcsvm`, and `predict` functions with default parameters, the iterative single data algorithm (ISDA), a linear kernel function, and heuristic kernel scale parameters. The SVMs were trained and cross-validated 10-fold to distinguish TBI participants whose AD-like mean FA deviations from normality (i.e., equivalences across TBI and AD) were either relatively *moderate* or relatively *extensive*, respectively. Such deviations were defined as *moderate* or *extensive* depending on whether they belonged to the lowest or highest terciles, respectively, of the TOST statistics' empirical distribution. The number of true negatives (TNs), true positives (TPs), false negatives (FNs), and false positives (FPs) were computed, as were the true positive rate (TPR, or sensitivity), true negative rate (TNR, or specificity), positive prediction value (PPV, or precision), and Matthews' correlation coefficient (MCC) [33].

Results

Participants

Demographics are summarized in Table 1. No significant group differences of sex composition were identified [$\chi^2 = 2.22$, degrees of freedom (df) = 1, $p = 0.136$]. Welch's t test found significant differences in mean age between AD and mTBI (Welch's $t = 6.38$, $df = 97$, $p = 6.31 \times 10^{-4}$), AD and HCs (Welch's $t = 5.28$, $df = 145$, $p = 4.57 \times 10^{-7}$), and mTBI and HCs (Welch's $t = -3.52$, $df = 112$, $p = 6.03 \times 10^{-9}$). CMB counts were found to range from 0 to 2 ($\mu \pm \sigma = 0.27 \pm 0.65$) in HCs, from 0 to 7 ($\mu \pm \sigma = 2.52 \pm 1.91$) in mTBI volunteers, and from 0 to 25 ($\mu \pm \sigma = 1.66 \pm 4.49$) in AD patients. Significant differences in MMSE scores were found between HC and mTBI participants (Welch's $t = -7.49$, $df \approx 35$, $p = 4.53 \times 10^{-9}$), between HC and AD participants (Welch's $t = 17.01$, $df \approx 131$, $p < 0.001$) but not between mTBI participants and AD patients (Welch's $t = 4.69$, $df = 64$, $p = 0.99$). Significant differences in MoCA scores were found between HC and AD participants (Welch's $t = 17.26$, $df \approx 131$, $p = 9.33 \times 10^{-39}$), between acute mTBI participants and AD patients (Welch's $t = 10.65$, $df \approx 59$, $p = 1.04 \times 10^{-15}$), but not between HC and acute TBI participants (Welch's $t = -0.29$, $df \approx 42$, $p = 0.39$).

WM comparison between HC and mTBI

Figure 2(a) depicts regions where mTBI subjects had significantly lower mean FA than HCs ($p < 0.05$). In the mTBI group, these regions include the genu and body of the corpus callosum (GCC and BCC, respectively), body and column of the fornix (BCF), as well as crura of the fornix (CF). Table 2 lists WM structures in the descending order of the percentage of voxels within each structure where mean FA is significantly lower in mTBI participants than in HCs. In other words, the percentage of voxels quantifies the proportion of each structure's volume which exhibits significant mean FA differences between the two groups. For example, the first row of Table 2 lists the tapeta of the CC (TCC) and the number 100 in the middle, halfway below the headings labeled "left" and "right." This should be interpreted as indicating that 100% of the TCC spans voxels with statistically significant findings (i.e., the mTBI cohort has significantly lower mean FA values than the HC group across 100% of the TCC). In the

Table 1 Summary of cohort demographics and cognitive assessment data. Dashes indicate data unavailability. Stated are sample sizes (N), mean (μ), standard deviation (σ), minimum value (min), and maximum value (max). Abbreviations: Alzheimer’s disease

(AD), Clinical Dementia Rating Sum-of-Boxes (CDR-SB), cerebral microbleed (CMB), healthy control (HC), Montreal Cognitive Assessment (MoCA), Mini Mental State Examination (MMSE), traumatic brain injury (TBI), years (yr)

	Age (yr)			MoCA			MMSE			CDR-SB			CMBs		
	HC	TBI	AD	HC	TBI	AD	HC	TBI	AD	HC	TBI	AD	HC	TBI	AD
N	81	33	66	72	33	61	72	33	61	72	—	61	81	32	66
μ	69	63	76	26	26	22	29	25	22	0.05	—	5.35	0.27	1.72	1.66
σ	7	11	9	3	5	3	1	3	3	0.25	—	2.34	0.65	1.67	4.49
min	55	47	55	20	23	2	22	23	11	0	—	1	0	0	0
max	87	83	92	30	30	28	30	30	29	2	—	14	2	7	25

mTBI cohort, the structures whose volumes’ mean FAs differ most between groups are the TCC, the uncinate fasciculi (UF), the anterior and posterior internal capsules (AICs and PICs, respectively), the external capsules (ECs), cingulum bundle (CB), superior cerebellar peduncles (SCbPs), BCF, GCC, and BCC. WM structures which (A) are more affected by mTBI in the right hemisphere and which (B) differ to the greatest extent in mTBI compared to HCs include, in descending order, the AIC, SCbP, sagittal stratum (SS), cerebral peduncle (CP), posterior corona radiata (PCR), medial lemniscus (ML), and corticospinal tract (CST). Structures which are more affected in the left hemisphere are the EC, UF, CB, PIC, CF, inferior cerebellar peduncle (ICbP), superior longitudinal fasciculus (SLF), retrolenticular internal capsule (RIC), posterior thalamic radiation (PTR), anterior corona radiata (ACR), superior fronto-occipital fasciculus (SFOF), and superior corona radiata (SCR). No WM fascicles in the mTBI cohort were found to have significantly higher mean FA than in HCs.

WM comparison between HC and AD

Figure 2(b) depicts significant differences in mean FA between the HC and AD cohorts. In AD, mean FA values were significantly lower along commissural fibers like the (A) splenium of the corpus callosum (SCC), the BCC, GCC, BCF, and CF. Table 3 lists WM structures in the descending order of the percentage of each structure’s voxels where mean FA is significantly lower in AD participants than in HCs. For example, row 8 of Table 3 lists the SS as well as the numbers 94 and 100 under the “Left” and “Right” headings, respectively. This should be interpreted as indicating that 94% of the left SS and 100% of the right SS span voxels with

statistically significant findings (i.e., compared to HCs, the AD cohort has a significantly lower mean FA value in 94% of the left SS and in 100% of the right SS). Thus, compared to HCs, AD patients’ mean FAs differ from those of HCs most extensively in the BCC, BCF, CF, UF, CB, GCC, TCC, EC, SS, and SFOF. In descending order according to the same criterion, fasciculi which are more affected in the right hemisphere and which differ most in AD compared to HCs are the CB, TCC, EC, SS, ACR, CP, ML, and PCR. For the left hemisphere, these are the SFOF, PTR, SCbP, AIC, SLF, ICbP, RIC, PIC, SCR, and CST. No WM structures in the AD cohort were found to have significantly greater mean FA than the HC group.

WM comparison between AD and mTBI

No significant differences in mean FA were revealed between the mTBI and AD groups. Equivalence testing comparing mTBI to AD revealed significant statistical similarities of mean FA throughout the brain. Table 4 lists the WM structures in the descending order of the percentage of each structure’s voxels for which mean FAs are statistically similar in AD and mTBI participants. For example, the third row in Table 4 lists the pontine crossing tract (PCT) and, halfway between the columns labeled “Left” and “Right,” the number 69 is listed. The fact that only one number is listed is due to the fact that there is only one PCT, rather than a “left PCT” or a “right PCT.” The numerical entry “69” indicates that 69% of the voxels spanned by the PCT are associated with statistically significant findings (i.e., the AD and mTBI cohorts have significantly similar mean FA values throughout 69% of the PCT). In descending

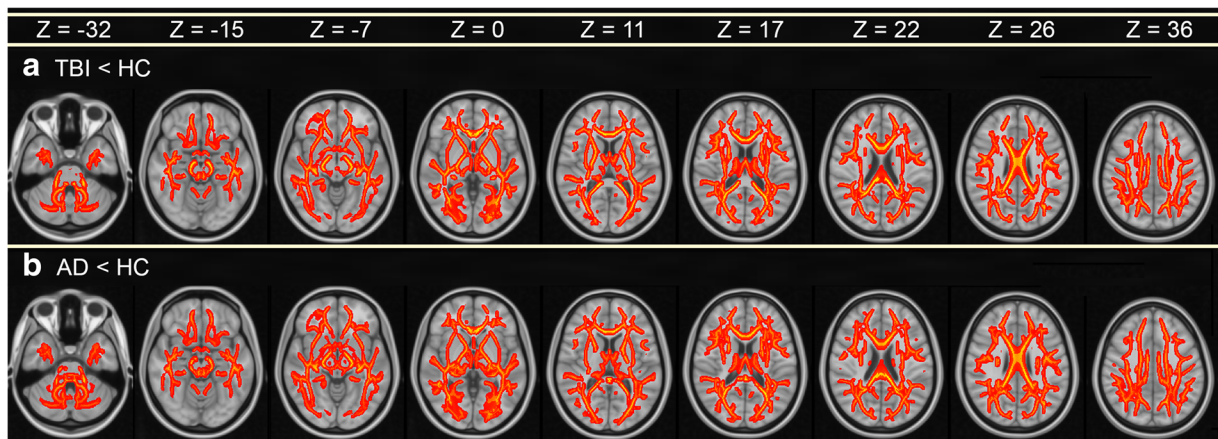


Fig. 2 Statistically significant differences in mean FA between (a) HCs and mTBI patients, and between (b) HCs and AD patients. Color encodes $-\log_{10} p$, ranging from 2 (red) to 5 (yellow), corresponding to p -values between 0.05 (red) and ~ 0.0005 (yellow). p values are for t tests using a significance threshold $\alpha =$

0.05, subject to multiple comparison correction. Smaller p values are associated with higher values of $-\log_{10} p$ and with greater differences in mean FA between the groups compared. Images are displayed in radiologic convention. The z coordinate of each slice in MNI₁₅₂ atlas space is provided

order according to the same criterion, these structures included the SFOF, CF, PCT, ACR, BCF, and SCR.

GM comparison between HC and mTBI

Figure 3(a) displays significant differences in cortical thickness between the HC and mTBI cohorts. In the latter, significantly thinner cortex (blue) is observed in the lateral superior portion of the left temporal lobe, in parietal and in frontal regions. Significantly lower cortical thickness in the HC group (red) is observed diffusely across the cortex. Such cortical thickening after TBI is relatively ubiquitous and has been hypothesized to be associated with chronic inflammation of the GM [17, 34–36].

GM comparison between HC and AD

Figure 3(b) displays significant differences in cortical thickness between the HC and AD cohorts. In the latter, significantly thinner cortex (blue) is found in the lateral and medial parts of the temporal and frontal lobes. In the HC group, significantly thinner cortex (red) is observed at very few locations on the medial surface of the brain, particularly in the cingulate gyri.

GM comparison between mTBI and AD

Figure 3(c) displays regions where cortical thinning was statistically indistinguishable between (i.e., significantly

similar across) mTBI and AD cohorts. Extensive areas of statistical similarity are observed in frontotemporal and frontoparietal regions and, more sparsely, in occipital areas. Table 5 lists gyri and sulci in descending order of each structure's percentage (i.e., proportion) of cortical area exhibiting an amount of cortical thinning which was statistically indistinguishable between mTBI and AD. The parcels whose cortical thinning was most statistically similar across mTBI and AD include the superior part of the precentral sulcus, the short insular gyri, the horizontal ramus of the anterior lateral sulcus, the marginal cingulate sulcus, and the orbital gyri. There are few regions whose statistical similarities were largely restricted to a single hemisphere across the AD and mTBI cohorts, including lateral occipital regions, the supramarginal gyri, anterior transverse marginal gyri, inferior parietal lobules, and superior temporal gyri (STG).

Cognitive impairment vs. brain connectivity alterations

Across 100 scenarios, the SVM trained to identify TBI patients whose WM similarities to AD were relatively modest (bottom tercile of equivalence statistic distribution) achieved the following means and standard deviations: TN = 20.0 ± 1.1 ; TP = 10.0 ± 0.8 ; FN = 1.6 ± 0.3 ; FP = 1.4 ± 0.2 ; TPR = 0.87 ± 0.09 ; TNR = 0.93 ± 0.09 ; PPV = 0.88 ± 0.2 ; MCC = 0.80 ± 0.2 . The SVM trained to predict which TBI patients' similarities to AD were relatively extensive (top tercile of equivalence statistic

Table 2 WM structures listed, in descending numerical order, according to the percentage of voxels associated with FA averages which are significantly lower ($p < 0.05$), for each structure, in the mTBI cohort compared to HCs. Values are reported for the left and

right hemispheres, except for structures which straddle both; in this latter case, only one value is reported between the left and right hemisphere columns

Abbreviation	Structure	Part	%	
			Left	Right
TCC	Corpus callosum	Tapetum	100	100
EC	External capsule	—	100	99
UF	Uncinate fasciculus	—	100	99
BCC	Corpus callosum	Body		98
GCC	Corpus callosum	Genu		97
CB	Cingulum bundle	—	97	96
AIC	Internal capsule	Anterior	94	97
BCF	Fornix	Body		95
SCbP	Cerebellar peduncle	Superior	91	95
PIC	Internal capsule	Posterior	91	90
SS	Sagittal stratum	—	85	94
CP	Cerebral peduncle	—	87	90
CF	Fornix	Cres	90	87
ICbP	Cerebellar peduncle	Inferior	87	86
SCC	Corpus callosum	Splenium		84
SLF	Longitudinal fasciculus	Superior	83	82
RIC	Internal capsule	Retrolenticular	92	72
PTR	Thalamic radiation	Posterior	90	74
ACR	Corona radiata	Anterior	83	73
MCbP	Cerebellar peduncle	Middle		78
SFOF	Fronto-occipital fasciculus	Superior	85	64
PCR	Corona radiata	Posterior	68	79
ML	Medial lemniscus	—	56	68
SCR	Corona radiata	Superior	60	48
CST	Corticospinal tract	—	18	23
PCT	Pontine crossing tract	—		9

distribution) yielded the following results: $TN = 19.2 \pm 0.5$; $TP = 9.1 \pm 0.9$; $FN = 1.1 \pm 0.3$; $FP = 1.9 \pm 0.9$; $TPR = 0.83 \pm 0.6$; $TNR = 0.95 \pm 0.5$; $PPV = 0.83 \pm 0.3$; $MCC = 0.79 \pm 0.4$.

Discussion

This study investigated cortical thickness and FA changes associated with geriatric mTBI and compared these changes to those observed in AD. The analysis demonstrated (i) broad, significant similarities in cortical thinning between mTBI and AD, primarily in the frontal and

temporal regions but also in the occipital lobe; (ii) bilateral patterns of significant similarities in mean FA across mTBI and AD; and (iii) significantly lower mean FA and thinner cortex in both mTBI and AD compared to HCs.

Translational significance

The high prevalence of geriatric mTBI and its subsequent risk for AD underscore the need to predict the latter. Studies have identified significant correlations between certain cognitive measures—like CDR-SB scores—and neural tissue integrity metrics, in that

Table 3 Like Table 2, comparing AD patients to HCs

Abbreviation	Structure	Part	%	
			Left	Right
BCC	Corpus callosum	Body		100
BCF	Fornix	Body		100
CF	Fornix	Cres	100	100
UF	Uncinate fasciculus	—	100	100
CB	Cingulum bundle	—	99	100
GCC	Corpus callosum	Genu		99
TCC	Corpus callosum	Tapetum	97	100
SS	Sagittal stratum	—	94	100
EC	External capsule	—	96	97
SFOF	Fronto-occipital fasciculus	Superior	98	95
PTR	Thalamic radiation	Posterior	99	88
ACR	Corona radiata	Anterior	85	91
SCbP	Cerebellar peduncle	Superior	90	82
SCC	Corpus callosum	Splenium		85
AIC	Internal capsule	Anterior	93	77
SLF	Longitudinal fasciculus	Superior	88	80
ICbP	Cerebellar peduncle	Inferior	84	79
MCbP	Cerebellar peduncle	Middle		78
RIC	Internal capsule	Retrolenticular	88	62
CP	Cerebral peduncle	—	73	75
ML	Medial lemniscus	—	72	73
PCR	Corona radiata	Posterior	63	66
PCT	Pontine crossing tract	—		63
PIC	Internal capsule	Posterior	69	43
SCR	Corona radiata	Superior	54	47
CST	Corticospinal tract	—	15	6

higher CDR-SB scores are indicative of lower integrity [37–39]. Our findings of significant similarities between AD and mTBI pertaining to cortical thickness, mean FA, and cognitive test scores provide clinical insight to identify individuals at high AD risk. Such information can be combined with cognitive test scores (e.g., CDR-SB scores), demographics, biological age prediction [40], and ApoE genotype information to predict the extent and pattern of cortical degeneration experienced by geriatric mTBI patients. Thus, our study may be useful for the stratification of geriatric mTBI patients in terms of their AD risk. Adding to our ability to make such prognostications is the fact that our SVM classification results suggest that the severity of acute cognitive deficits observed in TBI patients can be leveraged

acutely to predict, with high sensitivities and specificities, the *future* extent and breadth of their AD-like brain atrophy patterns. Such information can also complement information acquired using other functional measures like electroencephalography (EEG) and magnetic resonance spectroscopy (MRS) [41, 42] to gain insights into post-traumatic neuropathophysiology [43–46], including adverse effects of brain injury upon peripheral systems [47–49].

Cognitive testing

Our study features MoCA score ranges of 23–30, 2–28, and 20–30 for mTBI, AD, and HC participants, respectively. MMSE scores range from 23 to 30, 11–29, and

Table 4 WM structures listed, in descending numerical order, according to the percentage of voxels associated with mean FA values which are statistically similar ($p < 0.05$), across mTBI and AD cohorts. Values are reported for the left and right hemispheres,

except for structures which straddle both; in this latter case, only one value is reported between the right and left hemisphere columns

Abbreviation	Structure	Part	%	
			Left	Right
SFOF	Fronto-occipital fasciculus	Superior	91	95
CF	Fornix	Cres	65	80
PCT	Pontine crossing tract	—		69
ACR	Corona radiata	Anterior	58	53
BCF	Fornix	Body		49
SCR	Corona radiata	Superior	45	52
PTR	Thalamic radiation	Posterior	59	38
PCR	Corona radiata	Posterior	46	45
MCbP	Cerebellar peduncle	Middle		44
CST	Corticospinal tract	—	36	35
BCC	Corpus callosum	Body		35
ICbP	Cerebellar peduncle	Inferior	33	33
SLF	Longitudinal fasciculus	Superior	33	27
RIC	Internal capsule	Retrolenticular	28	31
TCC	Corpus callosum	Tapetum	9	43
ML	Medial lemniscus	—	22	30
GCC	Corpus callosum	Genu		23
CB	Cingulum bundle	—	29	15
SS	Sagittal stratum	—	19	23
SCbP	Cerebellar peduncle	Superior	19	21
PIC	Internal capsule	Posterior	16	23
SCC	Corpus callosum	Splenium		16
CP	Cerebral peduncle	—	11	13
AIC	Internal capsule	Anterior	13	9
EC	External capsule	—	4	12
UF	Uncinate fasciculus	—	0	7

20–30 for mTBI, AD, and HC subjects, respectively. Typical clinical diagnostic cutoffs for MCI are scores between 18 and 25 for MoCA, and scores between 20 and 25 for MMSE. Although TBI subjects were screened for MCI, it is possible that a minority of subjects had undiagnosed, *subclinical* MCI prior to injury because of MCI prevalence in older individuals [50] and because studying older TBI patients increases the likelihood of including subclinical MCI patients unintentionally [51]. Because both MCI and mTBI are associated with poorer cognition [52], the possibility of including TBI participants with subclinical, premorbid MCI suggests that the sample studied here may have

been affected by this condition to a limited extent and that the lower cognitive test scores of some participants could be attributable to both MCI and mTBI.

Structural neurodegeneration in TBI vs. AD

Table 2 lists WM structures with significantly lower average FA values in mTBI patients compared to HCs. The structures with the greatest differences in mean FA include the TCC, EC, UF, BCC, and GCC. Diffuse axonal injury (DAI) accompanies TBI often and commonly affects large WM structures (like the corpus callosum (CC)) as well as fasciculi innervating temporal

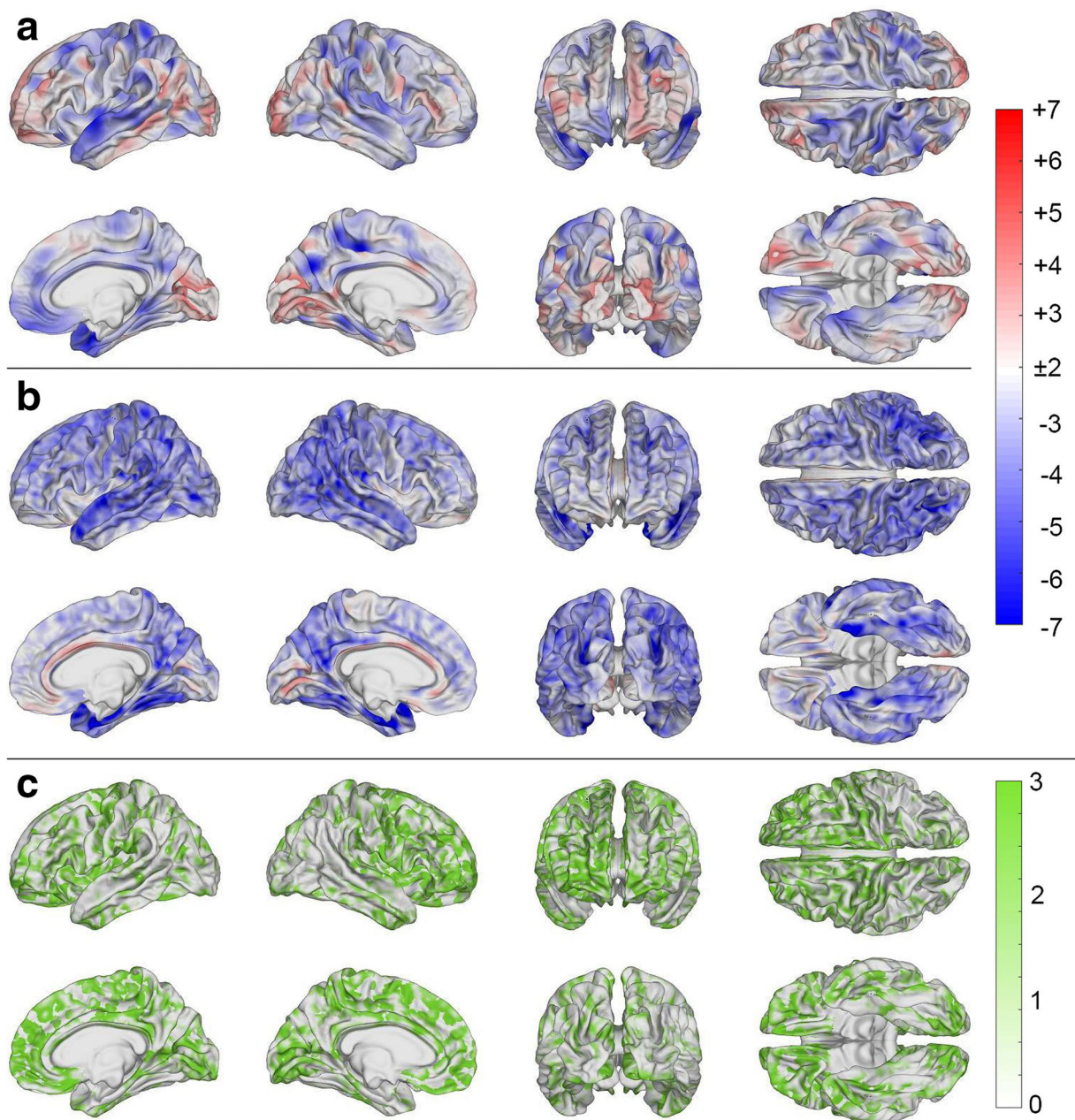


Fig. 3 Statistically significant differences in cortical thickness between (a) mTBI and HCs, (b) AD and HCs, and (c) mTBI and AD patients. Color encodes $-\log_{10} q$, where q is a p value adjusted for the false discovery rate (FDR). Cortical overlays were smoothed using a Gaussian kernel with a full width at half maximum (FWHM) of 5 mm. In (a) and (b), blue regions represent

areas where mTBI and AD subjects, respectively, have significantly thinner cortex compared to HCs. Regions colored in red represent areas where HCs have significantly thinner cortex. In (c), areas colored in green represent regions whose mean cortical thickness is statistically indistinguishable across mTBI and AD participants

or frontal regions, like the UF [53–55]. Our findings agree with these previous studies because the UF—which projects to the temporal lobe—is found here to exhibit extensive lower mean FA in mTBI subjects.

Structures listed in Table 2 exhibit similar extents of damage across hemispheres; this may be partly attributable to contrecoup injuries that can cause contusions and edema, which affect FA [56]. Thus, the listing of WM

Table 5 GM structures listed, in descending numerical order, according to the percentage of cortical mesh vertices associated with cortical thickness means which are statistically similar ($p < 0.05$), across the mTBI and AD cohorts

Structure	Part/segment	%	
		Left	Right
Part of the precentral sulcus	Superior	91	100
Of the lateral sulcus	Horizontal/anterior	75	86
Short insular gyri	—	71	83
Orbital gyri	—	76	74
Cingulate sulcus	Marginal branch	78	71
Frontomarginal gyrus & sulcus	—	66	79
Insular long gyrus & central sulcus	—	76	64
Of the lateral sulcus	Vertical anterior	72	65
Straight gyrus	—	74	55
Inferior frontal gyrus	Triangular	63	65
Inferior frontal gyrus	Opercular	59	67
Olfactory sulcus	—	57	68
Inferior frontal gyrus	Orbital	55	67
Cingulate gyrus	Posterior/ventral	56	65
Transverse frontopolar gyri & sulci	—	52	69
Subcentral gyrus & sulci	—	65	53
Superior frontal gyrus	—	54	62
Cuneus	—	53	63
Cingulate gyrus & sulcus	Anterior	62	50
Cingulate gyrus & sulcus	Middle/anterior	47	64
Lateral orbital sulcus	—	40	69
Cingulate gyrus & sulcus	Middle/posterior	45	62
Circular sulcus of the insula	Superior	53	49
Inferior temporal gyrus	—	55	47
Paracentral lobule & sulcus	—	58	39
Precentral gyrus	—	34	61
Parieto-occipital sulcus	—	47	47
Inferior frontal sulcus	—	28	66
Lingual gyrus	—	46	47
Middle frontal gyrus	—	35	58
Calcarine sulcus	—	47	44
Subcallosal area & gyrus	—	55	35
Cingulate gyrus	Posterior/dorsal	35	54
Heschl's gyrus	—	54	33
Collateral & lingual sulci	—	31	55
Temporal pole	—	49	36
Central sulcus	—	27	57
Circular sulcus of the insula	Inferior	44	39

Table 5 (continued)

Structure	Part/segment	%	
		Left	Right
Posterior transverse collateral sulcus	—	38	38
Occipital pole	—	37	38
Precuneus	—	35	38
Suborbital sulcus	—	33	37
Superior occipital gyrus	—	39	29
Precentral sulcus	Inferior	32	35
Postcentral gyrus	—	32	32
Supramarginal gyrus	—	36	25
Fusiform gyrus	—	28	32
Inferior occipital gyrus & sulcus	—	31	29
Anterior occipital sulcus	—	23	34
Parahippocampal gyrus	—	28	27
Postcentral sulcus	—	25	29
Middle temporal gyrus	—	24	27
Superior temporal gyrus	Lateral	13	35
Middle frontal sulcus	—	18	29
Anterior transverse collateral sulcus	—	6	39
Superior parietal lobule	—	15	29
Superior & transverse occipital sulci	—	34	9
Superior temporal gyrus	Polar plane	32	11
Circular sulcus of the insula	Anterior	23	19
Orbital sulci	—	17	24
Subparietal sulcus	—	16	20
Middle occipital gyrus	—	19	16
Lateral sulcus	Posterior	16	16
Pericallosal sulcus	—	17	13
Lateral occipito-temporal sulcus	—	18	12
Jensen's sulcus	—	12	13
Superior temporal gyrus	Temporal plane	13	12
Inferior temporal sulcus	—	13	8
Angular gyrus	—	14	1
Superior temporal sulcus	—	0	14
Superior frontal sulcus	—	13	1
Middle occipital & lunati sulci	—	7	4
Intraparietal & transverse parietal sulci	—	3	7

structures in Table 2 is consistent with the set of WM fiber bundles that are commonly reported as being affected by TBI-related DAI.

Table 3 lists the BCC, BCF, CF, UF, and CB as exhibiting significantly lower mean FAs in AD subjects. Two prominent scenarios for AD-related WM degeneration involve Wallerian degeneration and retrogenesis. In Wallerian degeneration, AD-related damage initiated in the GM extends to WM tracts connected to these degenerating GM areas [57]. By contrast, retrogenesis postulates that WM fibers undergoing myelogenesis latest during development are the first to degenerate [58]. Many researchers conceptualize AD neurodegeneration as being due to several competing mechanisms and, thus, as being the product of both phenomena. In Table 3, the structure with the fewest voxels exhibiting lower mean FA in AD is the CST. This agrees with the retrogenesis model, since the CST consists of long, motor-projecting fibers which are among the first to myelinate (and thus among the last to degrade, according to the retrogenesis model). Importantly, our findings of significantly lower mean FA in AD subjects in the BCC, BCF, CF, UF, and CB agree with studies suggesting that frontally- and temporally-projecting fibers are more susceptible to AD neurodegeneration [59–62].

Figures 3(a) and 3(b) depict cortical thinning in the temporal lobes of both mTBI and AD subjects, respectively. Previous studies suggest that such thinning is characteristic of AD and that it precedes the Wallerian degeneration of fibers projecting to these regions. Our study agrees with these findings because Tables 1 and 2 show both mTBI and AD victims as exhibiting significantly lower mean FA than HCs in temporally-projecting fibers like the CB, BCF, and CF. Thus, our findings agree with previous studies of AD-related WM neurodegeneration and may reflect the competing effects of several neurodegenerative mechanisms.

Table 4 illustrates how mTBI and AD are similar from the standpoint of mean FA decreases within major WM fasciculi. Studies have identified WM fibers proximal to the brain stem as being commonly affected by DAI following TBI [55, 63–66]; however, fibers like the PCT and CST are listed here as being relatively spared by both mTBI (Table 2) and AD (Table 3). Instead of appearing to be affected by TBI, these tracts exhibit damage resembling that observed in AD (Table 4). This may reflect similar neurodegeneration mechanisms following TBI and AD [67], and is consistent with the retrogenesis model as these structures are among the first to be myelinated during development [68–70].

Functional neurodegeneration in TBI vs. AD

At the microscale, parallels between TBI and AD have been identified by neuropathology studies [10, 71, 72]. Similarly, in neuropsychological and cognitive studies, neural correlates of cognitive deficits observed after TBI and AD have been found to share commonalities [6, 73]. Nevertheless, few studies have compared the effects of TBI and AD upon brain architecture at the macroscale, partly due to the challenges of MRI morphometry in TBI [74]. The present study found significant similarities between mTBI and AD subjects pertaining to the cortical thinning in the ACC, PCC, and temporal poles (Table 5). Our findings are consistent with those of previous studies [4, 75–78], which independently examined neurodegeneration after the two conditions. Such comparisons of cognitive symptoms across TBI and AD have identified similar deficits in processing speed, cognitive flexibility, attention, and memory [79]. The ACC and PCC are part of the default mode network, which may be hypoactive after mTBI, resulting in deficits of divided attention [80]. Similarly, AD studies of attention suggest that the ACC is involved in divided attention deficits [81]. Simultaneously, TBI-related damage to the ACC and temporal lobes has been implicated in poor self-awareness due to bilateral hyperactivity within these regions. Other studies have found strong involvement of the ACC and temporal poles in functional deficits pertaining to memory and perceptual ability [82, 83]. In what follows, we discuss potential relationships between deficits within specific cognitive domains and both AD- and TBI-related neurodegeneration patterns.

Social function deficits

Social function has been studied in the context of concepts like the *social brain* and the multi-faceted *social network*, which includes the orbitofrontal cortex (OFC), superior aspect of the lateral temporal lobe, the medial prefrontal cortex (PFC), ACC, and the amygdala [84]. The amount of cortical thinning identified by our investigation in the OFC was found to be statistically indistinguishable across the mTBI and AD cohorts (Table 5), which is consistent with studies identifying the OFC as modulating social function. Specifically, in TBI, the OFC has been cited as involved in social function (e.g., emotion recognition), and prominent mTBI-

related deficits pertain to social function [85–87]. This type of deficit has also been identified in AD, where social withdrawal and dysfunction are typical manifestations of the disease [84, 88, 89]. Thus, our findings suggest that TBI and AD share social function deficits which may be due to similar spatial neurodegeneration patterns.

Decision-making deficits

This study found that damage to the PIC, UF, orbital gyri, and orbital sulci is common in both mTBI and AD (Tables 3 and 4). Typically, decision-making after TBI is significantly poorer than in HCs, a phenomenon which often persists up to 5 years post injury [90]. There are, however, conflicting findings on how lesion location impacts decision-making. In mice, for example, spatially non-specific associations have been found between unilateral parietal and bilateral frontal lesions, on the one hand, and riskier decision-making and increased impulsivity, on the other hand [91, 92]. By contrast, however, human studies indicate that decision-making deficits are not limited to cases involving frontal lesions [93]. Thus, dMRI studies of patients with mild-to-moderate blast TBIs have revealed that the compromised integrities of the right UF, right inferior fronto-occipital fasciculus (IFOF), and right PIC are associated with decision-making deficits [94]. Aside from TBI, such deficits are also observed in AD, where structural changes within ventromedial PFC (vmPFC) are correlated with measurable deficits [95]. Thus, our findings are consistent with those of prior studies on decision-making and identify commonalities between decision making deficits and the neurodegenerative patterns of TBI and AD.

PS deficits

This study identified similar patterns of WM degradation across mTBI and AD in the left AIC, UF, CB, ACR, and GCC (Table 4). Such findings are consistent with those of previous dMRI studies that revealed correlations between reduced WM integrity in these areas and relatively low PS [96–99]. In mTBI, lower PS has been reported as early as 1-month post-injury and has been documented to persist for up to 6 years post-injury [100–103]. Commonly, lower PS is coexistent with other mTBI-related symptoms like fatigue, anxiety, and attention deficits. In particular, reports of fatigue

following mTBI are exceedingly common and may be explained by the *coping hypothesis*, which states that compensatory recruitment of areas increases cognitive load, resulting in fatigue which lowers PS [104–107]. Similar PS reductions have been observed in AD, as quantified by pause and reaction times [108, 109]. Thus, our findings agree with those of previous studies which identified neuroanatomic structure correlates of PS deficits in TBI and AD.

Verbal fluency deficits

Our study reports similarities between mTBI and AD pertaining to global reductions in cortical thickness (Table 5). Some of these affected structures and regions (e.g., the left ascending fibers in the CC, the frontal lobes, the left inferior frontal gyrus (IFG), the left middle temporal gyrus (MTG), and the left STG) have been identified as being responsible for reduced verbal fluency [110–112]. Verbal fluency can be broadly classified as phonemic or semantic, and deficits in both are frequent after TBI, with estimated prevalences of ~70% and ~87%, respectively, and with comparable magnitudes for each [113, 114]. Whereas other deficits following TBI can recover relatively well, verbal fluency deficits have been suggested to recover relatively poorly and slowly, since they persist for more than 6 weeks post-injury [115, 116]. In AD, deficits in both phonemic and semantic fluency have been observed. Importantly, the latter is reported as being significantly more impaired than the former [117]. Such differences in severity have been proposed to reflect the increased susceptibility of temporal regions—which have a role in semantic memory—to neurodegeneration following AD [118, 119]. Figure 2b displays reduced cortical thickness in the temporal regions of AD subjects, in agreement with previous studies [16, 120]. Thus, the degradation of brain regions reported here is consistent with the findings of previous studies reporting relatively slow recovery of verbal fluency after TBI. Together, our findings indicate that TBI and AD share neuroanatomic patterns of brain degradation which underlie verbal fluency deficits.

Executive function (EF) deficits

EF is greatly impacted by both mTBI and AD [121–124]. Here we identified relatively low mean FA in the ACCs, GCCs, SCCs, and PICs of both mTBI and

AD patients compared to HCs (Tables 1 and 2). Reduced integrity in these WM structures is correlated with impaired planning abilities [81, 125], although such findings are not unanimous across studies [126]. This may suggest that planning deficits are modulated by injury severity, particularly since some authors [127] did not identify planning deficits associated with WM damage. By contrast, AD patients' planning deficits have been documented extensively and there is substantial consensus on their profiles [81, 128–130]. Thus, our findings of similarly reduced WM integrity in the CCs of mTBI and AD subjects are consistent with previous studies tying these areas to EF deficits [131, 132].

Cognitive flexibility deficits

Reductions in cognitive flexibility are often noted after mTBI and have been documented both acutely and up to 2 months after injury. Our study revealed reduced WM integrity throughout the CCs of mTBI and AD patients, in agreement with investigations of these areas' involvement in EF. Inflexibility affects multiple facets of cognition, including the ability to integrate new information, to adapt one's behavior in response to stimuli, and to switch attention fluidly. Cognitive flexibility is intimately related to EF, which recruits frontal cortex and frontally-projecting fibers [122]. Because of this, similar methods like task switching have been used to reveal that reduced GM integrity—particularly in the superior frontal gyrus (SFG), PFC, precuneus, ACC, and in the fusiform gyrus—affects cognitive flexibility [133, 134]. In our mTBI and AD cohorts, reduced cortical thickness was observed in the superior FG, in the PFC, precuneus, ACC, and in the fusiform gyrus (Table 5). Thus, our findings support the hypothesis according to which AD and TBI patients share a previously documented neuroanatomic substrate of cognitive inflexibility.

Limitations

Although the results of this study support an association between mTBI and AD, it is imperative that they be interpreted cautiously because they do not establish a causal relationship between TBI and AD. Specifically, because the associations reported here pertaining to the relationship between mTBI and brain structure are of a

statistical nature, it is important to keep in mind that these statistical relationships may not be causally linked solely to TBI. Rather, our findings support the hypothesis that, to some extent, mTBI and AD share some commonality of trajectories. Furthermore, because the participant follow-up period is limited to the first ~6 months post-injury, our findings do not reflect the entire range of TBI progression, nor do they establish whether and when neurodegeneration trajectories diverge across the two conditions. To establish such cause–effect relationships between mTBI and AD, more definitive and larger prospective studies should evaluate, within a broader longitudinal design, the cerebral structure of geriatric mTBI victims. Thus, the possibility that our findings may in part be due to conditions other than TBI cannot be discarded and is, in fact, plausible. For example, it is important to acknowledge that comorbidities may influence the structural findings reported here. For example, in one UK study of geriatric TBI involving hospital admissions [135], 11% of patients had pre-existing dementia, 22% had pre-existing hypertension, and 99% had at least one pre-existing medical condition. Similarly, Mosenthal et al. [136] report that 73% of older TBI patients have a medical condition before injury, compared with only 28% of younger adults. Third, 80% of all adults aged 65 years and older have at least one chronic condition and 50% have at least two [137]. Thus, typically, older TBI patients suffer from at least one cardiovascular comorbidity, like hypertension. Pre-existing hypertension is common in geriatric TBI patients [138] and its association with lower FA compared to normotensive patients [139] may be due to the adverse effects of hypertension upon the neurovasculature. CMBs—whose presence can result in mean FA decreases [140]—are common in geriatric TBI and can significantly affect peri-hemorrhagic WM [4]. CMBs are also frequent in cases of cerebral amyloid angiopathy (CAA), which is a risk factor for AD [141, 142]. Thus, due to the high prevalence of CMB-positive TBI comorbidities in older adults, it is possible that our findings of structural similarities between mTBI and AD are partially due to pre-existing neurovascular conditions. Thus, ideally, the structural effects of AD and mTBI should be compared in the absence of CMBs, which may confound findings. However, this may be challenging due to the high prevalence of vascular disease in older adults; furthermore, findings from such normotensive older TBI patients who are free of vascular disease may be of somewhat limited applicability to

most clinical settings because only a relatively modest cross-section of older individuals lack either symptoms or post-mortem pathology indicative of vascular disease. Finally, it should be noted that CMB counts, although reported here, were not included in our analysis of WM degradation because accounting for local CMB effects is challenging and outside the scope of this study. The reader is referred to our previous research for findings on this topic [4].

The possibility of unintentional sampling bias is another study limitation that should be acknowledged. Thus, although random sampling from the entire TBI population—or at least from the local TBI population—would have been preferable, such sampling was logistically unfeasible for us as no comprehensive directory of geriatric TBI victims was available to us at the time of the study. Instead, our most viable option was reaching out to potential volunteers based on referrals from clinicians.

One technical limitation of this study is that the JHU WM atlas includes only 25 WM structures and omits some functionally prominent fascicles. For example, superficial WM streamlines—described as typically short cortical association fibers near the surface of the cortex [143]—are excluded here. Such connections are more difficult to segment and more poorly documented than larger WM structures, and since the JHU WM atlas does not include them, neither does our study. Future studies should use atlases that map more WM structures; in our case, this was beyond the scope of the study as our primary interest was in the largest and best-mapped WM structures in the brain. Another limitation is the fact that MRI data used in the study were acquired at distinct sites using different scanners. This is known to confound measurements of both cortical thickness and WM properties [144, 145], such that harmonization protocols like ComBat can be useful [144–146]. Nevertheless, because our MRI acquisition protocol parameters were very similar across sites and scanners, such confounds may not be substantial in this study.

Although age-related effects were regressed out in our statistical analyses, the groups included here did exhibit significant mean differences of age. These differences are partly due to our selection of subjects from retrospective samples of convenience, such that age matching across groups was possible to a very limited extent. Furthermore, because this is a longitudinal study involving both structural MRI and dMRI of individuals

with very specific eligibility criteria, only a relatively small subsample of the ADNI cohort was useful for our purposes. This also limited our ability to match subjects by age. Finally, AD occurs relatively rarely before the age of 65, whereas TBIs can occur at any age. This implies that comparing AD patients to TBI victims can be problematic if the latter are relatively young compared to the former. Thus, to some extent, the confound of age in studies like ours is unavoidable if young or middle-aged TBI patients are to be compared to AD patients. Nevertheless, because TBI patients younger than 65 may still be vulnerable to AD-analogous neurodegeneration (as suggested, in fact, by our study), the inability to match TBI and AD patients by age may be unavoidable in studies like ours, particularly if relatively young TBI patients are studied.

Conclusion

Upon comparing AD patients to mTBI participants imaged ~6 months post injury, this study identified statistical similarities between these groups pertaining to both WM and GM neurodegeneration, as evidenced by both mean FA and cortical thickness measurements. Whereas other studies explored the effects of TBI and AD on the brain without reference to one another, we directly compare such effects. Furthermore, this study focuses on chronic mTBI findings rather than on acute mTBI, thereby providing insight into the medium-to-long-term effects of mTBI upon macroscale brain structure. Our findings agree with those of previous studies of functional and structural correlates in these conditions, and additionally reveal AD-analogous patterns of neurodegeneration after mTBI, which may be proportional to AD risk. Thus, our findings are relevant to ongoing efforts to identify mTBI patients at high risk for AD. Future studies should quantitatively compare the neurological and neuropsychological consequences of mTBI and AD to further elucidate their relationship.

Acknowledgements The authors thank Sean Mahoney, Van Ngo, and Di Fan for suggestions and comments on the manuscript, Nikhil N. Chaudhari for assistance with CMB identification, data archiving, and data retrieval, as well as Nahian F. Chowdhury, Gloria Chia-Yi Chiang, Ammar Dharani, Jun H. Kim, Hyung Jun Lee, David J. Robles, and Shania H. Wang for assistance with CMB identification. Data used in preparation of this article were obtained from the Alzheimer's Disease Neuroimaging Initiative

(ADNI) database (adni.loni.usc.edu). As such, the investigators within the ADNI contributed to the design and implementation of ADNI and/or provided data but did not participate in analysis or writing of this report. A complete listing of ADNI investigators can be found at: http://adni.loni.usc.edu/wp-content/uploads/how_to_apply/ADNI_Acknowledgement_List.pdf.

Availability of data and material MRI data acquired from HC and AD participants are publicly available from the ADNI database (<http://adni.loni.usc.edu>). For TBI participants, primary data generated during and/or analyzed during the current study are available subject to a data transfer agreement. At the request of some participants, their written permission is additionally required in some cases.

Code availability The computer code used in this study is freely available. FreeSurfer (<https://surfer.nmr.mgh.harvard.edu>) and the FMRIB Software Library (<https://fsl.fmrib.ox.ac.uk>) are freely available. Equivalence testing was implemented using freely available MATLAB software (<https://www.mathworks.com/matlabcentral/fileexchange/63204>). Regression and SVM analyses were implemented in MATLAB (<http://mathworks.com>) using the `glmfit`, `fitcsvm`, and `predict` functions.

Author contribution K.A.R. and A.I. contributed to the study design, data analysis, result interpretation, and manuscript redaction.

Funding This work was supported by NIH grant R01 NS 100973 to A.I., by DoD award W81-XWH-1810413 to A.I., by a Hanson-Thorell Research Scholarship to A.I., and by a grant from the Undergraduate Research Associate Program (URAP) at the University of Southern California to A.I. Data collection and sharing for this project were funded by the Alzheimer’s Disease Neuroimaging Initiative (ADNI, NIH Grant U01 AG024904) and DoD ADNI (DoD award number W81XWH-12-2-0012). ADNI is funded by the National Institute on Aging, the National Institute of Biomedical Imaging and Bioengineering, and through generous contributions from the following: AbbVie, Alzheimer’s Association; Alzheimer’s Drug Discovery Foundation; Araclon Biotech; BioClinica, Inc.; Biogen; Bristol-Myers Squibb Company; CereSpir, Inc.; Cogstate; Eisai Inc.; Elan Pharmaceuticals, Inc.; Eli Lilly and Company; EuroImmun; F. Hoffmann-La Roche Ltd, and its affiliated company Genentech, Inc.; Fujirebio; GE Healthcare; IXICO Ltd.; Janssen Alzheimer Immunotherapy Research & Development, LLC.; Johnson & Johnson Pharmaceutical Research & Development LLC.; Lumosity; Lundbeck; Merck & Co., Inc.; Meso Scale Diagnostics, LLC.; NeuroRx Research; Neurotrack Technologies; Novartis Pharmaceuticals Corporation; Pfizer Inc.; Piramal Imaging; Servier; Takeda Pharmaceutical Company; and Transition Therapeutics. The Canadian Institutes of Health Research is providing funds to support ADNI clinical sites in Canada. Private sector contributions are facilitated by the Foundation for the National Institutes of Health (www.fnih.org). The grantee organization is the Northern California Institute for Research and Education, and the study is coordinated by the Alzheimer’s Therapeutic Research Institute at the University of Southern California. ADNI data are disseminated by the Laboratory for Neuro Imaging at the University of Southern California.

Declarations

Ethics approval This study was conducted with the approval of the Institutional Review Board at the University of Southern California and was carried out in accordance with the Declaration of Helsinki and with the U.S. Code of Federal Regulations (45 C.F.R. 46).

Consent to participate All subjects provided written informed consent.

Consent for publication Both authors approved the final version of the manuscript for publication.

Conflict of interest/Competing interests The authors declare that this research was conducted with no commercial or financial relationships that could be construed as a potential conflict of interest statement.

References

1. Georges A, Booker JG. Traumatic Brain Injury. Treasure Island (FL): StatPearls; 2020.
2. Jain S, Iverson LM. Glasgow Coma Scale. Treasure Island (FL): StatPearls; 2020.
3. Irimia A, Maher AS, Rostovsky KA, Chowdhury NF, Hwang DH, Law EM. Brain segmentation from computed tomography of healthy aging and geriatric concussion at variable spatial resolutions. *Front Neuroinform*. 2019;13:9. <https://doi.org/10.3389/fninf.2019.00009>.
4. Rostovsky KA, Maher AS, Irimia A. Macroscale white matter alterations due to traumatic cerebral microhemorrhages are revealed by diffusion tensor imaging. *Front Neurol*. 2018;9:948. <https://doi.org/10.3389/fneur.2018.00948>.
5. Moretti L, Cristofori I, Weaver SM, Chau A, Portelli JN, Grafman J. Cognitive decline in older adults with a history of traumatic brain injury. *Lancet Neurol*. 2012;11(12):1103–12. [https://doi.org/10.1016/S1474-4422\(12\)70226-0](https://doi.org/10.1016/S1474-4422(12)70226-0).
6. Kinnunen KM, Greenwood R, Powell JH, Leech R, Hawkins PC, Bonnelle V, et al. White matter damage and cognitive impairment after traumatic brain injury. *Brain*. 2011;134(Pt 2):449–63. <https://doi.org/10.1093/brain/awq347>.
7. Thompson HJ, McCormick WC, Kagan SH. Traumatic brain injury in older adults: epidemiology, outcomes, and future implications. *J Am Geriatr Soc*. 2006;54(10):1590–5. <https://doi.org/10.1111/j.1532-5415.2006.00894.x>.
8. LeBlanc J, de Guise E, Gosselin N, Feyz M. Comparison of functional outcome following acute care in young, middle-aged and elderly patients with traumatic brain injury. *Brain Inj*. 2006;20(8):779–90. <https://doi.org/10.1080/02699050600831835>.

9. Li Y, Li Y, Li X, Zhang S, Zhao J, Zhu X, et al. Head Injury as a risk factor for dementia and Alzheimer's Disease: a systematic review and meta-analysis of 32 observational studies. *PLoS One*. 2017;12(1):e0169650. <https://doi.org/10.1371/journal.pone.0169650>.
10. Washington PM, Villapol S, Burns MP. Polypathology and dementia after brain trauma: does brain injury trigger distinct neurodegenerative diseases, or should they be classified together as traumatic encephalopathy? *Exp Neurol*. 2016;275(Pt 3):381–8. <https://doi.org/10.1016/j.expneurol.2015.06.015>.
11. Edwards G 3rd, Moreno-Gonzalez I, Soto C. Amyloid-beta and tau pathology following repetitive mild traumatic brain injury. *Biochem Biophys Res Commun*. 2017;483(4):1137–42. <https://doi.org/10.1016/j.bbrc.2016.07.123>.
12. Irimia A, Fan D, Chaudhari N, Ngo V, Zhang F, Joshi SH, et al. Mapping cerebral connectivity changes after mild traumatic brain injury in older adults using diffusion tensor imaging and Riemannian matching of elastic curves. In: Conference Proceedings of the 17th IEEE International Symposium on Biomedical Imaging. Iowa City, IA, USA: IEEE; 2020. p. 1690–1693.
13. Chen SQ, Kang Z, Hu XQ, Hu B, Zou Y. Diffusion tensor imaging of the brain in patients with Alzheimer's disease and cerebrovascular lesions. *J Zhejiang Univ Sci B*. 2007;8(4):242–7. <https://doi.org/10.1631/jzus.2007.B0242>.
14. Davenport ND, Lim KO, Armstrong MT, Sponheim SR. Diffuse and spatially variable white matter disruptions are associated with blast-related mild traumatic brain injury. *Neuroimage*. 2012;59(3):2017–24. <https://doi.org/10.1016/j.neuroimage.2011.10.050>.
15. Santhanam P, Wilson SH, Oakes TR, Weaver LK. Accelerated age-related cortical thinning in mild traumatic brain injury. *Brain Behav*. 2019;9(1):e01161. <https://doi.org/10.1002/brb3.1161>.
16. Du AT, Schuff N, Kramer JH, Rosen HJ, Gorno-Tempini ML, Rankin K, et al. Different regional patterns of cortical thinning in Alzheimer's disease and frontotemporal dementia. *Brain*. 2007;130(Pt 4):1159–66. <https://doi.org/10.1093/brain/awm016>.
17. Govindarajan KA, Narayana PA, Hasan KM, Wilde EA, Levin HS, Hunter JV, et al. Cortical thickness in mild traumatic brain injury. *J Neurotrauma*. 2016;33(20):1809–17. <https://doi.org/10.1089/neu.2015.4253>.
18. Irimia A, Maher AS, Chaudhari NN, Chowdhury NF, Jacobs EB. Acute cognitive deficits after traumatic brain injury predict Alzheimer's disease-like degradation of the human default mode network. *Geroscience*. 2020;42(5):1411–1429. doi:<https://doi.org/10.1007/s11357-020-00245-6>
19. Sehgal V, Delproposto Z, Haacke EM, Tong KA, Wycliffe N, Kido DK, et al. Clinical applications of neuroimaging with susceptibility-weighted imaging. *J Magn Reson Imaging*. 2005;22(4):439–50. <https://doi.org/10.1002/jmri.20404>.
20. Petersen RC, Aisen PS, Beckett LA, Donohue MC, Gamst AC, Harvey DJ, et al. Alzheimer's Disease Neuroimaging Initiative (ADNI): clinical characterization. *Neurology*. 2010;74(3):201–9. <https://doi.org/10.1212/WNL.0b013e3181cb3e25>.
21. Andersson JL, Skare S, Ashburner J. How to correct susceptibility distortions in spin-echo echo-planar images: application to diffusion tensor imaging. *Neuroimage*. 2003;20(2):870–88. [https://doi.org/10.1016/S1053-8119\(03\)00336-7](https://doi.org/10.1016/S1053-8119(03)00336-7).
22. Dale AM, Fischl B, Sereno MI. Cortical surface-based analysis. I. Segmentation and surface reconstruction. *Neuroimage*. 1999;9(2):179–94. <https://doi.org/10.1006/nimg.1998.0395>.
23. Fischl B, Sereno MI, Dale AM. Cortical surface-based analysis. II: inflation, flattening, and a surface-based coordinate system. *Neuroimage*. 1999;9(2):195–207. <https://doi.org/10.1006/nimg.1998.0396>.
24. Desikan RS, Segonne F, Fischl B, Quinn BT, Dickerson BC, Blacker D, et al. An automated labeling system for subdividing the human cerebral cortex on MRI scans into gyral based regions of interest. *Neuroimage*. 2006;31(3):968–80. <https://doi.org/10.1016/j.neuroimage.2006.01.021>.
25. Smith SM, Jenkinson M, Johansen-Berg H, Rueckert D, Nichols TE, Mackay CE, et al. Tract-based spatial statistics: voxelwise analysis of multi-subject diffusion data. *Neuroimage*. 2006;31(4):1487–505. <https://doi.org/10.1016/j.neuroimage.2006.02.024>.
26. Bennett IJ, Madden DJ, Vaidya CJ, Howard DV, Howard JH Jr. Age-related differences in multiple measures of white matter integrity: a diffusion tensor imaging study of healthy aging. *Hum Brain Mapp*. 2010;31(3):378–90. <https://doi.org/10.1002/hbm.20872>.
27. Kanaan RA, Allin M, Picchioni M, Barker GJ, Daly E, Shergill SS, et al. Gender differences in white matter microstructure. *PLoS One*. 2012;7(6):e38272. <https://doi.org/10.1371/journal.pone.0038272>.
28. Smith SM, Nichols TE. Threshold-free cluster enhancement: addressing problems of smoothing, threshold dependence and localisation in cluster inference. *Neuroimage*. 2009;44(1):83–98. <https://doi.org/10.1016/j.neuroimage.2008.03.061>.
29. Han H, Glenn AL, Dawson KJ. Evaluating alternative correction methods for multiple comparison in functional neuroimaging research. *Brain Sci*. 2019;9:8. <https://doi.org/10.3390/brainsci9080198>.
30. Wellek S. A new approach to equivalence assessment in standard comparative bioavailability trials by means of the Mann-Whitney statistic. *Biometrical Journal*. 1996;38(6):695–710. <https://doi.org/10.1002/bimj.4710380608>.
31. Walker E, Nowacki AS. Understanding equivalence and noninferiority testing. *Journal of General Internal Medicine*. 2011;26(2):192–6. <https://doi.org/10.1007/s11606-010-1513-8>.
32. Hoffelder T, Gossel R, Wellek S. Multivariate equivalence tests for use in pharmaceutical development. *Journal of Biopharmaceutical Statistics*. 2015;25(3):417–37. <https://doi.org/10.1080/10543406.2014.920344>.
33. Matthews BW. Comparison of the predicted and observed secondary structure of T4 phage lysozyme. *Biochim Biophys Acta*. 1975;405(2):442–51. [https://doi.org/10.1016/0005-2795\(75\)90109-9](https://doi.org/10.1016/0005-2795(75)90109-9).
34. Dall'Acqua P, Johannes S, Mica L, Simmen H-P, Glaab R, Fandino J, et al. Prefrontal cortical thickening after mild traumatic brain injury: a one-year magnetic resonance

- imaging study. *Journal of Neurotrauma*. 2017a;34(23):3270–9. <https://doi.org/10.1089/neu.2017.5124>.
35. Guerriero RM, Giza CC, Rotenberg A. Glutamate and GABA imbalance following traumatic brain injury. *Curr Neurol Neurosci Rep*. 2015;15(5):27. <https://doi.org/10.1007/s11910-015-0545-1>.
 36. Shao M, Cao J, Bai L, Huang W, Wang S, Sun C, et al. Preliminary evidence of sex differences in cortical thickness following acute mild traumatic brain injury. *Front Neurol*. 2018;9:878. <https://doi.org/10.3389/fneur.2018.00878>.
 37. Ji F, Pasternak O, Liu S, Loke YM, Choo BL, Hilal S, et al. Distinct white matter microstructural abnormalities and extracellular water increases relate to cognitive impairment in Alzheimer's disease with and without cerebrovascular disease. *Alzheimers Res Ther*. 2017;9(1):63. <https://doi.org/10.1186/s13195-017-0292-4>.
 38. Hsu JL, Lee WJ, Liao YC, Limg JF, Wang SJ, Fuh JL. Posterior atrophy and medial temporal atrophy scores are associated with different symptoms in patients with Alzheimer's disease and mild cognitive impairment. *PLoS One*. 2015;10(9):e0137121. <https://doi.org/10.1371/journal.pone.0137121>.
 39. Wang B, Prastawa M, Awate SP, Irimia A, Chambers MC, Vespa PM, et al. Segmentation of serial MRIs of TBI patients using personalized atlas construction and topological change estimation. *Proc IEEE Int Symp Biomed Imaging*. 2012:1152–5. <https://doi.org/10.1109/isbi.2012.6235764>.
 40. Irimia A, Torgerson CM, Goh SY, Van Horn JD. Statistical estimation of physiological brain age as a descriptor of senescence rate during adulthood. *Brain Imaging Behav*. 2015;9(4):678–89. <https://doi.org/10.1007/s11682-014-9321-0>.
 41. Van Horn JD, Bhattarai A, Irimia A. Multimodal imaging of neurometabolic pathology due to traumatic brain injury. *Trends in Neurosciences*. 2017;40(1):39–59. <https://doi.org/10.1016/j.tins.2016.10.007>.
 42. Halgren E, Sherfey J, Irimia A, Dale AM, Marinkovic K. Sequential temporo-fronto-temporal activation during monitoring of the auditory environment for temporal patterns. *Hum Brain Mapp*. 2011;32(8):1260–76. <https://doi.org/10.1002/hbm.21106>.
 43. Irimia A, Van Horn JD. Functional neuroimaging of traumatic brain injury: advances and clinical utility. *Neuropsychiatr Dis Treat*. 2015;11:2355–65. <https://doi.org/10.2147/NDT.S79174>.
 44. Irimia A, Van Horn JD. Epileptogenic focus localization in treatment-resistant post-traumatic epilepsy. *Journal of Clinical Neuroscience*. 2015;22(4):627–31.
 45. Lima EA, Irimia A, Wikswo J. The magnetic inverse problem. In: Braginski AI, Clarke J, editors. *The SQUID Handbook*. Weinheim, Germany: Wiley-VCH; 2006. p. 139–267.
 46. Irimia A, Goh SY, Torgerson CM, Chambers MC, Kikinis R, Van Horn JD. Forward and inverse electroencephalographic modeling in health and in acute traumatic brain injury. *Clinical Neurophysiology*. 2013;124(11):2129–45.
 47. Irimia A, Bradshaw LA. Ellipsoidal electrogastrographic forward modelling. *Phys Med Biol*. 2005;50(18):4429–44. <https://doi.org/10.1088/0031-9155/50/18/012>.
 48. Irimia A, Richards WO, Bradshaw LA. Magnetogastrographic detection of gastric electrical response activity in humans. *Phys Med Biol*. 2006;51(5):1347–60. <https://doi.org/10.1088/0031-9155/51/5/022>.
 49. Irimia A. Electric field and potential calculation for a bioelectric current dipole in an ellipsoid. *Journal of Physics A: Mathematical and General*. 2005;38(37):8123–38.
 50. Eshkooor SA, Hamid TA, Mun CY, Ng CK. Mild cognitive impairment and its management in older people. *Clin Interv Aging*. 2015;10:687–93. <https://doi.org/10.2147/CIA.S73922>.
 51. Sachdev PS, Lipnicki DM, Kochan NA, Crawford JD, Thalamuthu A, Andrews G, et al. The prevalence of mild cognitive impairment in diverse geographical and ethnocultural regions: The COSMIC Collaboration. *PLoS One*. 2015;10(11):e0142388. <https://doi.org/10.1371/journal.pone.0142388>.
 52. de Freitas Cardoso MG, Faleiro RM, de Paula JJ, Kummer A, Caramelli P, Teixeira AL, et al. Cognitive impairment following acute mild traumatic brain injury. *Front Neurol*. 2019;10:198. <https://doi.org/10.3389/fneur.2019.00198>.
 53. Inglese M, Makani S, Johnson G, Cohen BA, Silver JA, Gonen O, et al. Diffuse axonal injury in mild traumatic brain injury: a diffusion tensor imaging study. *J Neurosurg*. 2005;103(2):298–303. <https://doi.org/10.3171/jns.2005.103.2.0298>.
 54. Meythaler JM, Peduzzi JD, Eleftheriou E, Novack TA. Current concepts: diffuse axonal injury-associated traumatic brain injury. *Arch Phys Med Rehabil*. 2001;82(10):1461–71. <https://doi.org/10.1053/apmr.2001.25137>.
 55. Mesfin FB, Gupta N, Hays Shapshak A, Taylor RS. *Diffuse Axonal Injury (DAI)*. Treasure Island (FL): StatPearls; 2020.
 56. Alexander AL, Lee JE, Lazar M, Field AS. Diffusion tensor imaging of the brain. *Neurotherapeutics*. 2007;4(3):316–29. <https://doi.org/10.1016/j.nurt.2007.05.011>.
 57. Alves GS, O'Dwyer L, Jurcoane A, Oertel-Knochel V, Knochel C, Prvulovic D, et al. Different patterns of white matter degeneration using multiple diffusion indices and volumetric data in mild cognitive impairment and Alzheimer patients. *PLoS One*. 2012;7(12):e52859. <https://doi.org/10.1371/journal.pone.0052859>.
 58. Amlien IK, Fjell AM. Diffusion tensor imaging of white matter degeneration in Alzheimer's disease and mild cognitive impairment. *Neuroscience*. 2014;276:206–15. <https://doi.org/10.1016/j.neuroscience.2014.02.017>.
 59. Chua TC, Wen W, Slavin MJ, Sachdev PS. Diffusion tensor imaging in mild cognitive impairment and Alzheimer's disease: a review. *Curr Opin Neurol*. 2008;21(1):83–92. <https://doi.org/10.1097/WCO.0b013e3282f4594b>.
 60. Kim YJ, Kwon HK, Lee JM, Kim YJ, Kim HJ, Jung NY, et al. White matter microstructural changes in pure Alzheimer's disease and subcortical vascular dementia. *Eur J Neurol*. 2015;22(4):709–16. <https://doi.org/10.1111/ene.12645>.
 61. Lee SH, Coutu JP, Wilkens P, Yendiki A, Rosas HD, Salat DH, et al. Tract-based analysis of white matter

- degeneration in Alzheimer's disease. *Neuroscience*. 2015;301:79–89. <https://doi.org/10.1016/j.neuroscience.2015.05.049>.
62. Bozzali M, Falini A, Franceschi M, Cercignani M, Zuffi M, Scotti G, et al. White matter damage in Alzheimer's disease assessed in vivo using diffusion tensor magnetic resonance imaging. *J Neurol Neurosurg Psychiatry*. 2002;72(6):742–6. <https://doi.org/10.1136/jnnp.72.6.742>.
 63. Su E, Bell M. Diffuse Axonal Injury. In: Laskowitz D, Grant G, editors. *Translational research in traumatic brain injury*. Boca Raton (FL): Frontiers in Neuroscience; 2016.
 64. Vik A, Kvistad KA, Skandsen T, Ingebrigtsen T. Diffuse axonal injury in traumatic brain injury. *Tidsskr Nor Laegeforen*. 2006;126(22):2940–4.
 65. Parizel PM, Ozsarlak, Van Goethem JW, van den Hauwe L, Dillen C, Verlooy J, et al. Imaging findings in diffuse axonal injury after closed head trauma. *Eur Radiol*. 1998;8(6):960–5. <https://doi.org/10.1007/s003300050496>.
 66. Arfanakis K, Haughton VM, Carew JD, Rogers BP, Dempsey RJ, Meyerand ME. Diffusion tensor MR imaging in diffuse axonal injury. *AJNR Am J Neuroradiol*. 2002;23(5):794–802.
 67. DeKosky ST, Asken BM. Injury cascades in TBI-related neurodegeneration. *Brain Inj*. 2017;31(9):1177–82. <https://doi.org/10.1080/02699052.2017.1312528>.
 68. Geng X, Gouttard S, Sharma A, Gu H, Styner M, Lin W, et al. Quantitative tract-based white matter development from birth to age 2 years. *Neuroimage*. 2012;61(3):542–57. <https://doi.org/10.1016/j.neuroimage.2012.03.057>.
 69. Gilmore JH, Lin W, Corouge I, Vetsa YS, Smith JK, Kang C, et al. Early postnatal development of corpus callosum and corticospinal white matter assessed with quantitative tractography. *AJNR Am J Neuroradiol*. 2007;28(9):1789–95. <https://doi.org/10.3174/ajnr.a0751>.
 70. Wang S, Ledig C, Hajnal JV, Counsell SJ, Schnabel JA, Deprez M. Quantitative assessment of myelination patterns in preterm neonates using T2-weighted MRI. *Sci Rep*. 2019;9(1):12938. <https://doi.org/10.1038/s41598-019-49350-3>.
 71. Lye TC, Shores EA. Traumatic brain injury as a risk factor for Alzheimer's disease: a review. *Neuropsychol Rev*. 2000;10(2):115–29. <https://doi.org/10.1023/a:1009068804787>.
 72. Van Den Heuvel C, Thornton E, Vink R. Traumatic brain injury and Alzheimer's disease: a review. *Prog Brain Res*. 2007;161:303–16. [https://doi.org/10.1016/S0079-6123\(06\)61021-2](https://doi.org/10.1016/S0079-6123(06)61021-2).
 73. Azouvi P, Arnould A, Dromer E, Vallat-Azouvi C. Neuropsychology of traumatic brain injury: an expert overview. *Rev Neurol (Paris)*. 2017;173(7-8):461–72. <https://doi.org/10.1016/j.neurol.2017.07.006>.
 74. Wang B, Liu W, Prastawa M, Irimia A, Vespa PM, van Horn JD, et al. 4d active cut: an interactive tool for pathological anatomy modeling. *Proc IEEE Int Symp Biomed Imaging*. 2014;2014:529–32. <https://doi.org/10.1109/ISBI.2014.6867925>.
 75. Rutgers DR, Toulgoat F, Cazejust J, Fillard P, Lasjaunias P, Ducreux D. White matter abnormalities in mild traumatic brain injury: a diffusion tensor imaging study. *AJNR Am J Neuroradiol*. 2008;29(3):514–9. <https://doi.org/10.3174/ajnr.A0856>.
 76. Lepage C, de Pierrefeu A, Koerte IK, Coleman MJ, Pasternak O, Grant G, et al. White matter abnormalities in mild traumatic brain injury with and without post-traumatic stress disorder: a subject-specific diffusion tensor imaging study. *Brain Imaging Behav*. 2018;12(3):870–81. <https://doi.org/10.1007/s11682-017-9744-5>.
 77. Parente DB, Gasparetto EL, da Cruz LC, Jr., Domingues RC, Baptista AC, Carvalho AC et al. Potential role of diffusion tensor MRI in the differential diagnosis of mild cognitive impairment and Alzheimer's disease. *AJR Am J Roentgenol*. 2008;190(5):1369–74. <https://doi.org/10.2214/AJR.07.2617>.
 78. Naggara O, Oppenheim C, Rieu D, Raoux N, Rodrigo S, Dalla Barba G, et al. Diffusion tensor imaging in early Alzheimer's disease. *Psychiatry Res*. 2006;146(3):243–9. <https://doi.org/10.1016/j.psychres.2006.01.005>.
 79. Hinkebein JH, Martin TA, Callahan CD, Johnstone B. Traumatic brain injury and Alzheimer's: deficit profile similarities and the impact of normal ageing. *Brain Inj*. 2003;17(12):1035–42. <https://doi.org/10.1080/0269905031000110490>.
 80. Dall'Acqua P, Johannes S, Mica L, Simmen HP, Glaab R, Fandino J, et al. Functional and structural network recovery after mild traumatic brain injury: a 1-year longitudinal study. *Front Hum Neurosci*. 2017;11:280. <https://doi.org/10.3389/fnhum.2017.00280>.
 81. Perry RJ, Hodges JR. Attention and executive deficits in Alzheimer's disease. A critical review. *Brain*. 1999;122(Pt 3):383–404. <https://doi.org/10.1093/brain/122.3.383>.
 82. McDonald BC, Saykin AJ, McAllister TW. Functional MRI of mild traumatic brain injury (mTBI): progress and perspectives from the first decade of studies. *Brain Imaging Behav*. 2012;6(2):193–207. <https://doi.org/10.1007/s11682-012-9173-4>.
 83. Cazalis F, Babikian T, Giza C, Copeland S, Hovda D, Asamow RF. Pivotal role of anterior cingulate cortex in working memory after traumatic brain injury in youth. *Front Neurol*. 2011;1:158. <https://doi.org/10.3389/fneur.2010.00158>.
 84. Porcelli S, Van Der Wee N, van der Werff S, Aghajani M, Glennon JC, van Heukelum S, et al. Social brain, social dysfunction and social withdrawal. *Neurosci Biobehav Rev*. 2019;97:10–33. <https://doi.org/10.1016/j.neubiorev.2018.09.012>.
 85. Lalonde G, Bernier A, Beaudoin C, Gravel J, Beauchamp MH. Investigating social functioning after early mild TBI: the quality of parent-child interactions. *J Neuropsychol*. 2018;12(1):1–22. <https://doi.org/10.1111/jnp.12104>.
 86. Temkin NR, Corrigan JD, Dikmen SS, Machamer J. Social functioning after traumatic brain injury. *J Head Trauma Rehabil*. 2009;24(6):460–7. <https://doi.org/10.1097/HTR.0b013e3181c13413>.
 87. Gomez-Hernandez R, Max JE, Kosier T, Paradiso S, Robinson RG. Social impairment and depression after traumatic brain injury. *Arch Phys Med Rehabil*. 1997;78(12):1321–6. [https://doi.org/10.1016/S0003-9993\(97\)90304-x](https://doi.org/10.1016/S0003-9993(97)90304-x).
 88. Bediou B, Ryff I, Mercier B, Milliere M, Henaff MA, D'Amato T, et al. Impaired social cognition in mild Alzheimer disease. *J Geriatr Psychiatry Neurol*.

- 2009;22(2):130–40. <https://doi.org/10.1177/0891988709332939>.
89. Gilmour G, Porcelli S, Bertaina-Anglade V, Arce E, Dukart J, Hayden A, et al. Relating constructs of attention and working memory to social withdrawal in Alzheimer's disease and schizophrenia: issues regarding paradigm selection. *Neurosci Biobehav Rev*. 2019;97:47–69. <https://doi.org/10.1016/j.neubiorev.2018.09.025>.
 90. Calvillo M, Irimia A. Neuroimaging and psychometric assessment of mild cognitive impairment after traumatic brain injury. *Front Psychol*. 2020;11:1423. <https://doi.org/10.3389/fpsyg.2020.01423>.
 91. Shaver TK, Ozga JE, Zhu B, Anderson KG, Martens KM, Vonder HC. Long-term deficits in risky decision-making after traumatic brain injury on a rat analog of the Iowa gambling task. *Brain Res*. 1704;2019:103–13. <https://doi.org/10.1016/j.brainres.2018.10.004>.
 92. Ozga-Hess JE, Whirtley C, O'Hearn C, Pechacek K, Vonder HC. Unilateral parietal brain injury increases risk-taking on a rat gambling task. *Exp Neurol*. 2020;327:113217. <https://doi.org/10.1016/j.expneurol.2020.113217>.
 93. Cotrena C, Branco LD, Zimmermann N, Cardoso CO, Grassi-Oliveira R, Fonseca RP. Impaired decision-making after traumatic brain injury: the Iowa Gambling Task. *Brain Inj*. 2014;28(8):1070–5. <https://doi.org/10.3109/02699052.2014.896943>.
 94. Levin HS, Wilde E, Troyanskaya M, Petersen NJ, Scheibel R, Newsome M, et al. Diffusion tensor imaging of mild to moderate blast-related traumatic brain injury and its sequelae. *J Neurotrauma*. 2010;27(4):683–94. <https://doi.org/10.1089/neu.2009.1073>.
 95. Sinha S, Tiwari SC, Shah S, Singh P, Tripathi SM, Pandey N, et al. Neural bases of impaired decision making process in Alzheimer's disease. *Society of Applied Neurosciences 2016; 6 Oct - 9 Oct. Corfu, Greece: Frontiers*; 2016.
 96. Niogi SN, Mukherjee P, Ghajar J, Johnson C, Kolster RA, Sarkar R, et al. Extent of microstructural white matter injury in postconcussive syndrome correlates with impaired cognitive reaction time: a 3T diffusion tensor imaging study of mild traumatic brain injury. *AJNR Am J Neuroradiol*. 2008;29(5):967–73. <https://doi.org/10.3174/ajnr.A0970>.
 97. Yin B, Li DD, Huang H, Gu CH, Bai GH, Hu LX, et al. Longitudinal changes in diffusion tensor imaging following mild traumatic brain injury and correlation with outcome. *Front Neural Circuits*. 2019;13:28. <https://doi.org/10.3389/fncir.2019.00028>.
 98. Alhilali LM, Yaeger K, Collins M, Fakhra S. Detection of central white matter injury underlying vestibulopathy after mild traumatic brain injury. *Radiology*. 2014;272(1):224–32. <https://doi.org/10.1148/radiol.14132670>.
 99. Duering M, Gesierich B, Seiler S, Pirpamer L, Gonik M, Hofer E, et al. Strategic white matter tracts for processing speed deficits in age-related small vessel disease. *Neurology*. 2014;82(22):1946–50. <https://doi.org/10.1212/WNL.0000000000000475>.
 100. McInnes K, Friesen CL, MacKenzie DE, Westwood DA, Boe SG. Mild traumatic brain injury (mTBI) and chronic cognitive impairment: a scoping review. *PLoS One*. 2017;12(4):e0174847. <https://doi.org/10.1371/journal.pone.0174847>.
 101. Konrad C, Geburek AJ, Rist F, Blumenroth H, Fischer B, Husstedt I, et al. Long-term cognitive and emotional consequences of mild traumatic brain injury. *Psychol Med*. 2011;41(6):1197–211. <https://doi.org/10.1017/S0033297170001728>.
 102. Johansson B, Andrell P, Ronnback L, Mannheimer C. Follow-up after 5.5 years of treatment with methylphenidate for mental fatigue and cognitive function after a mild traumatic brain injury. *Brain Inj*. 2020;34(2):229–35. <https://doi.org/10.1080/02699052.2019.1683898>.
 103. Mathias JL, Beall JA, Bigler ED. Neuropsychological and information processing deficits following mild traumatic brain injury. *J Int Neuropsychol Soc*. 2004;10(2):286–97. <https://doi.org/10.1017/S1355617704102117>.
 104. Jonasson A, Levin C, Renfors M, Strandberg S, Johansson B. Mental fatigue and impaired cognitive function after an acquired brain injury. *Brain Behav*. 2018;8(8):e01056. <https://doi.org/10.1002/brb3.1056>.
 105. Belmont A, Agar N, Azouvi P. Subjective fatigue, mental effort, and attention deficits after severe traumatic brain injury. *Neurorehabil Neural Repair*. 2009;23(9):939–44. <https://doi.org/10.1177/1545968309340327>.
 106. Ziino C, Ponsford J. Selective attention deficits and subjective fatigue following traumatic brain injury. *Neuropsychology*. 2006;20(3):383–90. <https://doi.org/10.1037/0894-4105.20.3.383>.
 107. Hillary FG, Genova HM, Medaglia JD, Fitzpatrick NM, Chiou KS, Wardecker BM, et al. The nature of processing speed deficits in traumatic brain injury: is less brain more? *Brain Imaging Behav*. 2010;4(2):141–54. <https://doi.org/10.1007/s11682-010-9094-z>.
 108. Nestor PG, Parasuraman R, Haxby JV. Speed of information processing and attention in early Alzheimer's dementia. *Dev Neuropsychol*. 2009;7(2):243–56. <https://doi.org/10.1080/87565649109540491>.
 109. Warkentin S, Erikson C, Janciauskiene S. rCBF pathology in Alzheimer's disease is associated with slow processing speed. *Neuropsychologia*. 2008;46(5):1193–200. <https://doi.org/10.1016/j.neuropsychologia.2007.08.029>.
 110. Croall ID, Cowie CJ, He J, Peel A, Wood J, Aribisala BS, et al. White matter correlates of cognitive dysfunction after mild traumatic brain injury. *Neurology*. 2014;83(6):494–501. <https://doi.org/10.1212/WNL.0000000000000666>.
 111. Kircher T, Nagels A, Kirner-Veselinovic A, Krach S. Neural correlates of rhyming vs. lexical and semantic fluency. *Brain Res*. 2011;1391:71–80. <https://doi.org/10.1016/j.brainres.2011.03.054>.
 112. Paek EJ, Murray LL, Newman SD. Neural correlates of verb fluency performance in cognitively healthy older adults and individuals with dementia: a pilot fMRI study. *Front Aging Neurosci*. 2020;12:73. <https://doi.org/10.3389/fnagi.2020.00073>.
 113. Kave G, Heled E, Vakil E, Agranov E. Which verbal fluency measure is most useful in demonstrating executive deficits after traumatic brain injury? *J Clin Exp Neuropsychol*. 2011;33(3):358–65. <https://doi.org/10.1080/13803395.2010.518703>.
 114. Henry JD, Crawford JR. A meta-analytic review of verbal fluency performance in patients with traumatic brain injury. *Neuropsychology*. 2004;18(4):621–8. <https://doi.org/10.1037/0894-4105.18.4.621>.

115. Mathias JL, Coats JL. Emotional and cognitive sequelae to mild traumatic brain injury. *J Clin Exp Neuropsychol.* 1999;21(2):200–15. <https://doi.org/10.1076/jcen.21.2.200.930>.
116. Voller B, Benke T, Benedetto K, Schnider P, Auff E, Aichner F. Neuropsychological, MRI and EEG findings after very mild traumatic brain injury. *Brain Inj.* 1999;13(10):821–7. <https://doi.org/10.1080/026990599121214>.
117. Henry JD, Crawford JR, Phillips LH. Verbal fluency performance in dementia of the Alzheimer's type: a meta-analysis. *Neuropsychologia.* 2004;42(9):1212–22. <https://doi.org/10.1016/j.neuropsychologia.2004.02.001>.
118. Kljajevic V. Verbal fluency and intrinsic brain activity in Alzheimer's disease. *Croat Med J.* 2015;56(6):573–7. <https://doi.org/10.3325/cmj.2015.56.573>.
119. Melrose RJ, Campa OM, Harwood DG, Osato S, Mandelkern MA, Sultzer DL. The neural correlates of naming and fluency deficits in Alzheimer's disease: an FDG-PET study. *Int J Geriatr Psychiatry.* 2009;24(8):885–93. <https://doi.org/10.1002/gps.2229>.
120. Brun A, Englund E. Regional pattern of degeneration in Alzheimer's disease: neuronal loss and histopathological grading. *Histopathology.* 1981;5(5):549–64. <https://doi.org/10.1111/j.1365-2559.1981.tb01818.x>.
121. Collette F, Van der Linden M, Salmon E. Executive dysfunction in Alzheimer's disease. *Cortex.* 1999;35(1):57–72. [https://doi.org/10.1016/s0010-9452\(08\)70785-8](https://doi.org/10.1016/s0010-9452(08)70785-8).
122. Guarino A, Favieri F, Boncompagni I, Agostini F, Cantone M, Casagrande M. Executive functions in Alzheimer Disease: a systematic review. *Front Aging Neurosci.* 2018;10:437. <https://doi.org/10.3389/fnagi.2018.00437>.
123. Ozga JE, Povroznik JM, Engler-Chiurazzi EB, Vonder HC. Executive (dys)function after traumatic brain injury: special considerations for behavioral pharmacology. *Behav Pharmacol.* 2018;29(7):617–37. <https://doi.org/10.1097/FBP.0000000000000430>.
124. Cossette I, Gagne ME, Ouellet MC, Fait P, Gagnon I, Sirois K, et al. Executive dysfunction following a mild traumatic brain injury revealed in early adolescence with locomotor-cognitive dual-tasks. *Brain Inj.* 2016;30(13-14):1648–55. <https://doi.org/10.1080/02699052.2016.1200143>.
125. Miles L, Grossman RI, Johnson G, Babb JS, Diller L, Inglesse M. Short-term DTI predictors of cognitive dysfunction in mild traumatic brain injury. *Brain Inj.* 2008;22(2):115–22. <https://doi.org/10.1080/02699050801888816>.
126. Shum D, Gill H, Banks M, Maujean A, Griffin J, Ward H. Planning ability following moderate to severe traumatic brain injury: performance on a 4-disk version of the Tower of London. *Brain Impairment.* 2009;10(3):320–4. <https://doi.org/10.1375/brim.10.3.320>.
127. Brooks J, Fos LA, Greve KW, Hammond JS. Assessment of executive function in patients with mild traumatic brain injury. *J Trauma.* 1999;46(1):159–63. <https://doi.org/10.1097/00005373-199901000-00027>.
128. Lange KW, Sahakian BJ, Quinn NP, Marsden CD, Robbins TW. Comparison of executive and visuospatial memory function in Huntington's disease and dementia of Alzheimer type matched for degree of dementia. *J Neurol Neurosurg Psychiatry.* 1995;58(5):598–606. <https://doi.org/10.1136/jnmp.58.5.598>.
129. Satler C, Guimaraes L, Tomaz C. Planning ability impairments in probable Alzheimer's disease patients: evidence from the Tower of London test. *Dement Neuropsychol.* 2017;11(2):137–44. <https://doi.org/10.1590/1980-57642016dn11-020006>.
130. Mack JL, Patterson MB. Executive dysfunction and Alzheimer's disease: performance on a test of planning ability, the Porteus Maze Test. *Neuropsychology.* 1995;9(4):556–64. <https://doi.org/10.1037/0894-4105.9.4.556>.
131. Marco EJ, Harrell KM, Brown WS, Hill SS, Jeremy RJ, Kramer JH, et al. Processing speed delays contribute to executive function deficits in individuals with agenesis of the corpus callosum. *J Int Neuropsychol Soc.* 2012;18(3):521–9. <https://doi.org/10.1017/S1355617712000045>.
132. Hinkley LB, Marco EJ, Findlay AM, Honma S, Jeremy RJ, Strominger Z, et al. The role of corpus callosum development in functional connectivity and cognitive processing. *PLoS One.* 2012;7(8):e39804. <https://doi.org/10.1371/journal.pone.0039804>.
133. Shin G, Kim C. Neural correlates of cognitive style and flexible cognitive control. *Neuroimage.* 2015;113:78–85. <https://doi.org/10.1016/j.neuroimage.2015.03.046>.
134. Leunissen I, Coxon JP, Caeyenberghs K, Michiels K, Snaert S, Swinnen SP. Subcortical volume analysis in traumatic brain injury: the importance of the fronto-striato-thalamic circuit in task switching. *Cortex.* 2014;51:67–81. <https://doi.org/10.1016/j.cortex.2013.10.009>.
135. Hawley C, Sakr M, Scapinello S, Salvo J, Wrenn P. Traumatic brain injuries in older adults—6 years of data for one UK trauma centre: retrospective analysis of prospectively collected data. *Emerg Med J.* 2017;34(8):509–16. <https://doi.org/10.1136/emered-2016-206506>.
136. Mosenthal AC, Livingston DH, Lavery RF, Knudson MM, Lee S, Morabito D, et al. The effect of age on functional outcome in mild traumatic brain injury: 6-month report of a prospective multicenter trial. *J Trauma.* 2004;56(5):1042–8. <https://doi.org/10.1097/01.ta.0000127767.83267.33>.
137. Centers for Disease Control and Prevention. Trends in aging—United States and worldwide. *MMWR Morb Mortal Wkly Rep.* 2003;52(6):101–4, 6.
138. Thompson HJ, Dikmen S, Temkin N. Prevalence of comorbidity and its association with traumatic brain injury and outcomes in older adults. *Res Gerontol Nurs.* 2012;5(1):17–24. <https://doi.org/10.3928/19404921-20111206-02>.
139. Burgmans S, van Boxtel MP, Gronenschild EH, Vuurman EF, Hofman P, Uylings HB, et al. Multiple indicators of age-related differences in cerebral white matter and the modifying effects of hypertension. *Neuroimage.* 2010;49(3):2083–93. <https://doi.org/10.1016/j.neuroimage.2009.10.035>.
140. Liu JY, Zhou YJ, Zhai FF, Han F, Zhou LX, Ni J, et al. Cerebral microbleeds are associated with loss of white matter integrity. *AJNR Am J Neuroradiol.* 2020;41(8):1397–404. <https://doi.org/10.3174/ajnr.A6622>.
141. Iscan Z, Jin TB, Kendrick A, Szeplin B, Lu H, Trivedi M, et al. Test-retest reliability of freesurfer measurements within and between sites: effects of visual approval process.

- Human Brain Mapping. 2015;36(9):3472–85. <https://doi.org/10.1002/hbm.22856>.
142. Irimia A, Van Horn JD, Vespa PM. Cerebral microhemorrhages due to traumatic brain injury and their effects on the aging human brain. *Neurobiology of Aging*. 2018;66:158–64.
143. Oishi K, Zilles K, Amunts K, Faria A, Jiang H, Li X, et al. Human brain white matter atlas: identification and assignment of common anatomical structures in superficial white matter. *Neuroimage*. 2008;43(3):447–57. <https://doi.org/10.1016/j.neuroimage.2008.07.009>.
144. Fortin JP, Cullen N, Sheline YI, Taylor WD, Aselcioglu I, Cook PA, et al. Harmonization of cortical thickness measurements across scanners and sites. *Neuroimage*. 2018;167:104–20. <https://doi.org/10.1016/j.neuroimage.2017.11.024>.
145. Fortin JP, Parker D, Tunc B, Watanabe T, Elliott MA, Ruparel K, et al. Harmonization of multi-site diffusion tensor imaging data. *Neuroimage*. 2017;161:149–70. <https://doi.org/10.1016/j.neuroimage.2017.08.047>.
146. Johnson WE, Li C, Rabinovic A. Adjusting batch effects in microarray expression data using empirical Bayes methods. *Biostatistics*. 2007;8(1):118–27. <https://doi.org/10.1093/biostatistics/kxj037>.

Publisher's note Springer Nature remains neutral with regard to jurisdictional claims in published maps and institutional affiliations.



Tractography methods and findings in brain tumors and traumatic brain injury



Fang-Cheng Yeh^{a,b,*}, Andrei Irimia^{c,d}, Dhiego Chaves de Almeida Bastos^e, Alexandra J. Golby^{e,f}

^a Department of Neurological Surgery, University of Pittsburgh Medical Center, Pittsburgh, Pennsylvania, USA

^b Department of Bioengineering, University of Pittsburgh, Pittsburgh, Pennsylvania, USA

^c Ethel Percy Andrus Gerontology Center, Leonard Davis School of Gerontology, University of Southern California, Los Angeles, California, USA

^d Corwin D. Denney Research Center, Department of Biomedical Engineering, Viterbi School of Engineering, University of Southern California, Los Angeles, California, USA

^e Department of Neurosurgery, Brigham and Women's Hospital, Harvard Medical School, Boston, Massachusetts, USA

^f Department of Radiology, Brigham and Women's Hospital, Harvard Medical School, Boston, Massachusetts, USA

ARTICLE INFO

Keywords:

Diffusion MRI
fiber tracking
tractography
brain tumor
glioma
traumatic brain injury

ABSTRACT

White matter fiber tracking using diffusion magnetic resonance imaging (dMRI) provides a noninvasive approach to map brain connections, but improving anatomical accuracy has been a significant challenge since the birth of tractography methods. Utilizing tractography in brain studies therefore requires understanding of its technical limitations to avoid shortcomings and pitfalls. This review explores tractography limitations and how different white matter pathways pose different challenges to fiber tracking methodologies. We summarize the pros and cons of commonly-used methods, aiming to inform how tractography and its related analysis may lead to questionable results. Extending these experiences, we review the clinical utilization of tractography in patients with brain tumors and traumatic brain injury, starting from tensor-based tractography to more advanced methods. We discuss current limitations and highlight novel approaches in the context of these two conditions to inform future tractography developments.

1. Introduction

Diffusion magnetic resonance imaging (dMRI) fiber tracking (Basser et al., 2000; Mori et al., 1999) has been available to the neuroscience community for two decades and remains the only non-invasive way to systematically map white matter tracts in the human brain (Craddock et al., 2013). Since their inception, fiber tracking approaches have been leveraged as powerful tools to understand the circuit mechanisms behind normal and abnormal brain functions (Behrens et al., 2003a; Schmahmann et al., 2007). The region-to-region connectivity mapped by tractography facilitates the inference of the *structural connectome* to elucidate brain network topology (Sporns et al., 2005) and inform how brain connectivity patterns contribute to brain functions. Although widely used in neuroscience research, fiber tracking has yet to acquire widespread clinical utility for neurological disorders. The primary limitation against such a more comprehensive application is that utilizing and interpreting tractography requires a substantial understanding of brain architecture (Schilling et al., 2020) and the tractography method (O'Donnell and Pasternak, 2014). These factors are essential because tractography can yield false positive and false nega-

tive results (Kupper et al., 2015; Maier-Hein et al., 2017; Thomas et al., 2014).

The purpose of this review is to provide background for an audience with neuroimaging backgrounds aiming to acquire essential knowledge on tractography to investigate brain conditions involving gross pathologies, such as brain tumors and traumatic brain injuries (TBIs). Sections are presented in the following order to provide the information we deem essential. First, with histology images, we highlight the challenges of fiber tracking in various brain regions. Second, we provide an overview of dMRI acquisition, modeling methods, and fiber tracking algorithms and discuss their relative strengths and weaknesses. Instead of providing a glimpse into all methods, we focus on a subset of methods and compare them in depth. Finally, we discuss tractography applications to brain tumors and TBI and outline the prospects of novel tractography modalities as tools for exploring and understanding brain diseases.

It is noteworthy that there are several terminology conventions used in tractography to describe brain connections. Here and throughout, *tract* refers to macroscopic white matter pathways, such as the corticospinal tract and other white matter tracts. By contrast, *track* (or *streamline*) refers to the inferred trajectories of underlying tracts, as calculated

* Corresponding author at: Department of Neurological Surgery, UPMC Presbyterian, Suite B-400, 200 Lothrop Street, Pittsburgh, PA, 15213, USA.
E-mail address: frank.yeh@pitt.edu (F.-C. Yeh).

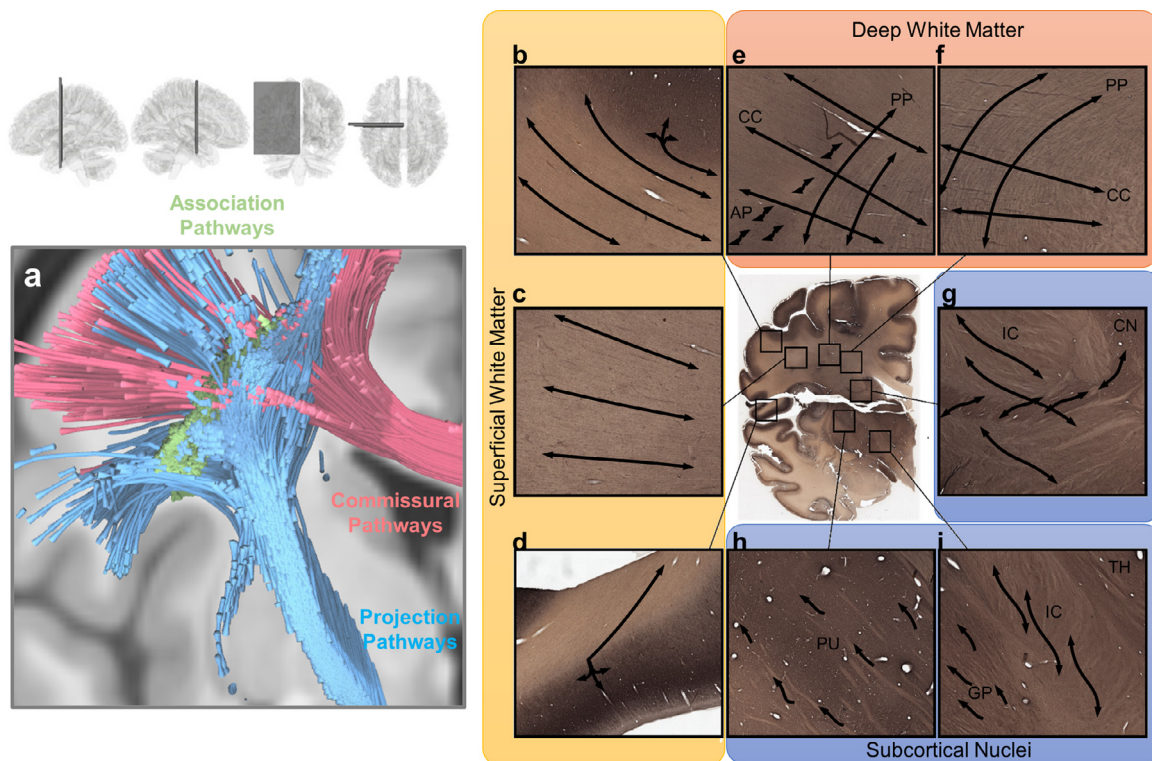


Fig. 1. Visualization of white matter pathways in the human brain and of challenges in mapping them across various white matter regions. (a) Brain pathways can be categorized into association pathways (green), projection pathways (blue), and commissural pathways (red). Mapping these pathways involves different challenges in different brain regions. (b), (c) and (d) show gyral blades in the superficial white matter on an immunohistochemistry section of a 34-year-old human brain. Connections with abrupt turning angles are often ignored in fiber tracking, leading to bias in tractography. (e) and (f) show deep white matter where corpus callosum (CC) bundles intersect projection pathways (PP) or association pathways (AP), demonstrating the challenge of mapping crossing tracts. (g), (h) and (i) show the white matter around subcortical nuclei. (g) enlarged view of the internal capsule (IC) and caudate nuclei (CN). The connections from caudate nuclei are small pathways, and mapping them requires higher angular and spatial resolution. (h) shows the putamen (PU), whereas (i) shows the boundary between the globus pallidus (GP), internal capsule (IC), and thalamus (TH). The fibers within the basal ganglia are often undetectable in dMRI due to the heavy T_2 -weighting caused by iron complex deposition.

by a fiber-tracking algorithm; such tracks include *spurious tracks*, which are colloquially referred to as *false tracks*. *Fiber* refers to a tract population within a voxel, where each population is oriented in a distinctly different direction. The term is used in expressions such as *crossing fibers*, which describes two or more tracts at a voxel, or *fiber resolving methods*, which refer to methods that resolve local white matter tract orientations at each voxel.

2. Challenges in mapping brain pathways

Common tractography targets can be classified into the association, projection, and commissural pathways. As shown in Fig. 1a, the association pathways (green), such as the arcuate fasciculus and cingulum, constitute the superficial and deep white matter structures. The projection pathways (blue) are vertically projecting tracts connecting cortical regions to subcortical nuclei or brainstem regions. The commissural pathways (red), such as the corpus callosum, are connections between the left and right hemispheres. They often pass through the deep white matter and intersect with association and projection pathways. We further show histology images from a coronal section of the thalamus and basal ganglia in the BrainSpan reference atlas (<https://www.brainspan.org/>) (Miller et al., 2014) to illustrate the challenges in mapping white matter tracts. Fig. 1b-i are parvalbumin-labeled immunohistology, which present line strips in the white matter to reveal fiber bundles' gross orientations. The superficial white matter, deep white matter, and subcortical nuclei pose three distinct challenges to fiber tracking:

2.1. Gyral bias

The first challenge is the *gyral bias* of tractography at the superficial white matter (Reveley et al., 2015; Schilling et al., 2018a). As shown in Fig. 1b-d, superficial white matter comprises *gyral blades*, which are bulging structures with fanning fibers aggregated into bundles (Cottaar et al., 2020). In this region, most fiber tracking algorithms, including probabilistic and deterministic, tend to track the least turning trajectories to the gyral tip (e.g., the left three trajectories in Fig. 1b) and ignore those with an abrupt turning to the sulcal bank (e.g., the turning trajectories in the right-upper corner in Fig. 1b). This least-turning preference avoids an abrupt turning that will produce considerable false turning in other white matter regions. However, in the superficial white matter, the resulting tractography only visualizes connections toward the gyral tip while ignoring many others along sulcal banks, leading to the false-negative mapping of the superficial pathways.

2.2. Crossing, turning, branching, and fanning structures

The second challenge of tractography occurs in the deep white matter (Fig. 1e and f), where tract bundles from different brain regions meet and intersect. The challenge here is to resolve the crossing, turning, branching, and fanning architectures formed by these pathways (Grisot et al., 2021). Many of them coexist within a white matter region, and thus resolving all of them could be a challenge. For example, fiber tracking methods may fail to capture the lateral fanning branches of the corpus callosum or projection pathways due to their relatively small sizes in this fiber crossing region (Reveley et al., 2015). The deep

white matter region in Fig. 1e and f, known as the *centrum semiovale* (CS), has three sets of pathways intersecting in a grid-like structure (Wedeen et al., 2012). The association pathways (as shown by label AP in the figure) such as the super longitudinal and arcuate fasciculi are often located laterally relative to projection pathways. More medially, there are vertically-oriented projection pathways (PP) such as the corticospinal and corticothalamic tracts. Those pathways have lateral branches forming branching and fanning architectures that also intersect the association pathways. The corpus callosum (CC) bridges the two hemispheres and crosses both the projection and association pathways. Fig. 1e shows the intersection of these pathways. The corpus callosum passes across the entire region, whereas projection pathways are oriented vertically; the association pathways (AP) have tracts oriented along the anterior-posterior (through-slice) axis. Much of the crossing geometry involves sharp crossing angles, and diffusion modeling methods may only resolve one fiber and miss others. Consequently, a tracking algorithm may only map a portion of the white matter connections and yield false-negative results in the deep white matter regions.

2.3. Subcortical nuclei

The third challenge of tractography involves white matter structures around subcortical nuclei (Fig. 1g-i), which are *hubs* of brain networks. Fig. 1g shows the caudate nuclei (CN) and internal capsule (IC). The large tracts in the internal capsule are intertwined with small connections between the caudate nuclei and the basal ganglia. Tracking these small tracts between large projection bundles around subcortical nuclei would require higher spatial resolution acquisitions. Fig. 1h and i further zoom in to the basal ganglia, including the putamen (PU) (Fig. 1h) and globus pallidus (GP) (Fig. 1i). The architecture of the basal ganglia features neuronal clusters enmeshed within white matter structures. Iron deposition in the basal ganglia introduces heavy T_2 -weighting into dMRI. Consequently, these regions yield low diffusion-weighted signals due to T_2 shine-through, and fiber orientations cannot be resolved. Tracking projection pathways down into the brainstem (not shown here) also has challenges due to limited spatial resolution, phase distortion, and related signal loss around the air space of the skull base (Sclocco et al., 2018). Among the above-mentioned brain regions, the subcortical nuclei and brain stem pose the most significant challenges to fiber tracking due to their complex fiber architecture and low dMRI signal quality.

3. Tractography methods—an overview

Tractography pipeline workflows can be divided into multiple steps, including preprocessing, fiber resolving, fiber tracking, and post-tracking processing (Fig. 2). The first step starts with preprocessing the diffusion-weighted images and proceeds with resolving fiber orientation(s) for each voxel. At the beginning of the pipeline, the images are often preprocessed to reduce eddy current distortion and phase distortion artifacts as well as other signal quality problems. Additional noise reduction or signal corrections can be conducted to improve the quality further. The acquisition optimization and preprocessing strategies are discussed in Section 4. After preprocessing, diffusion-weighted images and their associated *b-table* can be modeled using various fiber resolving methods to reconstruct one or multiple fiber orientations at each imaging voxel. There are various methods to resolve fibers, and they are discussed in Section 5. The results of this step empower fiber tracking algorithms to produce track trajectories that can be visualized using tractograms (see Section 6). Trajectories obtained via fiber tracking can be post-processed to generate clusters/bundles, discard unsatisfactory results, or classify clusters and bundles neuroanatomically. Fig. 2b shows a popularity survey of publicly available tractography tools or pipelines based on Google Scholar search results. The differences between these tools can be classified based on their fiber resolving and fiber tracking approaches, as listed in Fig. 2a.

4. Diffusion MRI acquisitions

The dMRI data are collected using diffusion-sensitization sequences (Stejskal and Tanner, 1965; Wu and Miller, 2017), such that the acquired signals are sensitive to the microscopic diffusion movements of water. The diffusion sensitization is achieved by adding one or more *diffusion sensitization gradients*, or simply *diffusion gradients*, to the pulse sequence. The diffusion gradients are added to the spin dephasing and rephasing stages of a spin-echo or a stimulated-echo sequence. Thus any spin diffusion parallel to the gradient directions will decrease MR signals by interfering with the dephasing and rephasing process. The orientation of the gradients is called *b-vector*, whereas the strength of ensemble diffusion sensitization is quantified by *b-value*, a collective product of diffusion time, diffusion gradient duration, and diffusion gradient magnitude. The MR signals without diffusion sensitization are thus called the b_0 signals, whereas the signals with diffusion sensitization will have attenuation due to diffusion. Faster diffusion or higher diffusion sensitization leads to more signal attenuation, whereas slower diffusion or lower diffusion sensitization retains more signal intensity. The signal attenuation at different directions provides the critical information to probe into the microscopic characteristics of the scanned tissue. In clinical applications, the optimization of a diffusion sequence considers scanning time, *b-value*, diffusion sampling scheme, distortions, and artifacts. We discuss each of them in the following:

4.1. Scanning time

The scanning time is a significant consideration in clinical applications. Diffusion MRI used to take a much longer scanning time than other MR modalities due to the need to acquire data at multiple diffusion directions. The development of simultaneous multi-slice acquisitions (Breuer et al., 2005; Setsompop et al., 2012a; Setsompop et al., 2012b) have allowed for reducing the scanning time by 2 to 4 folds. The shorter scanning time allows for more diffusion sampling directions, better slices coverage, or spatial resolution. For scanning patient populations, simultaneous multi-slice acquisition is a critical technique to reduce the scanning time. Ideally, a clinical study would limit dMRI acquisition to around 10 minutes. A shorter acquisition also reduces motion and signal quality issues associated with long scanning time.

Although simultaneous multi-slice acquisitions are practical solutions to reduce the scanning time, an under-recognized issue is the increased T_1 shine-through due to the reduced repetition time (TR). As more methods are introduced to achieve a higher acceleration factor, the reduced repetition time may eventually introduce substantial T_1 shine-through that decreases the diffusion signal. Pathological conditions that induce large T_1 -weighting will further cause unexpected bias in diffusion-weighted images.

Besides using simultaneous multi-slice acquisitions, another strategy to reduce scanning time is to reduce the number of slices at the cerebellum. For the imaging brainstem or thalamus, the dMRI data can be acquired using fewer sagittal slices that cover only the targeted brain regions. Nonetheless, reducing the slices number also reduces TR and possibly introduces T_1 shine-through issue mentioned above.

4.2. B-value

The second consideration in diffusion MRI acquisition is the *b-value*, which determines the diffusion contrast at different diffusion directions. The diffusion contrast enables a modeling method to resolve principle diffusion directions as fiber orientations. A higher diffusion sensitization will lead to higher diffusion contrast but will also have more signal decrease. A lower diffusion sensitization will retain the signal intensity but may not generate enough diffusion contrast to model the diffusion patterns. Recent studies have suggested the benefit of a high *b-value* in sensing restricted diffusion and resolving complex axonal architectures

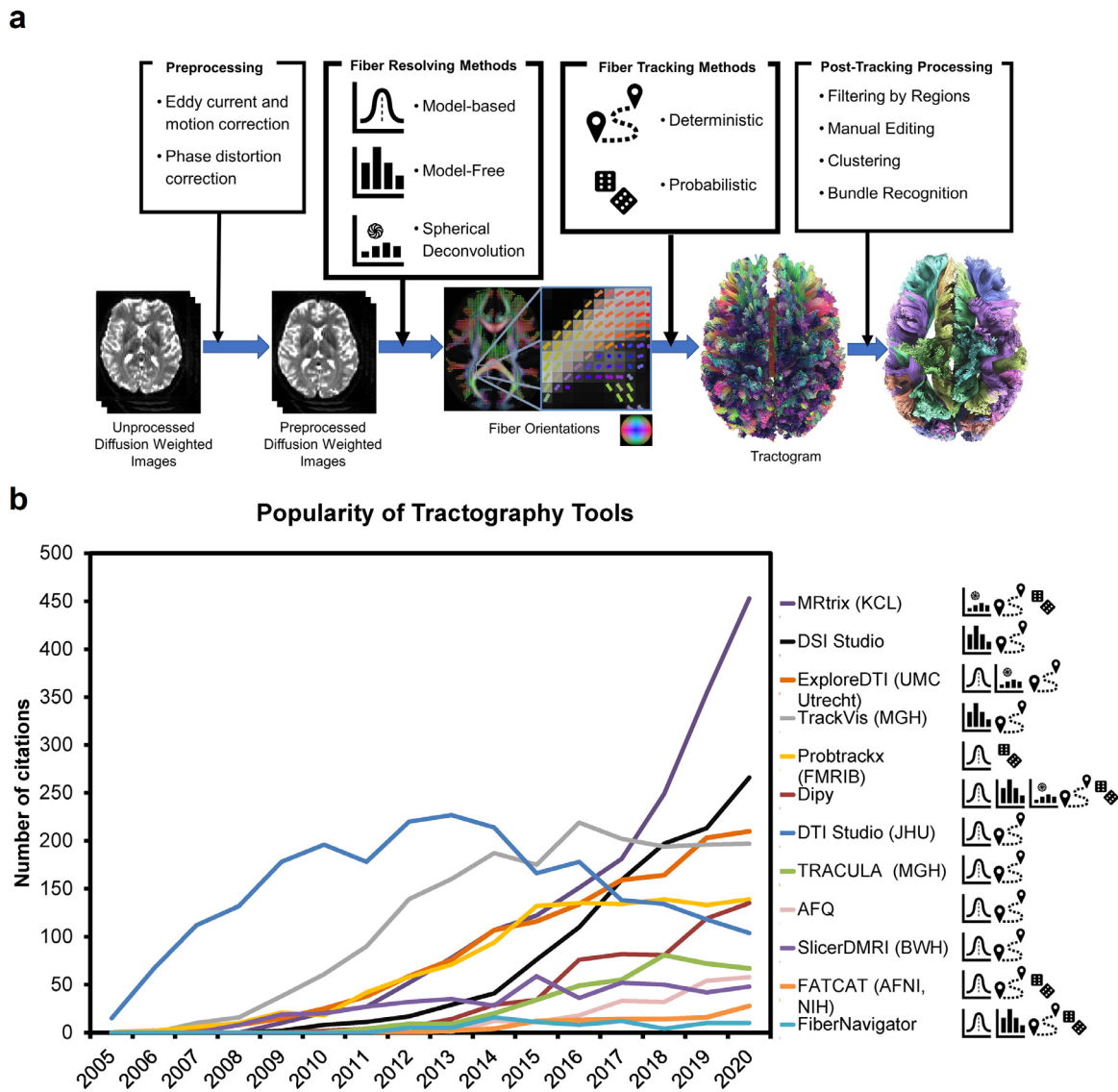


Fig. 2. Overview of tractography pipelines. (a) shows the snapshot of a typical tractography pipeline. The raw diffusion-weighted images are often preprocessed to remove eddy current and phase distortion artifacts or address other signal-related issues. The preprocessed images are then used to resolve fiber orientations and their associated diffusion metrics at each voxel. This information is then used by a fiber tracking method to produce tractograms for further post-processing. The tractogram can be color-coded by directional color (left-right: red anterior-posterior: green superior-inferior: blue) or by arbitrary colors after post-processing to visualize different bundles. (b) The popularity of publicly available tractography tools quantified by the number of Google Scholar search results from 2005 to 2020. The icons on the right label each tool’s methodological category (see (a) for the legend).

(Fan et al., 2014; Genc et al., 2020; Yeh et al., 2019). For clinical applications, a higher b-value can achieve a better sensitivity to early neuronal change. The optimal value depends on spatial resolution and any parameters that can affect the signal intensity. A way to determine whether the b-value is too high is to inspect the resulting diffusion-weighted image and examine whether the cortex contour is still visible. Currently, most studies limit the highest b-values below 5000 s/mm², as long as there are enough signals in the gray matter after diffusion sensitization.

4.3. Sampling scheme

A diffusion sampling scheme defines the combination of b-values and b-vectors used in the dMRI acquisition. Commonly used schemes include single-shell scheme, multi-shell scheme, and grid scheme. The naming is based on the spatial distribution of the diffusion gradients in the q-space, a gradient encoding space similar to k-space. The readout gradients encode the k-space signals, whereas the diffusion gradients

encode the q-space signals. Applying Fourier transform to the k-space signals will derive the spatial distribution of spins, whereas applying the inverted Fourier transform to the q-space signals will derive the displacement distribution of spin in the diffusion process. Each diffusion sampling scheme has its strength and weakness:

4.2.1. Single-shell scheme

The single-shell scheme acquires only one non-zero b-value at multiple diffusion directions, and thus the distribution of the diffusion gradients appears like a shell in the q-space. Examples of single-shell acquisitions include DTI acquisition and high angular resolution diffusion imaging (HARDI)(Tuch et al., 2002). Due to the single b-value used in the acquisition, the single-shell scheme is known for its limitation in differentiating different restricted diffusions, such as the hindered and restricted diffusion (Assaf and Basser, 2005; Assaf et al., 2004). Shell-like schemes densely sample *orientational* information to resolve fiber orientations, but it does not have enough *radial* information to resolve

Table 1
Diffusion schemes and their applicable methods.

	model-based methods						model-free methods				spherical deconvolution	
	tensor-based			beyond-tensor			DSI	QBI	GQI	MAP-MRI	CSD	MSMT-CSD
	DTI	BSM	FEW-DTI	multi-tensor	DKI	NODDI						
single-shell	x	x	x	x				x	x	x	x	
multi-shell	x	x	x	x	x	x		(x)*	x	x		x
grid	x	x	x	x	x	x	x		x	x		

x: applicable without resampling

*: only with constant solid angle QBI

DTI: diffusion tensor imaging, BSM: ball-and-sticks model, FEW-DTI: free water elimination DTI, DKI: diffusion kurtosis imaging, NODDI: neurite orientation dispersion and density imaging, CSD: constrained spherical deconvolution, MSMT-CSD: multi-shell multi-tissue CSD, DSI: diffusion spectrum imaging, QBI: q-ball imaging, GQI: generalized q-sampling imaging, MAP-MRI: Mean apparent propagator (MAP) MRI

different restricted diffusions. Methods based on single-shell acquisition are thus more susceptible to the partial volume of free diffusion caused by tissue edema, leading to possible false findings in tractography.

4.2.2. Multi-shell scheme

Multiple-shell acquisition addresses this limitation by acquiring 3~5 b-values with each b-value sampled at ~100 directions. The scheme thus presents multiple shells in the q-space and allows for differentiating different restricted diffusion. Examples include the hybrid diffusion imaging (Wu and Alexander, 2007) and the three-shell scheme used in the Human Connectome Project (Van Essen et al., 2012). Typically, low-b-value shells can be acquired by fewer sampling directions due to their lower diffusion contrast. The multi-shell acquisition will allow beyond-DTI methods to differentiate restricted diffusion and correlate with tissue characteristics.

4.2.3. Grid scheme

Still, some schemes do not use shell-like diffusion sampling. The grid scheme uses Cartesian sampling and is also known as q-space imaging (Callaghan, 1991). Similar to k-space imaging that usually samples MR signals at Cartesian locations, q-space imaging also samples at Cartesian points, and the scheme forms a grid sampling pattern. The resulting b-table often has 20~30 b-values with a total of 200~500 directions. The lowest non-zero b-value usually has only three directions, and the number of directions increases with the b-values. The multiple b-value setting of the grid scheme allows for fully characterizing a spectrum of restricted diffusion (Wedeen et al., 2005).

4.2.4. Choice of schemes

The choice between single-shell, multi-shell, and grid schemes largely depends on their applicable modeling methods. It is noteworthy that a scheme can work with many different modeling methods and vice versa. As listed in Table 1, the single-shell scheme, including the DTI dataset, can also be analyzed by other advanced methods, and similarly, an advanced scheme such as multi-shell or grid schemes can also be used by DTI. Single-shell schemes focus on *orientational* information because of their numerous sampling directions, but the single b-value setting does not have *radial* information to differentiate a spectrum of restricted diffusions. In comparison, a grid scheme focuses more on radial information by acquiring more than 10 b-values. The acquired data can be used to differentiate a spectrum of restricted diffusion. For clinical applications, the prevalence of pathological conditions would need multi-shell or grid schemes to characterize diffusion and correlate it with different pathological conditions.

4.4. Distortions and artifacts

Distortions and artifacts are common in dMRI acquisition because of the increased echo time to include the diffusion gradients. Commonly seen distortions and artifacts in dMRI include eddy current distortion

and susceptibility-induced distortion. Other signal issues include gradient nonlinearity and signal drift. Although correcting all of them is the goal, some corrections may require additional scanning time, while some may not be readily correctable. For cost-effectiveness, a compromise for clinical application would prioritize those with more significant effects.

4.4.1. Eddy current distortion

The most significant distortion in dMRI is caused by the eddy currents. The eddy current will interfere with the signal readout and generate a different shear distortion at each diffusion-weighted image. Its effect is global and readily visible on the anisotropy map or final tractography results, characterized by artificially high anisotropy and spurious fibers on the brain surface. Due to its wide-spreading effects across the brain regions, correcting eddy current distortion is always necessary and can be done by preprocessing or sequence design. FSL's *eddy* (FMRIB, Oxford)(Andersson and Sotiropoulos, 2016) is the most commonly used preprocessing approach for eddy current correction. It uses a Gaussian process to estimate the expected image (Andersson and Sotiropoulos, 2015) and calculate its transformation to the actual collected image. The correction is then achieved by inverting the distortion, and the process simultaneously handles additional rotation and translocation due to head motion.

Nonetheless, the Gaussian process in FSL's *eddy* needs sufficient data redundancy and only works on shell schemes. At a b-value of 1500 s/mm², at least 10~15 diffusion sampling directions are required to provide enough data redundancy (Andersson and Sotiropoulos, 2015), and higher b-values would need more sampling directions and scanning time to enable the correction. For data acquired by non-shell schemes or insufficient sampling directions, the correction can be achieved using bipolar diffusion gradients (Finsterbusch, 2009; Reese et al., 2003; Yang and McNab, 2019). These sequence-based eddy corrections may provide an alternative solution to cancel the eddy current and eliminate distortion. Some diffusion gradient designs (Aliotta et al., 2018) further achieved a shorter echo time to improve the signal performance.

4.4.2. Susceptibility-induced distortions and artifacts

Another prominent distortion in dMRI is the distortion and signal dropout caused by susceptibility-induced magnetic field gradients at the tissue junction. For echo-planar imaging, the susceptibility gradients parallel to the slice plane will cause geometric distortion, whereas the gradients perpendicular to the slice will cause signal dropout. The effects are most prominent at the prefrontal, orbitofrontal, and inferior temporal regions if the phase encoding direction is oriented at the anterior-posterior direction. Since the effect is more focal than global, some studies may ignore it as a compromise if their region of interest has no detectable distortion or signal dropout.

Correction can be achieved by FSL's *topup* (FMRIB, Oxford)(Andersson et al., 2003), a preprocessing approach that estimates

the distortion field to undo the effect through regularized optimization. The minimal requirement is an additional field map or an additional b_0 acquired at the opposite phase encoding direction. However, the induced distortion may not be fully restored at regions with a large susceptibility gradient, and the signal dropout can be uncorrectable. In such a condition, an effective strategy is to combine multi-shot EPI sequences (Butts et al., 1994; Holdsworth et al., 2008) to minimize susceptibility effects, while the residual distortion can be subsequently corrected by *topup*.

4.4.3. Other signal issues

Besides artifact and distortions mentioned above, other quality issues include gradient nonlinearity (Malyarenko et al., 2014; Tan et al., 2013), Gibbs ringing artifact (Perrone et al., 2015; Veraart et al., 2016), and signal drift (Hansen et al., 2019; Vos et al., 2017). Gibbs ringing is often deemed insignificant in dMRI because it is only visible at the sharp edge in high-resolution b_0 images. The effect caused by gradient nonlinearity is often close to the noise level in lower SNR acquisitions (Mesri et al., 2020), and not all modeling methods are significantly affected (Guo et al., 2021). Similarly, signal drift only affects up to 5% of the signals in a 15-min scan (Hansen et al., 2019; Vos et al., 2017). For scans that use a shorter scanning time, the effect is close to the noise level. Thus, these signal issues are not routinely corrected due to relatively insignificant effects on the diffusion metrics and tractography results.

4.5. Quality control

Quality control is a critical component in dMRI analysis because the diffusion contrast is generated by diffusion-induced signal attenuation. Signal loss due to quality issues can mimic diffusion signal attenuation and consequently lead to spurious tractography results. Despite correction approaches mentioned above, some data may be too corrupted to be correctable due to various acquisition issues, and not all scan data are suitable for processing. Thus, quality control for dMRI should include a screening step to identify and exclude uncorrectable data.

Several automated tools are available for quality control purposes (Bastiani et al., 2019; Cai et al., 2021; Cieslak et al., 2021). These automated tools can generate a report for quality assurance or calculate quality metrics. For example, dMRI-based quality metrics (Cieslak et al., 2021; Yeh et al., 2019) are sensitive to subject motion, eddy current distortion, or volume-wise signal dropout. A substantially low value in these metrics indicates an acquisition issue that requires further inspection to determine whether the issue is correctable. After passing the screening, the data can be preprocessed to eliminate distortions and artifacts for further tractography analysis. In clinical applications, reports from automated quality control tools can be integrated as a quality assurance procedure to ensure the reliability of the results for diagnostic, prognostic, or interventional purposes.

5. Fiber resolving methods

After preprocessing, the dMRI data will be modeled by fiber resolving methods to estimate the fiber orientations at each imaging voxel (Fig. 2a). Methods to resolve fiber orientations can be categorized into model-based and model-free approaches. In the following subsections, we summarize fiber resolving methods and discuss their strengths and weaknesses.

5.1. Model-based methods

Model-based methods fit data samples based on pre-defined models or distribution functions, including the standard tensor model (Basser et al., 1994), two-tensor model (Qazi et al., 2009), free water elimination tensor (Pasternak et al., 2009), ball-and-sticks model (Behrens et al., 2003b), kurtosis model (Fieremans et al., 2011), or

neurite orientation dispersion and density imaging (NODDI) model (Zhang et al., 2012). Model parameters provide fiber orientations for fiber tracking. One advantage of model-based approaches is that they often require fewer diffusion sampling directions than model-free methods. However, a common disadvantage is that the model assumptions can be violated due to the intricate diffusion patterns of biological tissues, particularly in the presence of gross pathology.

5.2. Model-free methods

Model-free methods seek to estimate orientation distribution functions (ODFs), which can be viewed as *histograms* quantifying the empirical distributions of diffusion at different orientations. ODF peaks can be used as fiber orientations for eventual tracking, and metrics can be calculated from ODFs to correlate with tissue characteristics. Model-free methods include diffusion spectrum imaging (DSI) (Wedeen et al., 2005), q -ball imaging (Aganj et al., 2010; Descoteaux et al., 2007; Tuch, 2004), generalized q -sampling imaging (GQI) (Yeh et al., 2010), and mean apparent propagator MRI (Ozarslan et al., 2013). These methods are also known as q -space imaging methods because they often rely upon the Fourier transform relation between diffusion distributions and q -space signals (Callaghan, 1991). Model-free methods often need more diffusion sampling directions and longer scanning time, but the strength is that they do not assume a specific diffusion model. This feature makes model-free methods ideal choices for clinical applications, where a disease or pathological condition may exhibit complex diffusion patterns caused by demyelination, hemorrhage, edema or infiltration of immune or tumor cells.

5.3. Spherical deconvolution

Spherical deconvolution (Tournier et al., 2004) and its derivatives (Dell'acqua et al., 2009; Jeurissen et al., 2014; Rokem et al., 2015; Tournier et al., 2007) leverage the strengths of both model-free and model-based methods. Similar to model-free methods, spherical deconvolution methods also calculate an ODF called the fiber orientation distribution (FOD). On the other hand, similar to model-based methods, spherical deconvolution methods use diffusion signals from selected fiber portions (i.e., the mid-sagittal part of the corpus callosum) as a diffusion model to design deconvolution kernels. These kernels are called *response functions* and are used as a unified diffusion model to resolve fiber orientations. The resulting FODs are often sharper and achieve relatively higher power to resolve crossing fibers. The multi-shell version of spherical deconvolution further provides tissue characterizations (Jeurissen et al., 2014).

5.4. Comparison

Fig. 3 displays fiber orientations calculated from diffusion tensors, diffusion ODFs, and FODs based on the same data from the first subject in the Penthera (Paquette et al., 2019) and traveling subjects dataset (Fig. 3a and b, respectively) (Tong et al., 2020). Fig. 3 data were generated using a cloud computation service provided by brain-life.io (Avesani et al., 2019) through its web applications of DSI Studio (<http://ds-studio.labsolver.org>) and MRtrix3 (Tournier et al., 2019). The diffusion ODF was calculated using GQI (Yeh et al., 2010), whereas the FOD was calculated using multi-shell, multi-tissue constrained spherical deconvolution (Jeurissen et al., 2014). The threshold for filtering fiber orientations was determined by a value that achieved the best consistency between the three approaches to facilitate comparison. The coronal slices in Fig. 3 are selected to include the thalamus and basal ganglia, thereby facilitating cross-reference with Fig. 1.

As shown in Fig. 3, the tensor model can only resolve one fiber orientation for each voxel in the centrum semiovale (CS), and thus DTI tractography cannot track the transverse branches of the corpus callosum (CC), as delineated by the dashed line. The fiber orientations re-

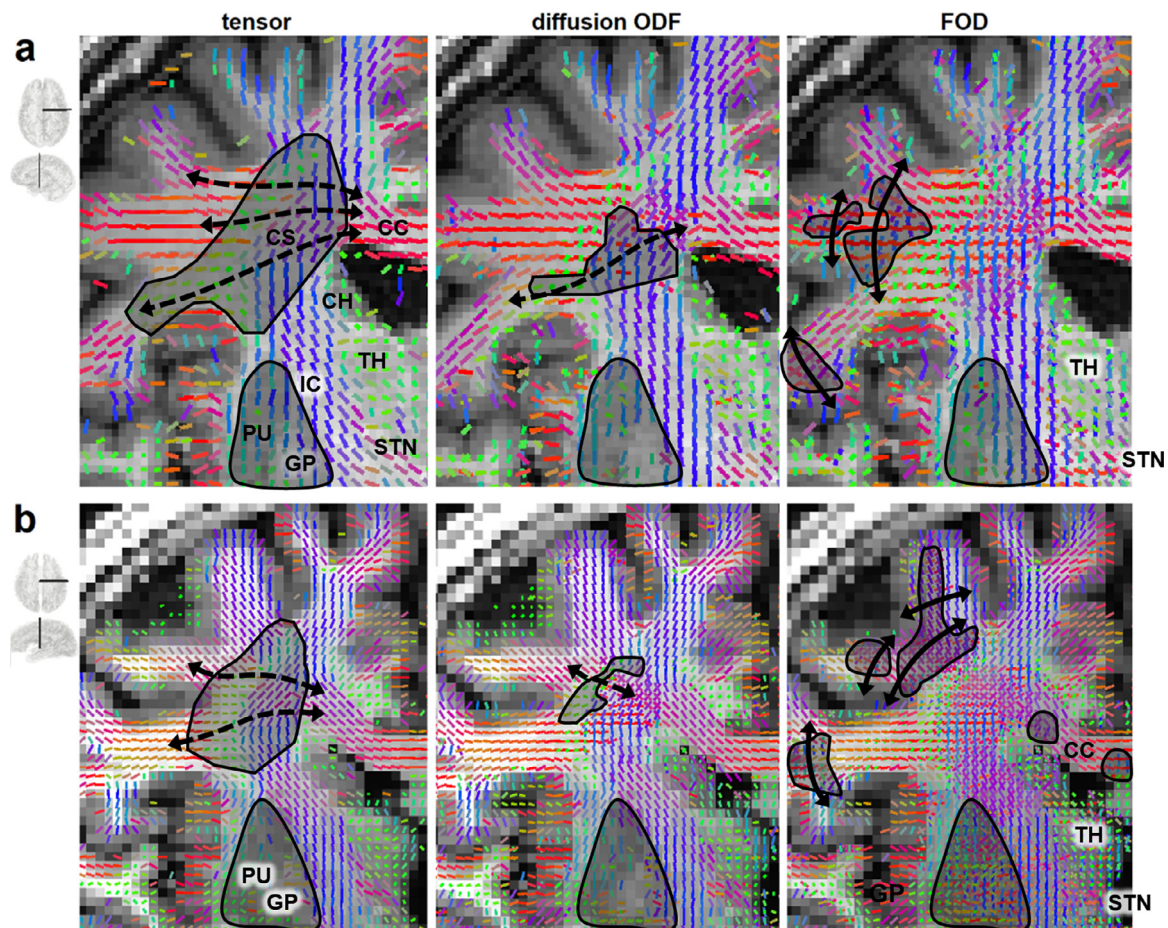


Fig. 3. Commonly encountered ambiguities in fiber orientations as resolved by the standard tensor model, diffusion orientation distribution functions (ODFs), and fiber orientation distributions (FODs). The illustrations are based on publicly available data from (a) the Penthera 3 T dataset (Paquette et al., 2019) and (b) the traveling subjects dataset (Tong et al., 2020). Data were processed using MRTrix3 and DSI Studio on a cloud computing platform (brainlife.io). The resolved fibers are shown by sticks colored by directional color (left-right: red, anterior-posterior: green, superior-inferior: blue). The tensor model (first column) only resolves one fiber orientation per voxel and cannot map the lateral branch of the corpus callosum (CC) (dashed line). The diffusion ODF model can resolve part of the crossing fibers but may still miss some lateral branches (dashed line) of the CC. FODs provide the highest resolving power for identifying crossing fibers but may occasionally produce arc-shaped spurious tracks perpendicular across the gyrus. The FOD results within the subthalamic nuclei (STN) and the thalamus may cause difficulties for tracking subcortical targets. For all three methods, the fiber orientations resolved for the putamen (PU) and globus pallidus (GP) are unreliable due to heavy T_2 -weighting caused by iron complex deposition. .

solved in the putamen (PU) and globus pallidus (GP) are unreliable due to weak dMRI signals. Nonetheless, the showcased limitation in resolving crossing fibers does not imply that DTI tractography is unusable in such cases. Specifically, DTI tractography has been used to track association pathways such as the arcuate fasciculus (Glasser and Rilling, 2008; Rilling et al., 2008; Saur et al., 2008) and the superior longitudinal fasciculus (Karlsgodt et al., 2008; Makris et al., 2005; Martino et al., 2013). Moreover, in the subcortical structures, DTI tractography has shown clinical benefit in mapping pathways near the thalamus (TH) and subthalamic nucleus (STN) for deep brain stimulation (Coenen et al., 2011; Vanegas-Arroyave et al., 2016). The accuracy of DTI tractography thus depends on white matter location, and researchers should be aware of DTI limitations in mapping crossing fibers.

Diffusion ODF can resolve fibers crossing at angles between 45 and 90° (Cho et al., 2008), but fibers crossing at smaller angles, such as those annotated by dashed lines in Fig. 3, cannot be resolved. As a result, tractography using diffusion ODF may still miss part of the callosal branches. Furthermore, diffusion ODF cannot resolve fibers at the putamen (PU) and globus pallidus (GP) due to iron deposition that causes low diffu-

sion MRI signals. The primary strength of diffusion ODF tractography is its applications under various pathological conditions that dramatically alter the diffusion pattern (Abhinav et al., 2015; Becker et al., 2020; Celtikci et al., 2018; Zhang et al., 2013). Overall, tractography based on diffusion ODF offers improvements over DTI by providing better mapping of crossing patterns (Gangolli et al., 2017). However, the former method still requires cautious interpretation due to its potential failure to capture specific crossing configurations (Neher et al., 2015).

FOD tractography has a better resolving power than DTI and diffusion ODF methods (Tournier et al., 2008; Wilkins et al., 2015a), making it ideal for delineating fibers crossing at a sharp angle (Neher et al., 2015). However, FOD approaches may occasionally yield false identifications of fibers perpendicular to gyri. These false fibers may manifest themselves as arc-shaped false tracks in gyral blades, as shown by the black lines in Fig. 3a and b, whereas histology (Fig. 1b and c) show no fibers spanning across the gyrus. These false fiber tracings are often found at larger crossing angles between 50 and 90° (Parker et al., 2013) and may be caused by the mismatch of response functions since tract bundles in different brain regions may have distinct diffusion patterns

(Schilling et al., 2019a). FOD tractography is usually more sensitive to crossing fibers, but attention should still be devoted to potential false findings (Knösche et al., 2015).

With many different fiber tracing methods available, researchers should take into careful consideration each method's pros and cons and their differential suitability for different brain regions and fiber tracing goals. This advice is supported by a recent histology study suggesting that fiber resolving methods can have different performances in different brain regions (Schilling et al., 2018b). For example, FOD tractography is often ideal for capturing sharp crossings, such as in the lateral branches of the projection pathways or corpus callosum (Jeurissen et al., 2011; Wilkins et al., 2015b). On the other hand, model-free methods can facilitate the study of various pathological conditions (e.g., TBI, encephalopathies, tumors), where fibers undergo demyelination or edema that induce deviations from normative diffusion models. In brain regions with no crossing fibers, DTI can still produce reliable tractography results (Kristo et al., 2013; Kristo et al., 2012). In mapping cardiac muscle fibers, DTI is still the method of choice for cardiac tractography (Sosnovik et al., 2009) due to its less stringent imaging requirements and to its lower risk of modeling crossing fibers inadequately. The fiber orientations resolved by any of these methods can be coupled with any fiber tracking method to generate tractography, as detailed in the next section.

6. Fiber tracking methods

Fiber tracking was initially addressed as a numerical estimation problem since its introduction 20 years ago (Basser et al., 2000; Mori et al., 1999). From a numerical perspective, the problem can be viewed as solving an *ordinary differential equation* (ODE), and the targeted track trajectory is the unknown function to be estimated. This numerical problem is often called the *first-order ODE problem* or *first-order initial value problem*. Fig. 4a uses a one-dimension function to visualize this numerical estimation process. The goal of the first-order ODE problem is to numerically estimate an unknown function (grayed dashed line) using both its first derivatives (black arrows) and an initial value of the function (black circle). In fiber tracking, the first derivatives of the function are the fiber orientations resolved by fiber resolving methods described previously, whereas the initial value is the *seeding point* used by fiber tracking algorithms to begin the fiber tracking process.

6.1. Euler method

One of the most popular numerical approaches to solving first-order ODEs is the Euler method due to its relative simplicity and adequate numerical stability. In fiber tracking, this method is used as an iterative approach to calculate fiber trajectories by iterating between a *direction estimation* step and a *propagation* step (Basser et al., 2000). The approach starts at a pre-defined starting location, $f(t_0)$, (a.k.a. the seed). The local fiber direction at this current location, $f/prime(t_0)$, is provided by the fiber resolving methods (e.g., the tensor model, diffusion ODF, or FOD mentioned in Section 5) and is used to define the propagation direction. The tracking process iteratively propagates the trajectory of the track in two opposing directions (Fig. 4a). At each iteration i , the spatial trajectory is extended by calculating $f(t_{i+1}) = f(t_i) + f/prime(t_i)\Delta s$, where Δs is a pre-defined distance called the *step size*. The above process is repeated until any of the termination criteria are met. Commonly-used termination criteria include (a) an anisotropy threshold (which terminates tracking if fractional anisotropy falls below a pre-defined value) (Yeh et al., 2013), (b) a brain mask (which terminates tracking if the end coordinate of a track falls outside the brain region) (Smith et al., 2012), and (c) an angular threshold (which terminates tracking if the fiber trajectory makes a sufficiently abrupt turn). Both deterministic and probabilistic fiber tracking often rely on this Euler estimation framework. The main typical distinction between approaches is whether the

propagation direction is randomly selected from the distribution of directions (thus probabilistic) or whether it is determined before tracking begins (thus deterministic) (Descoteaux et al., 2009).

6.2. Errors in fiber tracking

The standard numerical analysis shows that the numerical errors of the Euler method are reduced linearly as step size decreases (i.e., using big-oh notation, $O(\Delta s)$); for higher-order methods such as the Runge-Kutta method, the reduction is quartic (i.e., $O(\Delta s^4)$). However, this error estimation does not consider other errors associated with unique scenarios of fiber tracking, as shown in Fig. 4b-d. The figures illustrate three scenarios whose mathematical setting deviates from that of a typical first-order ODE problem.

In Fig. 4b, the first scenario is the *angular deviation* in the local fiber orientation. The deviation can be due to artifacts, modeling limitations, partial volume effects, or interpolation errors. The diffusion MRI community has devoted efforts to address the angular deviation problem (Tournier et al., 2011); however, the best approaches may still have a typical angular deviation of 6 to 10° shown by histology (Schilling et al., 2016). Higher-order ODE solutions may not necessarily be more accurate since the trajectory error caused by angular deviation is often more substantial than those caused by the step size. The second scenario, illustrated in Fig. 4c, occurs at the boundaries of tract bundles. A bundle may have an end surface near the gray matter, but fiber tracking can have *premature terminations* or *overshoots* due to an error in the termination criteria. As shown in Fig. 4d, the third scenario involves the existence of multiple trajectories at the same location. Specifically, each imaging voxel can be associated with more than one fiber orientation, and fiber tracking could generate an incorrect routing that bridges two unrelated bundles and creates spurious tracks. All three scenarios can occur in combination with one another and greatly complicate the task of fiber tracking. For example, tracking may start with a minor deviation due to an error in fiber orientations and then wrongly connect a bundle to unrelated nearby bundles. Alternatively, tracking may fail to terminate, as appropriate, at the gray-white matter junction and may instead bridge another bundle across a sulcus. Thus, identifying false tractography results requires an adequate understanding of how fiber tracking may fail due to scenarios like those shown in Fig. 4b-d.

Fig. 4e lists examples of spurious bundles identified by experts when constructing a human brain tractography atlas (Yeh et al., 2018). The blue arrows in the figure point to incorrect routing that bridges two unrelated bundles, whereas the red arrows point to premature track terminations. While identifying premature terminations can be accomplished by referring to structural anatomy images (Smith et al., 2012), identifying incorrect routings often require prior anatomical insights and knowledge because incorrect routing bundles may still contain (mostly) realistic trajectories. Moreover, the trajectories of spurious tracks may match local fiber orientations and diffusion patterns (Maier-Hein et al., 2017), meaning that the dMRI dataset itself may not provide sufficient information to reject such false trajectories. In such cases, prior independent information (e.g., from a tractography atlas) may be needed to map white matter pathways correctly.

Throughout the past 20 years of tractography algorithm development, the neuroimaging community has acknowledged that fiber tracking methods typically yield a substantial number of spurious results that should not be ignored (Reveley et al., 2015; Thomas et al., 2014). Although numerous tractography competitions and challenges have been organized, most have not identified a clear winner favoring any particular fiber tracking method (Fillard et al., 2011; Maier-Hein et al., 2017; Pujol et al., 2015; Schilling et al., 2019b). This suggests that tractography's accuracy challenges are more substantially rooted within the intrinsic limitations of dMRI as a technique rather than within numerical methodology. Thus, there is a need for independent information and anatomical priors to achieve higher accuracy in fiber tracking. We discuss this trend further in Section 9.

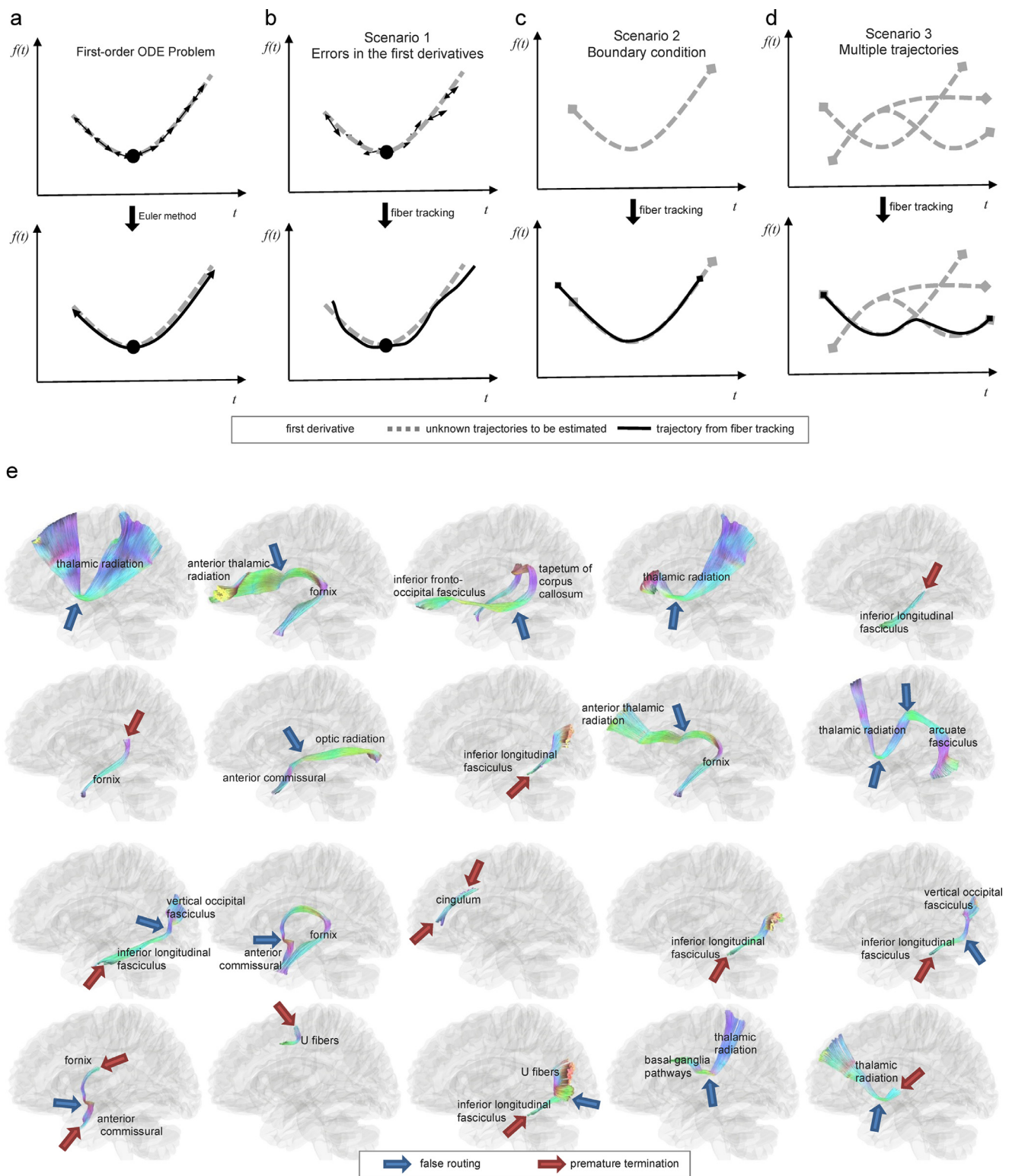


Fig. 4. Challenges in fiber tracking and examples of spurious tracks. (a) fiber tracking involves a numerical procedure to solve a first-order ordinary differential equation (ODE) whose parameters are specified by a starting location (i.e., the seeding point, black circle) and by the first derivative of a function (i.e., the resolved fiber orientation, arrows) at each voxel. The trajectory can then be calculated using the Euler method. However, the conventional ODE problem only considers numerical error due to finite step size and does not consider other error scenarios in fiber tracking. (b) The first scenario that raises challenges for standard fiber tracking involves errors in the estimation of first derivatives, which can cause substantial deviation of trajectories from their ground truth. (c) The second challenging scenario involves the boundary condition. Specifically, white matter tracts have termination locations, and fiber tracking may terminate at the wrong location, leading to a premature termination or an overshoot. (d) The third challenging scenario involves the coexistence of multiple trajectories at the same voxel location. Connecting unrelated trajectories may lead to incorrect streamline routing and spurious tracks. (e) example of spurious tracking results identified by neuroanatomists in an atlas construction study (Yeh et al., 2018). The tractogram is color-coded by directional color (left-right: red, anterior-posterior: green, superior-inferior: blue). The locations of incorrect routings and premature terminations are annotated by blue and red arrows, respectively. Incorrect routing is often due to a deviated tracking procedure that bridges two unrelated bundles and produces spurious trajectories. Identifying false results requires prior neuroanatomical knowledge—and even mapping nearby pathways—to rule out the possibility of incorrect routing.

7. Tractography in patients with brain tumors

Tractography has emerged as a standard tool in many institutions for preoperative assessment of white matter tracts perilesional to gliomas, primarily due to recent improvements in the image acquisition time and to the promising potential of its clinical applications (Henderson et al., 2020; Nimsy et al., 2005; Vanderweyen et al., 2020). To achieve optimal surgical outcomes, studies have demonstrated that maximal tumor resection is an independent prognostic factor for survival in high- and low-grade gliomas (Jakola et al., 2013; Lacroix et al., 2001; Li et al., 2016), whereas neurological deficits after resection of tumors are associated with a decrease in overall survival and quality of life (Rahman et al., 2017). For preoperative assessment, a safe maximal resection has been the surgical goal in brain tumor patients. To this end, tractography's primary role is to provide individualized reconstructions of tract trajectories and to reveal the relationship between the lesion and critical white matter tracts, thereby aiming to assist maximal tumor resection while avoiding new postsurgical deficits.

7.1. DTI tractography in brain tumors

Early in tractography development, DTI tractography was used to depict the pathological effects of brain tumor growth on white matter pathways, including infiltration, displacement, disruption, and destruction of tracts (Witwer et al., 2002). At least one study also showed good correspondence between positive subcortical stimulation sites and language tract mapping by DTI tractography (Leclercq et al., 2010a), although false-negative results require attention. Later studies have shown that tractography-based navigation associated with subcortical mapping contributes to maximal safe resection of cerebral gliomas involving the corticospinal tract (CST) (Wu et al., 2007; Zhu et al., 2012; Zolal et al., 2012). In low-grade gliomas, critical areas around the tumor, both cortical and subcortical, are among the most important factors limiting the extent of resection (Hervey-Jumper and Berger, 2019). Intra-tumoral DTI tractography in cases of low-grade gliomas has revealed that the presence of motor and language pathways within the tumor can predict eloquent areas and the extent of resection (Mato et al., 2021). In practice, preoperative tractography can be incorporated into surgical navigation devices to provide a three-dimensional visualization of white matter tracts of interest and their relationship to critical anatomical structures during surgical planning and resection (Coenen et al., 2001; Kuhnt et al., 2012; Nimsy et al., 2006) (Fig. 5). Functional MRI activation areas can be used as seed regions of interest for DTI tractography (Smits et al., 2007), resulting in better prediction of functional fascicles than anatomical-based tractography (Sanvito et al., 2020). Tractography data can be interactively visualized by the surgeon using dynamic seeding and region of interest to demonstrate the relationship of white matter tracts to the lesion and critical structures (Fekonja et al., 2019; Golby et al., 2011).

More recently, laser interstitial thermal therapy has become an increasingly used, minimally invasive, image-guided treatment option for patients with some brain tumors. In this procedure, a laser fiber is stereotactically inserted into the lesion to heat the tissue under MR thermometry and to ablate the lesion. Tractography can also be incorporated into pre- or intra-operative images to guide the safest approach trajectory and ablation of lesions (Fig. 6).

Overall, DTI tractography has helped neurosurgeons correctly identify patients with interrupted white matter tracts in whom a more aggressive extent of tumor resection can be pursued (Alexopoulos et al., 2019). The knowledge of the location and integrity of critical pathways is crucial to the neurosurgeon to preserve eloquent subcortical white matter and to avoid postoperative neurological deficits (Tuncer et al., 2021). Nonetheless, it is noteworthy that negative findings in DTI tractography are not sufficient to rule out the existence of functional tract pathways in the peritumoral region (Leclercq et al., 2010a).

In addition to trajectories obtained from tractography, the diffusion metrics associated with this technique can inform clinicians about the integrity of peritumoral white matter pathways. The combination of quantitative information along trajectories can provide clinically relevant information on the location and integrity of peritumoral tracts in a lesion vicinity. Clinically relevant findings include the destruction of tracts by aggressive lesions such as high-grade gliomas, infiltration by low-grade gliomas, and displacement by metastases or meningiomas, although any or all of these can co-occur (Young and Knopp, 2006). When integrated with track-based metrics, tractography can provide surgeons with qualitative and quantitative information regarding potentially affected tracts around an intracranial lesion. In DTI tractography, the tensor model provides fractional anisotropy (FA), which may reflect changes in tract integrity, and apparent diffusion coefficient (ADC), which may reflect changes in the perilesional area such as an increase in cellularity. These metrics have been used to evaluate the perilesional zone around gliomas, mainly to help distinguish infiltration from edema (Hoefnagels et al., 2014; Provenzale et al., 2004). However, it is noteworthy that FA and ADC can be affected by various factors (Alexander et al., 2001; Hui et al., 2010; Pasternak et al., 2009), and that changes can be nonspecific. Consequently, their clinical values in the diagnostic and prognostic evaluation are limited due to their relatively low specificity and sensitivity.

Tractography can also assist stereotactic radiosurgery (SRS) planning. SRS is a highly conformal treatment used to treat some brain tumors (and other lesions). SRS delivers a high dose of radiation in one, or up to five, treatment sessions. Reports in the literature have suggested that white matter tracts, particularly the optic radiation and arcuate fasciculus, are more vulnerable to radiation during SRS than previously thought (Maruyama et al., 2007; Maruyama et al., 2009). For treatment planning, DTI tractography images can be fused with stereotactic treatment images to analyze dosimetry for critical tracts (Maruyama et al., 2005). Integrating DTI tractography into SRS planning has been reported to help prevent morbidity related to radiosurgery in patients undergoing treatment for arteriovenous malformations (Koga et al., 2012). There is support for the view that delineation of functional structures and tracts in dosimetry planning is beneficial and could reduce the dose received by these healthy tissues, thus decreasing the risk of radiation-induced complications and increasing the quality of the delivered treatment (Pantelis et al., 2010). In a study with 23 patients with lesions adjacent to the CST where DTI-tractography was fused with stereotactic MRI, the CST was treated as an at-risk "organ," and the conformal dose was planned; clinical parameters between plans with and without tractography were then evaluated (Kawasaki et al., 2017). The maximum CST dose was significantly reduced by tractography planning, adding only a 3.5 min irradiation time prolongation. There was no significant difference in the dose covering 95% of the lesion volume (D95). The results suggested that the CST dose can be reduced while maintaining the D95 with clinically acceptable prolongation of the irradiation time (Kawasaki et al., 2017). Integration of tractography into SRS represents a promising tool for preventing radio-induced toxicity and complications (Maruyama et al., 2007).

7.2. Limitations of DTI tractography in brain tumors

DTI tractography and diffusivity-based measurements have several limitations despite their widespread clinical use. To recapitulate, the tensor model cannot describe multiple fiber orientations, and the estimation of axonal directions can be inaccurate in regions with crossing fibers (Alexander et al., 2001; Tuch et al., 2002). Moreover, a tumor can disrupt, displace, and infiltrate white matter while simultaneously causing peritumoral edema. Pure vasogenic edema is found around some meningiomas and metastatic lesions, whereas infiltrative gliomas can have vasogenic edema and neoplastic infiltration (Min et al., 2013). The diffusivity-based measurements can also be over-estimated or underestimated due to cell infiltration or peritumoral edema (Wang et al., 2011). DTI metrics, such as FA, can be affected by crossing fiber con-

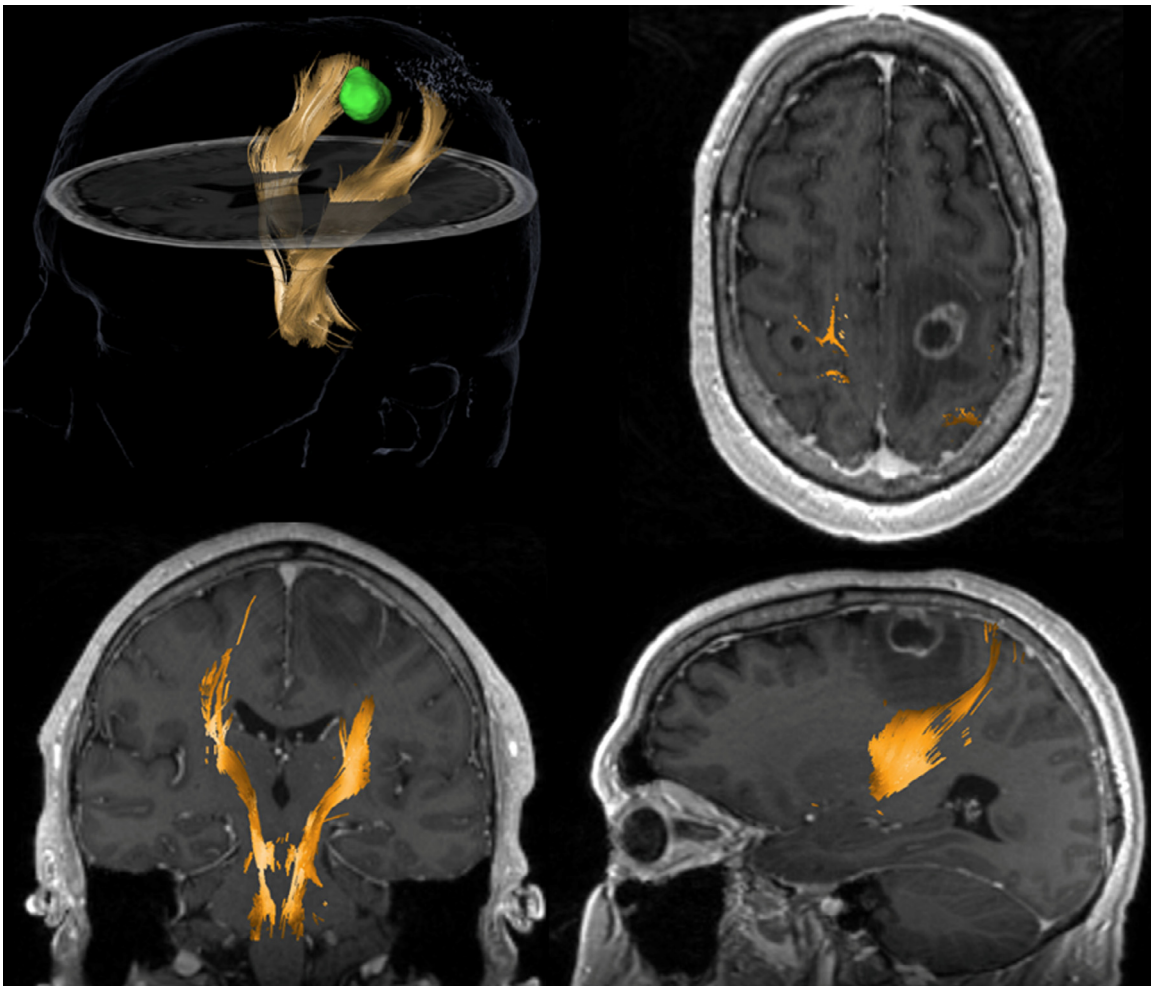


Fig. 5. DTI-based tractography from a surgical navigation system for a 58-year-old patient with non-small cell lung cancer which metastasized in the left frontoparietal region of the brain. The tracking used a multi-ROI (region of interest) approach with one cubic box positioned in the region of the posterior limb of the internal capsule, at the level of the interventricular foramina of Monro and another box placed at the anterior inferior pontine level, inserted caudally relative to the upper and middle cerebellar peduncle. The left corticospinal tract (yellow) is displaced posteriorly compared to the right (contralateral) branch. A region of hypointensity (low signal) around the lesion suggests vasogenic edema. It is crucial to notice that DTI tractography shows no tracks in the region of edema. This negative finding is likely due to the inability of DTI to track streamlines in edematous regions and does not unequivocally indicate tract disruption.

ditions or by partial volume effects in the edematous zone around the gliomas, which in turn can lead to premature termination of the fiber tracking and the risk for the incomplete reconstruction of a perilesional tract (Chen et al., 2015b)(Fig. 7). Change in the free water content of tissue lowers FA values, while the tracts might remain unaffected. Consequently, DTI-based tractography can fail to demonstrate tracts that are present—but not traced—due to several types of tissue abnormality around brain tumors, such as edema or tumor cell infiltration (Leclercq et al., 2010b) (Zhang et al., 2013). This drawback can cause DTI tractography reconstructions to become inaccurate and inconsistent in edematous regions around tumors, making it harder to differentiate destroyed white matter tracts from intact ones with edematous white matter, a critical task for neurosurgical planning (Kinoshita et al., 2005; Schonberg et al., 2006).

7.3. Advanced tractography in brain tumors

Several advanced tractography methods have been proposed to address the limitations of DTI tractography in the presurgical planning for brain tumor surgery. Their advantages include more reliable results in the presence of peritumoral edema and complete mapping of tract branches. Specifically, Zhang et al. (2013) compared DTI and GQI trac-

tography using preoperative and postoperative scans on brain tumor patients. The results showed that advanced tractography could comprehensively display existing tracts in the edema, whereas DTI tractograms were incomplete. Chen et al. (2015a) retrospectively compared DTI tractography with two-tensor unscented Kalman filter tractography and found that advanced tractography can provide better sensitivity in mapping arcuate fasciculus tractography in the presence of peritumoral edema. More recently, Gong et al. (2018) performed a similar retrospective comparison in patients harboring tumors near the CST and reached the same conclusion. Several studies comparing DTI tractography with advanced tractography have confirmed that the latter can map white matter tracts with higher accuracy and better safety margins for neurosurgical procedures. (Abhinav et al., 2015; Christiaens et al., 2015; Farquharson et al., 2013; Fernandez-Miranda et al., 2012). The metrics from advanced modeling may further offer additional information over conventional DTI metrics (Fekonja et al., 2020). Thus, replacing DTI tractography with advanced tractography has been recommended (Nimsky, 2014). The latter can be color-coded with other imaging modalities to evaluate white matter tracts around a brain lesion for diagnostic and prognostic assessment. The integrated tractogram can inform the extent of peritumoral edema or tumor cell infiltrations and help clinicians achieve a safe maximal resection (Fig. 8a and b).

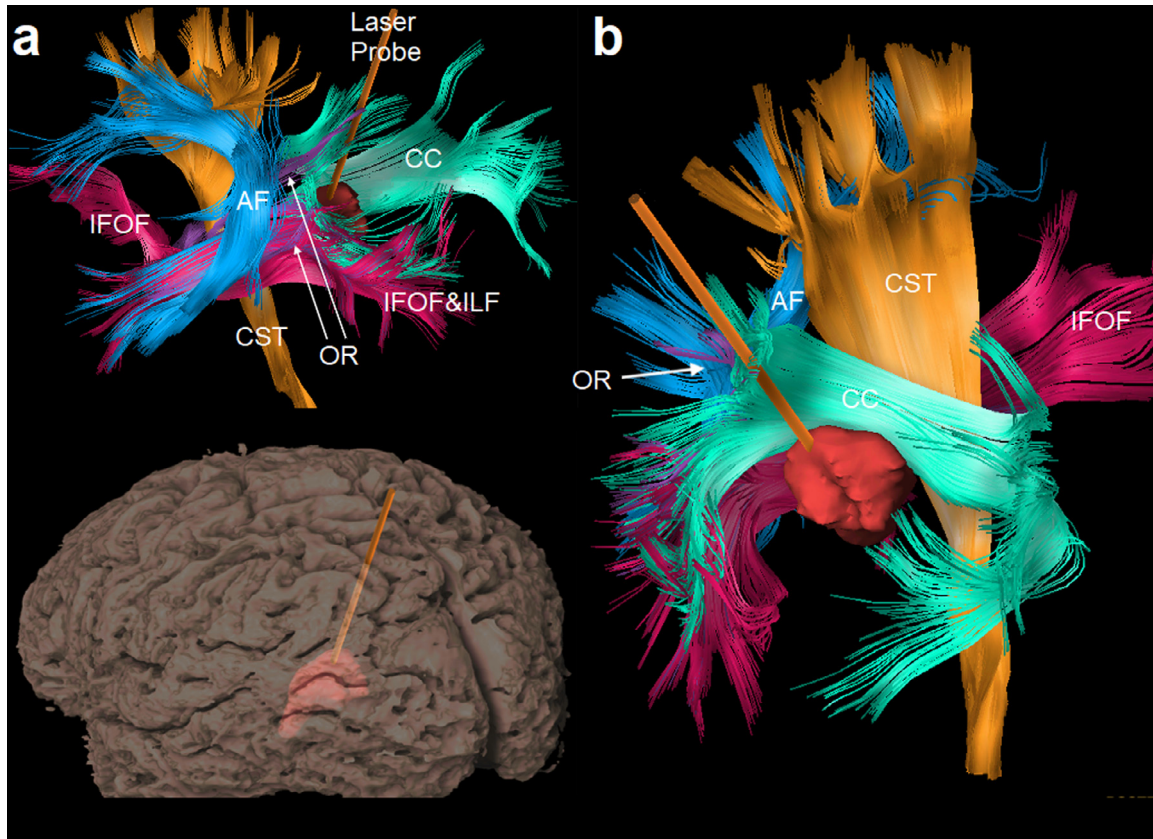


Fig. 6. Surgical planning for laser interstitial thermal therapy: an image-guided, minimally-invasive treatment that has been increasingly used to treat hard-to-reach primary or metastatic brain tumors. (a) Tractogram and the gyral surface viewed from the same left-posterior direction show a laser probe inserted into the tumor lesion to heat the tissue under MR thermometry and to ablate the lesion. Tractography of peritumoral pathways can be integrated with preoperative and intra-operative images to guide the safest ablation. Nearby tracts include the arcuate fasciculus (AF), corticospinal tract (CST), inferior frontal-occipital fasciculus (IFOF), inferior longitudinal fasciculus (ILF), optic radiation (OR), and corpus callosum (CC). (b) A view from the right-posterior-superior direction shows the relative location of the lesion to the surrounding critical tracts.

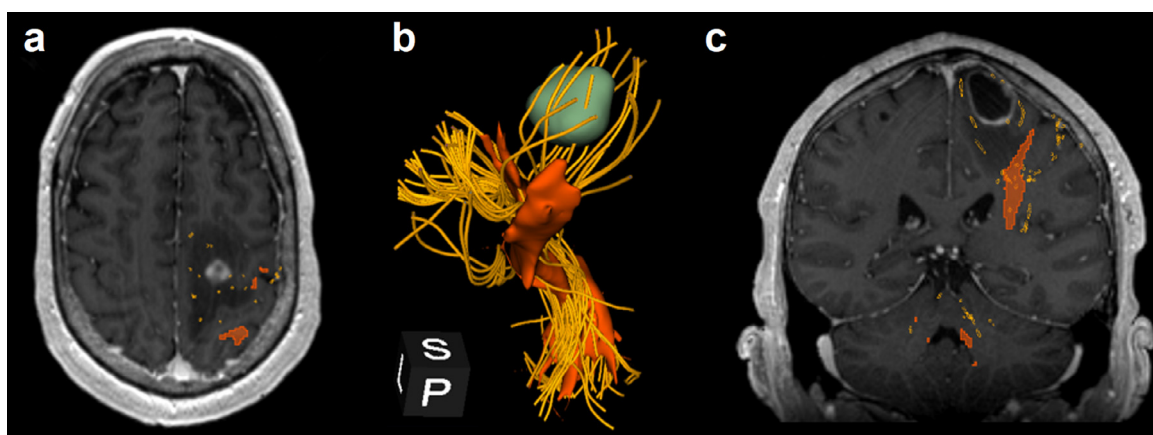


Fig. 7. Comparison of DTI tractography to advanced tractography using an unscented Kalman filter (UKF) in the same patient as in Fig. 5. (a) The corticospinal tract (CST) generated by DTI-based tractography (reddish-orange) and UKF (golden yellow). UKF tractography shows CST going through the edematous region around the tumor, whereas DTI tractography does not capture those peritumoral tracts. (b) The tractogram shows a 3D-reconstruction of the CST from DTI tractography (reddish-orange), using commercially available navigation software, and from UKF tractography (golden yellow), using the SlicerDMRI module in 3D Slicer. It is noteworthy that UKF tractography allows one to visualize CST innervating the lower extremities, upper extremities, and face (peripheral, extracerebral trajectories not shown). In contrast, DTI-based tractography shows only tracts from the same region of the motor cortex, likely corresponding to upper extremities. (c) Coronal, contrast-enhanced T_1 -weighted MRI integrated with tractogram illustrates the two tractography techniques and the ability of advanced tractography to identify tracts in the edematous region of the peritumoral area.

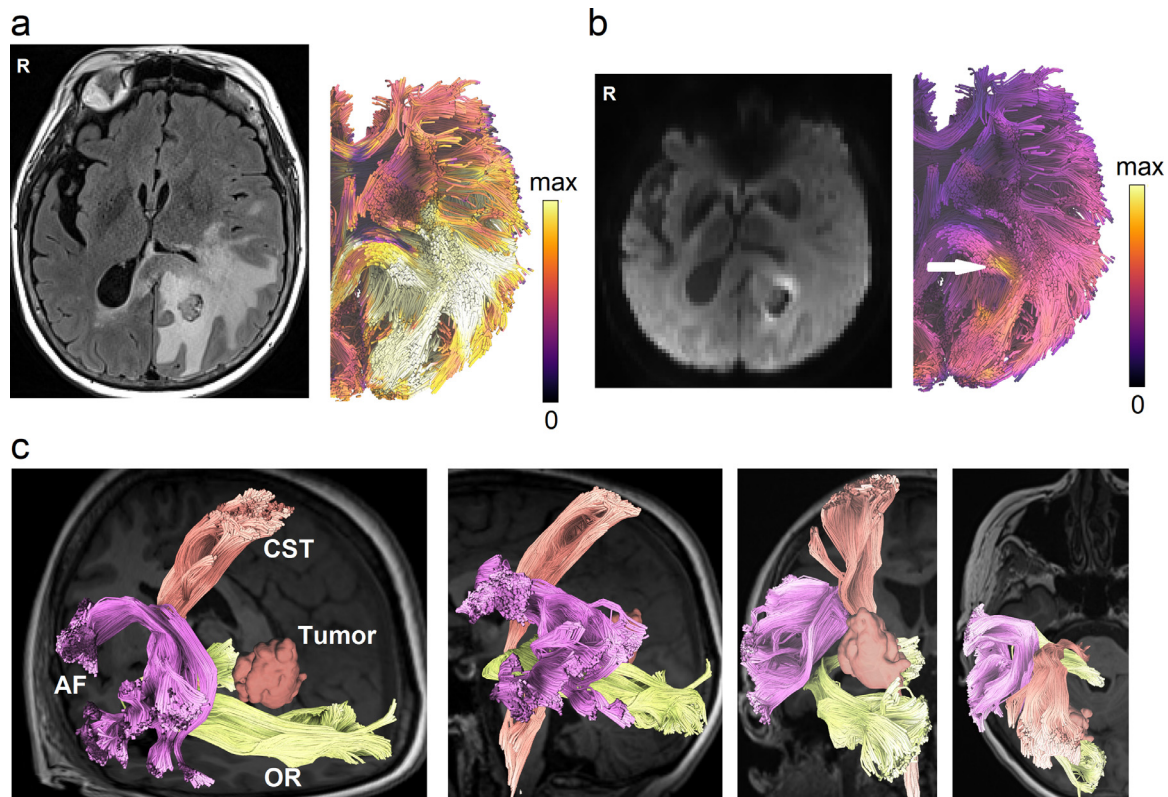


Fig. 8. Novel tractography approaches showing perilesional white matter pathways of a 65-year-old female patient with glioblastoma multiforme (GBM) to assist presurgical planning or postsurgical assessment. (a) Advanced tractography can be integrated with other imaging modalities to assist diagnostic and prognostic evaluation. The tractogram is color-coded by T_2 /FLAIR to visualize pathways affected by peritumoral edema. (b) Tractograms can be color-coded according to cell densities estimated from restricted diffusion imaging (Yeh et al., 2017) to highlight tracts infiltrated by tumor cells (annotated by the white arrow). The results may inform the extent of surgical resection to achieve better surgical results. (c) Automated tractography maps the arcuate fasciculus (AF), corticospinal tract (CST), and optic radiation (OR) of the patient to facilitate presurgical planning. This new tractography approach uses prior anatomical information from a tractography atlas to identify white matter pathways, eliminate spurious tracks, and cluster tracks into anatomically defined bundles. This process can reduce the tedious manual placement of seed regions and can improve the test-retest reliability of tractography mapping.

For clinical groups already using DTI tractography, transition to beyond-DTI can be readily achieved by combining two sets of DTI data at different b-values. For example, one DTI acquisition can be acquired at a b-value of 1500 s/mm^2 at 30 directions, whereas another DTI acquisition can be subsequently acquired at a b-value of 3000 s/mm^2 at 60 directions. Both acquisitions should use the identical isotropic resolution and identical TE and TR. These two DTI data combined is a two-shell dataset that can be readily utilized by more advanced modeling methods mentioned above, including and not limited to GQI, MSMT-CSD, NODDI, and DKI. Combining two-shell protocol and beyond-DTI methods offers the potential to remove free water and minimize the effect of peritumoral edema. Furthermore, many tractography tools shared their applicable imaging protocol to encourage reproducible research and open science (Norton et al., 2017). We also shared our 12-minute grid scheme protocol at the DSI Studio website (<http://dsi-studio.labsolver.org>), which acquired 23 b-values at 258 directions to characterize a spectrum of restricted and non-restricted diffusion.

Challenges remain for future advanced tractography methods to address when mapping white matter in brain tumor patients. Currently, there is no standardization of dMRI tractography methods used by different institutions. For example, as mentioned in previous sections, studies have demonstrated considerable variability in fully reconstructing the pyramidal pathway among different approaches (Pujol et al., 2015; Schilling et al., 2020). Research has already demonstrated that operator-dependent effects such as the choice of regions (e.g., either seed regions or region of interest) can often affect tractography results (Radmanesh et al., 2015). Even the same tractography method imple-

mented within different software environments can have a wide range of performance discrepancies (Maier-Hein et al., 2017; Schilling et al., 2021). Thus, reproducibility and standardization are critical challenges that must be overcome for tractography to gain further trust within the neurosurgery community. This issue is crucial in neurosurgical settings, where tractography errors can give clinicians incorrect information on the location of critical structures and could thus increase the risk of postoperative deficits for some patients (Duffau, 2014). One promising direction is automated tract identification for brain tumor patients (O'Donnell et al., 2017). Precisely, by using a tractography atlas, automated tractography can map white matter pathways in the eloquent areas to facilitate neurosurgical planning (Fig. 8c). Clinicians can specify tracts of interest to visualize their relationship to the lesion. This new tractography visualization approach can reduce the time needed for manual placement of regions, improve the reliability of pathway mapping, and potentially promote the future standardization of presurgical planning.

8. Tractography in patients with TBI

8.1. DTI tractography in TBI

DTI tractography has contributed substantially to our understanding of longitudinal TBI effects upon the connectome as a function of age (Irimia et al., 2015; Trotter et al., 2015), injury chronicity (Ewing-Cobbs et al., 2016), impact mechanism (Petrie et al., 2014; Tremblay et al., 2014), trauma severity (Ilvesmaki et al., 2014) and clin-

ical outcome (Yuh et al., 2014). Additionally, it has allowed scientists to study how white matter structures (Wright et al., 2016), cognitive abilities (Caeyenberghs et al., 2014; Calvillo and Irimia, 2020), and connectome properties (Fagerholm et al., 2015) are differentially vulnerable to TBI under a variety of conditions. Studies have combined standard tractography with sophisticated biomechanical models to identify structural connectome regions most vulnerable to mild injury (Sullivan et al., 2015; Zhao et al., 2017). Furthermore, DTI tractography has been leveraged to serve as a reliable surrogate biomarker for vasogenic edema in peri-hemorrhagic TBI regions (Yang et al., 2017) to identify post-traumatic blood-brain barrier permeability changes and to quantify abnormal iron deposition within the brain parenchyma (Wright et al., 2016). These critical contributions give rise to detectable cerebral microbleeds in susceptibility-weighted imaging suggesting traumatic axonal injury and blood-brain barrier breakdown (Irimia et al., 2018), which are relevant for mild traumatic brain injury (mTBI) diagnosis in the absence of other imaging findings (Rostowsky et al., 2018). Tractography has also served as a welcome adjuvant to electrophysiological methods for mapping functional connectome properties, the loci of post-traumatic epilepsy, and related functional manifestations of post-traumatic sequelae (Irimia et al., 2013; Irimia and Van Horn, 2015a).

8.2. Limitations of DTI tractography in TBI

Despite the breadth and value of DTI studies to characterize TBI sequelae within the connectome, the utility and interpretation of DTI measures in TBI remain equivocal (Van Horn et al., 2017). To a substantial extent, these challenges echo those described in the previous sections. Whereas FA is commonly assumed to decrease after mTBI, a sizeable number of studies have concluded otherwise (Arfanakis et al., 2002; Inglese et al., 2005; Kinnunen et al., 2011; Kumar et al., 2009; Lipton et al., 2009; Lo et al., 2009; Miles et al., 2008; Toth et al., 2013). This debate has not been settled even after accounting for the effects of confounds such as injury chronicity, age at injury, publication date, and methodological differences across studies (Dodd et al., 2014; Eierud et al., 2014). Furthermore, FA has been frequently associated with white matter damage in TBI because its mathematically related metrics, axial diffusivity (AD) and radial diffusivity (RD), are considered to be surrogate markers of axonal and myelin damage, respectively (Song et al., 2003; Song et al., 2002; Song et al., 2005; Sun et al., 2006; Winklewski et al., 2018). This relative consensus persists, although such measures remain challenging to interpret in the presence of inflammation and edema. For example, AD may decrease during acute demyelination in the presence of axonal edema and microglial activation, but not during chronic demyelination of the connectome (Lodygensky et al., 2010). Similarly, RD increases chronically in demyelinating conditions unless edema is present, in which case RD does not appear to change significantly (Xie et al., 2010). Thus, because brain trauma-related inflammation and scarring can substantially change white matter structure across time, the interpretation of AD, RD, and FA in TBI is challenging as it depends on factors like lesion content and temporal evolution. Thus, additional research is needed to understand how inflammation, hemorrhage, axotomy, axonal injury, and demyelination interact post-traumatically to affect both the connectome and DTI measures (Armstrong et al., 2016). Some investigators have even proposed that standard DTI tractography is insufficiently reliable for interpreting TBI pathology in the presence of such complex cellular phenomena (Winklewski et al., 2018) and that more sophisticated techniques should be used (Cross and Song, 2017).

Another challenge of using DTI tractography in TBI is that many tensor assumptions may be violated in the presence of traumatic axonal injury. This latter phenomenon involves axonal shearing, twisting, or swelling that affects cellular morphology. The ensuing dysregulation of homeostatic calcium transmembrane gradients compromises cellular permeability and exacerbates morphological alterations in the axonal microstructure. These changes are poorly captured by DTI, partic-

ularly in the ubiquitous scenario where vasogenic and cytotoxic edema compete in the extent to which they dysregulate cellular function and tissue integrity. In response to such concerns, NODDI and *q*-space metrics—which can quantify intra-axonal volume fractions—have been proposed as techniques that provide sensitive and specific biomarkers of post-traumatic white matter disruption, macroscale tissue alterations, or cognitive deficits associated with TBI sequelae (Wu et al., 2018). Nevertheless, while relying on electron microscopy data to validate FA values and DTI streamline orientations in a murine TBI model, Salo et al. found that the orientations of DTI tractography streamlines can accurately reflect electron microscopy (EM)-derived white matter fiber orientations (Salo et al., 2018). However, the extension of such findings to humans may be problematic because many tractography validation studies in animals have used spatial resolutions more than an order of magnitude higher than typical human studies (Salo et al., 2018).

FAs and DTI streamline orientations have been validated only for a limited range of lesion content types. Subsequent tractography validation studies involving the integration of histology, structural MRI, and GQI have led to the proposal of additional, novel connectome integrity metrics that may be superior to traditional measures like FA (Gangolli et al., 2017). Additional validation studies are much needed to establish further how well DTI and beyond-DTI findings can capture the accurate underlying presentation of TBI and its impact upon the mesoscale connectome, topics which remain understudied (Laitinen et al., 2015).

8.3. Advanced tractography in TBI

Hoping to overcome the current drawbacks of DTI as used in TBI studies, some scientists have proposed estimating fiber orientation distributions directly from advanced acquisitions and using spherical deconvolution measures such as apparent fiber density track-weighted imaging to characterize post-traumatic connectome alterations (Wright et al., 2017). Other scientists advocate using diffuse kurtosis imaging (DKI) and related methods to obtain novel insights into post-traumatic connectome reorganization (Hansen and Jespersen, 2017). More recently, tractography approaches have been integrated with functional MRI (fMRI)-derived blood oxygenation level-dependent (BOLD) models and with positron emission tomography (PET) (Wooten et al., 2019) or magnetic resonance spectroscopy (Li et al., 2017; Maudsley et al., 2015; Narayana et al., 2015). The multimodally datasets could establish the relationship between TBI and other neurological conditions and forecast post-traumatic risk for further cognitive deficits based on connectomic data (Irimia et al., 2020). This integration has assisted some researchers in gaining insights into the relationship between (a) tractography streamline properties and functional correlation metrics and between (b) clinical variables of neurodegeneration (like tau protein aggregate burden) and measures of metabolic damage and oxidative stress. Wooten et al. (2019) found that DTI-derived tractography measures traditionally associated with white matter integrity are related to fMRI functional correlations and tauopathies in complex ways, which may require substantial additional research to disentangle. Although DTI-derived tractography measures of post-traumatic white matter integrity loss and connectome degradation may translate into an elevated tau-aggregate burden, they may also be associated with higher—rather than lower—functional correlations mediated by white matter connections exhibiting such burden (Irimia and Van Horn, 2015b). More recent findings suggest that the relationship between oxygen consumption in neural tissue and white matter architecture parameters provided by DTI tractography remains woefully incomplete in TBI conditions (Armstrong et al., 2016; Wooten et al., 2019; Wright et al., 2016). Other novel tractography modalities like *differential tractography* (Yeh et al., 2019) may also provide new ways to investigate the injury mechanisms by mapping longitudinal alterations in brain connectivity (Fig. 9). Nevertheless, systematic testing and validation of this and many other DTI models remain to be undertaken, and future stud-

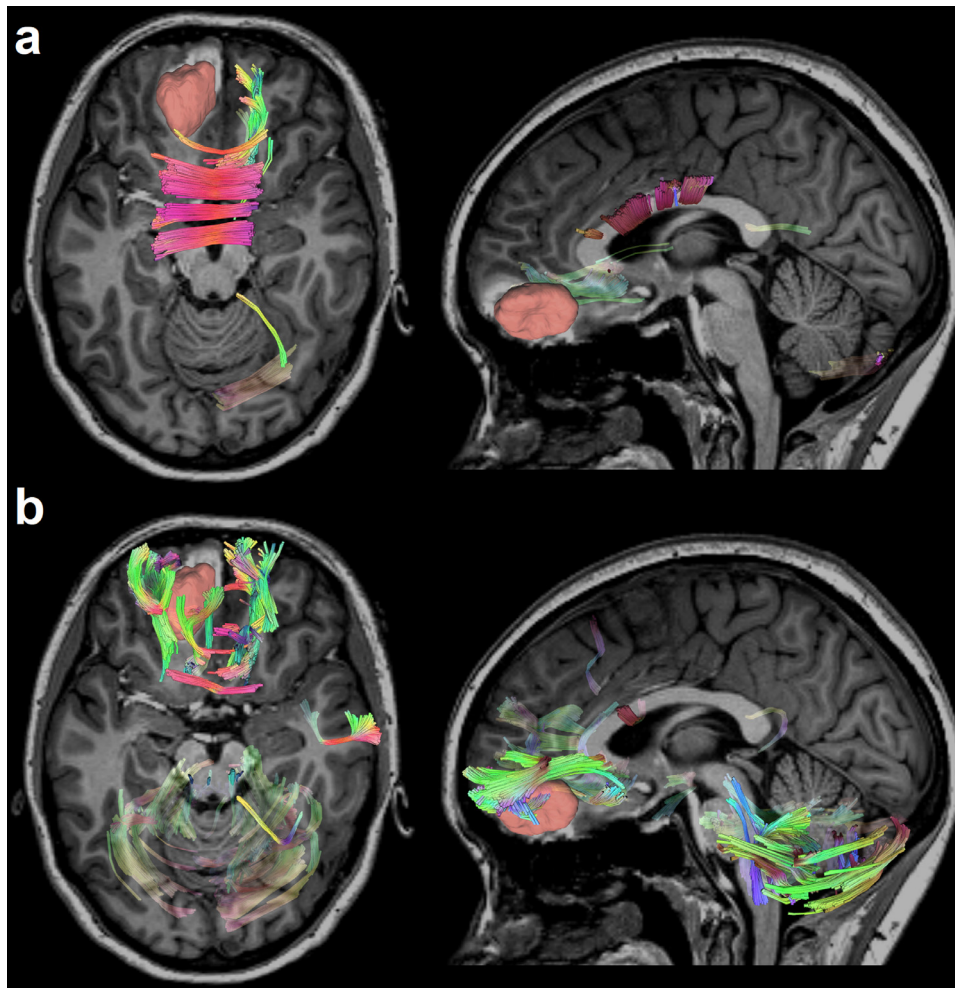


Fig. 9. Differential tractography of a 19-year-old female TBI patient highlighting the exact segments of neuronal pathways with anisotropy changes between a baseline scan acquired acutely (i.e., within a week after injury) and a follow-up scan (approximately 6 months post-TBI). The patient features a relatively large primary lesion located in the left orbitofrontal cortex, which is particularly vulnerable to TBI. Differential tractography (Yeh et al., 2019) tracks the precise segments of pathways exhibiting (a) FA decreases of more than 5% relative to the acute baseline and (b) quantitative anisotropy (QA) decreases of more than 15% relative to the same baseline. Directional coding is used to color the tractogram (left-right: red; anterior-posterior: green; superior-inferior: blue). The results reveal perilesional tracts and the genu of the corpus callosum (CC), which is the CC portion closest to the primary lesion (red). Traumatic axonal injury (TAI) of the CC is prevalent in TBI and can be explained by the interaction of TBI kinematics with the biomechanics of cerebral displacement within the cranial cavity (Hill et al., 2016). The decrease in cerebellar FA and QA is consistent with previous findings, according to which cerebellar volume and connectivity are both frequently and substantially affected by moderate and severe TBI regardless of primary injury location (Spanos et al., 2007). Although this fact is well documented (Caeyenberghs et al., 2011; Irimia et al., 2012; Park et al., 2006), its causal mechanisms are poorly understood and may be related to cerebellar involvement in motor coordination, control, and other brain functions. These functions are frequently and substantially impacted both by the primary injury and by decreases in TBI patients' abilities to carry out daily living activities as they recover. New tractography modalities like differential tractography may offer novel strategies to investigate white matter pathways and to answer outstanding questions in TBI research.

ies should also seek to (a) ascertain the validity of both established and novel diffusion MRI measures upon which tractography is reliant and to (b) resolve the complicated relationship between multimodal metrics provided by MRI, electroencephalography (EEG), magnetoencephalography (MEG), PET, and temporal connectome dynamics.

9. Prospect of tractography development

9.1. Automated tractography

Because recent tractography challenges have highlighted the inherent limitations of dMRI, strategies resorting to external information independent of this technique have gained more attention (Schilling et al., 2019b). One recent trend is to utilize a brain parcellation or tractography atlas to inform automated tractography, thus resulting in new tracking approaches or post-tracking

scrutiny routines (Garyfallidis et al., 2018; Guevara et al., 2012; O'Donnell and Westin, 2007; O'Donnell et al., 2017; Rheault et al., 2019; Warrington et al., 2020; Wassermann et al., 2016; Wasserthal et al., 2018; Yeatman et al., 2012; Yeh, 2020; Yendiki et al., 2011; Zollei et al., 2019). These methods often use prior anatomical information to identify tracts and simultaneously to reject spurious connections while improving anatomic accuracy. Automated tractography also eliminates human subjectivity in fiber tracking and vastly improves the reproducibility of fiber tracking. Furthermore, a study using repeat scans has shown that automated tractography can achieve high test-retest reliability when mapping association pathways (Fig. 10a) (Yeh, 2020). Although the accuracy and consistency between methods remain an issue, the high reproducibility within automated tractography methods can significantly improve their clinical utilities, where reliable results are prerequisites for further applications.

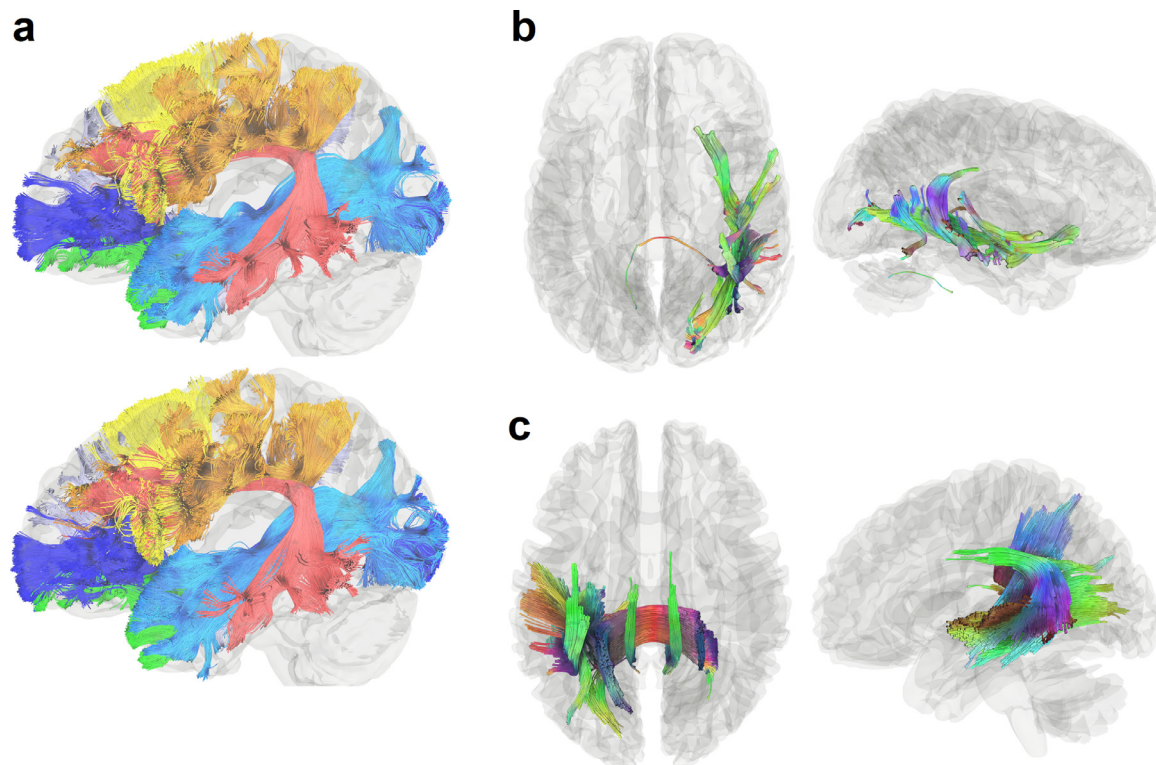


Fig. 10. Prospects of novel tractography developments to improve reliability and to explore the potential of new clinical applications. (a) Automated tractography from repeat MRI scans of the same healthy young adult subject shows high reproducibility in mapping human association pathways. Novel developments in automated tractography can mitigate quality variations due to human error and achieve better test-retest reliability. (b) Differential tractography is a new tractography modality that detects between-scan differences by tracking pathways with decreased anisotropy or any metrics. Here, differential tractography maps the precise segments of pathways with neuronal property changes by comparing the preoperative and postoperative scans of a 51-year-old male epileptic patient after anterior temporal lobectomy (Yeh et al., 2019). The affected tracts span beyond the operation location. Directional color coding is used to color the tractogram (left-right: red, anterior-posterior: green, superior-inferior: blue). (c) Correlational tractography shows connections correlated with aphasia severity in a stroke study with participants ranged from 31 to 82 years of age (Hula et al., 2020). The tractogram is colored by directional colors. This new tractography modality tracks correlation along white matter pathways to map the precise segment of connections correlated with the study variable (e.g., aphasia severity). It can be used to probe the circuit mechanism underlying brain dysfunction in neurological disorders.

9.2. New tractography modalities

Another prospect of tractography is leveraging new tractography modalities to overcome existing limitations and enable novel clinical applications. One known limitation of tractography is that streamline counts do not have biological meaning (Johansen-Berg and Behrens, 2006; Jones and Cercignani, 2010; O'Donnell and Pasternak, 2014), and track trajectories are not informative for many brain diseases. This is because a subtle change in anisotropy or diffusivity does not necessarily imply a lower streamline count unless the anisotropy value plunges below the termination threshold. This anisotropy threshold can be a value as low as 0.1 for FA, and thus subtle changes above this threshold are not typically detectable by standard tractography. In attempting to address this limitation, studies have imbued tractography with diffusion information to closely associate the streamline counts with neuronal changes (Girard et al., 2017; Smith et al., 2013). Such enhanced tractography could be used in diagnostic or prognostic evaluation of brain diseases and other pathological conditions without resorting to diffusion metrics (Conti et al., 2017; Ziegler et al., 2014). These approaches can be instrumental in TBI, where axonal counts may decrease or increase post-injury depending on whether individual anatomic white matter connections are weakened or strengthened as the brain recovers.

More recently, a new tractography modality called *differential tractography* was introduced to map the exact segments of white matter tracts with decreased anisotropy (Yeh et al., 2019). The method included an additional termination criterion to the fiber tracking algo-

rithm, such that the resulting differential tractography could be used as a whole-brain screening tool to reveal pathways with subtle anisotropy differences in longitudinal studies (Fig. 10b). For group studies, a similar paradigm can be followed to track correlation along pathways and, thereby, to produce *correlational tractography* (Fig. 10c), whose results can be compared statistically using permutation tests (Yeh et al., 2016). Studies have shown that correlational tractography can reveal the structural mechanism behind brain function and dysfunction (Hula et al., 2020; Sanchez-Catasus et al., 2020). These new modalities warrant additional research to examine their clinical values as novel track-based imaging biomarkers.

Credit author statement

FY, AI, DBC, and AJG wrote the manuscript.

Data and code

The HCP data are available at <https://db.humanconnectome.org>. The Penthera 3T data are available at <https://zenodo.org/record/2602049>. The Traveling adults subjects data are available at https://figshare.com/articles/dataset/Multicenter_dataset_of_multishell_diffusion_magnetic_resonance_imaging_in_healthy_traveling_adults_with_identical_setting/8851955. The MRI data for clinical patients are not available to the public due to privacy issues. DSI Studio is available at <http://dsi-studio.labsolver.org> with

source code available at <https://github.com/frankyeh/DSI-Studio>. SlicerDMRI is available at <http://dmri.slicer.org/>

Declaration of Competing Interest

FY, AI, DBC, and AJG declare that this review was conducted in the absence of any commercial or financial relationship that could be construed as a potential conflict of interest.

Acknowledgment

AI is supported by NIH grant R01 NS 100973, by DoD award W81XWH-1810413, and by a USC Hanson-Thorell Research Scholarship. AJG is supported by NIH grants U01 CA 199459 and P41 EB 015898, and by the Jennifer Oppenheimer Cancer Research Initiative. FY's work is partly supported by the Alba Tull Center for Neuro Imaging and Therapeutics funded by the Tull Family Foundation

References

Abhinav, K., Yeh, F.C., Mansouri, A., Zadeh, G., Fernandez-Miranda, J.C., 2015. High-definition fiber tractography for the evaluation of perilesional white matter tracts in high-grade glioma surgery. *Neuro. Oncol.* 17, 1199–1209.

Aganj, I., Lenglet, C., Sapiro, G., Yacoub, E., Ugurbil, K., Harel, N., 2010. Reconstruction of the orientation distribution function in single- and multiple-shell q-ball imaging within constant solid angle. *Magn. Reson. Med.* 64, 554–566.

Alexander, A.L., Hasan, K.M., Lazar, M., Tsuruda, J.S., Parker, D.L., 2001. Analysis of partial volume effects in diffusion-tensor MRI. *Magn. Reson. Med.* 45, 770–780.

Alexopoulos, G., Cikla, U., El Tecle, N., Kulkarni, N., Pierson, M., Mercier, P., Kemp, J., Coppens, J., Mahmoud, S., Sehi, M., Bucholz, R., Abdulrauf, S., 2019. The value of white matter tractography by diffusion tensor imaging in altering a neurosurgeon's operative plan. *World Neurosurg.* 132, e305–e313.

Aliotta, E., Moulins, K., Ennis, D.B., 2018. Eddy current-nulled convex optimized diffusion encoding (EN-CODE) for distortion-free diffusion tensor imaging with short echo times. *Magn. Reson. Med.* 79, 663–672.

Andersson, J.L., Skare, S., Ashburner, J., 2003. How to correct susceptibility distortions in spin-echo echo-planar images: application to diffusion tensor imaging. *Neuroimage* 20, 870–888.

Andersson, J.L., Sotiropoulos, S.N., 2015. Non-parametric representation and prediction of single- and multi-shell diffusion-weighted MRI data using Gaussian processes. *Neuroimage* 122, 166–176.

Andersson, J.L.R., Sotiropoulos, S.N., 2016. An integrated approach to correction for off-resonance effects and subject movement in diffusion MR imaging. *Neuroimage* 125, 1063–1078.

Arfanakis, K., Haughton, V.M., Carew, J.D., Rogers, B.P., Dempsey, R.J., Meyerand, M.E., 2002. Diffusion tensor MR imaging in diffuse axonal injury. *AJNR Am. J. Neuroradiol.* 23, 794–802.

Armstrong, R.C., Mierzwa, A.J., Marion, C.M., Sullivan, G.M., 2016. White matter involvement after TBI: Clues to axon and myelin repair capacity. *Exp. Neurol.* 328–333 275 Pt 3.

Assaf, Y., Basser, P.J., 2005. Composite hindered and restricted model of diffusion (CHARMED) MR imaging of the human brain. *Neuroimage* 27, 48–58.

Assaf, Y., Freidlin, R.Z., Rohde, G.K., Basser, P.J., 2004. New modeling and experimental framework to characterize hindered and restricted water diffusion in brain white matter. *Magn. Reson. Med.* 52, 965–978.

Avesani, P., McPherson, B., Hayashi, S., Caiafa, C.F., Henschel, R., Garyfallidis, E., Kitchell, L., Bullock, D., Patterson, A., Olivetti, E., Sporns, O., Saykin, A.J., Wang, L., Dinov, I., Hancock, D., Caron, B., Qian, Y., Pestilli, F., 2019. The open diffusion data derivatives, brain data upcycling via integrated publishing of derivatives and reproducible open cloud services. *Sci. Data* 6, 69.

Basser, P.J., Mattiello, J., LeBihan, D., 1994. Estimation of the effective self-diffusion tensor from the NMR spin echo. *J. Magn. Reson. B* 103, 247–254.

Basser, P.J., Pajevic, S., Pierpaoli, C., Duda, J., Aldroubi, A., 2000. In vivo fiber tractography using DT-MRI data. *Magn. Reson. Med.* 44, 625–632.

Bastiani, M., Cottaar, M., Fitzgibbon, S.P., Suri, S., Alfaro-Almagro, F., Sotiropoulos, S.N., Jbabdi, S., Andersson, J.L.R., 2019. Automated quality control for within and between studies diffusion MRI data using a non-parametric framework for movement and distortion correction. *Neuroimage* 184, 801–812.

Becker, D., Scherer, M., Neher, P., Jungk, C., Jesser, J., Pflüger, I., Brinster, R., Bendzus, M., Bruckner, T., Maier-Hein, K., 2020. Going Beyond Diffusion Tensor Imaging Tractography in Eloquent Glioma Surgery—High-Resolution Fiber Tractography: Q-Ball or Constrained Spherical Deconvolution? *World Neurosurg.* 134, e596–e609.

Behrens, T.E., Johansen-Berg, H., Woolrich, M.W., Smith, S.M., Wheeler-Kingshott, C.A., Boulby, P.A., Barker, G.J., Sillery, E.L., Sheehan, K., Ciccarelli, O., Thompson, A.J., Brady, J.M., Matthews, P.M., 2003a. Non-invasive mapping of connections between human thalamus and cortex using diffusion imaging. *Nat. Neurosci.* 6, 750–757.

Behrens, T.E., Woolrich, M.W., Jenkinson, M., Johansen-Berg, H., Nunes, R.G., Clare, S., Matthews, P.M., Brady, J.M., Smith, S.M., 2003b. Characterization and propagation of uncertainty in diffusion-weighted MR imaging. *Magn. Reson. Med.* 50, 1077–1088.

Breuer, F.A., Blaimer, M., Heidemann, R.M., Mueller, M.F., Griswold, M.A., Jakob, P.M., 2005. Controlled aliasing in parallel imaging results in higher acceleration (CAIPRI-NHA) for multi-slice imaging. *Magn. Reson. Med.* 53, 684–691.

Butts, K., Riederer, S.J., Ehman, R.L., Thompson, R.M., Jack, C.R., 1994. Interleaved echo planar imaging on a standard MRI system. *Magn. Reson. Med.* 31, 67–72.

Caeyenberghs, K., Leemans, A., Geurts, M., Linden, C.V., Smits-Engelsman, B.C., Sunaert, S., Swinnen, S.P., 2011. Correlations between white matter integrity and motor function in traumatic brain injury patients. *Neurorehabil. Neural Repair* 25, 492–502.

Caeyenberghs, K., Leemans, A., Leunissen, I., Gooijers, J., Michiels, K., Sunaert, S., Swinnen, S.P., 2014. Altered structural networks and executive deficits in traumatic brain injury patients. *Brain Struct. Funct.* 219, 193–209.

Cai, L.Y., Yang, Q., Hansen, C.B., Nath, V., Ramadass, K., Johnson, G.W., Conrad, B.N., Boyd, B.D., Begnoche, J.P., Beason-Held, L.L., Shafer, A.T., Resnick, S.M., Taylor, W.D., Price, G.R., Morgan, V.L., Rogers, B.P., Schilling, K.G., Landman, B.A., 2021. PreQual: An automated pipeline for integrated preprocessing and quality assurance of diffusion weighted MRI images. *Magn. Reson. Med.* 86, 456–470.

Callaghan, P.T., 1991. Principles of Nuclear Magnetic Resonance Microscopy. Oxford University Press.

Calvillo, M., Irimia, A., 2020. Neuroimaging and psychometric assessment of mild cognitive impairment after traumatic brain injury. *Front. Psychol.* 11, 1423.

Celtikci, P., Fernandes-Cabral, D.T., Yeh, F.C., Panesar, S.S., Fernandez-Miranda, J.C., 2018. Generalized q-sampling imaging fiber tractography reveals displacement and infiltration of fiber tracts in low-grade gliomas. *Neuroradiology* 60, 267–280.

Chen, Z., Tie, Y., Olubiyi, O., Rigolo, L., Mehrtash, A., Norton, I., Pasternak, O., Rath, Y., Golby, A.J., O'Donnell, L.J., 2015a. Reconstruction of the arcuate fasciculus for surgical planning in the setting of peritumoral edema using two-tensor unscented Kalman filter tractography. *Neuroimage: Clinical* 7, 815–822.

Chen, Z., Tie, Y., Olubiyi, O., Rigolo, L., Mehrtash, A., Norton, I., Pasternak, O., Rath, Y., Golby, A.J., O'Donnell, L.J., 2015b. Reconstruction of the arcuate fasciculus for surgical planning in the setting of peritumoral edema using two-tensor unscented Kalman filter tractography. *Neuroimage Clin.* 7, 815–822.

Cho, K.H., Yeh, C.H., Tournier, J.D., Chao, Y.P., Chen, J.H., Lin, C.P., 2008. Evaluation of the accuracy and angular resolution of q-ball imaging. *Neuroimage* 42, 262–271.

Christiaens, D., Reisert, M., Dhollander, T., Sunaert, S., Suetens, P., Maes, F., 2015. Global tractography of multi-shell diffusion-weighted imaging data using a multi-tissue model. *Neuroimage* 123, 89–101.

Cieslak, M., Cook, P.A., He, X., Yeh, F.C., Dhollander, T., Adebimpe, A., Aguirre, G.K., Basset, D.S., Betzel, R.F., Bourque, J., Cabral, L.M., Davatzikos, C., Detre, J.A., Earl, E., Elliott, M.A., Fadnavis, S., Fair, D.A., Foran, W., Fotiadis, P., Garyfallidis, E., Giesbrecht, B., Gur, R.C., Gur, R.E., Kelz, M.B., Keshavan, A., Larsen, B.S., Luna, B., Mackey, A.P., Milham, M.P., Oathes, D.J., Perrone, A., Pines, A.R., Roalf, D.R., Richie-Halford, A., Rokem, A., Sydnor, V.J., Taper, T.M., Tooley, U.A., Vettel, J.M., Yeatman, J.D., Grafton, S.T., Satterthwaite, T.D., 2021. QSIprep: an integrative platform for preprocessing and reconstructing diffusion MRI data. *Nat. Methods* 18, 775–778.

Coenen, V.A., Allert, N., Madler, B., 2011. A role of diffusion tensor imaging fiber tracking in deep brain stimulation surgery: DBS of the dentato-rubro-thalamic tract (drt) for the treatment of therapy-refractory tremor. *Acta Neurochir. (Wien)* 153, 1579–1585 discussion 1585.

Coenen, V.A., Krings, T., Mayfrank, L., Polin, R.S., Reinges, M.H., Thron, A., Gilsbach, J.M., 2001. Three-dimensional visualization of the pyramidal tract in a neuronavigation system during brain tumor surgery: first experiences and technical note. *Neurosurgery* 49, 86–92 discussion 92–83.

Conti, E., Mitra, J., Calderoni, S., Pannek, K., Shen, K.K., Pagnozzi, A., Rose, S., Maz-zotti, S., Scelfo, D., Tosetti, M., Muratori, F., Cioni, G., Guzzetta, A., 2017. Network over-connectivity differentiates autism spectrum disorder from other developmental disorders in toddlers: a diffusion MRI study. *Hum. Brain Mapp.* 38, 2333–2344.

Cottaar, M., Bastiani, M., Boddu, N., Glasser, M.F., Haber, S., van Essen, D.C., Sotiropoulos, S.N., Jbabdi, S., 2020. Modelling white matter in gyral blades as a continuous vector field. *Neuroimage* 227, 117693.

Craddock, R.C., Jbabdi, S., Yan, C.G., Vogelstein, J.T., Castellanos, F.X., Di Martino, A., Kelly, C., Heberlein, K., Colcombe, S., Milham, M.P., 2013. Imaging human connectomes at the macroscale. *Nat. Methods* 10, 524–539.

Cross, A.H., Song, S.K., 2017. A new imaging modality to non-invasively assess multiple sclerosis pathology. *J. Neuroimmunol.* 304, 81–85.

Dell'acqua, F., Scifo, P., Rizzo, G., Catani, M., Simmons, A., Scotti, G., Fazio, F., 2009. A modified damped Richardson-Lucy algorithm to reduce isotropic background effects in spherical deconvolution. *Neuroimage* 49, 1446–1458.

Descoteaux, M., Angelino, E., Fitzgibbons, S., Deriche, R., 2007. Regularized, fast, and robust analytical Q-ball imaging. *Magn. Reson. Med.* 58, 497–510.

Descoteaux, M., Deriche, R., Knosche, T.R., Anwander, A., 2009. Deterministic and probabilistic tractography based on complex fibre orientation distributions. *IEEE Trans. Med. Imaging* 28, 269–286.

Dodd, A.B., Epstein, K., Ling, J.M., Mayer, A.R., 2014. Diffusion tensor imaging findings in semi-acute mild traumatic brain injury. *J. Neurotrauma* 31, 1235–1248.

Duffau, H., 2014. The dangers of magnetic resonance imaging diffusion tensor tractography in brain surgery. *World Neurosurg.* 81, 56–58.

Eierud, C., Craddock, R.C., Fletcher, S., Aulakh, M., King-Casas, B., Kuehl, D., La-Conte, S.M., 2014. Neuroimaging after mild traumatic brain injury: review and meta-analysis. *Neuroimage Clin.* 4, 283–294.

Ewing-Cobbs, L., Johnson, C.P., Juranek, J., DeMaster, D., Prasad, M., Duque, G., Kramer, L., Cox, C.S., Swank, P.R., 2016. Longitudinal diffusion tensor imaging after pediatric traumatic brain injury: impact of age at injury and time since injury on pathway integrity. *Hum. Brain Mapp.* 37, 3929–3945.

Fagerholm, E.D., Hellyer, P.J., Scott, G., Leech, R., Sharp, D.J., 2015. Disconnection

- of network hubs and cognitive impairment after traumatic brain injury. *Brain* 138, 1696–1709.
- Fan, Q., Nummenmaa, A., Witzel, T., Zanzonico, R., Keil, B., Cauley, S., Polimeni, J.R., Tisdall, D., Van Dijk, K.R., Buckner, R.L., Wedeen, V.J., Rosen, B.R., Wald, L.L., 2014. Investigating the capability to resolve complex white matter structures with high b-value diffusion magnetic resonance imaging on the MGH-USC Connectom scanner. *Brain Connect.* 4, 718–726.
- Farquharson, S., Tournier, J.-D., Calamante, F., Fabin, G., Schneider-Kolsky, M., Jackson, G.D., Connelly, A., 2013. White matter fiber tractography: why we need to move beyond DTI. *J. Neurosurg.* 118, 1367–1377.
- Fekonja, L., Wang, Z., Bahrend, I., Rosenstock, T., Rosler, J., Wallmeroth, L., Vajkoczy, P., Picht, T., 2019. Manual for clinical language tractography. *Acta Neurochir. (Wien)* 161, 1125–1137.
- Fekonja, L.S., Wang, Z., Aydogan, D.B., Roine, T., Engelhardt, M., Dreyer, F.R., Vajkoczy, P., Picht, T., 2020. Detecting corticospinal tract impairment in tumor patients with fiber density and tensor-based metrics. *Front. Oncol.* 10, 622358.
- Fernandez-Miranda, J.C., Pathak, S., Engh, J., Jarbo, K., Verstyne, T., Yeh, F.C., Wang, Y., Mintz, A., Boada, F., Schneider, W., Friedlander, R., 2012. High-definition fiber tractography of the human brain: neuroanatomical validation and neurosurgical applications. *Neurosurgery* 71, 430–453.
- Fieremans, E., Jensen, J.H., Helpert, J.A., 2011. White matter characterization with diffusion kurtosis imaging. *Neuroimage* 58, 177–188.
- Fillard, P., Descoteaux, M., Goh, A., Gouttard, S., Jeurissen, B., Malcolm, J., Ramirez-Manzanares, A., Reisert, M., Sakaie, K., Tensaouti, F., 2011. Quantitative evaluation of 10 tractography algorithms on a realistic diffusion MR phantom. *Neuroimage* 56, 220–234.
- Finsterbusch, J., 2009. Eddy-current compensated diffusion weighting with a single refocusing RF pulse. *Magn. Reson. Med.* 61, 748–754.
- Gangolli, M., Holleran, L., Hee Kim, J., Stein, T.D., Alvarez, V., McKee, A.C., Brody, D.L., 2017. Quantitative validation of a nonlinear histology-MRI coregistration method using generalized Q-sampling imaging in complex human cortical white matter. *Neuroimage* 153, 152–167.
- Garyfallidis, E., Cote, M.A., Rheault, F., Sidhu, J., Hau, J., Petit, L., Fortin, D., Cunanne, S., Descoteaux, M., 2018. Recognition of white matter bundles using local and global streamline-based registration and clustering. *Neuroimage* 170, 283–295.
- Genc, S., Tax, C.M.W., Raven, E.P., Chamberland, M., Parker, G.D., Jones, D.K., 2020. Impact of b-value on estimates of apparent fibre density. *Hum. Brain Mapp.* 41, 2583–2595.
- Girard, G., Daducci, A., Petit, L., Thiran, J.P., Whittingstall, K., Deriche, R., Wassermann, D., Descoteaux, M., 2017. AxTract: Toward microstructure informed tractography. *Hum. Brain Mapp.* 38, 5485–5500.
- Glasser, M.F., Rilling, J.K., 2008. DTI tractography of the human brain's language pathways. *Cerebral Cortex* 18, 2471–2482.
- Golby, A.J., Kindlmann, G., Norton, I., Yarmarkovich, A., Pieper, S., Kikinis, R., 2011. Interactive diffusion tensor tractography visualization for neurosurgical planning. *Neurosurgery* 68, 496–505.
- Gong, S., Zhang, F., Norton, I., Essayed, W.I., Unadkat, P., Rigolo, L., Pasternak, O., Rath, Y., Hou, L., Golby, A.J., 2018. Free water modeling of peritumoral edema using multi-fiber tractography: application to tracking the arcuate fasciculus for neurosurgical planning. *PLoS One* 13, e0197056.
- Grist, G., Haber, S.N., Yendiki, A., 2021. Diffusion MRI and anatomic tracing in the same brain reveal common failure modes of tractography. *Neuroimage*, 118300.
- Guevara, P., Duclap, D., Poupon, C., Marrakchi-Kacem, L., Fillard, P., Le Bihan, D., Leboyer, M., Houenou, J., Mangin, J.F., 2012. Automatic fiber bundle segmentation in massive tractography datasets using a multi-subject bundle atlas. *Neuroimage* 61, 1083–1099.
- Guo, F., de Luca, A., Parker, G., Jones, D.K., Viergever, M.A., Leemans, A., Tax, C.M.W., 2021. The effect of gradient nonlinearities on fiber orientation estimates from spherical deconvolution of diffusion magnetic resonance imaging data. *Hum. Brain Mapp.* 42, 367–383.
- Hansen, B., Jespersen, S.N., 2017. Recent developments in fast kurtosis imaging. *Front. Phys.* 5.
- Hansen, C.B., Nath, V., Hainline, A.E., Schilling, K.G., Parvathaneni, P., Bayrak, R.G., Blaber, J.A., Irfanoglu, O., Pierpaoli, C., Anderson, A.W., Rogers, B.P., Landman, B.A., 2019. Characterization and correlation of signal drift in diffusion weighted MRI. *Magn. Reson. Imaging* 57, 133–142.
- Henderson, F., Abdullah, K.G., Verma, R., Brem, S., 2020. Tractography and the connectome in neurosurgical treatment of gliomas: the premise, the progress, and the potential. *Neurosurg. Focus* 48, E6.
- Hervey-Jumper, S.L., Berger, M.S., 2019. Evidence for improving outcome through extent of resection. *Neurosurg. Clin. N. Am.* 30, 85–93.
- Hill, C.S., Coleman, M.P., Menon, D.K., 2016. Traumatic axonal injury: mechanisms and translational opportunities. *Trends Neurosci.* 39, 311–324.
- Hoefnagels, F.W., De Witt Hamer, P., Sanz-Arigita, E., Idema, S., Kuijter, J.P., Pouwels, P.J., Barkhof, F., Vandertop, W.P., 2014. Differentiation of edema and glioma infiltration: proposal of a DTI-based probability map. *J. Neurooncol.* 120, 187–198.
- Holdsworth, S.J., Skare, S., Newbould, R.D., Guzman, R., Blevins, N.H., Bammer, R., 2008. Readout-segmented EPI for rapid high resolution diffusion imaging at 3 T. *Eur. J. Radiol.* 65, 36–46.
- Hui, E.S., Cheung, M.M., Chan, K.C., Wu, E.X., 2010. B-value dependence of DTI quantitation and sensitivity in detecting neural tissue changes. *Neuroimage* 49, 2366–2374.
- Hula, W.D., Panesar, S., Gravier, M.L., Yeh, F.C., Dresang, H.C., Dickey, M.W., Fernandez-Miranda, J.C., 2020. Structural white matter connectometry of word production in aphasia: an observational study. *Brain* 143, 2532–2544.
- Ivlesmaki, T., Luoto, T.M., Hakulinen, U., Brander, A., Ryymin, P., Eskola, H., Iversen, G.L., Ohman, J., 2014. Acute mild traumatic brain injury is not associated with white matter change on diffusion tensor imaging. *Brain* 137, 1876–1882.
- Inglese, M., Makani, S., Johnson, G., Cohen, B.A., Silver, J.A., Gonen, O., Grossman, R.I., 2005. Diffuse axonal injury in mild traumatic brain injury: a diffusion tensor imaging study. *J. Neurosurg.* 103, 298–303.
- Irimia, A., Chambers, M.C., Torgerson, C.M., Filippou, M., Hovda, D.A., Alger, J.R., Gerig, G., Toga, A.W., Vespa, P.M., Kikinis, R., 2012. Patient-tailored connectomics visualization for the assessment of white matter atrophy in traumatic brain injury. *Front. Neurol.* 3, 10.
- Irimia, A., Goh, S.Y., Torgerson, C.M., Chambers, M.C., Kikinis, R., Van Horn, J.D., 2013a. Forward and inverse electroencephalographic modeling in health and in acute traumatic brain injury. *Clin. Neurophysiol.* 124, 2129–2145.
- Irimia, A., Maher, A.S., Chaudhari, N.N., Chowdhury, N.F., Jacobs, E.B., 2013b. Acute cognitive deficits after traumatic brain injury predict Alzheimer's disease-like degradation of the human default mode network. *Geroscience* 42, 1411–1429.
- Irimia, A., Torgerson, C.M., Goh, S.Y., Van Horn, J.D., 2015. Statistical estimation of physiological brain age as a descriptor of senescence rate during adulthood. *Brain Imaging Behav.* 9, 678–689.
- Irimia, A., Van Horn, J.D., 2015a. Epileptogenic focus localization in treatment-resistant post-traumatic epilepsy. *J. Clin. Neurosci.* 22, 627–631.
- Irimia, A., Van Horn, J.D., 2015b. Functional neuroimaging of traumatic brain injury: advances and clinical utility. *Neuropsychiatr. Dis. Treat.* 11, 2355–2365.
- Irimia, A., Van Horn, J.D., Vespa, P.M., 2018. Cerebral microhemorrhages due to traumatic brain injury and their effects on the aging human brain. *Neurobiol. Aging* 66, 158–164.
- Jakola, A.S., Unsgård, G., Myrmed, K.S., Kloster, R., Torp, S.H., Losvik, O.K., Lindal, S., Solheim, O., 2013. Surgical strategy in grade II astrocytoma: a population-based analysis of survival and morbidity with a strategy of early resection as compared to watchful waiting. *Acta Neurochir. (Wien)* 155, 2227–2235.
- Jeurissen, B., Leemans, A., Jones, D.K., Tournier, J.D., Sijbers, J., 2011. Probabilistic fiber tracking using the residual bootstrap with constrained spherical deconvolution. *Hum. Brain Mapp.* 32, 461–479.
- Jeurissen, B., Tournier, J.D., Dhollander, T., Connelly, A., Sijbers, J., 2014. Multi-tissue constrained spherical deconvolution for improved analysis of multi-shell diffusion MRI data. *Neuroimage* 103, 411–426.
- Johansen-Berg, H., Behrens, T.E.J., 2006. Just pretty pictures? What diffusion tractography can add in clinical neuroscience. *Curr. Opin. Neurol.* 19, 379.
- Jones, D.K., Cercignani, M., 2010. Twenty-five pitfalls in the analysis of diffusion MRI data. *NMR Biomed.* 23, 803–820.
- Karlskog, T.H., van Erp, T.G., Poldrack, R.A., Bearden, C.E., Nuechterlein, K.H., Cannon, T.D., 2008. Diffusion tensor imaging of the superior longitudinal fasciculus and working memory in recent-onset schizophrenia. *Biol. Psychiatry* 63, 512–518.
- Kawasaki, K., Matsumoto, M., Kase, M., Nagano, O., Aoyagi, K., Kageyama, T., 2017. Quantification of the radiation dose to the pyramidal tract using tractography in treatment planning for stereotactic radiosurgery. *Radiol. Phys. Technol.* 10, 507–514.
- Kinnunen, K.M., Greenwood, R., Powell, J.H., Leech, R., Hawkins, P.C., Bonnelle, V., Patel, M.C., Counsell, S.J., Sharp, D.J., 2011. White matter damage and cognitive impairment after traumatic brain injury. *Brain* 134, 449–463.
- Kinoshita, M., Yamada, K., Hashimoto, N., Kato, A., Izumoto, S., Baba, T., Maruno, M., Nishimura, T., Yoshimine, T., 2005. Fiber-tracking does not accurately estimate size of fiber bundle in pathological condition: initial neurosurgical experience using neuronavigation and subcortical white matter stimulation. *Neuroimage* 25, 424–429.
- Knösche, T.R., Anwander, A., Liptrot, M., Dyrby, T.B., 2015. Validation of tractography: comparison with manganese tracing. *Hum. Brain Mapp.* 36, 4116–4134.
- Koga, T., Maruyama, K., Kamada, K., Ota, T., Shin, M., Itoh, D., Kunii, N., Ino, K., Terahara, A., Aoki, S., Masutani, Y., Saito, N., 2012. Outcomes of diffusion tensor tractography-integrated stereotactic radiosurgery. *Int. J. Radiat. Oncol. Biol. Phys.* 82, 799–802.
- Kristo, G., Leemans, A., de Gelder, B., Raemaekers, M., Rutten, G.-J., Ramsey, N., 2013. Reliability of the corticospinal tract and arcuate fasciculus reconstructed with DTI-based tractography: implications for clinical practice. *Eur. Radiol.* 23, 28–36.
- Kristo, G., Leemans, A., de Gelder, B., Raemaekers, M., Rutten, G.J., Ramsey, N., 2012. Reliability of the corticospinal tract and arcuate fasciculus reconstructed with DTI-based tractography: implications for clinical practice. *Eur. Radiol.*
- Kuhnt, D., Bauer, M.H., Becker, A., Merhof, D., Zolal, A., Richter, M., Grummich, P., Ganslandt, O., Buchfelder, M., Nimsky, C., 2012. Intraoperative visualization of fiber tracking based reconstruction of language pathways in glioma surgery. *Neurosurgery* 70, 911–919 discussion 919–920.
- Kumar, R., Gupta, R.K., Husain, M., Chaudhry, C., Srivastava, A., Saksena, S., Rathore, R.K., 2009. Comparative evaluation of corpus callosum DTI metrics in acute mild and moderate traumatic brain injury: its correlation with neuropsychometric tests. *Brain Inj.* 23, 675–685.
- Kupper, H., Groeschel, S., Alber, M., Klose, U., Schuhmann, M.U., Wilke, M., 2015. Comparison of different tractography algorithms and validation by intraoperative stimulation in a child with a brain tumor. *Neuropediatrics* 46, 72–75.
- Lacroix, M., Abi-Said, D., Fournay, D.R., Gokaslan, Z.L., Shi, W., DeMonte, F., Lang, F.F., McCutcheon, I.E., Hassenbusch, S.J., Holland, E., Hess, K., Michael, C., Miller, D., Sawaya, R., 2001. A multivariate analysis of 416 patients with glioblastoma multiforme: prognosis, extent of resection, and survival. *J. Neurosurg.* 95, 190–198.
- Laitinen, T., Sierra, A., Bolkvadze, T., Pitkanen, A., Grohn, O., 2015. Diffusion tensor imaging detects chronic microstructural changes in white and gray matter after traumatic brain injury in rat. *Front. Neurosci.* 9, 128.
- Leclercq, D., Duffau, H., Delmaire, C., Capelle, L., Gatignol, P., Ducros, M., Chiras, J., Lehericy, S., 2010a. Comparison of diffusion tensor imaging tractography of language tracts and intraoperative subcortical stimulations. *J. Neurosurg.* 112, 503–511.
- Leclercq, D., Duffau, H., Delmaire, C., Capelle, L., Gatignol, P., Ducros, M., Chiras, J.,

- Lhéricy, S., 2010b. Comparison of diffusion tensor imaging tractography of language tracts and intraoperative subcortical stimulations. *J. Neurosurg.* 112, 503–511.
- Li, J., Zhao, C., Rao, J.S., Yang, F.X., Wang, Z.J., Lei, J.F., Yang, Z.Y., Li, X.G., 2017. Structural and metabolic changes in the traumatically injured rat brain: high-resolution in vivo proton magnetic resonance spectroscopy at 7 T. *Neuroradiology* 59, 1203–1212.
- Li, Y.M., Suki, D., Hess, K., Sawaya, R., 2016. The influence of maximum safe resection of glioblastoma on survival in 1229 patients: can we do better than gross-total resection? *J. Neurosurg.* 124, 977–988.
- Lipton, M.L., Gulko, E., Zimmerman, M.E., Friedman, B.W., Kim, M., Gellera, E., Gold, T., Shifteh, K., Ardekani, B.A., Branch, C.A., 2009. Diffusion-tensor imaging implicates prefrontal axonal injury in executive function impairment following very mild traumatic brain injury. *Radiology* 252, 816–824.
- Lo, C., Shifteh, K., Gold, T., Bello, J.A., Lipton, M.L., 2009. Diffusion tensor imaging abnormalities in patients with mild traumatic brain injury and neurocognitive impairment. *J. Comput. Assist. Tomogr.* 33, 293–297.
- Lodygensky, G.A., West, T., Stump, M., Holtzman, D.M., Inder, T.E., Neil, J.J., 2010. In vivo MRI analysis of an inflammatory injury in the developing brain. *Brain Behav. Immun.* 24, 759–767.
- Maier-Hein, K.H., Neher, P.F., Houde, J.C., Cote, M.A., Garyfallidis, E., Zhong, J., Chamberland, M., Yeh, F.C., Lin, Y.C., Ji, Q., Reddick, W.E., Glass, J.O., Chen, D.Q., Feng, Y., Gao, C., Wu, Y., Ma, J., He, R., Li, Q., Westin, C.F., Deslauriers-Gauthier, S., Gonzalez, J.O.O., Paquette, M., St-Jean, S., Girard, G., Rheault, F., Sidhu, J., Tax, C.M.W., Guo, F., Mesri, H.Y., David, S., Froeling, M., Heemskerk, A.M., Leemans, A., Bore, A., Pinsard, B., Bedetti, C., Desrosiers, M., Brambati, S., Doyon, J., Sarica, A., Vasta, R., Cerasa, A., Quattrone, A., Yeatman, J., Khan, A.R., Hodges, W., Alexander, S., Romascano, D., Barakovic, M., Auria, A., Esteban, O., Lemkaddem, A., Thiran, J.P., Cetingul, H.E., Odry, B.L., Mailhe, B., Nadar, M.S., Pizzagalli, F., Prasad, G., Villalón-Reina, J.E., Galvis, J., Thompson, P.M., Requejo, F.S., Laguna, P.L., Lacerda, L.M., Barrett, R., Dell'Acqua, F., Catani, M., Petit, L., Caruyer, E., Daducci, A., Dyrbj, T.B., Holland-Letz, T., Hilgetag, C.C., Stieltjes, B., Descoteaux, M., 2017. The challenge of mapping the human connectome based on diffusion tractography. *Nat. Commun.* 8, 1349.
- Makris, N., Kennedy, D.N., McInerney, S., Sorensen, A.G., Wang, R., Caviness Jr., V.S., Pandya, D.N., 2005. Segmentation of subcomponents within the superior longitudinal fascicle in humans: a quantitative, in vivo, DT-MRI study. *Cereb. Cortex* 15, 854–869.
- Malyarenko, D.I., Ross, B.D., Chenevert, T.L., 2014. Analysis and correction of gradient nonlinearity bias in apparent diffusion coefficient measurements. *Magn. Reson. Med.* 71, 1312–1323.
- Martino, J., Hamer, P.C.D.W., Berger, M.S., Lawton, M.T., Arnold, C.M., de Lucas, E.M., Duffau, H., 2013. Analysis of the subcomponents and cortical terminations of the perisylvian superior longitudinal fasciculus: a fiber dissection and DTI tractography study. *Brain Struct. Funct.* 218, 105–121.
- Maruyama, K., Kamada, K., Shin, M., Itoh, D., Aoki, S., Masutani, Y., Tago, M., Kirino, T., 2005. Integration of three-dimensional corticospinal tractography into treatment planning for gamma knife surgery. *J. Neurosurg.* 102, 673–677.
- Maruyama, K., Kamada, K., Shin, M., Itoh, D., Masutani, Y., Ino, K., Tago, M., Saito, N., 2007. Optic radiation tractography integrated into simulated treatment planning for Gamma Knife surgery. *J. Neurosurg.* 107, 721–726.
- Maruyama, K., Koga, T., Kamada, K., Ota, T., Itoh, D., Ino, K., Igaki, H., Aoki, S., Masutani, Y., Shin, M., Saito, N., 2009. Arcuate fasciculus tractography integrated into Gamma Knife surgery. *J. Neurosurg.* 111, 520–526.
- Mato, D., Velasquez, C., Gómez, E., Marco de Lucas, E., Martino, J., 2021. Predicting the extent of resection in low-grade glioma by using intratumoral tractography to detect eloquent fascicles within the tumor. *Neurosurgery* 88, E190–e202.
- Maudsley, A.A., Govind, V., Levin, B., Saigal, G., Harris, L., Sheriff, S., 2015. Distributions of magnetic resonance diffusion and spectroscopy measures with traumatic brain injury. *J. Neurotrauma* 32, 1056–1063.
- Mesri, H.Y., David, S., Viergever, M.A., Leemans, A., 2020. The adverse effect of gradient nonlinearities on diffusion MRI: from voxels to group studies. *Neuroimage* 205, 116127.
- Miles, L., Grossman, R.I., Johnson, G., Babb, J.S., Diller, L., Inglese, M., 2008. Short-term DTI predictors of cognitive dysfunction in mild traumatic brain injury. *Brain Inj.* 22, 115–122.
- Miller, J.A., Ding, S.L., Sunkin, S.M., Smith, K.A., Ng, L., Zafer, A., Ebbert, A., Riley, Z.L., Royall, J.J., Aiona, K., Arnold, J.M., Bennett, C., Bertagnolli, D., Brouner, K., Butler, S., Caldejon, S., Carey, A., Cuhacian, C., Dalley, R.A., Dee, N., Dolbear, T.A., Facer, B.A., Feng, D., Fliess, T.P., Gee, G., Goldy, J., Gourley, L., Gregor, B.W., Gu, G., Howard, R.E., Jochim, J.M., Kuan, C.L., Lau, C., Lee, C.K., Lee, F., Lemon, T.A., Lesnar, P., McMurray, B., Mastan, N., Mosqueda, N., Nalua-Cecchini, T., Ngo, N.K., Nyhus, J., Oldre, A., Olson, E., Parente, J., Parker, P.D., Parry, S.E., Stevens, A., Pletikos, M., Reding, M., Roll, K., Sandman, D., Sarreal, M., Shapouri, S., Shapovalova, N.V., Shen, E.H., Sjoquist, N., Slaughterbeck, C.R., Smith, M., Sotd, A.J., Williams, D., Zollei, L., Fischl, B., Gerstein, M.B., Geschwind, D.H., Glass, I.A., Hawrylycz, M.J., Hevner, R.F., Huang, H., Jones, A.R., Knowles, J.A., Levitt, P., Phillips, J.W., Sestan, N., Wahnoutka, P., Dang, C., Bernard, A., Hohmann, J.G., Lein, E.S., 2014. Transcriptional landscape of the prenatal human brain. *Nature* 508, 199–206.
- Min, Z.G., Niu, C., Rana, N., Ji, H.M., Zhang, M., 2013. Differentiation of pure vasogenic edema and tumor-infiltrated edema in patients with peritumoral edema by analyzing the relationship of axial and radial diffusivities on 3.0T MRI. *Clin. Neurol. Neurosurg.* 115, 1366–1370.
- Mori, S., Crain, B.J., Chacko, V.P., van Zijl, P.C., 1999. Three-dimensional tracking of axonal projections in the brain by magnetic resonance imaging. *Ann. Neurol.* 45, 265–269.
- Narayana, P.A., Yu, X., Hasan, K.M., Wilde, E.A., Levin, H.S., Hunter, J.V., Miller, E.R., Patel, V.K., Robertson, C.S., McCarthy, J.J., 2015. Multi-modal MRI of mild traumatic brain injury. *Neuroimage Clin.* 7, 87–97.
- Neher, P.F., Descoteaux, M., Houde, J.-C., Stieltjes, B., Maier-Hein, K.H., 2015. Strengths and weaknesses of state of the art fiber tractography pipelines—a comprehensive in-vivo and phantom evaluation study using Tractometer. *Med. Image Anal.* 26, 287–305.
- Nimsky, C., 2014. Fiber tracking—we should move beyond diffusion tensor imaging. *World Neurosurg.* 82, 35–36.
- Nimsky, C., Ganslandt, O., Fahlbusch, R., 2006. Implementation of fiber tract navigation. *Neurosurgery* 58 ONS-292-303; discussion ONS-303-294.
- Nimsky, C., Ganslandt, O., Hastreiter, P., Wang, R., Benner, T., Sorensen, A.G., Fahlbusch, R., 2005. Preoperative and intraoperative diffusion tensor imaging-based fiber tracking in glioma surgery. *Neurosurgery* 56, 130–137 discussion 138.
- Norton, I., Essayed, W.I., Zhang, F., Pujol, S., Yarmarkovich, A., Golby, A.J., Kindlmann, G., Wassermann, D., Estepar, R.S.J., Rathi, Y., 2017. SlicerDMRI: open source diffusion MRI software for brain cancer research. *Cancer Res.* 77, e101–e103.
- O'Donnell, L.J., Pasternak, O., 2014. Does diffusion MRI tell us anything about the white matter? An overview of methods and pitfalls. *Schizophr. Res.*
- O'Donnell, L.J., Westin, C.F., 2007. Automatic tractography segmentation using a high-dimensional white matter atlas. *IEEE Trans. Med. Imaging* 26, 1562–1575.
- O'Donnell, L.J., Suter, Y., Rigolo, L., Kahali, P., Zhang, F., Norton, I., Albi, A., Olubiyi, O., Meola, A., Essayed, W.I., 2017. Automated white matter fiber tract identification in patients with brain tumors. *Neuroimage: Clinical* 13, 138–153.
- Ozarslan, E., Koay, C.G., Shepherd, T.M., Komlosh, M.E., Irfanoglu, M.O., Pierpaoli, C., Basser, P.J., 2013. Mean apparent propagator (MAP) MRI: a novel diffusion imaging method for mapping tissue microstructure. *Neuroimage* 78, 16–32.
- Pantelis, E., Papadakis, N., Verigos, K., Stathochristopoulou, I., Antypas, C., Lekas, L., Tzouras, A., Georgiou, E., Salvaras, N., 2010. Integration of functional MRI and white matter tractography in stereotactic radiosurgery clinical practice. *Int. J. Radiat. Oncol. Biol. Phys.* 78, 257–267.
- Paquette, M., Gilbert, G., M., D., 2019. Penthera 3T. Zenodo.
- Park, E., McKnight, S., Ai, J., Baker, A.J., 2006. Purkinje cell vulnerability to mild and severe forebrain head trauma. *J. Neuropathol. Exp. Neurol.* 65, 226–234.
- Parker, G.D., Marshall, A.D., Rosin, P.L., Drage, N., Richmond, S., Jones, D.K., 2013. A pitfall in the reconstruction of fibre ODFs using spherical deconvolution of diffusion MRI data. *Neuroimage* 65, 433–448.
- Pasternak, O., Sochen, N., Gur, Y., Intrator, N., Assaf, Y., 2009. Free water elimination and mapping from diffusion MRI. *Magn. Reson. Med.* 62, 717–730.
- Perrone, D., Aelterman, J., Pizurica, A., Jeurissen, B., Philips, W., Leemans, A., 2015. The effect of Gibbs ringing artifacts on measures derived from diffusion MRI. *Neuroimage* 120, 441–455.
- Petrie, E.C., Cross, D.J., Yarnykh, V.L., Richards, T., Martin, N.M., Pagulayan, K., Hoff, D., Hart, K., Mayer, C., Tarabochia, M., Raskind, M.A., Minoshima, S., Peskind, E.R., 2014. Neuroimaging, behavioral, and psychological sequelae of repetitive combined blast/impact mild traumatic brain injury in Iraq and Afghanistan war veterans. *J. Neurotrauma* 31, 425–436.
- Provenzale, J.M., McGraw, P., Mhatre, P., Guo, A.C., Delong, D., 2004. Peritumoral brain regions in gliomas and meningiomas: investigation with isotropic diffusion-weighted MR imaging and diffusion-tensor MR imaging. *Radiology* 232, 451–460.
- Pujol, S., Wells, W., Pierpaoli, C., Brun, C., Gee, J., Cheng, G., Vemuri, B., Commowick, O., Prima, S., Stamm, A., 2015. The DTI challenge: toward standardized evaluation of diffusion tensor imaging tractography for neurosurgery. *J. Neuroimaging* 25, 875–882.
- Qazi, A.A., Radmanesh, A., O'Donnell, L., Kindlmann, G., Peled, S., Whalen, S., Westin, C.F., Golby, A.J., 2009. Resolving crossings in the corticospinal tract by two-tensor streamline tractography: Method and clinical assessment using fMRI. *Neuroimage* 47 (2), T98–T106 Suppl.
- Radmanesh, A., Zamani, A.A., Whalen, S., Tie, Y., Suarez, R.O., Golby, A.J., 2015. Comparison of seeding methods for visualization of the corticospinal tracts using single tensor tractography. *Clinical neurology and neurosurgery* 129, 44–49.
- Rahman, M., Abbattamatteo, J., De Leo, E.K., Kubilis, P.S., Vaziri, S., Bova, F., Sayour, E., Mitchell, D., Quinones-Hinojosa, A., 2017. The effects of new or worsened postoperative neurological deficits on survival of patients with glioblastoma. *J. Neurosurg.* 127, 123–131.
- Reese, T.G., Heid, O., Weisskoff, R.M., Wedeen, V.J., 2003. Reduction of eddy-current-induced distortion in diffusion MRI using a twice-refocused spin echo. *Magn. Reson. Med.* 49, 177–182.
- Reveley, C., Seth, A.K., Pierpaoli, C., Silva, A.C., Yu, D., Saunders, R.C., Leopold, D.A., Ye, F.Q., 2015. Superficial white matter fiber systems impede detection of long-range cortical connections in diffusion MR tractography. *Proc. Natl. Acad. Sci. U. S. A.* 112, E2820–E2828.
- Rheault, F., St-Onge, E., Sidhu, J., Maier-Hein, K., Tzourio-Mazoyer, N., Petit, L., Descoteaux, M., 2019. Bundle-specific tractography with incorporated anatomical and orientational priors. *Neuroimage* 186, 382–398.
- Rilling, J.K., Glasser, M.F., Preuss, T.M., Ma, X., Zhao, T., Hu, X., Behrens, T.E., 2008. The evolution of the arcuate fasciculus revealed with comparative DTI. *Nat. Neurosci.* 11, 426–428.
- Rokem, A., Yeatman, J.D., Pestilli, F., Kay, K.N., Mezer, A., van der Walt, S., Wandell, B.A., 2015. Evaluating the accuracy of diffusion MRI models in white matter. *PLoS One* 10, e0123272.
- Rostovsky, K.A., Maher, A.S., Irimia, A., 2018. Macroscale white matter alterations due to traumatic cerebral microhemorrhages are revealed by diffusion tensor imaging. *Front. Neurol.* 9.
- Salo, R.A., Belevich, I., Manninen, E., Jokitalo, E., Grohn, O., Sierra, A., 2018. Quantification of anisotropy and orientation in 3D electron microscopy and diffusion tensor imaging in injured rat brain. *Neuroimage* 172, 404–414.
- Sanchez-Catusas, C.A., Bohnen, N.I., Yeh, F.C., D'Cruz, N., Kanel, P., Muller, M., 2020.

- Dopaminergic nigrostriatal connectivity in early Parkinson disease: in vivo neuroimaging study of (11)C-DTBZ PET combined with correlational tractography. *J. Nucl. Med.*
- Sanvito, F., Caverzasi, E., Riva, M., Jordan, K.M., Blasi, V., Scifo, P., Iadanza, A., Crespi, S.A., Cirillo, S., Casarotti, A., Leonetti, A., Puglisi, G., Grimaldi, M., Bello, L., Gorno-Tempini, M.L., Henry, R.G., Falini, A., Castellano, A., 2020. fMRI-Targeted High-Angular Resolution Diffusion MR Tractography to Identify Functional Language Tracts in Healthy Controls and Glioma Patients. *Front. Neurosci.* 14, 225.
- Saur, D., Kreher, B.W., Schnell, S., Kummerer, D., Kellmeyer, P., Vry, M.S., Umarova, R., Musso, M., Glauche, V., Abel, S., Huber, W., Rijntjes, M., Hennig, J., Weiller, C., 2008. Ventral and dorsal pathways for language. *Proc. Natl. Acad. Sci. U. S. A.* 105, 18035–18040.
- Schilling, K., Gao, Y., Janve, V., Stepniewska, I., Landman, B.A., Anderson, A.W., 2018a. Confirmation of a gyral bias in diffusion MRI fiber tractography. *Hum. Brain Mapp.* 39, 1449–1466.
- Schilling, K., Janve, V., Gao, Y., Stepniewska, I., Landman, B.A., Anderson, A.W., 2016. Comparison of 3D orientation distribution functions measured with confocal microscopy and diffusion MRI. *Neuroimage* 129, 185–197.
- Schilling, K.G., Gao, Y., Stepniewska, I., Janve, V., Landman, B.A., Anderson, A.W., 2019a. Histologically derived fiber response functions for diffusion MRI vary across white matter fibers—An ex vivo validation study in the squirrel monkey brain. *NMR Biomed.* 32, e4090.
- Schilling, K.G., Janve, V., Gao, Y., Stepniewska, I., Landman, B.A., Anderson, A.W., 2018b. Histological validation of diffusion MRI fiber orientation distributions and dispersion. *Neuroimage* 165, 200–221.
- Schilling, K.G., Nath, V., Hansen, C., Parvathaneni, P., Blaber, J., Gao, Y., Neher, P., Aydogan, D.B., Shi, Y., Ocampo-Pineda, M., 2019b. Limits to anatomical accuracy of diffusion tractography using modern approaches. *Neuroimage* 185, 1–11.
- Schilling, K.G., Petit, L., Rheault, F., Remedios, S., Pierpaoli, C., Anderson, A.W., Landman, B.A., Descoteaux, M., 2020. Brain connections derived from diffusion MRI tractography can be highly anatomically accurate—if we know where white matter pathways start, where they end, and where they do not go. *Brain Struct. Funct.* 225, 2387–2402.
- Schilling, K.G., Rheault, F., Petit, L., Hansen, C.B., Nath, V., Yeh, F.-C., Girard, G., Barakovic, M., Rafael-Patino, J., Yu, T., 2021. Tractography dissection variability: what happens when 42 groups dissect 14 white matter bundles on the same dataset? *bioRxiv* 2020.2010. 2007.321083.
- Schmahmann, J.D., Pandya, D.N., Wang, R., Dai, G., D'Arceuil, H.E., de Crespigny, A.J., Wedeen, V.J., 2007. Association fibre pathways of the brain: parallel observations from diffusion spectrum imaging and autoradiography. *Brain* 130, 630–653.
- Schonberg, T., Pianka, P., Hendler, T., Pasternak, O., Assaf, Y., 2006. Characterization of displaced white matter by brain tumors using combined DTI and fMRI. *Neuroimage* 30, 1100–1111.
- Sclocco, R., Beissner, F., Bianciardi, M., Polimeni, J.R., Napadow, V., 2018. Challenges and opportunities for brainstem neuroimaging with ultrahigh field MRI. *Neuroimage* 168, 412–426.
- Setsompop, K., Cohen-Adad, J., Gagoski, B.A., Raij, T., Yendiki, A., Keil, B., Wedeen, V.J., Wald, L.L., 2012a. Improving diffusion MRI using simultaneous multi-slice echo planar imaging. *Neuroimage* 63, 569–580.
- Setsompop, K., Gagoski, B.A., Polimeni, J.R., Witzel, T., Wedeen, V.J., Wald, L.L., 2012b. Blipped-controlled aliasing in parallel imaging for simultaneous multislice echo planar imaging with reduced g-factor penalty. *Magn. Reson. Med.* 67, 1210–1224.
- Smith, R.E., Tournier, J.D., Calamante, F., Connelly, A., 2012. Anatomically-constrained tractography: improved diffusion MRI streamlines tractography through effective use of anatomical information. *Neuroimage* 62, 1924–1938.
- Smith, R.E., Tournier, J.D., Calamante, F., Connelly, A., 2013. SIFT: Spherical-deconvolution informed filtering of tractograms. *Neuroimage* 67, 298–312.
- Smits, M., Vernooij, M.W., Wielopolski, P.A., Vincent, A.J., Houston, G.C., van der Lugt, A., 2007. Incorporating functional MR imaging into diffusion tensor tractography in the preoperative assessment of the corticospinal tract in patients with brain tumors. *AJNR Am. J. Neuroradiol.* 28, 1354–1361.
- Song, S.K., Sun, S.W., Ju, W.K., Lin, S.J., Cross, A.H., Neufeld, A.H., 2003. Diffusion tensor imaging detects and differentiates axon and myelin degeneration in mouse optic nerve after retinal ischemia. *Neuroimage* 20, 1714–1722.
- Song, S.K., Sun, S.W., Ramsbottom, M.J., Chang, C., Russell, J., Cross, A.H., 2002. Demyelination revealed through MRI as increased radial (but unchanged axial) diffusion of water. *Neuroimage* 17, 1429–1436.
- Song, S.K., Yoshino, J., Le, T.Q., Lin, S.J., Sun, S.W., Cross, A.H., Armstrong, R.C., 2005. Demyelination increases radial diffusivity in corpus callosum of mouse brain. *Neuroimage* 26, 132–140.
- Sosnovik, D.E., Wang, R., Dai, G., Reese, T.G., Wedeen, V.J., 2009. Diffusion MR tractography of the heart. *J. Cardiovasc. Magn. Resonance* 11, 1–15.
- Spanos, G., Wilde, E., Bigler, E., Cleavinger, H., Fearing, M., Levin, H., Li, X., Hunter, J., 2007. Cerebellar atrophy after moderate-to-severe pediatric traumatic brain injury. *Am. J. Neuroradiol.* 28, 537–542.
- Sporns, O., Tononi, G., Kotter, R., 2005. The human connectome: a structural description of the human brain. *PLoS Comput. Biol.* 1, e42.
- Stejskal, E.O., Tanner, J.E., 1965. Spin Diffusion Measurements: spin Echoes in the Presence of a Time-Dependent Field Gradient. *J. Chem. Phys.* 42, 288–292.
- Sullivan, S., Eucker, S.A., Gabrieli, D., Bradfield, C., Coats, B., Maltese, M.R., Lee, J., Smith, C., Margulies, S.S., 2015. White matter tract-oriented deformation predicts traumatic axonal brain injury and reveals rotational direction-specific vulnerabilities. *Biomech. Model. Mechanobiol.* 14, 877–896.
- Sun, S.W., Liang, H.F., Trinkaus, K., Cross, A.H., Armstrong, R.C., Song, S.K., 2006. Noninvasive detection of cuprizone induced axonal damage and demyelination in the mouse corpus callosum. *Magn. Reson. Med.* 55, 302–308.
- Tan, E.T., Marinelli, L., Slavens, Z.W., King, K.F., Hardy, C.J., 2013. Improved correction for gradient nonlinearities effects in diffusion-weighted imaging. *J. Magn. Reson. Imaging* 38, 448–453.
- Thomas, C., Ye, F.Q., Irfanoglu, M.O., Modi, P., Saleem, K.S., Leopold, D.A., Pierpaoli, C., 2014. Anatomical accuracy of brain connections derived from diffusion MRI tractography is inherently limited. *Proc. Natl. Acad. Sci. U. S. A.* 111, 16574–16579.
- Tong, Q., He, H., Gong, T., Li, C., Liang, P., Qian, T., Sun, Y., Ding, Q., Li, K., Zhong, J., 2020. Multicenter dataset of multi-shell diffusion MRI in healthy traveling adults with identical settings. *Sci. Data* 7, 157.
- Toth, A., Kovacs, N., Perlaki, G., Orsi, G., Aradi, M., Komaromy, H., Ezer, E., Bukovics, P., Farkas, O., Janszky, J., Doczi, T., Buki, A., Schwarcz, A., 2013. Multi-modal magnetic resonance imaging in the acute and sub-acute phase of mild traumatic brain injury: can we see the difference? *J. Neurotrauma* 30, 2–10.
- Tournier, J.D., Calamante, F., Connelly, A., 2007. Robust determination of the fibre orientation distribution in diffusion MRI: non-negativity constrained super-resolved spherical deconvolution. *Neuroimage* 35, 1459–1472.
- Tournier, J.D., Calamante, F., Gadian, D.G., Connelly, A., 2004. Direct estimation of the fiber orientation density function from diffusion-weighted MRI data using spherical deconvolution. *Neuroimage* 23, 1176–1185.
- Tournier, J.D., Mori, S., Leemans, A., 2011. Diffusion tensor imaging and beyond. *Magn. Reson. Med.* 65, 1532–1556.
- Tournier, J.D., Smith, R., Raffelt, D., Tabbara, R., Dhollander, T., Pietsch, M., Christiaens, D., Jeurissen, B., Yeh, C.H., Connelly, A., 2019. MRtrix3: a fast, flexible and open software framework for medical image processing and visualisation. *Neuroimage* 202, 116137.
- Tournier, J.D., Yeh, C.H., Calamante, F., Cho, K.H., Connelly, A., Lin, C.P., 2008. Resolving crossing fibres using constrained spherical deconvolution: validation using diffusion-weighted imaging phantom data. *Neuroimage* 42, 617–625.
- Tremblay, S., Henry, L.C., Bedetti, C., Larson-Dupuis, C., Gagnon, J.F., Evans, A.C., Theoret, H., Lassonde, M., De Beaumont, L., 2014. Diffuse white matter tract abnormalities in clinically normal ageing retired athletes with a history of sports-related concussions. *Brain* 137, 2997–3011.
- Trotter, B.B., Robinson, M.E., Milberg, W.P., McGlinchey, R.E., Salat, D.H., 2015. Military blast exposure, ageing and white matter integrity. *Brain* 138, 2278–2292.
- Tuch, D.S., 2004. Q-ball imaging. *Magn. Reson. Med.* 52, 1358–1372.
- Tuch, D.S., Reese, T.G., Wiegell, M.R., Makris, N., Belliveau, J.W., Wedeen, V.J., 2002. High angular resolution diffusion imaging reveals intravoxel white matter fiber heterogeneity. *Magn. Reson. Med.* 48, 577–582.
- Tuncer, M.S., Salvati, L.F., Grittner, U., Hardt, J., Schilling, R., Bahrend, I., Silva, L.L., Fekonja, L.S., Faust, K., Vajkoczy, P., Rosenstock, T., Picht, T., 2021. Towards a tractography-based risk stratification model for language area associated gliomas. *Neuroimage Clin.* 29, 102541.
- Van Essen, D.C., Ugurbil, K., Auerbach, E., Barch, D., Behrens, T.E., Bucholz, R., Chang, A., Chen, L., Corbetta, M., Curtiss, S.W., Della Penna, S., Feinberg, D., Glasser, M.F., Harel, N., Heath, A.C., Larson-Prior, L., Marcus, D., Michalareas, G., Moeller, S., Oostenveld, R., Petersen, S.E., Prior, F., Schlaggar, B.L., Smith, S.M., Snyder, A.Z., Xu, J., Yacoub, E., 2012. The Human Connectome Project: a data acquisition perspective. *Neuroimage* 62, 2222–2231.
- Van Horn, J.D., Bhattarai, A., Irimia, A., 2017. Multimodal imaging of neurometabolic pathology due to traumatic brain injury. *Trends Neurosci.* 40, 39–59.
- Vanderweyden, D.C., Theaud, G., Sidhu, J., Rheault, F., Sarubbo, S., Descoteaux, M., Fortin, D., 2020. The role of diffusion tractography in refining glial tumor resection. *Brain Struct. Funct.*
- Vanegas-Arroyave, N., Lauro, P.M., Huang, L., Hallett, M., Horovitz, S.G., Zaghlool, K.A., Lungu, C., 2016. Tractography patterns of subthalamic nucleus deep brain stimulation. *Brain* 139, 1200–1210.
- Veraart, J., Fieremans, E., Jolescu, I.O., Knoll, F., Novikov, D.S., 2016. Gibbs ringing in diffusion MRI. *Magn. Reson. Med.* 76, 301–314.
- Vos, S.B., Tax, C.M., Luijten, P.R., Ourselin, S., Leemans, A., Froeling, M., 2017. The importance of correcting for signal drift in diffusion MRI. *Magn. Reson. Med.* 77, 285–299.
- Wang, Y., Wang, Q., Haldar, J.P., Yeh, F.C., Xie, M., Sun, P., Tu, T.W., Trinkaus, K., Klein, R.S., Cross, A.H., Song, S.K., 2011. Quantification of increased cellularity during inflammatory demyelination. *Brain* 134, 3590–3601.
- Warrington, S., Bryant, K.L., Khrapitchev, A.A., Sallet, J., Charquero-Ballester, M., Douaud, G., Jbabdi, S., Mars, R.B., Sotiropoulos, S.N., 2020. XTRACT - Standardised protocols for automated tractography in the human and macaque brain. *Neuroimage* 217, 116923.
- Wassermann, D., Makris, N., Rathi, Y., Shenton, M., Kikinis, R., Kubicki, M., Westin, C.F., 2016. The white matter query language: a novel approach for describing human white matter anatomy. *Brain Struct. Funct.*
- Wasserthal, J., Neher, P., Maier-Hein, K.H., 2018. TractSeg - fast and accurate white matter tract segmentation. *Neuroimage* 183, 239–253.
- Wedeen, V.J., Hagmann, P., Tseng, W.Y., Reese, T.G., Weisskoff, R.M., 2005. Mapping complex tissue architecture with diffusion spectrum magnetic resonance imaging. *Magn. Reson. Med.* 54, 1377–1386.
- Wedeen, V.J., Rosene, D.L., Wang, R., Dai, G., Mortazavi, F., Hagmann, P., Kaas, J.H., Tseng, W.Y., 2012. The geometric structure of the brain fiber pathways. *Science* 335, 1628–1634.
- Wilkins, B., Lee, N., Gajawelli, N., Law, M., Lepore, N., 2015a. Fiber estimation and tractography in diffusion MRI: development of simulated brain images and comparison of multi-fiber analysis methods at clinical b-values. *Neuroimage* 109, 341–356.
- Wilkins, B., Lee, N., Gajawelli, N., Law, M., Lepore, N., 2015b. Fiber estimation and tractography in diffusion MRI: development of simulated brain images and comparison of multi-fiber analysis methods at clinical b-values. *Neuroimage* 109, 341–356.
- Winkiewicz, P.J., Sabisz, A., Naumczyk, P., Jodzio, K., Szurawska, E., Szurmach, A., 2018.

- Understanding the physiopathology behind axial and radial diffusivity changes-what do we know? *Front. Neurol.* 9, 92.
- Witwer, B.P., Mofattakhar, R., Hasan, K.M., Deshmukh, P., Haughton, V., Field, A., Arfanakis, K., Noyes, J., Moritz, C.H., Meyerand, M.E., Rowley, H.A., Alexander, A.L., Badie, B., 2002. Diffusion-tensor imaging of white matter tracts in patients with cerebral neoplasm. *J. Neurosurg.* 97, 568–575.
- Wooten, D.W., Ortiz-Teran, L., Zubcevik, N., Zhang, X., Huang, C., Sepulcre, J., Atassi, N., Johnson, K.A., Zafonte, R.D., El Fakhri, G., 2019. Multi-modal signatures of tau pathology, neuronal fiber integrity, and functional connectivity in traumatic brain injury. *J. Neurotrauma* 36, 3233–3243.
- Wright, D.K., Johnston, L.A., Kershaw, J., Ordidge, R., O'Brien, T.J., Shultz, S.R., 2017. Changes in apparent fiber density and track-weighted imaging metrics in white matter following experimental traumatic brain injury. *J. Neurotrauma* 34, 2109–2118.
- Wright, D.K., Trezise, J., Kamnaksh, A., Bekdash, R., Johnston, L.A., Ordidge, R., Semple, B.D., Gardner, A.J., Stanwell, P., O'Brien, T.J., Agoston, D.V., Shultz, S.R., 2016. Behavioral, blood, and magnetic resonance imaging biomarkers of experimental mild traumatic brain injury. *Sci. Rep.* 6, 28713.
- Wu, J.S., Zhou, L.F., Tang, W.J., Mao, Y., Hu, J., Song, Y.Y., Hong, X.N., Du, G.H., 2007. Clinical evaluation and follow-up outcome of diffusion tensor imaging-based functional neuronavigation: a prospective, controlled study in patients with gliomas involving pyramidal tracts. *Neurosurgery* 61, 935–948 discussion 948-939.
- Wu, W., Miller, K.L., 2017. Image formation in diffusion MRI: a review of recent technical developments. *J. Magn. Reson. Imaging* 46, 646–662.
- Wu, Y.C., Alexander, A.L., 2007. Hybrid diffusion imaging. *Neuroimage* 36, 617–629.
- Wu, Y.C., Mustafi, S.M., Harezlak, J., Kodiweera, C., Flashman, L.A., McAllister, T.W., 2018. Hybrid Diffusion Imaging in Mild Traumatic Brain Injury. *J. Neurotrauma* 35, 2377–2390.
- Xie, M., Tobin, J.E., Budde, M.D., Chen, C.I., Trinkaus, K., Cross, A.H., McDaniel, D.P., Song, S.K., Armstrong, R.C., 2010. Rostrocaudal analysis of corpus callosum demyelination and axon damage across disease stages refines diffusion tensor imaging correlations with pathological features. *J. Neuropathol. Exp. Neurol.* 69, 704–716.
- Yang, G., McNab, J.A., 2019. Eddy current nulled constrained optimization of isotropic diffusion encoding gradient waveforms. *Magn. Reson. Med.* 81, 1818–1832.
- Yang, J., Li, Q., Wang, Z., Qi, C., Han, X., Lan, X., Wan, J., Wang, W., Zhao, X., Hou, Z., Gao, C., Carhuapoma, J.R., Mori, S., Zhang, J., Wang, J., 2017. Multimodality MRI assessment of grey and white matter injury and blood-brain barrier disruption after intracerebral haemorrhage in mice. *Sci. Rep.* 7, 40358.
- Yeatman, J.D., Dougherty, R.F., Myall, N.J., Wandell, B.A., Feldman, H.M., 2012. Tract profiles of white matter properties: automating fiber-tract quantification. *PLoS One* 7, e49790.
- Yeh, F.C., 2020. Shape analysis of the human association pathways. *Neuroimage* 223, 117329.
- Yeh, F.C., Badre, D., Verstynen, T., 2016. Connectometry: a statistical approach harnessing the analytical potential of the local connectome. *Neuroimage* 125, 162–171.
- Yeh, F.C., Liu, L., Hitchens, T.K., Wu, Y.L., 2017. Mapping immune cell infiltration using restricted diffusion MRI. *Magn. Reson. Med.* 77, 603–612.
- Yeh, F.C., Panesar, S., Fernandes, D., Meola, A., Yoshino, M., Fernandez-Miranda, J.C., Vettel, J.M., Verstynen, T., 2018. Population-averaged atlas of the macroscale human structural connectome and its network topology. *Neuroimage* 178, 57–68.
- Yeh, F.C., Verstynen, T.D., Wang, Y., Fernandez-Miranda, J.C., Tseng, W.Y., 2013. Deterministic diffusion fiber tracking improved by quantitative anisotropy. *PLoS One* 8, e80713.
- Yeh, F.C., Wedeen, V.J., Tseng, W.Y., 2010. Generalized q-sampling imaging. *IEEE Trans. Med. Imaging* 29, 1626–1635.
- Yeh, F.C., Zaydan, I.M., Suski, V.R., Lacomis, D., Richardson, R.M., Maroon, J.C., Barrios-Martinez, J., 2019. Differential tractography as a track-based biomarker for neuronal injury. *Neuroimage* 202, 116131.
- Yendiki, A., Panneck, P., Srinivasan, P., Stevens, A., Zollei, L., Augustinack, J., Wang, R., Salat, D., Ehrlich, S., Behrens, T., Jbabdi, S., Gollub, R., Fischl, B., 2011. Automated probabilistic reconstruction of white-matter pathways in health and disease using an atlas of the underlying anatomy. *Front. Neuroinform.* 5, 23.
- Young, R.J., Knopp, E.A., 2006. Brain MRI: tumor evaluation. *J. Magn. Resonance Imaging* 24, 709–724.
- Yuh, E.L., Cooper, S.R., Mukherjee, P., Yue, J.K., Lingsma, H.F., Gordon, W.A., Valadka, A.B., Okonkwo, D.O., Schnyer, D.M., Vassar, M.J., Maas, A.I., Manley, G.T., Track-Tbi, I., 2014. Diffusion tensor imaging for outcome prediction in mild traumatic brain injury: a TRACK-TBI study. *J. Neurotrauma* 31, 1457–1477.
- Zhang, H., Schneider, T., Wheeler-Kingshott, C.A., Alexander, D.C., 2012. NODDI: practical in vivo neurite orientation dispersion and density imaging of the human brain. *Neuroimage* 61, 1000–1016.
- Zhang, H., Wang, Y., Lu, T., Qiu, B., Tang, Y., Ou, S., Tie, X., Sun, C., Xu, K., Wang, Y., 2013. Differences between generalized q-sampling imaging and diffusion tensor imaging in the preoperative visualization of the nerve fiber tracts within peritumoral edema in brain. *Neurosurgery* 73, 1044–1053 discussion 1053.
- Zhao, W., Cai, Y., Li, Z., Ji, S., 2017. Injury prediction and vulnerability assessment using strain and susceptibility measures of the deep white matter. *Biomech. Model. Mechanobiol.* 16, 1709–1727.
- Zhu, F.P., Wu, J.S., Song, Y.Y., Yao, C.J., Zhuang, D.X., Xu, G., Tang, W.J., Qin, Z.Y., Mao, Y., Zhou, L.F., 2012. Clinical application of motor pathway mapping using diffusion tensor imaging tractography and intraoperative direct subcortical stimulation in cerebral glioma surgery: a prospective cohort study. *Neurosurgery* 71, 1170–1183 discussion 1183-1174.
- Ziegler, E., Rouillard, M., Andre, E., Coolen, T., Stender, J., Balteau, E., Phillips, C., Garraux, G., 2014. Mapping track density changes in nigrostriatal and extranigral pathways in Parkinson's disease. *Neuroimage* 99, 498–508.
- Zolal, A., Hejčl, A., Vachata, P., Bartoš, R., Humhej, I., Malucelli, A., Nováková, M., Hrach, K., Derner, M., Sameš, M., 2012. The use of diffusion tensor images of the corticospinal tract in intrinsic brain tumor surgery: a comparison with direct subcortical stimulation. *Neurosurgery* 71, 331–340 discussion 340.
- Zollei, L., Jaimes, C., Saliba, E., Grant, P.E., Yendiki, A., 2019. TRActs constrained by UnderLying INfant anatomy (TRACULInA): an automated probabilistic tractography tool with anatomical priors for use in the newborn brain. *Neuroimage* 199, 1–17.



Older age, male sex, and cerebral microbleeds predict white matter loss after traumatic brain injury

David J. Robles · Ammar Dharani · Kenneth A. Rostowsky ·
Nikhil N. Chaudhari · Van Ngo · Fan Zhang · Lauren J. O'Donnell ·
Lauren Green · Nasim Sheikh-Bahaei · Helena C. Chui · Andrei Irimia 

Received: 12 August 2021 / Accepted: 11 September 2021 / Published online: 26 October 2021
© The Author(s), under exclusive licence to American Aging Association 2021

Abstract Little is known on how mild traumatic brain injury affects white matter based on age at injury, sex, cerebral microbleeds, and time since injury. Here, we study the fractional anisotropy of white matter to study these effects in 109 participants aged 18–77 (46 females, age $\mu \pm \sigma = 40 \pm 17$ years) imaged within ~ 1 week and ~ 6 months post-injury. Age is found to be linearly associated with white

matter degradation, likely due not only to injury but also to cumulative effects of other pathologies and to their interactions with injury. Age is associated with mean anisotropy decreases in the corpus callosum, middle longitudinal fasciculi, inferior longitudinal and occipitofrontal fasciculi, and superficial frontal and temporal fasciculi. Over ~ 6 months, the mean anisotropies of the corpus callosum, left superficial frontal fasciculi, and left corticospinal tract decrease significantly. Independently of other predictors, age and cerebral microbleeds contribute to anisotropy decrease in the callosal genu. Chronically, the white matter of commissural tracts, left superficial frontal fasciculi, and left corticospinal tract degrade appreciably, independently of other predictors. Our findings suggest that large commissural and intra-hemispheric structures are at high risk for post-traumatic degradation. This study identifies detailed neuroanatomic substrates consistent with brain injury patients' age-dependent deficits in information processing speed, interhemispheric communication, motor coordination, visual acuity, sensory integration, reading speed/comprehension, executive function, personality, and memory. We also identify neuroanatomic features underlying white matter degradation whose severity is associated with the male sex. Future studies should compare our findings to functional measures and other neurodegenerative processes.

D. J. Robles · A. Dharani · K. A. Rostowsky ·
N. N. Chaudhari · V. Ngo · A. Irimia (✉)
Ethel Percy Andrus Gerontology Center, Leonard Davis
School of Gerontology, University of Southern California,
Los Angeles, CA 90089, USA
e-mail: irimia@usc.edu

F. Zhang · L. J. O'Donnell
Department of Radiology, Brigham and Women's
Hospital, Harvard Medical School, Boston, MA 02115,
USA

L. Green · N. Sheikh-Bahaei · H. C. Chui
Department of Neurology, Keck School of Medicine,
University of Southern California, Los Angeles,
CA 90033, USA

N. Sheikh-Bahaei
Department of Radiology, Keck School of Medicine,
University of Southern California, 1520 San Pablo Street,
Los Angeles, CA 90033, USA

A. Irimia
Corwin D. Denney Research Center, Department
of Biomedical Engineering, Viterbi School of Engineering,
University of Southern California, Los Angeles,
CA 90089, USA

Keywords Diffusion tensor imaging · Fractional anisotropy · Susceptibility-weighted imaging · Sensory integration · Executive function

Introduction

Traumatic brain injuries (TBIs) are brain function disruptions caused by physical impacts leading to neural tissue damage. In industrialized countries, TBIs' burden on healthcare systems parallels the growing number of aging adults [1]. Even in mild TBI (mTBI), injury effects can be profound and long-lasting because TBI accelerates brain aging while increasing the risk for neurodegenerative diseases like Alzheimer's dementia. Every year, ~2.8 million Americans experiencing TBIs seek medical attention, with substantial age and sex disparities among them. Whereas males are more commonly affected [2], older adults' TBI vulnerability translates into their poorer clinical outcomes compared to all other age groups [3–5]. Because these outcomes reflect neural and cognitive deficits, delineating how sex- and age-related brain connectivity changes drive these deficits could help to inform future strategies for the mitigation of TBI sequelae.

The Glasgow Coma Scale (GCS) categorizes TBIs as mild, moderate, or severe, and mTBIs account for 70–90% of all cases [6, 7]. In acute geriatric TBI, susceptibility-weighted imaging (SWI, a type of magnetic resonance imaging sensitive to ferromagnetic compound deposits) frequently reveals cerebral microbleeds (CMBs, biomarkers of blood–brain barrier breakdown). CMB incidence increases with age due to blood vessel stiffening and to increases in blood–brain barrier permeability, both phenomena contributing to CMB risk [8]. Aside from occurring more frequently after geriatric mTBI, CMBs can be associated with persistent brain circuitry abnormalities, including white matter (WM) degradation. Although age and sex modulate such degradation, the relationship between CMBs and WM trajectories is largely unknown [9]. Understanding this relationship could help to reduce disparities in the neurocognitive outcome as a function of sex, age, CMB findings, and mTBI stage. Furthermore, quantifying the statistical effects of the latter factors upon WM degradation can complement our understanding of how neurophysiological, cognitive, and affective TBI sequelae are underlain by brain circuitry.

The first aim of this cohort study is to assess, across the first ~6 months post-injury, the statistical effects of age at injury, sex, and CMBs on fractional anisotropy (FA), a diffusion MRI measure reflecting WM properties. For major WM structures, we investigate how sex, age at injury, and CMBs predict mean FA at the acute and chronic stages of mTBI (within ~7 days and ~6 months post-injury, respectively). Our second aim is to study whether mean FA decreases significantly across the follow-up period above and beyond the effects of age, sex, and CMBs. We highlight how these variables modulate WM changes and explore how the latter may reflect the most common neurophysiological, cognitive, and affective outcomes of TBI patients. This is the first study to explore, in a systematic fashion, how age at injury, sex, CMBs, and their statistical interactions contribute to post-traumatic WM degradation.

Materials and methods

Study design and participants

This study was undertaken in adherence to the US Code of Federal Regulations (45 CFR 46) and with approval from the Institutional Review Board at the University of Southern California. Participants were recruited through community outreach via advertisements and flyers and/or with the assistance of healthcare professionals who had referred volunteers for neuroimaging and neurocognitive assessments. All subjects who satisfied inclusion criteria and who could provide written informed consent were invited to participate. Inclusion criteria included (1) an acute GCS score of at least 13 upon initial evaluation ($\mu \pm \sigma = 14 \pm 1$), (2) MRIs acquired within ~1 week and ~6 months post-injury, (3) a TBI related to a ground-level fall involving direct head trauma, (4) loss of consciousness (LOC) shorter than 30 min ($\mu \pm \sigma \approx 9 \pm 4$ min), and (5) post-traumatic amnesia shorter than 24 h ($\mu \pm \sigma \approx 3.6 \pm 2.1$ h). Exclusion criteria included (1) imaging findings other than CMB-related SWI hypointensities and (2) a documented clinical history of pre-traumatic neurological disease, psychiatric disorder, or drug/alcohol abuse. Cases of larger intracranial hemorrhage identified from SWIs were excluded. A total of 109 mTBI participants (46 females; age $\mu = 40.2$ years (y), $\sigma = 16.7$ y, range: 18–79 y) were included.

Neuroimaging

Two sets of magnetic resonance imaging (MRI) scans were acquired acutely (~ 7 days) and at ~ 6 months follow-up after injury. T_1 MRIs were acquired using a 3D magnetization-prepared rapid acquisition gradient echo sequence [repetition time (T_R)=1950 ms; echo time (T_E)=2.98 ms; inversion time (T_I)=900 ms; voxel size=1.0 mm \times 1.0 mm \times 1.0 mm]. T_2 MRIs were acquired using a 3D sequence (T_R =2500 ms; T_E =360 ms; voxel size=1.0 mm \times 1.0 mm \times 1.0 mm). Flow-compensated SWI volumes were acquired axially (T_R =30 ms; T_E =20 ms; voxel size=1.3 mm \times 1.33 mm \times 1.6 mm). Diffusion-weighted images (DWIs) were acquired axially in 64 gradient directions (T_R =8,300 ms; T_E =72 ms; voxel size=2.7 mm \times 2.7 mm \times 2 mm). Scans were de-identified and de-linked to preserve participants' confidentiality.

Preprocessing

DWIs were processed using 3DSlicer. DTIPrep was used with default parameters to correct eddy current and patient motion artifacts. Brain masks were created from DWI using SlicerDMRI. BRAINSFit was used for affine registration of both skull-stripped DWIs and B_0 volumes to T_1 volumes. Tractography was performed using unscented Kalman filter (UKF) two-tensor tractography and whole-brain seeding, with one seed per voxel and default parameters. UKF tractography is a deterministic fiber tracking method that fits two tensors at each step while tracking. Unlike single tensor deterministic tractography, where voxels are treated as independent and pathways are reconstructed by tracking in the direction of the principal eigenvector, two-tensor UKF tractography uses information from previous positions to guide model estimation and tracking at the current position. UKF tractography is very consistent in tracking fibers based on diffusion MRI data from independent samples across ages, health conditions, and image acquisitions [10]. FAs were calculated from UKF-derived tensors.

CMB identification

At least three expert raters with training in CMB identification found and segmented each CMB on SWI. CMBs were defined as small, intraparenchymal, round/ovoid SWI hypointensities distinct from blood vessels. Hypointensities connected to the exterior boundary of the brain were not labeled because CMBs are not connected to meninges. CMB labeling discrepancies were resolved by consensus. The distance between each cortical mesh vertex and the closest CMB was calculated for each subject, and this distance was plotted on the cortical surface. Such cortical maps were transformed to a common average template (atlas) and averaged over subjects to generate an average map of expected CMB proximities.

Cortical reconstruction and WM analysis

Automatic T_1 MRI segmentation was applied in FreeSurfer 6.0 (<https://surfer.nmr.mgh.harvard.edu/>) with default parameters. FreeSurfer (A) strips non-cortical voxels using a hybrid-watershed deformation procedure, (B) normalizes image intensities, (C) registers images into Talairach space, (D) segments WM and gray matter (GM), (E) tessellates the WM/GM boundary, and (F) corrects topological inaccuracies. WM parcellation was performed using an anatomically curated fiber clustering pipeline [11]. Input tractography data were affinely registered to the O'Donnell Research Group tractography atlas (<http://dmri.slicer.org/atlasses/>). WM tracts were identified automatically in each subject using the WM Analysis (WMA) package. WMA uses machine learning to identify subjects' WM tracts based on neuroanatomist-curated WM atlas. The atlas contains 58 deep WM tracts including major long-range association and projection tracts, commissural tracts, tracts related to the brainstem and cerebellar connections, and 198 short- and medium-range superficial fiber clusters organized into 16 categories according to the brain lobes that they connect. The left and right cortico-ponto-cerebellar tracts were treated as a single structure. Potential false positive tracts were annotated automatically to filter out outlier fibers. The mean FA of each WM structure was calculated.

Feature selection

Data dimensionality was reduced using a strategy proposed by Jolliffe [12, 13, 14] and adapted to our needs. Specifically, the mean FAs of each WM structure were assembled in an $N \times M$ matrix ($N = 109$ and $M = 73$ are the number of subjects and structures, respectively). A principal component analysis (PCA) with varimax rotations was applied to this matrix to identify the proportion of variance explained by each PC, which weighted each WM structure's contribution to the total variance. PCs were sorted in decreasing order by their explained variance, and PCs which together accounted for at least 50% of the variance were retained. Each retained PC was inspected to determine which WM structures' PC weights had the largest magnitude, and only those structures were retained. Thus, WM structures were retained based on PC weight magnitudes, subject to the constraint that both left and right portions of each structure had to have relatively large magnitudes. Thus, if a structure had a large magnitude for the left—but not for the right—hemisphere, the structure in question was not retained. By contrast, if a structure's left and right portions both had relatively large magnitudes, the structure was retained. This strategy ensured that only WM structures affected by TBI *bilaterally* were retained. This allowed us to investigate *global*—rather than *unilateral*—TBI effects. Whereas the latter can be of interest, their existence is more confounded by primary injury location. In samples like ours, unilateral effects are more likely driven by focal injury location rather than by the greater global vulnerability of WM structures to injury. It was also deemed judicious to focus on bilateral changes in WM fasciculi partly because (1) no information on primary injury locations (e.g., accelerometry data and neurological examinations) was available and (2) such information could confound our data in ways we could not quantify. After statistical feature selection, the seven Witelson subdivisions of the corpus callosum (CC) were combined based on whether they belonged to the genu (GCC), body (BCC), or splenium (SCC), thus reducing the number of CC structures in the analysis from seven to three. This was done to facilitate interpretation of results and comparison with previous studies, which typically describe findings pertaining to the GCC, BCC, and/or SCC rather than to Witelson subdivisions.

Analysis 1

We examined the relationship between sex, age, and CMB count, on the one hand, and WM mean FA, on the other hand. The mean FAs of the left and right parts of the WM structures of interest were included as a set of bivariate outcomes in a multivariate analysis of variance (MANOVA) whose independent variables were the participants' ages, sexes, and CMB counts. The omnibus null hypothesis stated that both bivariate regression coefficients are identically equal to zero, i.e., that there is no statistical relationship between the mean FAs of the left and right WM structures, on the one hand, and participants' ages, sex, and CMBs counts, on the other hand. We explored each predictor's contribution to the multivariate main effect, above and beyond all other predictors' contributions. Data associated with the first (i.e., acute) and second (i.e., chronic) time points were analyzed separately. The null hypothesis was tested at $\alpha = 0.05$. Both confidence intervals (CIs) for test statistics and p -values were computed. Effect sizes were assessed using Cohen's η^2 , and *post-hoc* statistical power was estimated.

Analysis 2

We implemented a repeated-measures MANOVA where age, sex, and CMB counts (independent variables) predicted mean FA changes (dependent variables) within the left and right portions of each WM structure. We used Hotelling's T^2 test for paired multivariate samples to identify WM structures whose mean FAs changed significantly by testing the omnibus null hypothesis of no mean FA change within each WM structure. Like in analysis 1, test statistics, CIs, p -values, Cohen's η^2 , and *post-hoc* statistical power were calculated.

Analysis 3

Using MANOVA, we investigated whether each predictor (age, sex, or CMB count) contributed significantly, above and beyond all other predictors, to mean FA changes within WM structures.

Results

Feature selection

Three PCs were retained because their sum was sufficient to explain ~50% of the mean FA variance (PC_1 : 39.6%; PC_2 : 5.3%; PC_3 : 4.7%). Our feature selection strategy identified ten WM structures for analysis: the GCC, BCC, SCC, inferior longitudinal fasciculus (ILF), middle longitudinal fasciculus (MdLF), inferior occipitofrontal fasciculus (IOFF), the corticospinal tract (CST), as well as superficial frontal (Sup-F), parietal (Sup-P), and temporal (Sup-T) fasciculi.

CMB locations

After computing the distance between each cortical mesh vertex and the closest CMB, this distance was plotted on the cortical surface for each subject and results were averaged across subjects to generate an average map of expected CMB proximities. This map (Fig. 1) revealed that, on average, CMBs could be localized close to the cortical

surface within (A) the lateral and medial aspects of the frontal and parietal lobes, (B) orbitofrontal cortex, (C) the left medial temporal lobe, (D) the insula, and (E) right temporo-parieto-occipital junction. Within the cortical regions where most CMBs occurred, the average shortest distance between the cortex and the nearest CMB was $\mu \pm \sigma = 7.1 \pm 1.8$ mm.

Analysis 1

MANOVA identified WM structures whose mean FAs were significantly associated with sex, age, and CMB counts (Table 1, Figs. 2, 3, and 4). For the acute timepoint, Table 1 shows a multivariate main effect of age on the GCC ($F_{2,104} = 19.85$, $p < 0.001$, $\eta^2 = 0.28$), BCC ($F_{2,104} = 9.07$, $p < 0.001$, $\eta^2 = 0.21$), and SCC ($F_{2,104} = 4.03$, $p = 0.021$, $\eta^2 = 0.07$), on the ILFs ($F_{2,104} = 4.20$, $p = 0.02$, $\eta^2 = 0.07$), MdLFs ($F_{2,104} = 4.25$, $p = 0.017$, $\eta^2 = 0.08$), Sup-F fasciculi ($F_{2,104} = 8.09$, $p = 0.001$, $\eta^2 = 0.14$), and Sup-T fasciculi ($F_{2,104} = 13.70$, $p < 0.001$, $\eta^2 = 0.21$). Table 1 also indicates a multivariate main effect of sex on

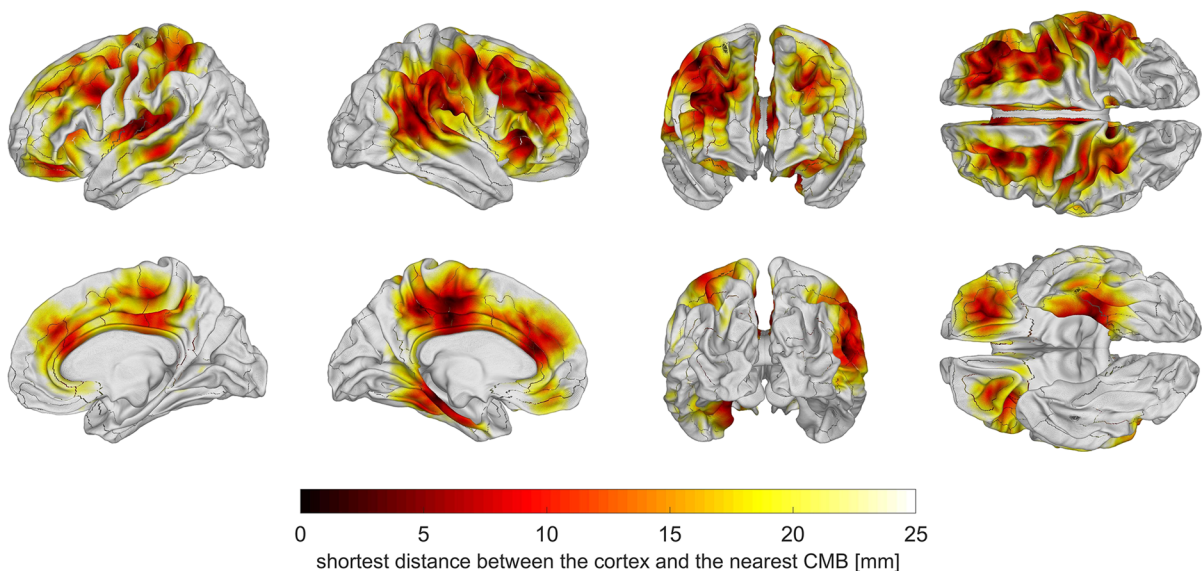


Fig. 1 Cortical map of average shortest distances from the GM/WM interface to the nearest CMB. To generate this map, the distance between each cortical mesh vertex and the closest CMB was calculated for each subject, and this distance was plotted on the cortical surface. The subjects' cortical maps were transformed to a common average template (atlas) and averaged over to generate the map above. CMBs were local-

ized near the cortical surface within the lateral and medial aspects of the frontal and parietal lobes, orbitofrontal cortex, the temporal lobes, the insulae, and the right temporo-parieto-occipital junction. Within these cortical regions, the average shortest distance between the cortex and the nearest CMB was $\mu \pm \sigma = 7.1 \pm 1.8$ mm

Table 1 Results of the multivariate analysis of variance (MANOVA, statistical analysis 1)

Structure	Timepoint	Variable	$F_{2, 104}$	p	η^2	Power
GCC	Acute	Age	19.85	0.001	0.28	1.00
		Sex	0.04	0.958	0.00	0.06
		CMBs	0.87	0.423	0.02	0.20
	Chronic	Age	22.70	0.001	0.30	1.00
		Sex	0.21	0.808	0.00	0.08
		CMBs	0.21	0.812	0.00	0.08
BCC	Acute	Age	9.07	0.001	0.21	1.00
		Sex	0.62	0.604	0.02	0.18
		CMBs	0.85	0.468	0.02	0.23
	Chronic	Age	6.82	0.001	0.17	0.97
		Sex	1.81	0.150	0.05	0.46
		CMBs	0.03	0.993	0.00	0.05
SCC	Acute	Age	4.03	0.021	0.07	0.71
		Sex	0.87	0.424	0.02	0.20
		CMBs	1.08	0.342	0.02	0.24
	Chronic	Age	0.40	0.671	0.01	0.11
		Sex	0.54	0.585	0.01	0.14
		CMBs	0.38	0.688	0.01	0.11
ILF	Acute	Age	4.20	0.020	0.08	0.73
		Sex	1.85	0.162	0.03	0.38
		CMBs	1.04	0.259	0.02	0.23
	Chronic	Age	3.26	0.042	0.06	0.61
		Sex	0.32	0.725	0.01	0.10
		CMBs	0.72	0.425	0.06	0.61
MdLF	Acute	Age	4.25	0.017	0.08	0.73
		Sex	2.34	0.102	0.04	0.46
		CMBs	0.54	0.587	0.01	0.14
	Chronic	Age	3.20	0.045	0.06	0.60
		Sex	1.00	0.371	0.02	0.22
		CMBs	2.73	0.070	0.05	0.53
IOFF	Acute	Age	0.43	0.653	0.01	0.12
		Sex	1.26	0.287	0.02	0.27
		CMBs	1.44	0.242	0.03	0.30
	Chronic	Age	0.12	0.886	0.00	0.07
		Sex	5.59	0.005	0.10	0.85
		CMBs	1.14	0.249	0.03	0.30
Sup-F	Acute	Age	8.09	0.001	0.14	0.95
		Sex	1.19	0.309	0.02	0.26
		CMBs	0.44	0.643	0.01	0.12
	Chronic	Age	5.64	0.005	0.10	0.85
		Sex	1.28	0.283	0.02	0.27
		CMBs	0.14	0.879	0.00	0.07

Table 1 (continued)

Structure	Timepoint	Variable	$F_{2, 104}$	p	η^2	Power
Sup-T	Acute	Age	8.76	0.001	0.14	0.97
		Sex	3.26	0.042	0.06	0.61
		CMBs	0.12	0.886	0.00	0.07
	Chronic	Age	13.70	0.001	0.21	1.00
		Sex	0.32	0.729	0.01	0.10
		CMBs	0.45	0.641	0.01	0.12

The mean FAs of the left and right WM structures of interest were included as one bivariate vector of dependent variables. Participants' ages, sex, and CMB counts were independent variables. Acute and chronic data were acquired ~ 7 days and ~ 6 months post-injury, respectively. Null hypotheses were tested at a significance level of $\alpha = 0.05$, and significant findings are in **bold case**. F statistics with 2 and 104 degrees of freedom, effect sizes (Cohen's η^2), and statistical power are listed

BCC, body of the corpus callosum; *CMB*, cerebral microbleed; *CST*, corticospinal tract; *FA*, fractional anisotropy; *GCC*, genu of the corpus callosum; *ILF*, inferior longitudinal fasciculus; *IOFF*, inferior occipitofrontal fasciculus; *MdLF*, middle longitudinal fasciculus; *SCC*, splenium of the corpus callosum; *Sup-F*, superficial frontal; *Sup-P*, superficial parietal; *Sup-T*, superficial temporal; *WM*, white matter

Sup-T fasciculi ($F_{2, 104} = 3.26$, $p = 0.042$, $\eta^2 = 0.06$) at the acute timepoint. For the chronic timepoint, Table 1 indicates a multivariate main effect of age on the GCC ($F_{2, 104} = 22.70$, $p < 0.001$, $\eta^2 = 0.30$) and BCC ($F_{2, 104} = 6.82$, $p < 0.001$, $\eta^2 = 0.17$), on the ILFs ($F_{2, 104} = 3.26$, $p = 0.042$, $\eta^2 = 0.06$), MdLFs ($F_{2, 104} = 3.20$, $p = 0.045$, $\eta^2 = 0.06$), Sup-F fasciculi ($F_{2, 104} = 5.64$, $p = 0.005$, $\eta^2 = 0.10$), and Sup-T fasciculi ($F_{2, 104} = 13.70$, $p < 0.001$, $\eta^2 = 0.21$). Table 1 also reports a multivariate main effect of sex on the IOFFs ($F_{2, 104} = 5.59$, $p = 0.001$, $\eta^2 = 0.14$) for the chronic timepoint. CMB counts had no significant effects on mean FAs at either timepoint.

Analysis 2

Repeated-measures MANOVA identified significant mean FA changes (Table 2, Figs. 1, 2, 3, and 4) within the anterior BCC (Hotelling's $T_{108}^2 = 3.04$, $p = 0.003$, Cohen's $d = 0.29$), posterior BCC ($T_{108}^2 = 2.68$, $p = 0.009$, $d = 0.26$) and SCC ($T_{108}^2 = 2.47$, $p = 0.015$, $d = 0.24$), the left Sup-F fasciculi ($T_{108}^2 = 2.72$, $p = 0.008$, $d = 0.26$), and the left branch of the CST ($T_{108}^2 = 2.77$, $p = 0.007$, $d = 0.27$). CMB counts had no significant effects on mean FA changes. WM fasciculi with significant findings are displayed together for simultaneous illustration in Fig. 5.

Analysis 3

Factorial MANOVA revealed the significant individual contributions of age, sex, or CMB count to mean FA changes (Table 3) above and beyond those of other contributions. For the acute timepoint, there was a multivariate main effect of age on the BCC ($F_{45, 11} = 2.61$, $p = 0.04$, $\eta^2 = 0.91$), but no significant interactions. For the chronic timepoint, there was a multivariate main effect of age on the GCC ($F_{46, 11} = 5.52$, $p < 0.001$, $\eta^2 = 0.96$), BCC ($F_{46, 11} = 3.99$, $p = 0.01$, $\eta^2 = 0.94$), and MdLFs ($F_{46, 11} = 2.61$, $p = 0.04$, $\eta^2 = 0.92$). There was also a multivariate main effect of CMB count on the BCC ($F_{7, 11} = 3.33$, $p = 0.04$, $\eta^2 = 0.68$) and MdLFs ($F_{7, 11} = 3.34$, $p = 0.04$, $\eta^2 = 0.68$). We identified a significant age-by-sex interaction on the GCC ($F_{6, 11} = 3.92$, $p = 0.02$, $\eta^2 = 0.68$) and a significant age-by-CMB-count interaction on the GCC ($F_{21, 11} = 3.02$, $p = 0.03$, $\eta^2 = 0.85$).

Discussion

Aside from statistical analyses, our study provides convenient visualizations of the strongest spatiotemporal associations between WM fasciculi and effects

Fig. 2 WM fasciculi whose mean FAs are significantly associated with age at injury either acutely or chronically. Fiber trajectories are encoded by colors (red: left–right; green: anterior–posterior; blue: inferior–superior). Axial, sagittal, and coronal views of WM structures are superimposed on a translucent model of the brain. The gyri and sulci connected by the corresponding WM pathways are also displayed. **(A)** GCC damage is associated with deficits of functions localized to the frontal and prefrontal cortex, including executive function and interhemispheric communication [24]. **(B)** BCC damage is frequently associated with somatomotor deficits [26]. **(C)** SCC injury can result in damage to circuits mediating visual, auditory, and somatosensory function, as well as multimodal sensory integration [25]

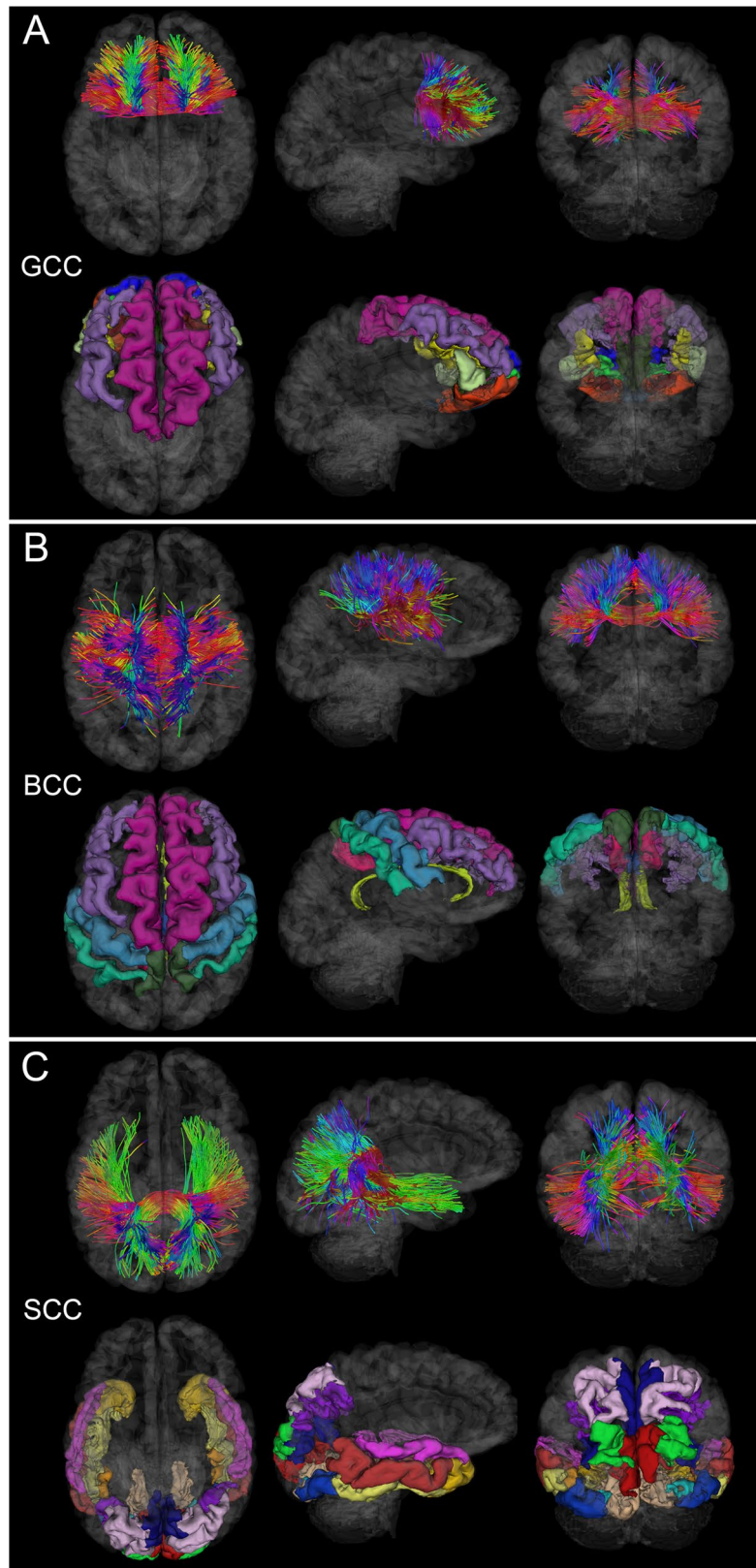


Fig. 3 Like Fig. 2, for the MdLF, ILF, and IOFF. (A) MdLF damage can result in deficits of attention [31] and both visual and auditory information processing [30]. (B) ILF injury may be associated with deficits in the processing of complex information associated with visual object recognition [35]. (C) IOFF degradation may result in damage to visual and motor pathways [35]

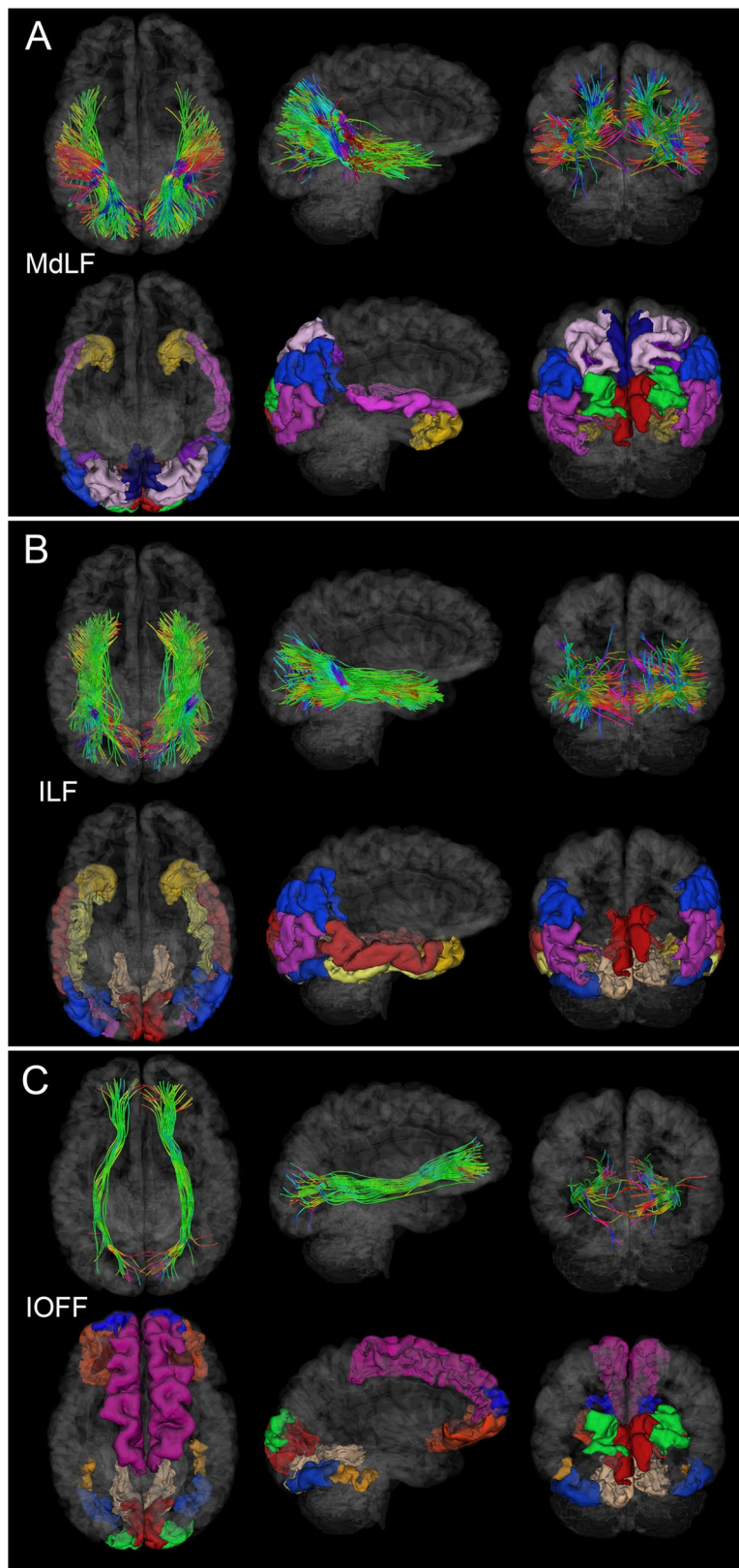


Table 2 Results of paired-sample *t*-tests for the null hypothesis of no change in mean FA between the acute and chronic time points (statistical analysis 2)

Structure	μ	σ	95% CI	T^2_{108}	<i>p</i>	<i>d</i>
Anterior GCC	0.00	0.77	[-0.14, 0.15]	0.00	0.998	0.00
Posterior GCC	0.04	0.60	[-0.07, 0.16]	0.75	0.458	0.07
Anterior BCC	0.06	0.63	[-0.06, 0.18]	1.04	0.302	0.10
Middle BCC	0.20	0.68	[-0.07, 0.33]	3.04	0.003	0.29
Posterior BCC	0.20	0.79	[-0.05, 0.35]	2.68	0.009	0.26
Anterior SCC	0.04	0.75	[-0.10, 0.18]	0.55	0.587	0.05
Posterior SCC	0.19	0.81	[-0.04, 0.35]	2.47	0.015	0.24
Left ILF	0.04	0.57	[-0.07, 0.14]	0.64	0.524	0.06
Right ILF	0.04	0.72	[-0.10, 0.17]	0.54	0.587	0.05
Left MdLF	0.06	0.84	[-0.10, 0.22]	0.76	0.452	0.07
Right MdLF	0.13	0.72	[-0.01, 0.26]	1.90	0.063	0.18
Left Sup-F	0.17	0.67	[-0.05, 0.20]	2.72	0.008	0.26
Right Sup-F	0.08	0.66	[-0.04, 0.21]	1.30	0.197	0.12
Left Sup-T	0.04	0.96	[-0.14, 0.23]	0.46	0.643	0.04
Right Sup-T	0.11	0.96	[-0.08, 0.29]	1.16	0.247	0.11
Left Sup-P	0.11	0.73	[-0.03, 0.24]	1.53	0.129	0.15
Right Sup-P	0.08	0.64	[-0.04, 0.20]	1.32	0.190	0.13
Left IOFF	0.01	0.79	[-0.14, 0.16]	0.11	0.913	0.01
Right IOFF	0.12	0.77	[-0.03, 0.27]	1.60	0.113	0.15
Left CST	0.22	0.84	[-0.06, 0.38]	2.77	0.007	0.27
Right CST	0.09	0.88	[-0.07, 0.26]	1.11	0.268	0.11

The mean μ and standard deviation σ of the time difference in mean standardized residuals for mean FA are listed. The null hypothesis was tested at a significance level of $\alpha = 0.05$, and significant findings are displayed in **bold case**. Hotelling's T^2 statistics with 108 degrees of freedom, effect sizes (Cohen's *d*), and statistical power are listed

BCC, body of the corpus callosum; *CST*, corticospinal tract; *GCC*, genu of the corpus callosum; *ILF*, inferior longitudinal fasciculus; *IOFF*, inferior occipitofrontal fasciculus; *MdLF*, middle longitudinal fasciculus; *SCC*, splenium of the corpus callosum; *Sup-F*, superficial frontal; *Sup-P*, superficial parietal; *Sup-T*, superficial temporal

due to age, sex, and time (Fig. 5). In what follows, we discuss these and related findings as they pertain to effects associated with age, sex, CMBs, biomechanics, demyelination, and natural aging.

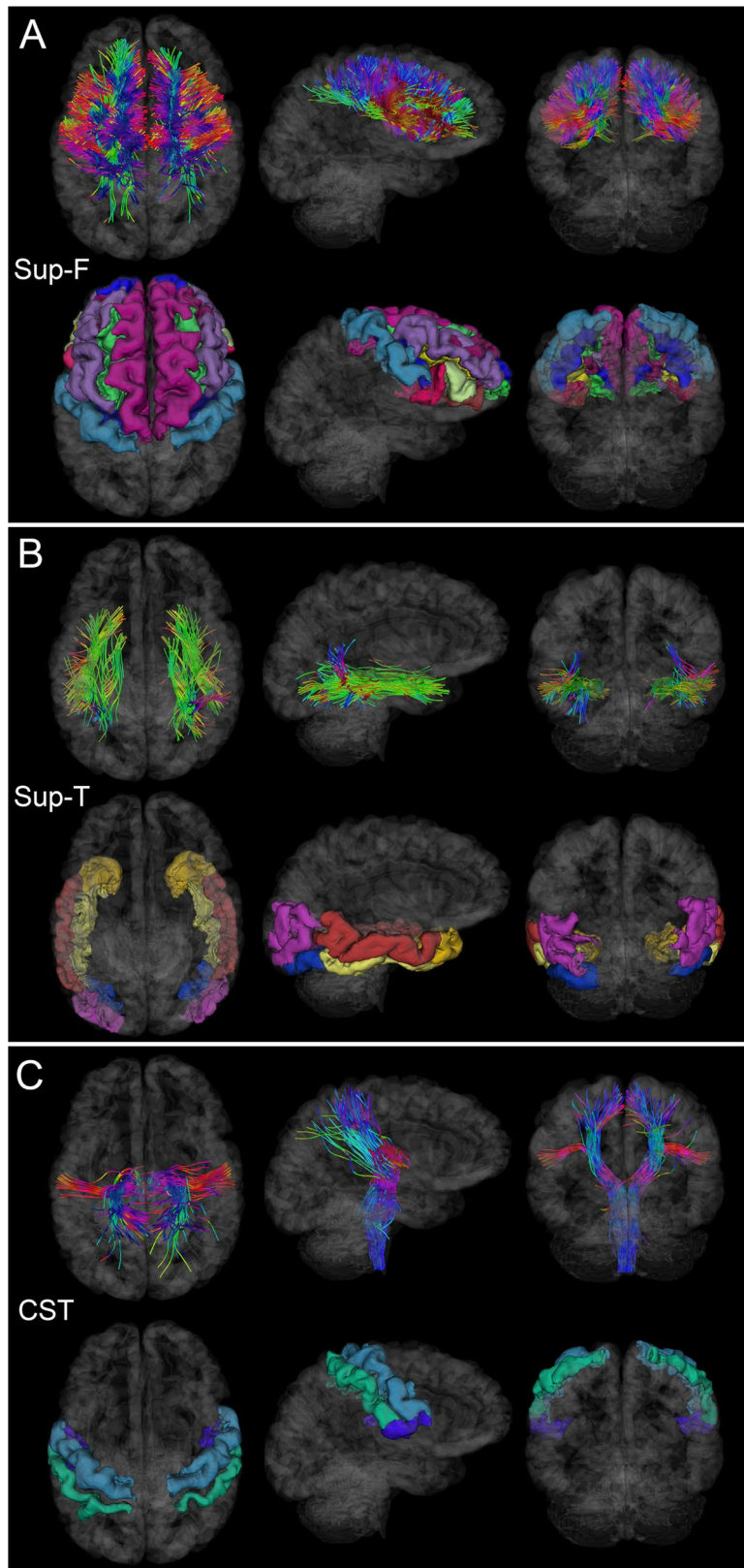
Age effects

Whereas the literature on age-related effects in *moderate-to-severe* TBI is extensive, studies like ours on how age at injury modulates *mild* TBI sequelae remain scarce. Nevertheless, extensive research supports our findings on the progressive effects of age at injury on TBI-related WM degradation and on subsequent cognitive and functional impairments [15–20, 21, 22, 23]. Below, we describe age-related WM

alterations after mTBI and postulate their potential associations with cognitive and functional impairment based on this existing body of knowledge.

Our results suggest that age at injury has a linear association with CC degradation (Table 1), likely due not only to TBI, but also to the accumulative effect of other pathologies and to their interactions with TBI. The associations between mean FA decrease in the GCC and BCC and this variable are significant. Furthermore, age at injury is associated with significantly lower mean FA in the SCC at the acute—but not chronic—timepoint. WM degradation observed both acutely and chronically in the GCC could be associated with motor coordination decline [24], such that our findings may underscore how injuries to this WM structure can translate into neurological deficits

Fig. 4 Like Fig. 2, for the Sup-F, Sup-T, and CST. (A) Sup-F fasciculi affected by injury can result in deficits of executive control [28]. (B) Sup-T fasciculi, when affected significantly by injury, may result in deficits pertaining to the recognition of faces and objects. (C) CST damage can affect the functions of the primary somatomotor cortex [40]



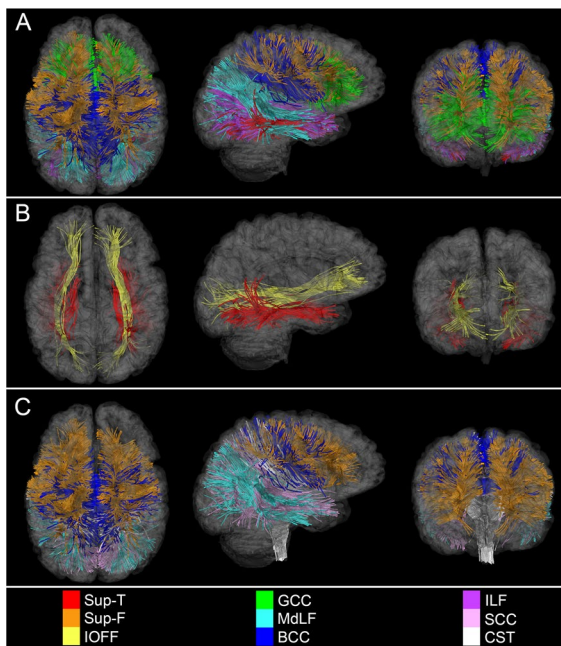


Fig. 5 Simultaneous visualization of WM structures with the most significant statistical associations. Displayed are WM fasciculi with the most statistically significant associations between mean FA, on the one hand, and (A) age, (B) sex, as well as (C) time, on the other hand. These depictions emphasize the potential WM degradation substrates of post-traumatic executive dysfunction (as reflected in the vulnerability of Sup-F fasciculi to injury), audiovisual impairment and attention deficits (highlighted by WM degradation within the MdLF), and motor deficits (underlined by degeneration of the CST). Axial, sagittal, and coronal views of each WM structure are superimposed on translucent models of the GM surface

whose typical severity increases with age. Older adults' significantly lower mean FA in the GCC and SCC have been associated with declines in reading speed and comprehension [25], two cognitive abilities that rely on the speed of interhemispheric information transfer, a key CC function. Funnell et al. [26] found that the anterior midbody of the CC transmits motor information, whereas the posterior midbody transmits somatosensory information between hemispheres. Ota et al. [27] showed that age at injury is correlated with the FAs of the GCC and anterior BCC. Thus, our results indicate that mTBI may accelerate aging-related WM FA decrease in the CC and could contribute to a faster decline of motor functioning, processing speed, and interhemispheric information transfer.

Whereas superficial WM tracts are challenging to investigate due to their structural complexity and

inter-subject variability, our study benefits from an approach with validated high consistency in mapping such tracts. Aside from the CC, Sup-F and Sup-T fasciculi also exhibit mean FA decreases whose magnitudes increase with age (Table 1). Sup-F fasciculi consist of relatively short-range connections between ipsilateral frontal areas, whereas Sup-T fasciculi connect GM regions within temporal lobes (Fig. 4). In agreement with our findings of reduced mean FA within superficial WM, a study of youths aged 8–22 by Stojanovski et al. [28] concluded that mTBI damage can lead to FA decreases within superficial WM and to connectivity damage typically associated with deficits of attention and processing speed. Our findings complement these and suggest that WM integrity reductions in the superficial WM of pediatric TBI patients are similar to those observed in adulthood. Future studies should explore if these structural findings translate into attention and processing speed deficits.

The evidence on the existence of a spatial gradient in age-related superficial WM reductions is equivocal. Phillips et al. [29] found an anteroposterior gradient of age-related FA reductions in superficial frontal WM which, they suggested, is more vulnerable to aging effects than that in occipital areas. By contrast, Table 1 and Fig. 4 suggest that, relative to anterior Sup-F fasciculi ($\eta^2 = 0.10$), posterior Sup-T fasciculi experience larger mean FA decreases with age ($\eta^2 = 0.21$). Thus, more research on the existence of an anteroposterior gradient in age-related superficial WM changes is needed.

Compared to younger participants, older adults exhibited lower mean FAs in the MdLFs and ILFs, both acutely and chronically (Table 1). The MdLF is a major pathway in the dorsal stream of semantic processing, with roles in language comprehension, visuospatial integration, attentional processing, and audiovisual integration. Herbert et al. [30] describe the ILF as a significant component of the semantic ventral stream and indicate that structural IF alterations are associated with semantic/lexical retrieval impairments and visual agnosia. Goldstein and Levin [31] highlight that older adults' effortful attention and language processing (i.e., visual naming and word association) are significantly impaired after mTBI. Thus, the relationship found here between older age and larger mean FA decreases in the MdLFs and ILFs

Table 3 Results of MANOVA investigating whether each predictor (age, sex, or CMB count) contributed significantly, above and beyond the contributions of all other predictors, to the changes in FA means observed in various structures (statistical analysis 3)

Structure	Stage	Variable(s)	<i>F</i>	<i>df</i> ₁	<i>df</i> ₂	<i>p</i>	η^2	Power
GCC	Acute	CMB	1.20	7	11	0.38	0.43	0.31
		Age	1.82	45	11	0.14	0.88	0.64
		Sex	0.67	2	10	0.54	0.12	0.13
		Sex × age	0.64	6	11	0.70	0.26	0.17
		CMBs × age	1.38	22	11	0.30	0.73	0.45
	Chronic	CMB	0.73	7	11	0.65	0.32	0.19
		Age	5.52	46	11	0.01	0.96	1.00
		Sex	0.16	2	10	0.86	0.03	0.07
		Sex × age	3.92	6	11	0.02	0.68	0.81
		CMB × age	3.02	21	11	0.03	0.85	0.85
BCC	Acute	CMB	1.14	7	11	0.41	0.42	0.29
		Age	2.61	45	11	0.04	0.91	0.83
		Sex	0.01	3	9	1.00	0.00	0.05
		Sex × age	1.85	6	11	0.18	0.50	0.45
		CMB × age	1.00	22	11	0.53	0.67	0.33
	Chronic	CMB	3.33	7	11	0.04	0.68	0.76
		Age	3.99	46	11	0.01	0.94	0.96
		Sex	1.04	3	9	0.42	0.26	0.20
		Sex × age	1.68	6	11	0.22	0.48	0.41
		CMB × age	1.89	21	11	0.14	0.78	0.61
SCC	Acute	CMB	0.61	7	11	0.74	0.28	0.17
		Age	1.34	45	11	0.31	0.85	0.48
		Sex	0.03	2	10	0.97	0.01	0.05
		Sex × age	0.46	6	11	0.82	0.20	0.13
		CMB × age	0.61	22	11	0.85	0.55	0.20
	Chronic	CMB	1.14	7	11	0.41	0.42	0.29
		Age	2.33	46	11	0.06	0.91	0.78
		Sex	1.20	2	10	0.34	0.19	0.21
		Sex × age	1.37	6	11	0.31	0.43	0.34
		CMB × age	1.79	21	11	0.16	0.77	0.58
ILF	Acute	CMB	1.82	7	11	0.18	0.54	0.46
		Age	2.49	45	11	0.05	0.91	0.81
		Sex	0.24	2	10	0.79	0.05	0.08
		Sex × age	1.11	6	11	0.42	0.38	0.27
		CMB × age	1.91	22	11	0.13	0.79	0.62
	Chronic	CMB	2.75	7	11	0.07	0.64	0.66
		Age	1.03	46	11	0.52	0.81	0.37
		Sex	0.46	2	10	0.64	0.08	0.11
		Sex × age	2.16	6	11	0.13	0.54	0.52
		CMB × age	1.21	21	11	0.39	0.70	0.39

could underlie post-traumatic deficits in attention and language processing.

Within both the CC and superficial cerebral fasciculi, WM degradation occurs with typical aging. We found the GCC to be more susceptible to degradation than the SCC, both acutely and chronically

(Table 2). However, because this effect has also been documented in normal aging, it is possible that TBI only accelerates post-traumatic CC degradation already underway due to aging. Similarly, the mean FA of superficial WM tracts was found to decrease with both age and injury chronicity (Tables 1 and 2).

Table 3 (continued)

Structure	Stage	Variable(s)	<i>F</i>	<i>df</i> ₁	<i>df</i> ₂	<i>p</i>	η^2	Power
MdLF	Acute	CMB	1.53	7	11	0.25	0.49	0.39
		Age	1.20	45	11	0.39	0.83	0.43
		Sex	1.15	2	10	0.35	0.19	0.20
		Sex \times age	0.89	6	11	0.53	0.33	0.22
		CMB \times age	1.24	7	11	0.37	0.71	0.41
	Chronic	CMB	3.34	45	11	0.04	0.68	0.76
		Age	2.61	2	10	0.04	0.92	0.83
		Sex	0.85	6	11	0.45	0.15	0.16
		Sex \times age	0.85	22	11	0.56	0.32	0.21
		CMB \times age	1.51	7	11	0.24	0.74	0.49
IOFF	Acute	CMB	0.52	46	11	0.81	0.25	0.15
		Age	1.09	45	11	0.47	0.82	0.39
		Sex	1.11	2	10	0.37	0.18	0.19
		Sex \times age	1.11	6	11	0.42	0.38	0.27
		CMB \times age	1.17	22	11	0.41	0.70	0.38
	Chronic	CMB	0.71	7	11	0.66	0.31	0.19
		Age	1.06	46	11	0.49	0.82	0.38
		Sex	1.46	2	10	0.28	0.23	0.24
		Sex \times age	0.83	6	11	0.57	0.31	0.21
		CMB \times age	1.16	21	11	0.41	0.69	0.38
Sup-F	Acute	CMB	1.35	7	11	0.31	0.46	0.35
		Age	1.59	45	11	0.21	0.87	0.57
		Sex	0.31	2	10	0.74	0.06	0.09
		Sex \times age	1.23	6	11	0.36	0.40	0.30
		CMB \times age	2.15	22	11	0.09	0.81	0.68
	Chronic	CMB	2.55	7	11	0.08	0.62	0.62
		Age	2.50	46	11	0.05	0.91	0.81
		Sex	1.83	2	10	0.21	0.27	0.29
		Sex \times age	2.74	6	11	0.07	0.60	0.63
		CMB \times age	1.79	21	11	0.16	0.77	0.58
Sup-T	Acute	CMB	1.10	7	11	0.43	0.41	0.28
		Age	1.90	45	11	0.12	0.89	0.67
		Sex	1.99	2	10	0.19	0.29	0.32
		Sex \times age	1.10	6	11	0.42	0.38	0.27
		CMB \times age	1.36	22	11	0.30	0.73	0.45
	Chronic	CMB	3.69	7	11	0.03	0.70	0.81
		Age	2.42	46	11	0.06	0.91	0.79
		Sex	0.54	2	10	0.60	0.10	0.12
		Sex \times age	1.86	6	11	0.18	0.50	0.45
		CMB \times age	2.10	21	11	0.10	0.80	0.66

Table 3 (continued)

Structure	Stage	Variable(s)	<i>F</i>	<i>df</i> ₁	<i>df</i> ₂	<i>p</i>	η^2	Power
Sup-P	Acute	CMB	2.86	7	11	0.06	0.65	0.68
		Age	1.62	45	11	0.19	0.87	0.58
		Sex	0.27	2	10	0.77	0.05	0.08
		Sex × age	1.68	6	11	0.22	0.48	0.41
		CMB × age	0.90	22	11	0.60	0.64	0.29
	Chronic	CMB	1.05	7	11	0.45	0.40	0.27
		Age	1.11	46	11	0.46	0.82	0.40
		Sex	0.16	2	10	0.85	0.03	0.07
		Sex × age	2.02	6	11	0.15	0.52	0.49
		CMB × age	0.96	21	11	0.56	0.65	0.31
CST	Acute	CMB	1.14	7	11	0.41	0.42	0.29
		Age	1.53	45	11	0.23	0.86	0.55
		Sex	1.16	2	10	0.35	0.19	0.20
		Sex × age	0.72	6	11	0.65	0.28	0.18
		CMB × age	1.10	22	11	0.46	0.69	0.36
	Chronic	CMB	1.20	7	11	0.38	0.43	0.31
		Age	1.01	46	11	0.53	0.81	0.36
		Sex	0.69	2	10	0.52	0.12	0.14
		Sex × age	1.19	6	11	0.38	0.39	0.29
		CMB × age	1.62	21	11	0.21	0.76	0.53

The acute and chronic time points correspond to ~7 days and ~6 months post-injury, respectively. Null hypotheses were tested at a significance level of $\alpha = 0.05$, and findings that are both significant and well-powered (power > 0.8) are in **bold case**. *F* statistics, numerator and denominator degrees of freedom (*df*₁ and *df*₂), effect sizes (Cohen's η^2), and statistical power are listed.

BCC, body of the corpus callosum; CMB, cerebral microbleed; CST, corticospinal tract; FA, fractional anisotropy; GCC, genu of the corpus callosum; ILF, inferior longitudinal fasciculus; IOFF, inferior occipitofrontal fasciculus; MdLF, middle longitudinal fasciculus; SCC, splenium of the corpus callosum; Sup-F, superficial frontal; Sup-P, superficial parietal; Sup-T, superficial temporal; WM, white matter

However, FA decreases in *superficial* WM are more strongly associated with age-related cognitive decline than those in *deep* WM [32], which suggests the hypothesis that the former are more strongly associated with cognitive decline than the latter. Tables 1 and 2 suggest that the degradation of superficial WM in frontal and temporal lobes depends significantly on injury chronicity and age at injury. Because changes in executive function, personality, and memory are strongly mediated by superficial neural circuits in frontal and temporal areas, future research should seek to deepen our insights on the interaction between TBI and age-related cognitive decline in these regions, which are highly vulnerable to injury.

Importantly, falls in older adults can be secondary to vascular brain injury or to neurodegenerative diseases like Parkinson's disease, Lewy body dementia,

and normal-pressure hydrocephalus. Although our study participants did not have documented histories of such conditions, they were not specifically screened for them either. Because such diseases can alter WM integrity above and beyond TBI alone, some of our findings may be partially due to such (undiagnosed) neurological disorders; we acknowledge this as a weakness of our study.

Sex effects

Consistently, males have been found to be relatively more vulnerable to WM degradation post-TBI [33]. For example, male sex predicts lower mean FA values in Sup-T fasciculi (Fig. 4). In agreement with our findings, Fakhra et al. [34] found a similar male sex-related vulnerability to WM degradation and to

cognitive impairment after TBI. However, in contrast to our study, these authors found significant sex-related differences in WM degradation only in the uncinate fasciculus (UF). Although our analysis did not isolate the UF, Sup-T fasciculi are adjacent to it. Thus, the discrepancy between our study and that of Fakhran et al. may be due to methodological differences, at least pertaining to tractography. Nevertheless, because the integrity of superficial WM is a biomarker of age-related cognitive decline [32], males' lower FA in Sup-T fasciculi compared to females' (Table 1) could partly explain males' more appreciable impairment of functions modulated by these circuits.

Table 1 indicates a significant relationship between male sex and lower mean FA in the IFOFs after TBI. The IFOF is a direct ventral route for the semantic network involved in language processing, object use, and object recognition. In agreement with our findings, another study [35] found that reduced post-traumatic IFOF integrity are associated with (non) verbal semantic task performance deficits. Thus, IFOF involvement in semantic processing suggests that lower mean FA values in males' IFOFs could be associated with more severe impairments of semantic processing networks.

CMB effects

CMBs are relatively more common in older adults and, in a post-traumatic setting, SWIs can reveal both traumatic and non-traumatic CMBs. For example, some non-traumatic CMBs can be linked to vascular or metabolic disease, and to risk factors like hypercholesterolemia and hypertension. Because CMB etiology could not be ascertained, it is possible that at least some CMB identified here were non-traumatic. Thus, the CMB-related effects discussed here in the context of post-traumatic WM degradation may not be related to TBI alone. For this reason, our post-traumatic CMB findings should be interpreted with caution. Specifically, although our results indicate that CMB findings are a risk factor for post-traumatic WM degradation, that risk is not necessarily TBI-related. Future studies should establish the distinct contributions of traumatic vs. non-traumatic CMBs to post-traumatic WM degradation.

CMB count has been identified as an injury severity marker and is linked to increased risk for cognitive

impairment [36, 37]. Our findings complement those of previous studies and suggest that the relationship between CMBs identified after TBI and WM degradation could help to prognosticate the risk of chronic cognitive deficits. Lawrence et al. [36] found a significant association between GCS and post-traumatic CMB count. They suggest that acute CMB identification could aid to improve the accuracy of TBI severity estimation. In our study, the mean FAs of the BCC, MdLF, and Sup-T fasciculi are significantly and negatively associated with CMB count (Table 3), which highlights the putative relationship between CMB count and WM degradation. Our analysis does not account for CMBs' anatomical locations, which could moderate the extent of TBI-related cognitive decline. For this reason, future studies should investigate how CMB locations impact WM.

Biomechanical effects

This study illustrates how TBI biomechanics translate into WM degradation patterns. For example, we document significant mean FA decreases within the commissural tracts (BCC and SCC), right MdLF, left Sup-F tracts, and left CST (Table 1). Callosal WM is relatively more vulnerable to post-traumatic degradation for two primary reasons. Firstly, its connections are interhemispheric, which renders them more vulnerable to traumatic forces and to mechanical strain [38]. Secondly, the CC is relatively less myelinated than other WM structures, which makes it more fragile. Thirdly, because the CC connects the brain hemispheres, this structure plays a key role in conferring mechanical stability and integrity to the telencephalon. Since the hemispheres are relatively large and mechanically inert, the physical momenta of TBI forces can be easily transferred biomechanically to the CC, where they can lead to shearing, twisting, and tearing commissural axons.

Bigler et al. [39] found that TBI of the temporal stem (TS), as inferred using diffusion tensor imaging, correlates with specific FA decreases in the ILF, arcuate fasciculus, and IFOF, as well as with memory impairments modulated by injuries to these structures. Because our findings indicate post-traumatic FA decreases in the ILF, arcuate fasciculus and IFOF, the findings of Bigler et al. provide context to our own. Conta and Stelzner [40] showed that CST axons are much more vulnerable to injury than other

supraspinal projections, partly because TBI is often associated with sudden forces imparted to the neck and brainstem. CST axons are exceptionally long (since they extend along the brain stem and spinal cord), such that mechanical forces can affect them more than they impact the relatively shorter WM tracts encased within—and protected by—the cranial cavity.

Demyelination effects

The MdLF, a prominent cerebral association fiber tract, runs principally between the superior temporal gyrus and the parietal lobe [41, 42]. The extent of demyelination along this WM structure has been related to impairments in the ability to distinguish tone pitch and to process speech sounds [43]. Relatedly, the TS is a major WM structure that bridges the temporal and frontal lobes and that includes fibers traversing temporal WM, such as the ILF, UF, and IFOF. The myelination of superficial WM axons terminates last during brain development (i.e., as late as the fourth and fifth decades of life), which may partly explain the relatively high vulnerability of superficial axons to blunt trauma during ongoing myelination [44]. Furthermore, oligodendrocytes in superficial WM provide less myelination to axons compared to those in deep WM, thus offering less protection to superficial WM and conferring to it a higher vulnerability to axonal damage [45]. These findings may explain our own results, which indicate that superficial WM is affected significantly by mTBI. The fact that frontotemporal injuries are among the most common types of TBI further highlights the high susceptibility of superficial frontal and temporal WM to trauma. Because post-traumatic degradation of superficial WM has not been quantified systematically, our findings are illustrative of typical frontotemporal TBI effects even in *mild* TBI, where the WM at highest injury risk includes superficial dorsolateral WM in frontal, temporal, parietal, and occipital areas. This, in conjunction with the fact that ~75 to 90% of all TBIs are mild, highlights the potential significance of our findings, and the importance of quantifying superficial WM degradation.

Natural aging effects

Our study compares only the acute and chronic (~7 days and ~6 months post-injury, respectively)

stages of mTBI. However, Edlow et al. [46] suggest that quantifiers of the *sub-acute* stage of an injury (~8 days to rehabilitation discharge) may better predict functional outcomes than measures obtained during the acute stage. Thus, to further understand the roles of age, sex, and CMBs on WM degradation, future studies should monitor TBI patients sub-acute and across longer time intervals, including ~1 year post-injury and beyond. Due to limitations related to data availability and statistical power, this cohort study does not include healthy controls (HCs). For this reason, we could not directly quantify the relative extent to which the structural changes identified here are associated with mTBI vs. with typical aging. Nevertheless, because of our relatively short (~6-month) follow-up interval, statistical effects due to typical aging are likely much weaker than those due to TBI [46–49]. For this reason, the FA changes reported here are likely due primarily to TBI and typical aging effects would be relatively minor by comparison. This assertion is strongly supported by the existing body of literature on this topic, as elaborated below.

Upon quantifying WM changes in HCs aged 21 to 49 y ($\mu \pm \sigma = 27 \pm 7$ y) across 3–5 months, Mayer et al. [50] found no statistically significant FA changes in the left superior corona radiata, left UF, left internal capsule, left corona radiata, GCC, or SCC. In the SCC, we found TBI-related mean FA changes with Cohen's $d = 0.24$ (Table 2). By contrast, Mayer et al. found an effect size of 0.05 in this structure across a comparable interval. In a study replicating that of Mayer et al., Ling et al. [51] found, unexpectedly to us, mean FA *increases* in the CCs of HCs, rather than *decreases* as found here in TBI participants. Partly because the sample of Ling et al. included adult HCs, these authors proposed that head motion—rather than natural aging—accounted for the FA increases they identified.

Across ~6 months, Lancaster et al. [52] found no significant diffusion tensor imaging-derived diffusivity changes in HCs aged 18–20 y ($\mu \pm \sigma = 20 \pm 2$ y). Although these authors quantified radial and axial diffusivities rather than FA, their findings likely parallel ours due to the algebraic relationship between these three variables [53]. In HCs, like Mayer et al., Lancaster et al. found an axial diffusivity *increase* in the BCC as a function of increasing age. Similarly, Vik et al. [54] found an FA *increase* in the left CSTs of

HCs aged 52–66 y ($\mu \pm \sigma = 59 \pm 7$ y) and imaged across 3–4 years, whereas we found an FA *decrease*. Finally, Yin et al. [55] quantified WM changes in HCs aged 26–50 ($\mu \pm \sigma = 38 \pm 12$ y) and found no effect (Cohen's $d = 0$) associated with FA change in the BCC. This is in contrast with our effect size of $d = 0.29$ associated with FA decrease in TBI participants (Table 2).

In summary, previous studies found either very small increases or no change in callosal mean FA among HCs, whereas we found moderate FA decreases among TBI participants across comparable time intervals. Other studies' findings of very small FA increase in HCs are incompatible with natural aging effects on callosal WM (whose mean FA decreases with age), such that the increases in question are likely artifactual [51]. This may indicate that in HCs, across a ~6-month period, aging effects on mean FA may be comparable to those of DWI motion artifacts, such that detecting the former could be very challenging. Nevertheless, we acknowledge that our lack of a reference sample is a limitation of this study.

As individuals age, they accumulate multiple pathologies related not only to typical aging but also to processes related to Alzheimer's disease, neurovascular disease, and/or to proteinopathies involved in other clinical conditions. For this reason, the WM degradation quantified in this study is likely due not only to TBI but also, at least in part, to non-traumatic processes. Because such processes can interact with TBI, the statistical associations identified here may be multifactorial rather than associated with TBI alone. Nevertheless, as already stated, previous studies of older control participants without TBI found hardly any WM degradation over the follow-up period of our study. The longer temporal course associated with typical aging supports the interpretation that TBI is the predominant cause of the WM degradation quantified here over ~6 months.

Abbreviations BCC: Body of the corpus callosum; CC: Corpus callosum; CI: Confidence interval; CMB: Cerebral microbleed; CST: Corticospinal tract; DWI: Diffusion-weighted imaging; FA: Fractional anisotropy; GCC: Genu of the corpus callosum; GCS: Glasgow Coma Scale; GM: Gray matter; ILF: Inferior longitudinal fasciculus; IOFF: Inferior occipitofrontal fasciculus; MdLF: Middle longitudinal fasciculus; mTBI: Mild traumatic brain injury; PC: Principal component; PCA: Principal component analysis; SCC: Splenium of the corpus callosum; Sup-F: Superficial frontal; Sup-P: Superficial parietal; Sup-T: Superficial temporal; SWI: Susceptibility-weighted

imaging; TBI: Traumatic brain injury **Acknowledgements** The authors are thankful to study participants and to Alexander S. Maher for his editorial assistance.

Author contribution Authors contributed to study design (D.J.R., D.J.O., H.C.C., A.I.), participant recruitment (L.G., A.I.), data analysis (D.J.R., A.D., K.A.R., N.N.C., V.N., F.Z.), result interpretation (D.J.R., A.D., L.G., N.S.-B., H.C.C., A.I.), and manuscript redaction (D.J.R., A.D., N.S.-B., H.C.C., A.I.).

Funding This work was supported by the National Institutes of Health (grant R01 NS 100973 to A.I.), by the Department of Defense (award W81-XWH-1810413 to A.I.), by a grant from the James J. and Sue Femino Foundation to A.I., by a Hanson-Thorell Research Scholarship to A.I., by the Undergraduate Research Associate Program (URAP) at the University of Southern California, and by the Center for Undergraduate Research in Viterbi Engineering (CURVE) at the University of Southern California. L.J.O. and F.Z. acknowledge funding from the National Institutes of Health, including the National Institute of Biomedical Imaging and Bioengineering (grants P41 EB 015902, P41 EB 015898, P41 EB 028741) and the National Institute of Mental Health (grants R01 MH 074794, R01 MH 125860, and R01 MH 119222).

Data availability Primary data generated and/or analyzed during the current study are available subject to a data transfer agreement. At the request of some participants, their written permission is additionally required in some cases.

Code availability Programming code developed and used for the study is available from the corresponding author subject to an intellectual property agreement.

Declarations

Ethics approval This study was undertaken in adherence to the US Code of Federal Regulations (45 CFR 46) and with approval from the Institutional Review Board at the University of Southern California.

Consent to participate All participants provided written informed consent.

Consent for publication All authors provided their consent to publish this study in its current form.

Competing interests The authors declare no competing interests.

References

1. Rockhill CM, et al. Health care costs associated with traumatic brain injury and psychiatric illness in adults. *J Neurotrauma*. 2012;29(6):1038–46.

2. Taylor CA, et al. Traumatic brain injury-related emergency department visits, hospitalizations, and deaths – United States, 2007 and 2013. *MMWR Surveill Summ.* 2017;66(9):1–16.
3. Biswas RK, Kabir E, King R. Effect of sex and age on traumatic brain injury: a geographical comparative study. *Arch Public Health.* 2017;75:43.
4. Marquez de la Plata CD, et al. Impact of age on long-term recovery from traumatic brain injury. *Arch Phys Med Rehabil.* 2008;89(5):896–903.
5. Testa JA, et al. Outcome after traumatic brain injury: effects of aging on recovery. *Arch Phys Med Rehabil.* 2005;86(9):1815–23.
6. Najem D, et al. Traumatic brain injury: classification, models, and markers. *Biochem Cell Biol.* 2018;96(4):391–406.
7. Skandsen T, et al. Incidence of mild traumatic brain injury: a prospective hospital, emergency room and general practitioner-based study. *Front Neurol.* 2019;10:638.
8. Freeze WM, et al. Blood–brain barrier leakage and microvascular lesions in cerebral amyloid angiopathy. *Stroke.* 2019;50(2):328–35.
9. Rostowsky KA, Maher AS, Irimia A. Macroscale white matter alterations due to traumatic cerebral microhemorrhages are revealed by diffusion tensor imaging. *Front Neurol.* 2018;9:948.
10. Liao R, et al. Performance of unscented Kalman filter tractography in edema: analysis of the two-tensor model. *Neuroimage Clin.* 2017;15:819–31.
11. Zhang F, et al. An anatomically curated fiber clustering white matter atlas for consistent white matter tract parcellation across the lifespan. *Neuroimage.* 2018;179:429–47.
12. Jolliffe IT. Discarding variables in a principal component analysis. I: artificial data. *Appl Stat Ser C.* 1972;21(2):160–73.
13. Jolliffe IT. Discarding variables in a principal component analysis. II: real data. *Appl Stat Ser C.* 1973;22(1):21–31.
14. Irimia, A, Bradshaw, LA. Ellipsoidal electrogastric forward modelling. *Physics Med Biol.* 2005; 50(18):4429.
15. Tremblay S, et al. Diffuse white matter tract abnormalities in clinically normal ageing retired athletes with a history of sports-related concussions. *Brain.* 2014;137(Pt 11):2997–3011.
16. Liu H, et al. Aging of cerebral white matter. *Ageing Res Rev.* 2017;34:64–76.
17. Tremblay S, et al. Mild traumatic brain injury: the effect of age at trauma onset on brain structure integrity. *Neuroimage Clin.* 2019;23:101907.
18. Gardner A, et al. A systematic review of diffusion tensor imaging findings in sports-related concussion. *J Neurotrauma.* 2012;29(16):2521–38.
19. Stamm JM, et al. Age at first exposure to football is associated with altered corpus callosum white matter microstructure in former professional football players. *J Neurotrauma.* 2015;32(22):1768–76.
20. Trotter BB, et al. Military blast exposure, ageing and white matter integrity. *Brain.* 2015;138(Pt 8):2278–92.
21. Irimia, A, Van Horn, JD. Functional neuroimaging of traumatic brain injury: advances and clinical utility. *Neuropsychiatr Dis Treat.* 2011;11:2355.
22. Irimia, A, Torgerson, CM, Goh, SYM, Van Horn, JD. Statistical estimation of physiological brain age as a descriptor of senescence rate during adulthood. *Brain Imaging Behav.* 2015;9(4):678–689.
23. Halgren E, Sherfey JS, Irimia A, Dale AM, Marinkovic K. Sequential temporo-fronto-temporal activation during monitoring of the auditory environment for temporal patterns. *Human Brain Mapping.* 2011;32(8):1260.
24. Caeyenberghs K, et al. Bimanual coordination and corpus callosum microstructure in young adults with traumatic brain injury: a diffusion tensor imaging study. *J Neurotrauma.* 2011;28(6):897–913.
25. Ewing-Cobbs L, et al. Corpus callosum diffusion anisotropy correlates with neuropsychological outcomes in twins discordant for traumatic brain injury. *AJNR Am J Neuroradiol.* 2006;27(4):879–81.
26. Funnell MG, Corballis PM, Gazzaniga MS. Insights into the functional specificity of the human corpus callosum. *Brain.* 2000;123(5):920–6.
27. Ota M, et al. Age-related degeneration of corpus callosum measured with diffusion tensor imaging. *NeuroImage.* 2006; 31(4).
28. Stojanovski S, et al. Microstructural abnormalities in deep and superficial white matter in youths with mild traumatic brain injury. *NeuroImage Clin.* 2019; 24.
29. Phillips OR, et al. Superficial white matter: effects of age, sex, and hemisphere. *Brain Connect.* 2013;3(2):146–59.
30. Herbet G, Moritz-Gasser S, Duffau H. Direct evidence for the contributive role of the right inferior fronto-occipital fasciculus in non-verbal semantic cognition. *Brain Struct Funct.* 2017;222(4):1597–610.
31. Goldstein FC, Levin HS. Cognitive outcome after mild and moderate traumatic brain injury in older adults. *J Clin Exp Neuropsychol.* 2001;23(6):739–53.
32. Nazeri A, et al. Superficial white matter as a novel substrate of age-related cognitive decline. *Neurobiol Aging.* 2015;36(6).
33. Bazarian JJ, et al. Sex differences in outcome after mild traumatic brain injury. *J Neurotrauma.* 2010;27(3):527–39.
34. Fakhran S, et al. Sex differences in white matter abnormalities after mild traumatic brain injury: localization and correlation with outcome. *Radiology.* 2014;272:815–23.
35. Han Z, et al. White matter structural connectivity underlying semantic processing: evidence from brain damaged patients. *Brain.* 2013;136(Pt 10).
36. Lawrence TP, et al. Early detection of cerebral microbleeds following traumatic brain injury using MRI in the hyper-acute phase. *Neurosci Lett.* 2017;655:143–50.
37. Gyanwali B, et al. Mixed-location cerebral microbleeds: an imaging biomarker for cerebrovascular pathology in cognitive impairment and dementia in a memory clinic population. *J Alzheimers Dis.* 2019;71(4):1309–20.
38. Reeves TM, Phillips LL, Povlishock JT. Myelinated and unmyelinated axons of the corpus callosum differ in vulnerability and functional recovery following traumatic brain injury. *Exp Neurol.* 2005;196(1).
39. Bigler E, et al. The temporal stem in traumatic brain injury: preliminary findings. *Brain Imaging Behav.* 2010;4(3):270–82.

40. Conta A, Stelzner D. Differential vulnerability of propriospinal tract neurons to spinal cord contusion injury. *J Comp Neurol*. 2004;479:347–59.
41. Makris N, et al. Human middle longitudinal fascicle: segregation and behavioral-clinical implications of two distinct fiber connections linking temporal pole and superior temporal gyrus with the angular gyrus or superior parietal lobule using multi-tensor tractography. *Brain Imaging Behav*. 2013;7(3):335–52.
42. Makris N, et al. Mapping temporo-parietal and temporo-occipital cortico-cortical connections of the human middle longitudinal fascicle in subject-specific, probabilistic, and stereotaxic Talairach spaces. *Brain Imaging Behav*. 2017;11(5):1258–77.
43. Shimizu Y, Sakai KL. Visualization of gray matter myelin and fiber bundles critical for relative pitch: a role of the left posterior long insular cortex. *Brain Nerve*. 2015;67(9):1147–55.
44. Bartzokis G. Age-related myelin breakdown: a developmental model of cognitive decline and Alzheimer's disease. *Neurobiol Aging*. 2004; 25(1).
45. Butt AM, Berry M. Oligodendrocytes and the control of myelination in vivo: new insights from the rat anterior medullary velum. *J Neurosci Res*. 2000;59(4).
46. Edlow BL, et al. Diffusion tensor imaging in acute-to-sub-acute traumatic brain injury: a longitudinal analysis. *BMC Neurol*. 2016;16(1):2.
47. Ling JM, et al. Biomarkers of increased diffusion anisotropy in semi-acute mild traumatic brain injury: a longitudinal perspective. *Brain*. 2012;135(Pt 4).
48. Newcombe V, et al. Dynamic changes in white matter abnormalities correlate with late improvement and deterioration following TBI: a diffusion tensor imaging study. *Neurorehabil Neural Repair*. 2016;30(1).
49. Patel JB, et al. Structural and volumetric brain MRI findings in mild traumatic brain injury. *Am J Neuroradiol*. 2020;41(1):92.
50. Mayer AR, et al. Functional connectivity in mild traumatic brain injury. *Hum Brain Mapp*. 2011;32(11):1825–35.
51. Ling J, et al. Head injury or head motion? Assessment and quantification of motion artifacts in diffusion tensor imaging studies. *Hum Brain Mapp*. 2012;33(1):50–62.
52. Lancaster MA, et al. Chronic differences in white matter integrity following sport-related concussion as measured by diffusion MRI: 6-month follow-up. *Hum Brain Mapp*. 2018;39(11):4276–89.
53. Winklewski PJ, et al. Understanding the physiopathology behind axial and radial diffusivity changes – what do we know? *Front Neurol*. 2018;9:92.
54. Vik A, et al. Fractional anisotropy shows differential reduction in frontal-subcortical fiber bundles – a longitudinal MRI study of 76 middle-aged and older adults. *Front Aging Neurosci*. 2015;7:81.
55. Yin B, et al. Longitudinal changes in diffusion tensor imaging following mild traumatic brain injury and correlation with outcome. *Front Neural Circuits*. 2019;13:28.

Publisher's note Springer Nature remains neutral with regard to jurisdictional claims in published maps and institutional affiliations.